SEDE ADMINISTRATIVA

INSTITUTO DE CIÊNCIAS BIOMÉDICAS ABEL SALAZAR
FACULDADE DE FARMÁCIA

New anticancer drug candidates by targeting p53/p73: structural studies and nanodelivery systems
Ana Sara de Carvalho Gomes

U.PORTO

Ana Sara de Carvalho Gomes. New anticancer drug candidates by targeting p53/p73: structural studies and nanodelivery systems

D.ICBAS 2019

U.PORTO

DOCTORAL STUDIES IN
MOLECULAR AND CELLULAR BIOTECHNOLOGY APPLIED TO HEALTH SCIENCES

New anticancer drug candidates by targeting p53/p73: structural studies and nanodelivery systems

Ana Sara de Carvalho Gomes

D
2019

DOCTORAL STUDIES IN

MOLECULAR AND CELLULAR BIOTECHNOLOGY APPLIED TO HEALTH SCIENCES

New anticancer drug candidates by targeting p53/p73: structural studies and nanodelivery systems

Ana Sara de Carvalho Gomes

D

2019

Ana Sara de Carvalho Gomes

New anticancer drug candidates by targeting p53/p73: structural studies and nanodelivery systems

Tese de Candidatura ao grau de Doutor em Biotecnologia Molecular e Celular Aplicada às Ciências da Saúde;
Programa Doutoral da Universidade do Porto (Instituto de Ciências Biomédicas de Abel Salazar e Faculdade de Farmácia)

Orientadora – Lucília Helena Ataíde Saraiva

Categoria – Professora Auxiliar

Afiliação – LAQV-REQUIMTE, Laboratório de Microbiologia, Departamento de Ciências Biológicas, Faculdade de Farmácia da Universidade do Porto

Co-orientadora – Maria Emília da Silva Pereira de Sousa

Categoria – Professora Auxiliar

Afiliação – Laboratório Química Orgânica e Farmacêutica, Departamento de Ciências Químicas, Faculdade de Farmácia da Universidade do Porto; CIIMAR - Interdisciplinary Centre of Marine and Environmental Research, Porto, Portugal

Co-orientadora – Maria de La Salette de Freitas Fernandes Hipólito Reis Dias Rodrigues

Categoria – Professora Associada

Afiliação – LAQV-REQUIMTE, Laboratório de Química Aplicada, Departamento de Ciências Químicas, Faculdade de Farmácia da Universidade do Porto

The work presented in this thesis was developed at:

Host institution:

LAQV-REQUIMTE, Lab. de Microbiologia, Departamento de Ciências Biológicas,
Faculdade de Farmácia, Universidade do Porto, 4050-313 Porto, Portugal

and

Collaborating institutions:

CEB-Centre of Biological Engineering, University of Minho,
Campus Gualtar, 4710-057 Braga, Portugal

UCIBIO-REQUIMTE, Departamento de Química, Faculdade de Ciências e
Tecnologia, Universidade Nova de Lisboa, 2829-516 Caparica, Portugal

CIIMAR - Interdisciplinary Centre of Marine and Environmental Research,
4450-208 Matosinhos, Portugal

Drug Research Program, Division of Pharmaceutical Chemistry and Technology,
Faculty of Pharmacy, University of Helsinki, FI-00014 Helsinki, Finland

Financial support

This work was supported by European Union (FEDER funds POCI/01/0145/FEDER/007728 through Programa Operacional Factores de Competitividade – COMPETE), by National Funds (FCT/MCTES, Fundação para a Ciência e Tecnologia, and Ministério da Ciência, Tecnologia e Ensino Superior) through UID/QUI/50006/2019, and the projects (3599-PPCDT) PTDC/DTP-FTO/1981/2014 – POCI-01-0145-FEDER-016581, and (3599-PPCDT) PTDC/MAR-BIO/4694/2014-POCI-01-0145-FEDER-016790, and by the University of Helsinki Research Funds. We also thank FCT for the financial support of the fellowships PD/BI/105912/2014 and PD/BD/114046/2015 (A. S. Gomes), through the BiotechHealth Programme (Doctoral Programme on Cellular and Molecular Biotechnology Applied to Health Sciences; PD/00016/2012).

Cofinanciado por:

Publications

This thesis is composed by the following literature review and research works already published, submitted and under revision, or in preparation:

Ana Sara Gomes, Helena Ramos, Joana Soares, Lucília Saraiva (2018) **“***p53 and glucose metabolism: an orchestra to be directed in cancer therapy”* Pharmacological Research, 131:75-86. doi: 10.1016/j.phrs.2018.03.015. (Review)

Ana Sara Gomes, Alexandra Carvalho, Lucília Saraiva (2019) “*Structural insights on p53: inputs on its druggability”*, manuscript in preparation. (Review)

Ana Sara Gomes*, Filipa Trovão*, Benedita Andrade Pinheiro, Filipe Freire, Sara Gomes, Carla Oliveira, Lucília Domingues, Maria João Romão, Lucília Saraiva, Ana Luísa Carvalho (2018) “*The crystal structure of the R280K mutant of human p53 explains the loss of DNA binding”* International Journal of Molecular Sciences, 19(4). pii: E1184. doi: 10.3390/ijms19041184. (Research)

Ana Sara Gomes*, Helena Ramos*, Sara Gomes, Joana B Loureiro, Joana Soares, Valentina Barcherini, Paola Monti, Gilberto Fronza, Carla Oliveira, Lucília Domingues, Margarida Bastos, Daniel FAR Dourado, Ana Luísa Carvalho, Maria João Romão, Benedita Andrade Pinheiro, Alexandra Carvalho, Filipa Marcelo, Maria MM Santos, Lucília Saraiva (2018) *“SLMP53-1 reactivates mutant p53 by targeting DNA-binding domain”,* under revision. (Research)

Ana Sara Gomes, Alexandra Correia, Antti Rahikkala, Flavia Fontana, João Pedro Martins, Zehua Liu, Dongfei Liu, Madalena M Pinto, Emília Sousa, Lucília Saraiva, Hélder Santos (2019) “*Hyaluronic acid and folic acid functionalized mesoporous silicon nanoparticles for enhancement of LEM2 anticancer activity”*, manuscript in preparation. (Research)

*The authors contributed equally to the work.

Acknowledgements

I thank Professor Lucília Saraiva, my supervisor, for welcoming me in her laboratory, and giving me the chance to learn about and do research in microbiotechnology and onco-pharmacology, specifically in the exciting universe of the tumor suppressor protein p53. I am truly thankful for our talks, her guidance and resilience with me. I thank her scientific knowledge, curiosity and ambition, proposing me different challenges, I have learnt a lot from her. I have grown as a person and as a scientist under her active watch. Also, I thank her for giving me the opportunity to engage with different research groups, contributing widely to my knowledge and break the boundaries among different scientific fields, of utmost importance in p53 investigation.

To my co-supervisor, Professor Emília Sousa, I thank for all advices and always believing in me, since my early steps in research. I thank Professor Emília for all her teachings, friendship, and for inspiring me in Pharmaceutical Chemistry, and how to embrace a multi-sided approach regarding Pedagogy and Science contributing to the education of new generations. This had imbuing in me the will to grow as a mentor, the reason that led me to apply for PhD.

I thank Professor Salette Reis, my co-supervisor, for her experience and availability in helping me. I have learnt the ABC of nanotechnology from her.

I thank Professor Lucília Domingues for receiving me at her lab at CEB-University of Minho. I am very thankful to Dr. Carla Oliveira for all her close guidance and effort in teaching me molecular biology methodologies and recombinant protein production. It was a big and challenging task, and I cannot thank enough for her patience and valuable knowledge. I am also thankful to Dr. Tatiana Aguiar for her help and good advices. Thanks to the PhD students Joana Cunha and Rui Silva for the good lab environment.

I thank Professors Ana Luísa Carvalho and Maria João Romão for kindly welcoming me at Xtal group at FCT-Universidade Nova Lisboa. I thank Professor Ana Luísa Carvalho for the supervision and introducing protein structural studies to me. I am thankful to Drs. Filipe Freire, Benedita Pinheiro, and MSc Filipa Trovão for the support in recombinant protein production, crystallization screenings, and structure elucidation. I thank to other group members, namely Drs. Márcia Correia, Catarina Coelho, Marino Santos, Angelina Palma, Teresa Silva, and PhD students Diana Ribeiro, Raquel Costa, Francisco Leisico, and Viviana Correia for the scientific exchange and kindness.

I am very thankful to Dr. Filipa Marcelo for the NMR analysis, her precious time, vast knowledge and valuable scientific discussions. I am also thankful to Dr. Alexandra Carvalho for the *in silico* analysis.

I thank Professor Margarida Bastos, Dr. Tânia Silva, from Faculty of Sciences, University of Porto, and Dr. Xavier Salvatella, from Institute for Research in Biomedicine Barcelona, for their teachings in binding assays.

To Professor Hélder Santos, I thank for welcoming me in Santos' Lab, University of Helsinki, it was an honor to be a visitant student in his multicultural group. I am thankful for his precious time and expertise in nanotechnology, also for all the teachings and productive scientific discussions. I also thank his dynamism, widening my horizons by enrolling different group, division and faculty meetings. I thank to Dr. Dongfei Liu for the advices and scientific discussions. I am very thankful to Alexandra Correia, the coolest technician ever! I have no words for all her dedication, support and friendship. Thanks for helping me with many experiments, and keep my moral up, even when the day was already long. I am very thankful to Dr. Antti Rahikalla for the TEM analysis, valuable knowledge, friendship and finest humor! To the PhD students João Pedro Martins, Flavia Fontana and Zehua Liu, I am very thankful for sharing their experience about confocal and FACS analysis, and nanoparticles functionalization. I am also greatly thankful to the other group and division members at that time, namely PhD students Patrícia Figueiredo, Serena Bertoni, Giulia Torrieri, Emma Hokkala, Nazanin Ezazi, Jernej Štukelj, Tomás Ramos, and Drs. Mónica Ferreira, Sami Svanbäck, Vimalkumar Balasubramanian, Wei Li, Yaping Ding, and Patrick Almeida, and many others. Thanks for all advices, friendship, great science, and the incredible cooperative environment. I feel very lucky to have met all of them. Lots of love and successes for you!

I am tremendously thankful to my lab colleagues and friends, Drs. Joana Soares, Cláudia Bessa, PhD students Sara Gomes, Helena Ramos, Liliana Raimundo and Joana Loureiro. Uau! They are the best! Thanks for welcoming and embracing me, even when I was feeling an outcast. Thanks for teaching me, for the complicity, science and dreams exchange. You are inexhaustible and my warmest wishes of success go to you! I thank Sara, Helena and Joana S. for the co-work developed; also, Sara, for our trips to Braga, Lisbon and around Porto, what a great company! I also thank to other group members with whom I have shared a shorter period, but also important for our good lab environment, namely Drs. Mariana Leão, Nair Campos, MSc Sofia Salazar, Agostinho Lemos, Bryan Fernandes, Beatriz Silva, Madalena Monteiro, Rute Pinheiro e Joana Almeida. I also thank Cristina Costa for her friendship and help.

I thank the members of the Lab. of Organic and Pharmaceutical Chemistry, FFUP, for all the confidence they deposited on me as Invited Assistant. I am very thankful to Professor Madalena Pinto for inviting me to that incredible adventure, her dynamism and wise advices. I also thank to Professors Emília Sousa, Carla Oliveira, Marta Correia da Silva, Drs. Elisângela Costa and Andreia Palmeira for sharing the teaching of laboratory classes of Pharmaceutical Chemistry I and II. I am also very thankful to everyone for the scientific and experience exchange, and friendly support, namely Professors Carlos Afonso, Honorina Cidade, and Maria José Gonzalez, technicians Sara Cravo and Gisela Adriano, and PhD student José Soares. A special word to Marta Correia da Silva and Mafalda Paiva for our talks, friendship and being there!

I thank my BiotechHealth colleagues. I have learnt a lot from all of them, either in the symposia or by casual meetings. I am especially thankful to my 2nd Edition mates, Joana Magalhães, Joana Marques, Daniela Vasconcelos, Daniela Freitas, José Plácido, and Flávia Castro for all our exchanges, the supportive spirit in the challenges that we faced together, and always having a friendly attitude. I wish a bright future for all of them! Also, I would like to thank to the BiotechHealth Scientific Committee and Support Team for being always nice and prompt to help.

Also, a special word to the ESSA project organizers from FPCEUP and participant auditor colleagues, for the remarkable adventure on Social Responsibility in Universities! Thanks for the pedagogic approach, the search for a holistic university, and friendship!

I thank to all my friends! What a journey it has been and how lucky I have been! They are my buffers. To the beautiful and perfect girls that have been always there when I most needed in good and bad moments, Sónia Garrido, Marta Almada, Rita Pinto, Tatiana Guimarães, Ana Rute Vaz, Francisca Martins, Inês Martins, Maria Luís Gonçalves, Rita Almada, Helena Pimentel and Ana Santos. I have no words to thank Sónia for having me at her place for the almost six months that I had lived in Lisbon. It was a lovely time. João Pinheiro, he is one of a kind, doesn´t matter how far we are, but how close we support each other. Thanks! I also thank Aleksi Wallenius, and new friends Luisa Woestmann, Jhon Alves, Mary Karyda, Anna Lue, Cristiana Correia, and Antti Korpin Tie community for making me feel home in Helsinki, for all the adventures and sharings.

Carlos Trancoso! Obrigada por me teres dado ziliões de novas perspectivas todos os dias. Obrigada por dançares comigo ao som de qualquer música que possa estar a tocar. Tu mantiveste-me na linha tantas e tantas vezes. Obrigada por toda a nossa partilha, pelo teu cuidado, carinho, amor e amizade. És essencial. Obrigada também à tua família, São, Duarte, Catarina, Cris, Zé, Natália por me terem acolhido de forma tão genuína. Gosto muito de vós!

Por fim, tenho um agradecimento muito especial à minha família por todo o apoio, amor, e relembrarem-me inúmeras vezes de que o que os cientistas fazem é único e pioneiro. Agradeço à minha Tia Lourdes, ao meu Tio Albino, ao meu primo Virgílio, ao meu afilhado Diogo, e principalmente à minha mãe Emília e à minha prima Fátima. Mãe e Fátima, sem vós não seria possível, sois incansáveis, obrigada por todos os colos, todos os risos e puxões de orelhas.

Abstract

Cancer is a major public health concern with increasing incidence and mortality worldwide. The tumor suppressor protein p53, the so called “guardian of the genome”, is impaired in most human cancers, over 50% due to missense mutations. The advances in understanding cancer pathobiology have highlighted the crucial role of mutant (mut)p53 in tumor initiation, progression and dissemination, rendering mutp53 one of the most promising targets for anticancer therapy. Great advances have been achieved in the discovery of diverse mutp53 reactivators that are able to restore the wild-type (wt)-like activity to mutp53. Nonetheless, mutp53 reactivators are still not available for clinical use, and only two small-molecules are under clinical trials (PRIMA-1^{MET} and COTI-2). In fact, drugging mutp53 has shown to be a challenging task, which has prompted researchers and clinicians to investigate new possibilities in the universe of mutp53 pharmacology, structure, and biology to discover more efficient mutp53-targeting agents able to be successfully translated into the clinic.

Recently, our group has reported the *(S)*-tryptophanol-derived oxazoloisoindolinone SLMP53-1 as a new reactivator of mutp53 R280K. SLMP53-1 restores the DNA-binding ability, and subsequent transcriptional activity, to mutp53 R280K. Its promising *in vivo* p53-dependent antitumor activity against tumors bearing mutp53 R280K led us to further investigate the molecular mechanism by which SLMP53-1 reactivates mutp53 R280K, and its potential to reactivate other mutp53 forms besides R280K. To address the proposed objectives, the recombinant human mutp53 R280K DNA binding domain (DBD) was produced and its structure was elucidated by X-ray crystallography. The results obtained revealed that, in mutp53 R280K, the substitution of the arginine for the lysine, a shorter amino acid residue, halts p53 transcriptional function, as it abrogates the establishment of hydrogen bonds essential for DNA recognition. By saturation transfer difference (STD)-NMR, it was verified that SLMP53-1 binds to recombinant mutp53 R280K DBD, being the SLMP53-1 aromatic regions, particularly the indole moiety, important for molecular interactions. Consistently, the full-length mutp53 R280K target engagement with SLMP53-1 was confirmed in cancer cells by cellular thermal shift assay (CETSA). As wtp53, the mutp53 R280K DBD lacks well-defined pockets capable to dock ligands. Accordingly, *in silico* analysis indicated that SLMP53-1 may establish non-covalent interactions with positively charged regions of mutp53 R280K DBD surface. Additionally, using yeast and cancer cells ectopically expressing a wide panel of mutp53 forms, the ability of SLMP53-1 to reactivate other mup53s, namely R175H, G245D, R248Q, R273H and R282W, was also demonstrated.

Our group has also reported the xanthone derivative LEM2 as an activator of the p53 family transcription protein TAp73, by inhibiting its interaction with both murine double minute (MDM)2 and mutp53. Despite the promising antitumor activity of LEM2 against cancer cells, including patient-derived neuroblastoma cancer cells, its poor aqueous solubility limited further *in vivo* studies. In this thesis, it was intended to improve LEM2 bioavailability by developing mesoporous silicon (PSi) nanodelivery systems. For a targeted drug delivery, nanoparticles (NPs) were functionalized with hyaluronic acid or folic acid. LEM2-loaded NPs increased drug aqueous solubility and LEM2 antitumor activity when compared to the bulk drug. Nevertheless, for *in vivo* assays a further optimization of the loading degree is still required.

Collectively, the present thesis brings new insights on mutp53 structure, biology, and druggability. In addition, the elucidation of SLMP53-1 molecular mechanism of action further reinforces its potential as drug candidate in personalized anticancer therapy. Also, the PSi-based nanodelivery systems proved to be a promising strategy to improve LEM2 bioavailability and antitumor activity, which will be relevant for the potential use of this potent TAp73 activator in anticancer therapy.

Keywords:

Anticancer therapy; cancer; mutant p53; mesoporous silicon nanoparticles; reactivator; TAp73

Resumo

O cancro é uma das maiores preocupações em Saúde Pública com taxas de incidência e mortabilidade crescentes a nível mundial. A proteína supressora tumoral p53, também designada por “guardiã do genoma”, tem a sua função comprometida na maioria dos cancros humanos, devendo-se cerca de 50% dos casos a mutações pontuais do tipo *missense*. Os avanços na compreensão da patobiologia do cancro identificaram o papel crucial que a p53 mutante (mutp53) tem na iniciação, progressão e disseminação do tumor, tornando a mutp53 um dos alvos mais promissores para a terapêutica anticancerígena. Avanços notórios têm sido alcançados na descoberta de diversos reactivadores da mutp53 capazes de restaurar a actividade nativa à mutp53. No entanto, o uso destes reactivadores ainda não se encontra disponível para uso na clínica, e somente dois compostos estão em ensaios clínicos (PRIMA-1^{MET} e COTI-2). De facto, a regulação farmacológica da mup53 tem-se revelado um grande desafio, o que tem estimulado os investigadores e clínicos a explorar novas possibilidades no universo da farmacologia, estrutura e biologia da p53. Estas abordagens têm como objectivo promover a descoberta de agentes eficazes dirigidos à mutp53 que sejam capazes de alcançar a prática clínica.

Recentemente, o nosso grupo descreveu a *(S)*-oxazoloisoindolinona derivada do triptofano SLMP53-1 como sendo um novo reactivador da mutp53 R280K. O SLMP53-1 restaura a ligação da mutp53 R280K ao DNA, e subsequentemente a sua actividade transcricional. A demonstrada actividade antitumoral *in vivo* dependente da p53, levou-nos a querer compreender o mecanismo pelo qual o SLMP53-1 é capaz de reactivar a mutp53 R280K, tal como o seu potencial em reactivar outras mutp53. Para responder aos objectivos propostos, o domínio de ligação ao DNA (DBD) da proteína recombinante mutp53 R280K foi produzido e a sua estrutura elucidada por cristalografia de raio-X. Os resultados obtidos revelaram que a substituição da arginina por um aminoácido mais curto de lisina suprime as interações de hidrogénio essenciais para o reconhecimento do DNA, e subsequente função transcricional. Usando a metodologia de transferência de saturação por diferença em ressonância magnética nuclear (STD-NMR), foi verificado que o SLMP53-1 liga-se à proteína recombinante mutp53 R280K DBD, sendo que as suas regiões aromáticas, especialmente o grupo indol, são importantes para a interacção. A ligação do SLMP53-1 à proteína mutp53 R280K foi confirmada em células tumorais através da técnica de desvio térmico celular (CETSA). Tal como a proteína nativa, a mutp53 R280K DBD é desprovida de locais hidrofóbicos bem definidos capazes de acomodar ligandos. Uma análise *in silico* indicou que o SLMP53-1 pode estabelecer interacções não-covalentes com regiões positivas da superfície da mutp53 R280K DBD.

Adicionalmente, expressando um painel de diferentes mutp53 em modelo de células de levedura e tumorais, observou-se a capacidade do SLMP53-1 reactivar outras mutp53s, nomeadamente R175H, G245D, R248Q, R273H, and R282W.

O nosso grupo também reportou um derivado xantónico LEM2 como activador de uma proteína da família da p53, a TAp73, através da inibição das suas interações com MDM2 e mutp53. Apesar da promissora actividade antitumoral do LEM2 em células tumorais, incluindo células de neuroblastoma derivadas de pacientes, a sua reduzida solubilidade em água limita a realização de ensaios *in vivo*. No âmbito da presente tese pretendeu-se melhorar a biodisponibilidade do LEM2 através do desenvolvimento de nanovectores de *silicon* mesoporoso (PSi). De forma a obter uma libertação dirigida, as nanopartículas (NPs) foram funcionalizadas com ácido hialurónico ou ácido fólico. As NPs carregadas com LEM2 aumentaram a sua solubilidade e actividade antitumoral, quando comparadas com o LEM2 não encapsulado. No entanto, para a aplicação das LEM2-NPs desenvolvidas em ensaios *in vivo,* será necessário optimizar a carga de LEM2 nas NPs.

Em conclusão, a presente tese revela novos conhecimentos sobre a estrutura, biologia e farmacologia da mutp53. Adicionalmente, a elucidação do mecanismo de acção molecular do SLMP53-1 reforça o seu potencial como candidato a fármaco na terapêutica personalizada do cancro. As NPs de PSi provaram ser uma estratégia promissora para melhorar a biodisponibilidade e actividade antitumoral do LEM2, o que será relevante para a sua potencial utilização na terapêutica oncológica, como um activador potente da TAp73.

Palavras-chave:

Cancro; p53 mutante; nanopartículas de *silicon* mesoporoso; reactivador; TAp73; terapêutica anticancerígena

Acronyms and abbreviations

(BOC)$_2$O – Di-*tert*-butyldicarbonate
ΔN – Truncated *N*-terminal
53BP2 – TP53-binding protein 2
APTES – 3-(Aminopropyl)triethoxysilane
APTES-TCPSi – 3-(Aminopropyl)triethoxysilane modified thermally carbonized mesoporous silicon
ATP – Adenosine triphosphate
BOC - *tert*-Butyloxycarbonyl
CDKN1A – Cyclin-dependent kinase inhibitor 1a
CETSA – Cellular thermal shift assay
CHIP – Carboxy terminus of HSP70-interacting protein
DBD – DNA binding domain
DCE – Dichloroethane
DCM – Dichloromethane
DLS – Dynamic light scattering
DMSO – Dimethyl sulfoxide
DNE – Dominant negative effect
DSF – Differential scanning fluorimetry
DTT – Dithiothreitol
EDC – 1-Ethyl-3-(3-dimethylaminopropyl) carbodiimide
ELS – Electrophoretic light scattering
EM – Electron mycroscopy
ESRF – European Synchrotron Radiation Facility
ETC – Electron transporter chain
FA – Folic acid
FBS – Fetal bovine serum
FITC – Fluorescein isothiocyanate
FR – Folate receptor
FTIR – Fourier-transform infrared spectroscopy
GOF – Gain of function
H – Helix
HA – Hyaluronic acid
HBSS – Hank’s Balanced Salt Solution
HDAC – Histone deacetylase
HEPES – 4-(2-Hydroxyethyl)-1-piperazineethanesulfonic acid

HPLC – High performance liquid chromatography
HSP – Heat shock proteins
IARC – International Agency for Research on Cancer
L – Loop
LD (%) – Loading degree
LOF – Loss of function
LSH – Loop-sheet-helix motif
MDM2/4 – Murine double minute 2/4
MES – 2-(*N*-morpholino) ethanesulfonic acid
Mut – mutant
NHS – *N*-hydroxysuccinimide
NMR – Nuclear magnetic resonance
NPs – Nanoparticles
NRD – Negative regulatory domain
OD – Oligomerization domain
OXPHOS – Oxidative phosphorylation
P300 – Histone acetyltransferase
PDB ID – Protein data bank identification
PdI – Polydispersity index
PEG – polyethylene glycol
Pin1 – Peptidyl-prolyl cis-trans isomerase NIMA-interacting 1
PSi – Mesoporous silicon
PTM – Post translational modification
R.M.S.D. – Root-mean-square deviation of atomic positions
RE – Response element
REDOX – Reduction-oxidation
ROS – Reactive oxygen species
RPMI – Roswell Park Memorial Institute
S – Strand
S100 – S100 calcium binding protein
SAXS – Small angle X-ray scattering
SEC – Size exclusion chromatography
SP – Spermine
SRB – Sulforhodamine B
STD – Saturation transfer difference
TA – Full *N*-terminal
TAD – *N*-terminal transactivation domain

TCPSi – Thermally carbonized mesoporous silicon

TEM – Transmission electron microscopy

THCPSi – Thermally hydrocarbonized mesoporous silicon

TP53 – p53 gene

Un – Undecylenic acid

UnTHCPSi – Undecylenic acid modified thermally hydrocarbonized mesoporous silicon

Wt – Wild-type

Amino acid residues code

A – Alanine

C – Cysteine

D – Aspartic acid

E – Glutamic acid

F – Phenylalanine

G – Glycine

H – Histidine

I – Isoleucine

K – Lysine

L – Leucine

M – Methionine

N – Asparagine

P – Proline

Q – Glutamine

R – Arginine

S – Serine

T – Threonine

V – Valine

W – Tryptophan

Y – Tyrosine

Table of contents

Financial support iii

Publications iv

Acknowledgements v

Abstract ix

Resumo xi

Acronyms and abbreviations xiii

Chapter I - Literature overview 1

- **1. Cancer and p53: general considerations** 2
- **2. Cellular functions of p53** 5
  - 2.1. Regulation of glucose metabolism by p53 8
- **3. Structural features of p53** 11
  - 3.1. DNA recognition by p53 12
- **4. Dynamics and regulation of p53** 17
- **5. Mutant p53** 21
  - 5.1. Mutant p53 deleterious effects on DNA binding and protein stability 23
- **6. Targeting mutant p53** 29
  - 6.1. Cysteine targeting compounds 35
  - 6.2. Thermal stabilizers 38
  - 6.3. Zinc chelating compounds 38
  - 6.4. Non-covalent binding compounds 40
  - 6.5. Compounds indirectly-targeting mutp53 42
  - 6.6. Compounds targeting mutp53 with unknown binding mechanism 42
  - 6.7. Disruptors of protein-protein interaction 43
  - 6.8. Compounds depleting mutp53 44
- **7. Nanotechnology as a strategy to improve pharmacokinetics of drug candidates for anticancer therapy** 45
  - 7.1. Mesoporous silicon nanoparticles 46
- **8. Scope and aims** 50

Chapter II - The crystal structure of the R280K mutant of human p53 explains the loss of DNA binding 51

- **1. Summary** 52
- **2. Materials and methods** 52
  - 2.1. Expression plasmid construction of mutp53 R280K DBD 52
  - 2.2. Recombinant production and purification of mutp53 R280K DBD 53
  - 2.3. Differential scanning fluorimetry (DSF) screening for buffer optimization 53
  - 2.4. Crystallization of mutp53 R280K DBD 54
  - 2.5. Data collection, structure solution, and refinement 54
- **3. Results** 56
  - 3.1. Expression and purification of mutp53 R280K DBD 56
  - 3.2. Crystallization and structural elucidation of mutp53 R280K DBD 56
  - 3.3. Comparison of mutp53 R280K with wtp53 structural model 59
- **4. Discussion** 63

Chapter III - SLMP53-1 reactivates mutant p53 by targeting DNA-binding domain 65

- **1. Summary** 66
- **2. Materials and methods** 66

2.1. Compounds 66
2.2. Yeast and mammalian expression vectors 66
2.3. Saturation transfer difference (STD)-NMR 67
2.4. Computational modeling and molecular docking 68
2.4.1. Molecular dynamics (MD) simulations 68
2.5. Yeast assay 69
2.6. Human cancer cell lines and growth conditions 69
2.7. Cellular thermal shift assay (CETSA) 70
2.8. Transient transfection assay of mutp53 in human NCI-H1299 cancer cells 70
2.9. Sulforhodamine B (SRB) assay 70
2.10. Western blot analysis 70
2.11. Statistical analysis 71
3. Results 71
3.1. SLMP53-1 directly binds to mutp53 R280K DBD 71
3.2. SLMP53-1 restores wt-like function to distinct hotspot mutp53 forms 74
4. Discussion 76

Chapter IV - Hyaluronic acid and folic acid functionalized mesoporous silicon nanoparticles for enhancement of LEM2 anticancer activity 79
1. Summary 80
2. Materials and methods 80
2.1. General 80
2.2. Production of UnTHCPSi and APTES-TCPSi NPs 81
2.3. Nanoparticles functionalization 81
2.3.1. UnTHCPSi-SP-PEG-FA and APTES-TCPSi-PEG-FA 82
2.3.2. UnTHCPSi-SP-HA and APTES-TCPSi-HA 83
2.4. Physicochemical characterization of NPs 83
2.4.1. Pore volume and diameter, and specific surface area of UnTHCPSi and APTES-TCPSi 83
2.4.2. Functionalization, size, dispersity, and surface charge of modified NPs 83
2.5. LEM2 loading in unmodfied and modified NPs 84
2.6. Payload release studies of LEM2-loaded unmodified and modified NPs 85
2.7. Stability study of unmodified and modified NPs in tumor cell culture medium 85
2.8. Human cancer cell lines (general) 85
2.8.1. *In vitro* cytotoxicity studies of bare NPs and LEM2 loaded NPs in MDA-MB-231 and HCT116 cancer cells 85
2.8.2. *In vitro* NPs uptake and association studies in MDA-MB-231 and HCT116 cancer cells 86
2.9. Statistical analysis 87
3. Results 87
3.1. Preparation and physicochemical characterization of the nanoparticles 87
3.2. LEM2 loading, *in vitro* release profile, and stability of the nanoparticles 91
3.3. Modified and unmodified nanoparticles are stable, taken-up and cytocompatible, increasing LEM2 cytotoxicity in human cancer cells 93
4. Discussion 100

Chapter V - General discussion and future perspectives 105

References 111

Annex I - Supporting information of Chapter II xix

Annex II - Supporting information of Chapter III xxv

Annex III - Supporting information of Chapter IV xxxiii

Chapter I

Literature overview

This chapter contains parts of the following articles:

Ana Sara Gomes, Helena Ramos, Joana Soares, Lucília Saraiva L, (2018), “*p53 and glucose metabolism: an orchestra to be directed in cancer therapy”* Pharmacological Research, 131:75-86. doi: 10.1016/j.phrs.2018.03.015.

Ana Sara Gomes, Alexandra Carvalho, Lucília Saraiva, (2019), “*Structural insights on p53: inputs on its druggability”*, manuscript in preparation.

1. Cancer and p53: general considerations

Cancer is a worldwide public health concern related with diverse risk factors, including genetic, environment, population life styles, and increasing ageing. Many advances have been made in cancer prevention, early diagnosis and treatment, reflecting a strong effort and investment from public and private sectors exceeding 115 billion euros, in 2017, for medicines-related costs [1, 2]. Despite this, data from 2018, accounted for an incidence of 18.1 million new cancer cases, 9.6 million deaths, and a 5-year prevalence of 43.8 million cancer cases worldwide [3-6]. Additionally, a projection for 2040 predicts an incidence of 29.5 million new cancer cases and 16.4 million deaths [3, 7]. Although new targeted and innovative biological therapies have emerged on the clinical practice [8], the aforementioned previsions make predictable the requirement of new and more efficient preventive and therapeutic anticancer strategies. For that, a deeper understanding of the complexity of cancer pathobiology has helped in the discovery of key targets to develop new anticancer therapeutic alternatives, in the setting of personalized medicine.

Different cellular oncogenic transforming signatures have been described in tumorigenesis, also known as the hallmarks of cancer [9]. In this context, the tumor suppressor protein p53 rises as a key protein regulator of these hallmarks by inhibiting tumorigenesis, or allowing the tumor onset and progression when lost or inactivated (**Figure 1**) [9-12]. In fact, p53 has represented one of the most promising candidate targets in cancer treatment.

For the past four decades, p53 has presented innumerous challenges to the resilient scientific community. p53 is encoded by the *TP53* gene, and was first reported in 1979 by several groups as an oncogene associated with simian vacuolating virus 40 infection once it was frequently found in cancers [13, 14]. However, in 1989, its status was corrected to tumor suppressor with main function as transcriptional factor, which is compromised in the majority of human cancers due to mutation or inhibition by overexpression of negative regulators, particularly murine double minute (MDM)2 and MDM4 [15, 16]. Since its discovery, p53 has attracted the attention of innumerous researchers, who have scrutinized crucial aspects of its structure, molecular biology, and pharmacology [9, 17, 18]. However, despite the exhaustive integrated multidisciplinary research on p53, the knowledge seems to be still restricted to allow the clinical translation of p53 as an anticancer therapeutic target.

p53 is a complex multi-domain protein with 393 amino acid residues, and a molecular weight of 53 kDa. Its structure is divided into different domains with folded and unfolded nature, and with distinct roles in p53 stability, regulation, assembly in a tetramer, DNA recognition, and transactivation (**Figure 2**): *N*-terminal transactivation domain (TAD;

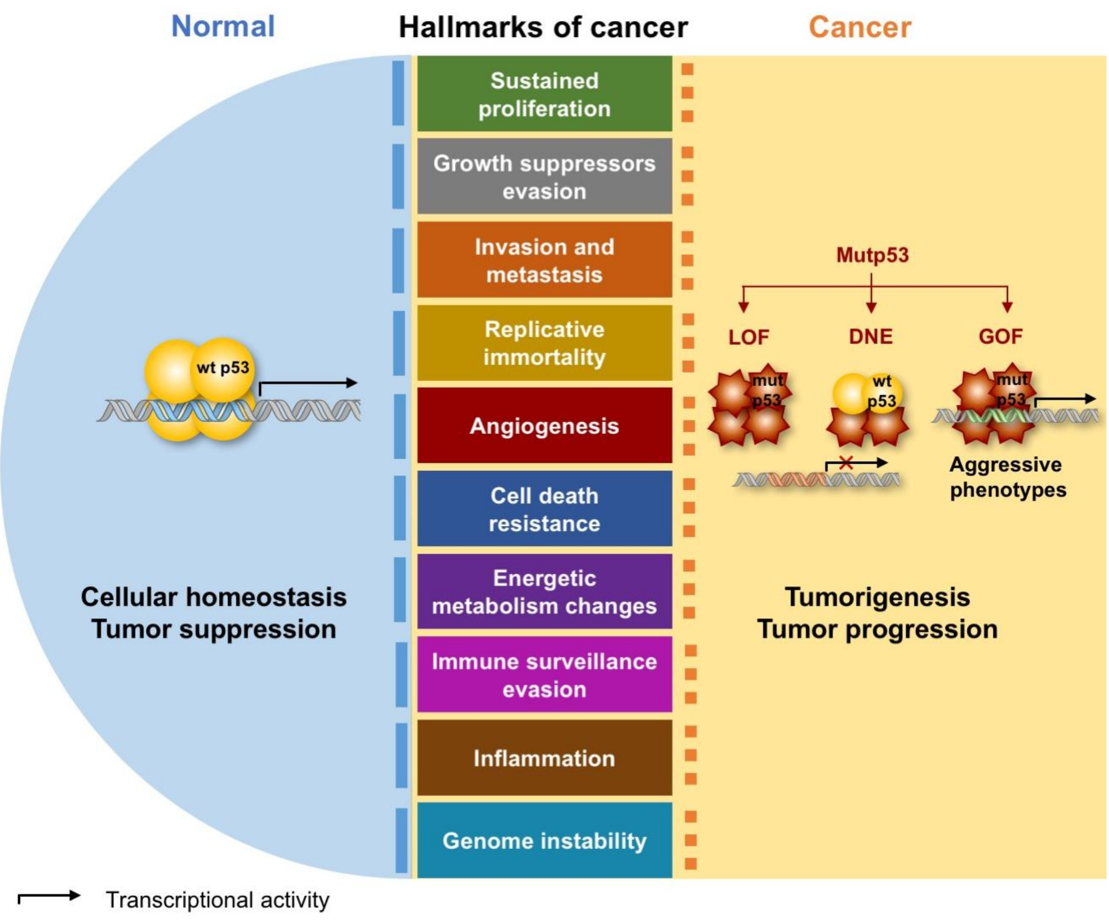
Normal
Hallmarks of cancer
Cancer
Sustained proliferation
Growth suppressors evasion
Invasion and metastasis
Replicative immortality
Angiogenesis
Cell death resistance
Energetic metabolism changes
Immune surveillance evasion
Inflammation
Genome instability
wt p53
Cellular homeostasis
Tumor suppression
Mutp53
LOF
DNE
GOF
mut p53
wt p53
mut p53
Aggressive phenotypes
Tumorigenesis
Tumor progression
Transcriptional activity

Figure 1. Roles of wild-type (wt) and mutant (mut)p53 in the hallmarks of cancer. Cancer occurs via different altered cellular processes that determine oncogenic signals, so called hallmarks of cancer. As a tumor suppressor, wtp53 suppresses these oncogenic pathways (blue solid line), ensuring cellular homeostasis. Conversely, when mutated, p53 promotes tumorigenesis (orange dashed line) due to the loss of function (LOF), dominant negative effect (DNE), or gain of neomorphic oncogenic functions (GOF) related with more aggressive phenotypes. Adapted from [9, 12, 19].

disordered, residues 1–62), proline rich sequence (disordered, residues 63–92), core domain or DNA-binding domain (DBD; ordered, residues 93–312), oligomerization domain (OD; ordered, residues 325–355), and the negative regulatory domain at *C*-terminal (NRD; disordered, residues 356–393) [17]. Furthermore, p53 belongs to a family of structurally related-proteins including p63 and p73, which are also transcriptional factors [20-22]. It is important to refer that p53, p63, and p73 have different isoforms that result from either alternative promoters and alternative splicing (**Figure 2**) [23]. Truncated *N*-terminal (ΔN) and full *N*-terminal (TA) isoforms are products of alternative gene promoters. Generally, ΔN isoforms are transcriptionally inactive, and may act by a dominant negative effect (DNE) over active isoforms, being related with oncogenesis [23, 24]. In opposition, TA isoforms are transcriptionally active. Different ΔN and TA isoforms (*e.g.,* *α*, *β*, and *γ*) are obtained by *C*-terminal alternative splicing and have different biological functions [23, 25]. Despite the relevance of TAp63 and TAp73 in embryonic and nervous system development, respectively, they also have a similar tumor suppressor activity to p53, sharing a common set of target genes and subsequent functions [20, 26]. Some conventional chemotherapies interfere with TAp63 and TAp73, highlighting their therapeutic relevance in cancer treatment [24]. Indeed, in cases of p53 deletion or impairment, TAp73 and TAp63 rise as viable alternatives to p53 in anticancer targeted therapy [20, 26, 27].

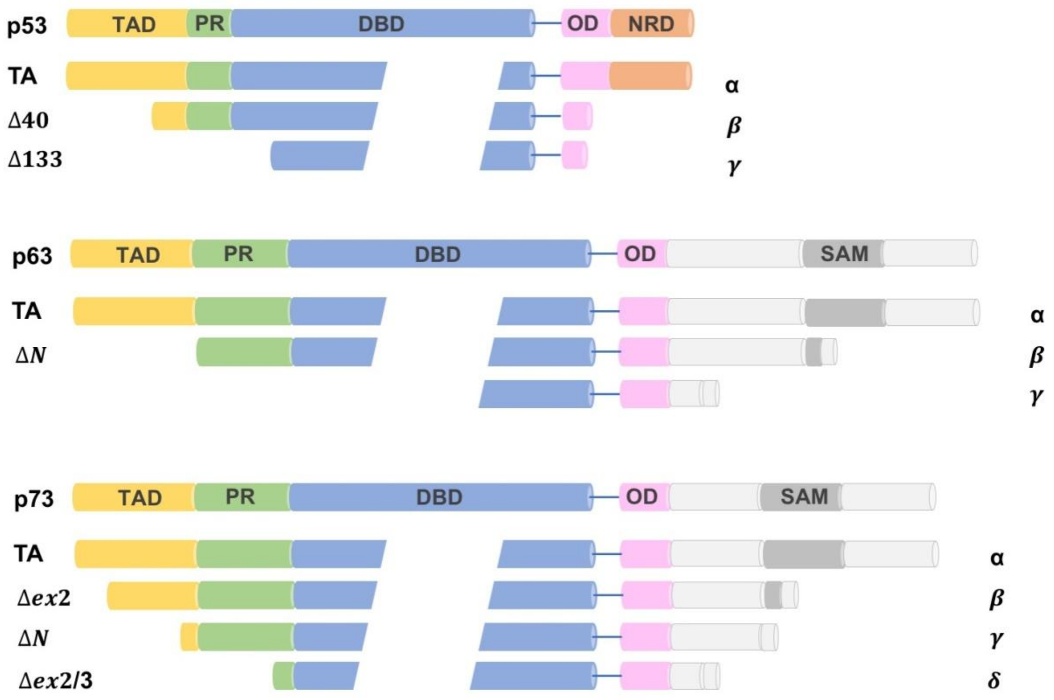

Figure 2. Representation of p53 family proteins structure and their principal isoforms. p63 and p73 bear an additional *C*-terminal sterile-*α* motif (SAM). Limited overall homology is observed among family members, but strong similarity is found in the DBD (approximately 60% between p53 and p63/p73 and approximately 85% between p63 and p73). Adapted from [20].

The next sections of this chapter will be focused on p53 structure, function, regulation, and pharmacology, important for the overall conception of the scope of the present thesis. Some concepts on drug nanodelivery systems will also be addressed as a cancer therapeutic strategy to improve drug pharmacokinetics and toxicity profiles.

2. Cellular functions of p53

The tumor suppressor protein p53 is recognized as the “guardian of the genome” and acts like a sentinel avoiding deleterious effects to progeny, preventing tumorigenic events (**Figure 3**) [28]. p53 activity is triggered by several intrinsic and extrinsic stress signals, such as oncogenic modifications (*e.g.,* GTPase KRas (*KRAS)* mutation with proto-oncogene *c*-Myc activation leading to hyperproliferation [29]), acute or low level chronic DNA damage (*e.g.*, telomere attrition, replication, and oxidative stress), ribonucleotide depletion, and microenvironmental stress (*e.g.*, starvation, and hypoxia) [30]. Its function has been attributed to the transcription of genes involved in cellular responses, including DNA repair, cell cycle arrest, apoptosis, and senescence, the so called canonical or classical p53 responses that dictate cellular survival or death (**Figure 3**). But p53 can also regulate other cellular responses such as metabolism, autophagy, non-cell-autonomous functions, stemness, invasion, and metastasis (**Figure 3**) [30, 31]. In fact, *in vivo* studies with mice models have highlighted the role of p53 in tumor suppression through transcription of key target genes involved in cell cycle arrest (*e.g.,* cyclin-dependent kinase inhibitor 1a, *CDKN1A*; growth arrest and DNA-damage-inducible 45α, *GADD45A*) and apoptosis (*e.g.,* apoptosis regulator BAX, *BAX*; p53 up-regulated modulator of apoptosis, *PUMA*) (**Figure 3**). Cell cycle arrest is of great importance in tumor suppression once it is crucial for DNA repair processes, avoiding the propagation of potentially oncogenic mutations [32-34]. Indeed, mice lacking DNA repair genes are prone to cancer [35-38]. Moreover, cell cycle-competent and apoptosis-deficient mice models present resistance to early onset of cancer, comparing to p53-null mice, evidencing the importance of cell cycle in tumor suppression and suggesting the role of absent apoptosis in later cancer onset [39, 40]. In other mice models, apoptotic events have shown to be crucial to avoid cancer onset [41-46]. Interestingly, cell cycle arrest- and apoptosis-deficient mice show longer cancer latency than p53-null mice, suggesting that other processes, also regulated by p53, may be important in tumor suppression, such as cellular metabolism [42, 47]. Evidences have also demonstrated that the p53 response and cellular outcomes are remarkably flexible and highly depend on cell type, stress conditions, and collaborating environmental signals (reviewed in [30, 48]).

Genome-wide data, based on genomic studies using chromatin immunoprecipitation, followed by DNA sequencing (ChIP-seq), expression profile and microarray techniques, have contributed to the identification of p53 transcriptional target genes, which to date account more than 300, unveiling the networks involved in p53 responses [49]. However, it has been also reported that p53 can bind specifically to more than 900 genes [50]. Although, p53 is a direct transcriptional activator, its ability to repress

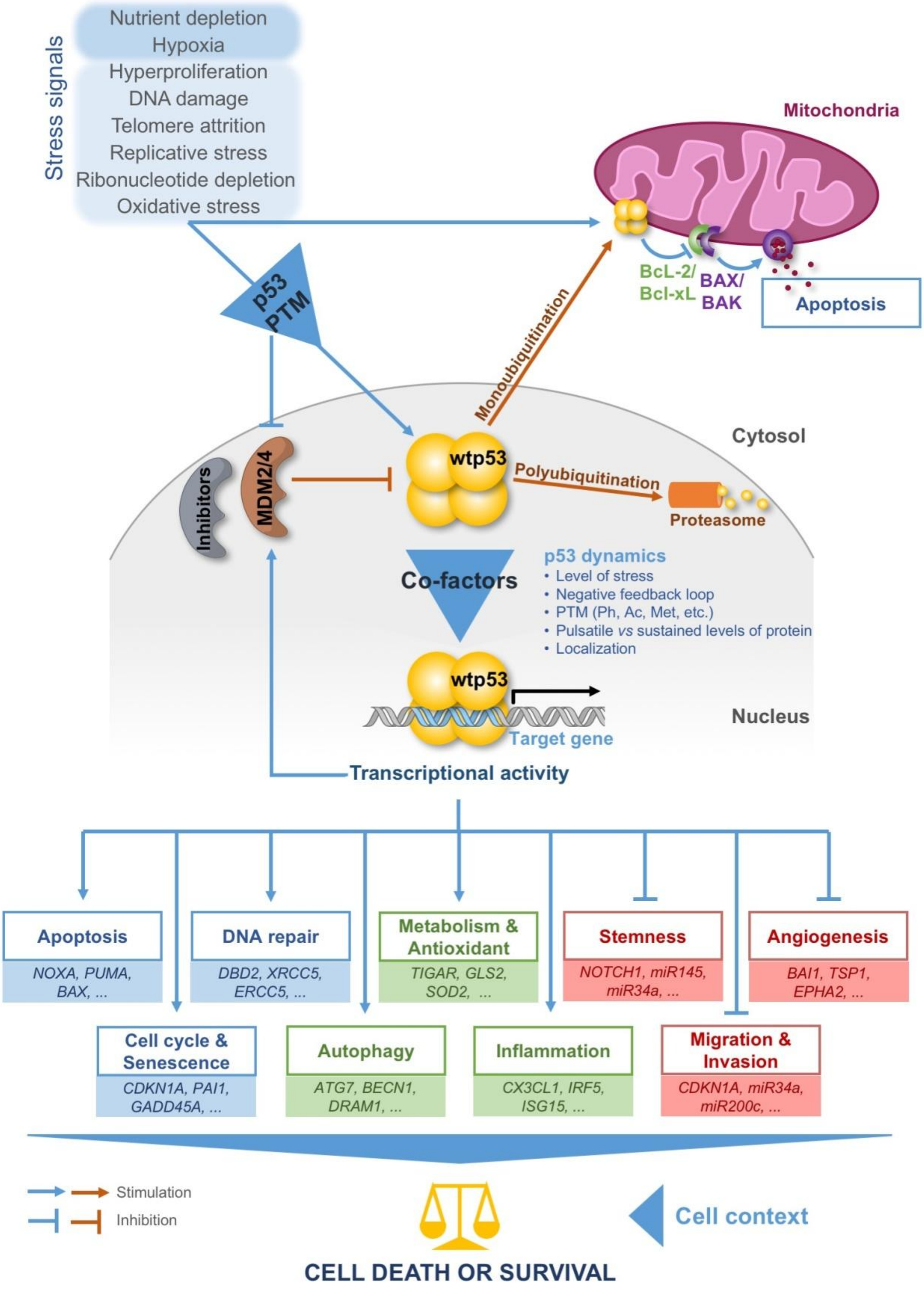
Stress signals
Nutrient depletion
Hypoxia
Hyperproliferation
DNA damage
Telomere attrition
Replicative stress
Ribonucleotide depletion
Oxidative stress
Mitochondria
BcL-2/
Bcl-xL
BAX/
BAK
Apoptosis
p53
PTM
Monoubiquitination
Cytosol
Inhibitors
MDM2/4
wtp53
Polyubiquitination
Proteasome
Co-factors
p53 dynamics
• Level of stress
• Negative feedback loop
• PTM (Ph, Ac, Met, etc.)
• Pulsatile vs sustained levels of protein
• Localization
wtp53
Target gene
Nucleus
Transcriptional activity
Apoptosis
NOXA, PUMA, BAX, ...
DNA repair
DBD2, XRCC5, ERCC5, ...
Metabolism & Antioxidant
TIGAR, GLS2, SOD2, ...
Stemness
NOTCH1, miR145, miR34a, ...
Angiogenesis
BAI1, TSP1, EPHA2, ...
Cell cycle & Senescence
CDKN1A, PAI1, GADD45A, ...
Autophagy
ATG7, BECN1, DRAM1, ...
Inflammation
CX3CL1, IRF5, ISG15, ...
Migration & Invasion
CDKN1A, miR34a, miR200c, ...
Stimulation
Inhibition
Cell context
CELL DEATH OR SURVIVAL

Figure 3. Regulation and function of p53. In normal conditions, p53 transcriptional activity is negatively regulated by different inhibitors, including MDM2 via binding and ubiquitination. According to the ubiquitination pattern, p53 can be proteasome degraded (polyubiquitination) or translocated to mitochondria (monoubiquitination), where it can exert non-transcriptional functions. At mitochondria, and under stress stimuli, p53 can bind to Bcl-2 or Bcl-xL, inhibiting their antiapoptotic functions. This leads BAX or BAK to oligomerize, creating pores in the mitochondrial outer membrane, and subsequent apoptosis. Under stress conditions, p53 is dislocated from the regulation of inhibitors through post-translational modifications (PTMs), like phosphorylation, which induce p53 stabilization, with increased p53 protein levels, and p53 transcriptional activity. Also, the type of PTMs and the rescue of different co-factors influence the set of p53 transcriptional genes and cellular responses. Depending on the stimulus and cell context, p53 can positively regulate canonical (blue boxes) and non-canonical (green boxes) cellular responses, culminating in cell death or survival. p53 can also halt oncogenic events (red boxes) by the transcription of key target genes. Ac – acetylation; ATG7 – autophagy related protein 7; BAI1 – brain-specific angiogenesis inhibitor 1; BAK – pro-apoptotic Bcl-2 homologous antagonist/killer; BAX – apoptosis regulator BAX; Bcl-2 – apoptosis regulator Bcl-2; Bcl-xL – Bcl-2-like protein 1; BECN1 – Beclin-1; CDKN1A – cyclin-dependent kinase inhibitor 1a; CX3CL1 – chemokine (C-X3-C motif) ligand 1; DBD2 – damage-specific DNA-binding protein 2; DRAM1 – DNA-damage regulated autophagy modulator 1; EPHA2 – ephrin type-A receptor 2; ERCC5 – excision repair 5, endonuclease; GADD45A – growth arrest and DNA-damage-inducible 45*α*; GLS2 – glutaminase 2; Irf5 – interferon regulatory factor 5; ISG15 – interferon-induced 15 kDa protein; MDM2/4 – murine double minute 2/4; Met – methylation; miRNA – microRNA;NOTCH1 – neurogenic locus notch homolog protein 1; NOXA – phorbol-12-myristate-13-acetate-induced protein 1 (PMAIP1); PAI1 – plasminogen activator inhibitor 1; Ph – phosphorylation; PUMA – p53 up-regulated modulator of apoptosis; SOD2 – superoxide dismutase 2, mitochondrial; TIGAR – TP53-induced glycolysis and apoptosis regulator; TSP1 – thrombospondin-1; XRCC5 – X-Ray Repair Cross Complementing 5, codifies for Ku86 protein. Image based on [30, 31, 48].

genes expression is indirect. Therefore, p53-mediated repression occurs mainly by upregulating p21 (product of *CDKN1A*) leading to cell cycle genes downregulation via dimerization partners RB-like, E2F, and multi-vulval class B (DREAM), or RB-E2F4 complexes, and indirect post-transcriptional repression via microRNAs (miRNAs) targeting mRNAs for degradation or translational repression via the RNA-induced silencing complex [51]. In addition, p53 can coordinate transcription-independent activities by interacting with different downstream proteins, in the cytoplasm and mitochondria, such as apoptosis regulator Bcl-2 and Bcl-2-like protein 1 (Bcl-xL), allowing the BAX or pro-apoptotic Bcl-2 homologous antagonist/killer (BAK) proteins to oligomerize and permeate mitochondrial outer membrane with subsequent apoptosis (**Figure 3**) [30, 52, 53]. It is interesting to note that p53 mitochondria-mediated apoptosis is faster than p53 nuclear-mediated apoptosis, suggesting that these two mechanisms are orchestrated to decide cell fate accordingly with the stress signal [54].

As referred above, p53 is a key regulator of a myriad of cellular responses. Given the impossibility of addressing all cellular processes in which p53 is involved, the present thesis summarizes the major concepts of metabolic regulation by p53, specifically of glucose metabolism, and explores how this knowledge can be used to selectively target p53 for cancer therapy.

2.1. Regulation of glucose metabolism by p53

Cell metabolism has a central role in cell growth and survival. It involves diverse signaling pathways regulated by different factors, including oncogenes, tumor suppressor genes, growth factors, pH, oxygen and nutrient levels (**Figure 4**). The metabolism is reprogrammed to meet the cellular needs of energy (adenosine triphosphate, ATP, production), macromolecules, and a sustained reduction-oxidation (REDOX) reaction status [55-58]. Compelling studies have revealed a crucial role of p53 in the regulation of cellular metabolism [59]. Specifically, in glucose metabolism under normal conditions, p53 reduces glycolytic flux and favors oxidative phosphorylation (OXPHOS) (**Figure 4**) [60, 61].

Currently, metabolic reprogramming is a hallmark of cancer (**Figure 1**) [9], which is closely related to other hallmarks supporting the malignant transformation [62]. Indeed, during the last decade, glucose metabolism has gained relevance in cancer pathophysiology and pharmacology. In opposition to normal cells, in cancer cells with impaired p53, an enhancement of glycolysis in detriment of OXPHOS is observed (**Figure 4**), even in the presence of oxygen, an event known as the Warburg effect [63, 64]. Glycolysis is a faster process, but less efficient than OXPHOS in terms of ATP production. To compensate the energetic production, cancer cells enhance glucose uptake through upregulation of glucose transporters [65-68]. Glycolysis confers other advantages to cancer cells, particularly by providing intermediates for various biosynthetic pathways (*e.g.,* nucleic acids, lipids, and proteins; **Figure 4**), and an adaptation to hypoxic conditions often observed in solid tumors. Additionally, it enhances REDOX balance, by increasing the levels of antioxidants and reducing reactive oxygen species (ROS; **Figure 4**) [59, 65]. Accumulated data have demonstrated that p53 activation promotes the reversion of the Warburg effect [69, 70]. In this case, the sustained tumor growth is halted with metabolic intermediates diverted from biosynthetic pathways to the tricarboxylic acid (TCA) cycle, and enhanced OXPHOS with ROS production, inducing an imbalance in REDOX cell state that contributes to cell death [71]. This highlights the relevance of mitochondrial maintenance and biogenesis, which is also promoted by functional p53

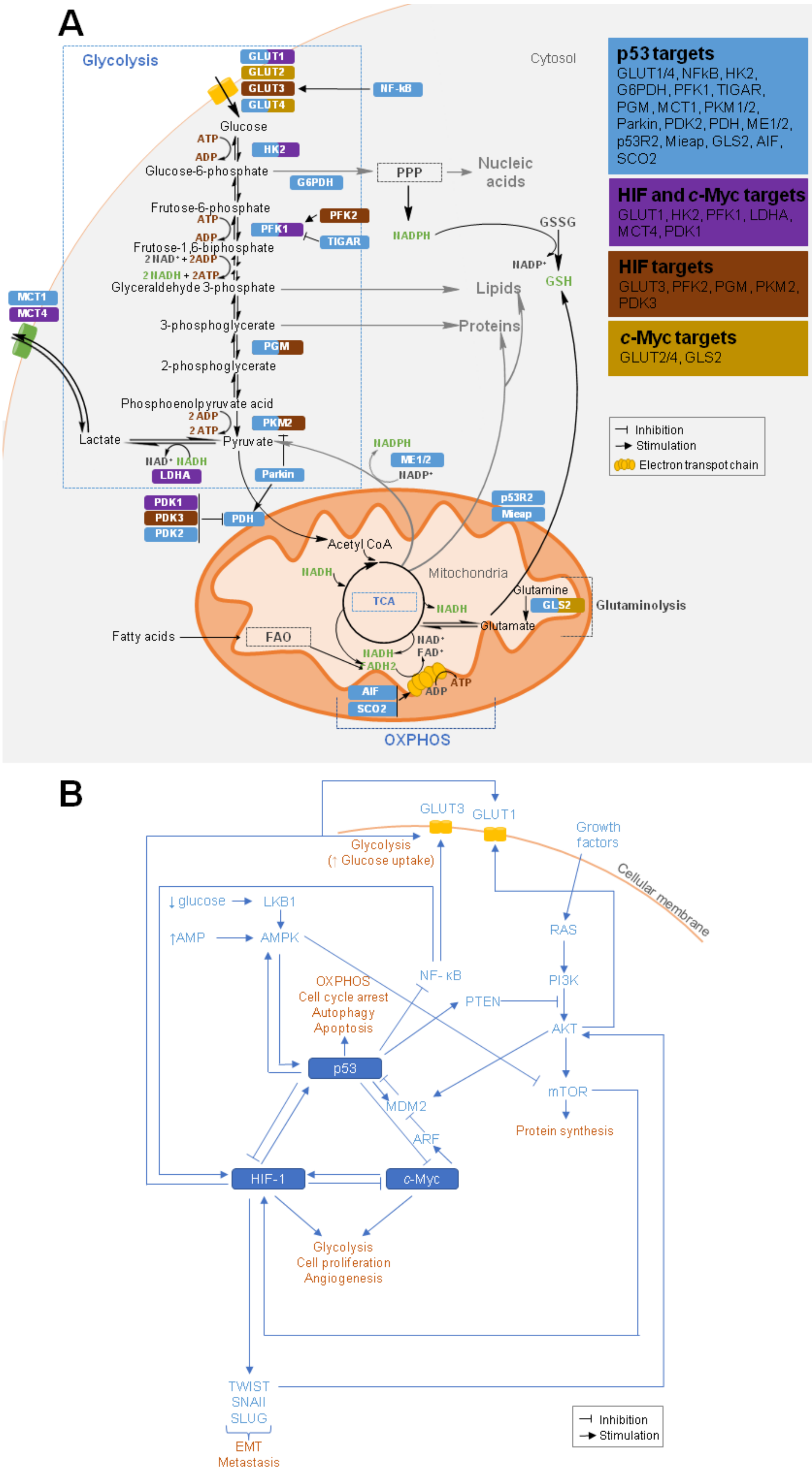
A
Glycolysis
Cytosol
GLUT1
GLUT2
GLUT3
GLUT4
NF-κB
Glucose
ATP
ADP
HK2
Glucose-6-phosphate
G6PDH
PPP
Nucleic acids
Frutose-6-phosphate
PFK2
PFK1
TIGAR
NADPH
GSSG
Frutose-1,6-biphosphate
2 NAD⁺ + 2ADP
2 NADH + 2ATP
NADP⁺
GSH
Glyceraldehyde 3-phosphate
Lipids
MCT1
MCT4
3-phosphoglycerate
Proteins
PGM
2-phosphoglycerate
Phosphoenolpyruvate acid
2 ADP
2 ATP
PKM2
Lactate
Pyruvate
NAD⁺
NADH
LDHA
Parkin
NADPH
ME1/2
NADP⁺
PDK1
PDK3
PDK2
PDH
p53R2
Mieap
Acetyl CoA
NADH
Mitochondria
TCA
Glutamine
GLS2
Glutaminolysis
NADH
Glutamate
Fatty acids
FAO
NAD⁺
FAD⁺
NADH
FADH2
ATP
ADP
AIF
SCO2
OXPHOS
p53 targets
GLUT1/4, NFkB, HK2, G6PDH, PFK1, TIGAR, PGM, MCT1, PKM1/2, Parkin, PDK2, PDH, ME1/2, p53R2, Mieap, GLS2, AIF, SCO2
HIF and c-Myc targets
GLUT1, HK2, PFK1, LDHA, MCT4, PDK1
HIF targets
GLUT3, PFK2, PGM, PKM2, PDK3
c-Myc targets
GLUT2/4, GLS2
Inhibition
Stimulation
Electron transport chain
B
GLUT3
GLUT1
Growth factors
Glycolysis
(↑ Glucose uptake)
Cellular membrane
↓glucose
LKB1
↑AMP
AMPK
RAS
NF- κB
PI3K
OXPHOS
Cell cycle arrest
Autophagy
Apoptosis
PTEN
AKT
p53
mTOR
MDM2
Protein synthesis
ARF
HIF-1
c-Myc
Glycolysis
Cell proliferation
Angiogenesis
TWIST
SNAIl
SLUG
EMT
Metastasis
Inhibition
Stimulation

Figure 4. Schematic representation of glucose metabolic pathways: interplay between p53 and other signaling pathways with respective cellular outcomes. (A) Regulation of glycolysis

and OXPHOS by p53: in normal cells, functional p53 stimulates OXPHOS upregulating mitochondrial enzymes and downregulating glycolytic enzymes (blue box). In cancer cells, p53 is found inactivated with increase of glycolysis through upregulation of glucose transporters and glycolytic enzymes by both HIF-1 and *c*-Myc transcriptional factors (purple, brown and yellow boxes). Gray arrows highlight the interplay of glucose metabolism (glycolysis and OXPHOS) with nucleic acids (pentose phosphate pathway, PPP), lipids, and protein synthesis. Glutaminolysis and fatty acid oxidation (FAO) contributed for fueling tricarboxylic acid (TCA) cycle and OXPHOS. **(B)** Interplay between p53 and other signaling pathways: p53 stimulates OXPHOS, whereas HIF-1 and *c*-Myc, alone or in cooperation, stimulate glycolysis; LKB1/AMPK (sensing cellular glucose and AMP levels) upregulates p53 expression and blocks mTOR pathway, reestablishing ATP levels and promoting cell cycle arrest and/or apoptosis; p53 inhibits NF-κB, as well as AKT/mTOR pathway via PTEN. Under p53 inactivation, glycolysis is increased through upregulation of GLUT3 (by NF-κB and HIF-1) and HIF-1 (by NF-κB and mTOR) leading to cell survival; HIF-1 upregulates TWIST, SNAIL and SLUG transcriptional factors important in metastasis. Cellular events are highlighted in orange. ADP – adenosine diphosphate; AIF – apoptosis inducing factor; AKT – RAC-alpha serine/threonine-protein kinase; AMP – adenosine monophosphate; AMPK – 5'-AMP-activated protein kinase; ARF – ADP-ribosylation factor; ATP – adenosine triphosphate; *c*-Myc – proto-oncogene *c*-Myc; CoA – coenzyme A; EMT – epithelial-mesenchymal transition; FADH2/FAD – flavin adenine dinucleotide oxidized/reduced form; G6PDH – glucose-6-phosphate dehydrogenase; GLS2 – glutaminase 2; GLUT1-4 – glucose transporters 1-4; GSH – glutathione; GSSG - glutathione disulfide; HIF-1 – hypoxia-inducible factor 1; HK2 – hexokinase 2; LDHA – lactate dehydrogenase A; LKB1 – liver kinase B1; MCT1/4 – monocarboxylate transporter isoforms 1/4; ME1/2 – malic enzyme isoforms 1/2; Mieap – mitochondria-eating protein; mTOR – mechanistic target of rapamycin; NADH/NAD$^+$ – nicotinamide adenine dinucleotide oxidized/reduced form; NADPH/NADP$^+$ – nicotinamide adenine dinucleotide phosphate oxidized/reduced form; NF-κB – factor nuclear kappa B; P53R2 – ribonucleoside-diphosphate reductase subunit M2 B; Parkin – E3 ubiquitin-protein ligase parkin; PDH – pyruvate dehydrogenase; PDK 1/2/3 – pyruvate dehydrogenase kinase 1/2/3; PFK1 – phosphofructokinase 1; PGM – phosphoglycerate mutase; PI3K – phosphoinositide 3-kinase; PKM1/2 – pyruvate kinase isoforms M1/M2; PPP – pentose phosphate pathway; PTEN – phosphatase and tensin homolog; RAS – GTPase HRas; SCO2 – cytochrome c oxidase assembly factor; SLUG – zinc finger protein SNAI2;SNAI1 – zinc finger protein SNAI1; TIGAR – p53-inducible glycolysis and apoptosis regulator; TWIST – Twist-related protein 1.

through expression of ribonucleoside-diphosphate reductase subunit M2 B (p53R2) and mitochondria-eating protein (Mieap; **Figure 4**) [72, 73].

Additionally, the impact of glucose metabolism in cancer progression, dissemination, and chemoresistance, prompted a new generation of small-molecules for anticancer targeted therapy. In fact, several inhibitors of glycolysis and OXPHOS by targeting p53 downstream effectors have entered in clinical trials, such as silybin (GLUT1; NCT00487721) [74], 2-deoxiglucose (hexokinase 2 inhibitor; NCT00633087) [75], metformin (hexokinase 2 and electron transport chain inhibitor; NCT01981525, NCT02978547) [76, 77], dichloroacetate (pyruvate dehydrogenase kinase inhibitor; NCT01029925, NCT01386632, NCT00566410) [78], and VLX600 (electron transport chain inhibitor; NCT02222363) [79], and some of them are already in the treatment of some types of cancer. Notably, several studies have demonstrated that the status and activity of p53 in cancer cells are determinant for the success of metabolic therapy. Besides the impact on metabolic interveners, p53 activators are also relevant for the abrogation of the chemoresistance commonly observed in cancers with dysfunctional p53 [77, 80-84]. However, considering the cancer cell metabolic heterogeneity, a single metabolic strategy proves to be not sufficient for efficient cancer eradication. Despite the effectiveness of combination therapies involving glycolysis and OXPHOS inhibitors to eliminate heterogeneous cancer cell populations counteracting mutp53-mediated Warburg effect or acting as bioenergetic catastrophic agents, their potential effects on normal cells and common resistance in p53 dysfunctional cancers have made their combination with p53 activators a promising therapeutic strategy. In fact, this approach combining p53-activating agents will allow a more efficient and safe anticancer therapy by decreasing the doses of metabolic therapies and by redirecting the treatment to cancer cells with compromised p53.

3. Structural features of p53

Structural studies have strongly contributed to the knowledge about p53 stability, its behavior in the presence of inhibitors or co-factors, and how it recognizes and binds to target DNA sequences allowing gene transcription. In fact, in its extended and complex regulatory network, structural features of p53 have been basilar to the understanding of its own regulation and function. Also, it has provided insights into wt and mutp53 pharmacology at molecular levels, fostering the design and development of p53-based targeted therapies to halt cancer.

Structural studies with full-length p53 became a challenge. Indeed, its flexibility and labile stability prone to aggregate have hampered crystallographic studies. Its high molecular weight represents a limitation for studies using conventional nuclear magnetic resonance (NMR) spectroscopy. On the other hand, p53 size is at the limits for cryo-electron microscopy (EM) methodology [17]. To circumvent these limitations, a combined multi-technique approach was followed to construct a jigsaw from individual domain data.

For that, specific recombinant p53 domains were produced by bioengineering techniques and analyzed by X-ray crystallography and NMR spectroscopy. In addition, some studies to check the spatial 3D arrangement of folded domains were pursued with the full-length protein using suitable methodologies such as small angle X-ray scattering (SAXS), cryo-EM and fluorescence resonance energy transfer (FRET) [17, 85]. NMR spectroscopy revealed to be important to understand protein-protein and protein-DNA interactions in solution [86]. To complement these studies, electrophoretic mobility shift assay (EMSA), ultracentrifugation, protein microarrays, transactivation assays, fluorescence anisotropy, and isothermal calorimetric (ITC) titrations, among others, have been also performed to unveil binding and characterize binding affinities with DNA and other proteins, peptides, or small-molecules [86-90]. Recombinant p53 proteins with specific mutations have also contributed to study p53 and the relevance of specific amino acid residues in its stability and activity [91-94]. Furthermore, computational studies, such as molecular superposition and dynamics, have been used with predictive and comparison purposes in structure-function relationship [17].

3.1. DNA recognition by p53

In solution, using SAXS, NMR, and EM techniques, it was possible to understand that full-length p53 forms a tetramer with opened, cross-shaped structure, having the OD at its center and a pair of loosely coupled DBD dimers at the ends, which are accessible to bind to cognate DNA and partner proteins. Upon DNA binding, the structure closes around DNA and becomes more compact (**Figure 5**) [86, 95, 96]. In solution, p53 DBD plus OD exists mainly as dimers, binding to DNA mostly as tetramers, whereas p53 DBD is mostly in monomeric state, but it forms tetramers with DNA targets incorporating two decameric repeats [97]. Although p53 DBD lacks the OD, upon tetramerization in the presence of DNA, protein-protein interactions are established between the DBDs [97]. These findings suggested that p53 is a biologically active transcription factor as a homotetramer (assembling as a dimer of dimers, once p53 dimers are formed co-translationally [98]), and DNA recognition occurs upon a cooperative binding process [97]. This means that the formation of dimers followed by the tetramer is favored in the presence of DNA, being that either protein-protein or protein-DNA interactions contribute to the overall complex stability [99].

p53 exerts its transcriptional activity through recognition of a short specific DNA sequence in the target gene promoter, called response element (RE) [28, 99]. The REs enable a coordinated response, once they can be repeated or shared strategically among

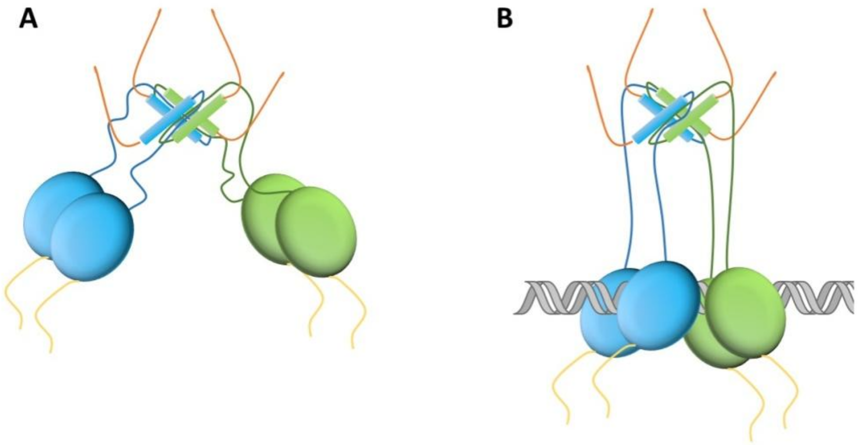

Figure 5. Representation of p53 quaternary structure in solution. (A) Open unbound and (**B**) closed/compact bound p53 tetramer to DNA sequence spatial conformations. Blue and green spheres represent the DBDs (each color for one dimer), and sticks represent the ODs. Disorganized *N*-terminal and *C*-terminal are depicted in orange and yellow, respectively. Cartoons based on NMR, SAXS, and EM experimental studies [86, 95, 96].

different genes. Thus, upon stress stimuli, the transcription factor can bind to the scattered REs in the genome eliciting the transcription of a set of genes and related cellular responses [100]. The p53 target RE binding site consist in two decameric motifs (half-sites) with the consensus sequence RRR**C**WW**G**YYY (R = A, G; W = A, T; Y = C, T), being that C4 and G7 positions should be conserved among the variant sequences [101, 102]. This means, that there are variant sequences of REs among the different p53 target genes. Thus, different binding affinities are correlated with sequence-specific variations in the protein-DNA contact geometry, providing insights into the mechanism of p53 function and regulation [99, 103].

In 1994, Cho and colleagues reported for the first time the crystallographic model of p53 DBD with DNA at 2.2 Å [104]. The p53 DBD is an immunoglobulin-like central *β*-sandwich of two antiparallel *β*-sheets providing the basic scaffold for the DNA-binding surface (**Figure 6**). This surface is constituted by two large loops L2 and L3 intercalated by a short helix H1, which are stabilized by a tetrahedral coordination of two residues of each loop to a zinc atom (L2 – C176, H179; L3 – C238, C242) and by a loop-sheet-helix (LSH) motif (L1, *β*-strands S2 and S2’, the end of *β*-strand S10 and *C*-terminal of H2) (**Figure 6**).

The LSH motif makes specific contacts with the major groove of the target DNA, through hydrogen bonds, salt-bridges and structural water molecules in a tight network of hydrogen bonds that ensures the correct orientation of each amino acid residue. In the

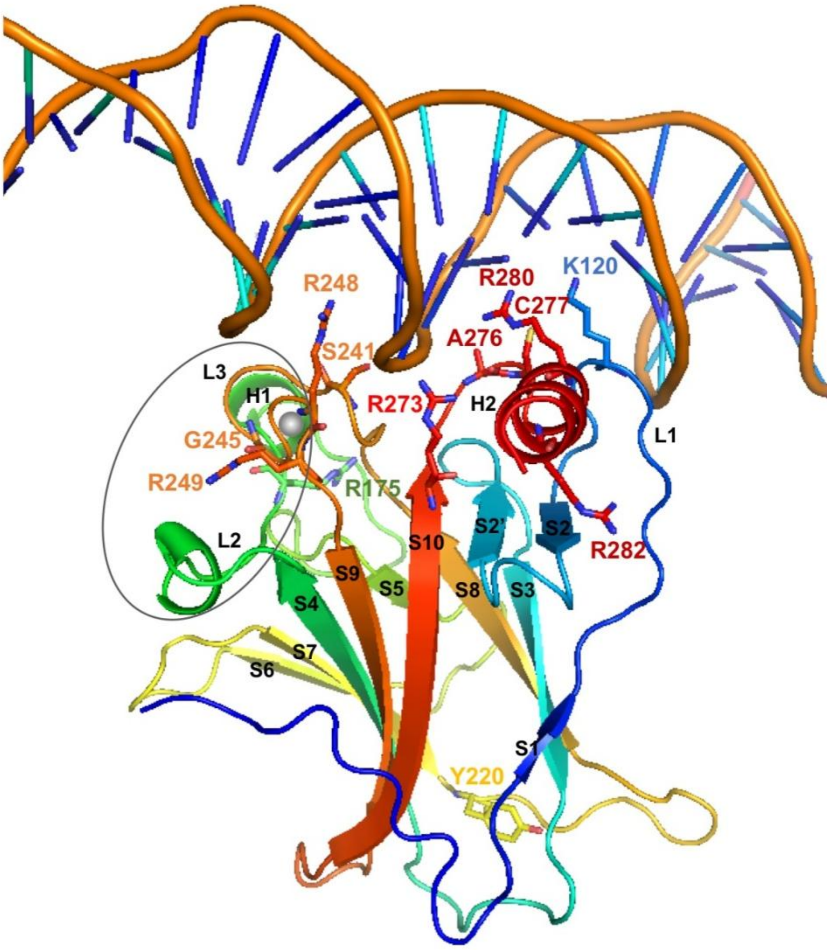

Figure 6. Structural insights on p53 and DNA binding. The 3D structure model of the DBD binding to cognate DNA sequence (PDB ID code: 1TUP, [104]) highlights the structural organization in helixes, loops, strands in the *β*-sandwich. Furthermore, it depicts the amino acid residues involved in DNA recognition establishing interactions with the DNA, specifically K120 (L1), S241 and R248 (L3), R273 (S10), A276, C277, and R280 (H2). Other residues are also key partners for the correct binding positioning or structural stability, such as R175 (L2), Y220 (S7-S8 turn), D245 (L3), R249 (L3), and R282 (H2). Other regions of the DBD are important for the assembly in dimers, namely H1, L2 and L3, highlighted by a gray circle. Image created using PyMOL software [105]. H – helix; L – loop; S – strand. Adapted from [17].

DNA major groove, the side chains of residues K120 (L1), A276, C277 and R280 (H2) interact with DNA bases via hydrogen bonds, and the side chain of residue R273 (H2) and the backbone amide of residues K120 and A276 establish interactions with the DNA backbone phosphates via salt bridges interactions (**Figure 6, 7**). The L3 contains the residues S241 and R248 that perform contacts with DNA backbone phosphates in the DNA minor groove, being R248 essential for DNA recognition (**Figure 6, 7**) [104, 106].

Other residues play also an important role in stabilizing the p53 DNA-binding surface such as R175 (L2), G245 (L3), R249 (L3) and R282 (H2) (**Figure 6**) [104, 106].

The finer details of DNA-contact geometry show an interesting variation that depends on the DNA sequence [99]. To better understand this, a description of the known modes of binding of each residue to the DNA consensus region is provided in **Figure 7**. Briefly, residues R280 and R273 are crucial for DNA recognition and therefore their spatial orientation is of great importance. Both residues are responsible for invariant contacts to the DNA target sequences, and are involved in an extensive network of hydrogen bonds involving the side chain of D281, R273, the main chain of A276 and C277, and a highly conserved water molecule making four optimally-orientated hydrogen bonds to A276/C277, R280, D281, and DNA backbone phosphates. The correct orientation of R280 and R273 side chains is also buttressed by the residue D281 via a salt bridge network with the guanidinium group of the arginines and the aspartic acid [99]. Besides these contact geometries to DNA, the specific interactions established by residues K120, A276, and C277 change dramatically depending on DNA variant sequences (**Figure 7**) [99]. Also, some p53 structural characteristics influence DNA binding, such as the inherent flexibility of L1, which harbors residue K120, allowing that the contacts occur in an induced-fit mode depending on the DNA sequence [99]. Additionally, L3 conformation guides the residue R248 to dock the DNA minor groove. Of note that R248 residue shows a wide variability of conformations from fully extended to folded side chains, making direct contacts with DNA backbone or, more frequently, via water molecules (**Figure 6, 7**) [99]. Overall, p53 DNA-binding affinities depend on the number of established contacts by the residues of amino acids to the RE half-site. Indeed, p53 showed higher binding affinity with DNA half-site when an extra interaction is mediated by A276 side chain (**Figure 7 C**) [99].

Each half-site is recognized by a symmetrical dimer of two p53 DBD with a relatively small, self-complementary protein-protein interface with around 600 $Å^2$ of buried surface area [94]. The interface is stabilized by hydrophobic, water-mediated polar interactions and hydrogen bonds between the zinc regions, involving H1, L2 and L3, of the two p53 DBD (**Figure 6**). There are two buried water molecules that provide an internal hydrogen-bonding network as a central anchor linking the two zinc regions, which support H1 and L3 configuration. Then, a nonpolar interaction shell is formed by surface residues from H1 and L3 hairpin via residues P177, H178, M243, and G244. Next to this hydrophobic area, there are two hydrophilic networks that contribute to its stability, one far from DNA that involves charged residues from the two monomers (specifically R174, E180, R181, and several water molecules), and the second one near to DNA with a first-shell hydration of the protein surface facing DNA, via N239, S241, and R248 side chains.

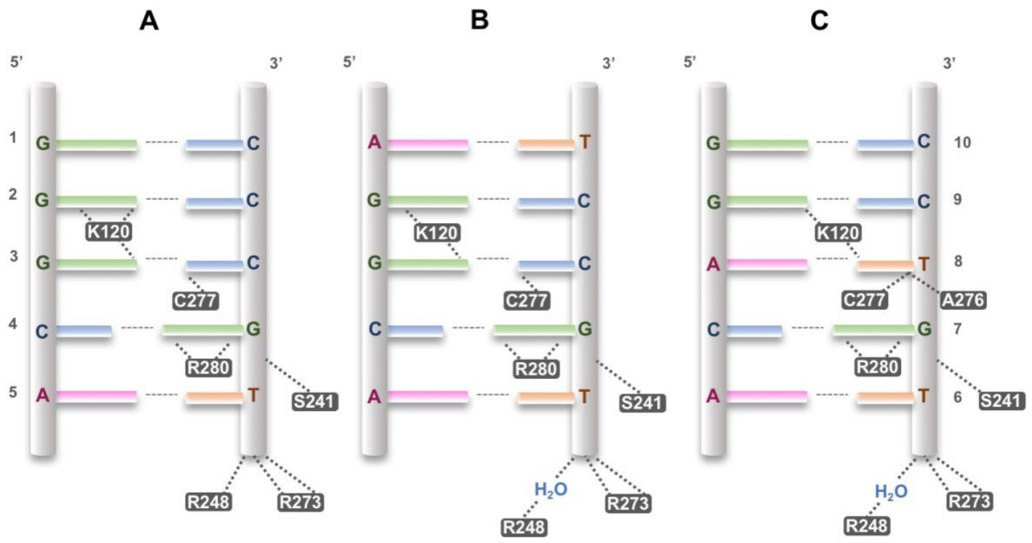

Figure 7. p53 specific DNA-binding modes. p53 binding to three pentameric DNA sequences belonging to decameric half-sites of the consensus region of p53 target genes. The side chain of residue R280 is a steady point of contact between p53 and DNA, making two invariant hydrogen-bonds to the conserved guanine base (G7) in the DNA major groove. The residue R273 anchors p53 to DNA backbone phosphates (grey pipe), in the central region of each half-site. The side chain of residue S241 also makes invariant contacts to DNA backbone phosphates. The specific interactions established by residues K120, A276, and C277 dramatically change when the base pair, at positions 3 and 8 of the DNA half-site, is changed from G/C to A/T. When in presence of the G/C base pair, the residue K120 makes three **(A)** or two **(B)** hydrogen-bonds with successive guanine bases (G2 and G3); when in presence of A/T base pair **(C)**, it establishes interactions with G2 and T8, creating a cross-link between DNA strands. Still regarding positions 3 and 8, the residue C277 interacts with C8 of the opposite DNA strand in case of G/C base pair **(A and B)**; in case of A/T base pair **(C)**, it establishes van der Waals interactions with T8. The most marked binding difference is observed with the residue A276, the interaction between its side chain and the DNA base only occurs with the A/T base pair **(C)**, with a hydrophobic interaction occurring among the methyl groups of A276 and T8. The doublet central DNA half-site A/T base pairs (positions 5 and 6) do not mediate direct contacts with the protein, but are crucial in water-mediated interactions, playing an essential role in the cooperative binding of the core dimer to its DNA half-site through minor groove hydration. This interaction is directly mediated by the side chain of residue R248 **(A),** or indirectly via water molecules **(B and C)**. The base pairs at positions 1 and 10 do not interfere with protein-DNA complex stability. Adapted from [99, 107].

The interaction of protein-DNA is the ultimate contribution to dimer stabilization. Dimer protein-protein interactions may also contribute for DBD integrity, considering the bidentated salt bridges between the polar and charged surface residues D184 with R175, and R249 with E171 on opposite sides of each monomer [99, 108]. Kantarci and colleagues, besides acknowledging that both p53 DBD monomers in the dimer establish the same interactions with the DNA RE, advanced the hypothesis that in a dimer the p53 DBD interactions with DNA were stronger for one monomer than for the other. This raised the possibility of the tetrameric p53 form to move throughout the DNA sequence enabling genes transcription [109], which has been also supported by the spatial rearrangement of the tetramer complexed with DNA verified in cryo-EM works [86, 95, 96].

4. Dynamics and regulation of p53

Although intrinsic domain disorder/flexibility poses a difficulty in p53 studies, it allows a structural plasticity reflected in binding promiscuity observed by p53 interaction with a wide range of target DNA sequences, and interacting proteins (**Figure 8**) [107]. Additionally, intrinsic disorder is directly correlated with low thermodynamic and kinetic stability, meaning that its half-life time at body temperature is about 9 min with rapid cycles between folded and unfolded states [87, 110, 111]. Thus, these phenomena have been postulated as an evolutionary advantage providing a tight regulation of functionally active p53 cellular levels [107]. Additionally, in normal cells, under no stress conditions, p53 levels are low as it is negatively regulated by different proteins, including its major endogenous inhibitor MDM2 (**Figure 3**). This protein not only prevents DNA recognition by directly binding to p53, but also targets p53 for proteasomal degradation via polyubiquitination or nuclear export via monoubiquitination by its E3 ligase activity (**Figure 3, 8**). Under stress stimuli, p53 is displaced from MDM2 negative regulation, with subsequent stabilization and activation of its transcriptional functions (**Figure 3**) [30]. Furthermore, heat shock proteins (HSP), such as HSP40/70/90, act like chaperones transiently binding to free p53 and promoting its correct folding upon their dissociation for DNA RE binding [112-115].

Besides p53 protein stabilization, several other factors seem to reinforce the fine-tuning of stimuli-dependent p53 regulation and cell fate decision, including the protein level dynamics, cellular location, and PTMs (**Figure 3, 8**) [54]. *MDM2* is itself a target of p53 leading to a tight negative feedback loop regulation (**Figure 3**) [116]. If the stress is given in transient pulses, cell cycle arrest is preferred due to repeated oscillations in p53 cellular levels via MDM2 regulation, and because *CDKN1A* promoter is sensitive to short pulses [54, 117-119]. Nevertheless, under prolonged stress signals, p53 activates other upstream effectors that stimulate MDM2 degradation with consequent sustained p53 levels. These protein levels are adequate, for example, for tumor necrosis factor receptor superfamily member 6 gene (*FAS*) promoter binding/dissociation rate and consequently apoptosis [54, 118, 119].

PTMs are promoted by different p53 regulators and mostly occurring in p53 TAD and NRD, which are important for p53 function modulation (**Figure 8**), interfering with p53 stability and affinity for different target genes [20, 120, 121]. The presence of a functional TAD is essential to p53 transcriptional activity [122]. TAD is intrinsically disordered with two regions of nascent secondary structure [17, 123], designated as TAD1 (residues 1–42) and TAD2 (residues 43–63) subdomains. TAD-occurring PTMs modulate the interaction with different negative regulators, or transcriptional co-activators and mediators (**Figure 8**) [17, 51, 122]. TAD has 10 phosphorylation sites (**Figure 8**) and the pattern of phosphorylation will dictate which regulatory proteins will interact with p53 [122]. For instance, the MDM2 *N*-terminal (residues 25–109) docks p53 TAD1 (residues 18–26) [124, 125]. However, this interaction is halted upon p53 phosphorylation at T18, due to the electrostatic repulsion of the phosphate group with the negatively charged surface of MDM2. On the other hand, p53 phosphorylation favors the interaction between TAD and histone acetyltransferase p300, facilitating p53 transactivation [17]. In a structural 3D perspective, upon binding of MDM2 [124] or p300 [126], TAD1 becomes fully helical. TAD2 also folds into an amphipathic-α-helix upon binding to replication protein A [127]. These short sequences that undergo disorder-to-order transition upon binding to partners are molecular recognition features commonly observed in transactivation domains of transcription factors, allowing a multitude of possibilities of binding to diverse targets because of their conformational adaptability [128-130]. p53 can be phosphorylated by different kinases, according to the stress signal and activated pathways (reviewed in [120, 121]). Interestingly, the pattern of phosphorylation also dictates the cellular response, once given a stress signal p53 is primarily phosphorylated at S15 and S20, leading to cell cycle arrest. Under sustained stress signal conditions, p53 can be further phosphorylated at S46 resulting in apoptosis [131].

Besides phosphorylation, the p53 NRD is target of various PTMs, such as acetylation, methylation, ubiquitination, sumoylation and neddylation, which frequently occur at six lysines (K370, K372, K373, K381, K382, and K386; **Figure 8**). Specifically, acetylation, often occurs at K370, K372, L373, K381, and K382 by the p53 co-factor p300/CREB-binding protein (CBP), and at K120 by histone acetyltransferases KAT5 (TIP60)/8 (MOF)/6A (MOZ), increasing p53 DNA-binding affinity to target genes [132]. On the other hand, in the absence of stress signal, p53 may be deacetylated and methylated at lysine (K370, K373, and K382), histidine and arginine residues, leading to its inactivation. However, the methylation at K372 contributes to p53 stability and recruitment at *CDKN1A* gene promoter [133]. Like TAD, the NRD also suffers conformational changes

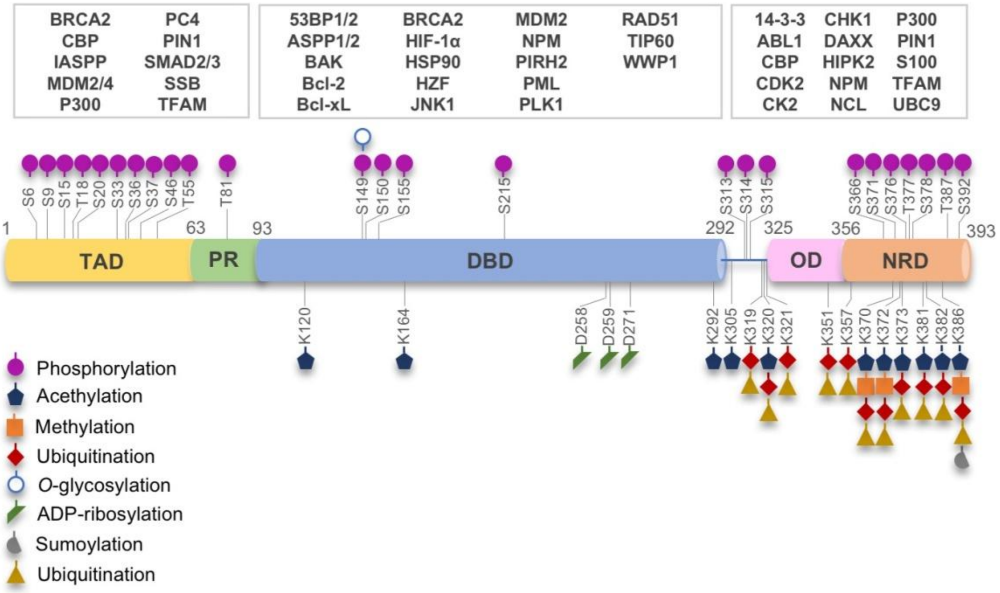
BRCA2
CBP
IASPP
MDM2/4
P300
PC4
PIN1
SMAD2/3
SSB
TFAM
53BP1/2
ASPP1/2
BAK
Bcl-2
Bcl-xL
BRCA2
HIF-1α
HSP90
HZF
JNK1
MDM2
NPM
PIRH2
PML
PLK1
RAD51
TIP60
WWP1
14-3-3
ABL1
CBP
CDK2
CK2
CHK1
DAXX
HIPK2
NPM
NCL
P300
PIN1
S100
TFAM
UBC9
S6
S9
S15
T18
S20
S33
S36
S37
S46
T55
T81
S149
S150
S155
S215
S313
S314
S315
S366
S371
S376
T377
S378
T387
S392
1
63
93
292
325
356
393
TAD
PR
DBD
OD
NRD
K120
K164
D258
D259
D271
K292
K305
K319
K320
K321
K351
K357
K370
K372
K373
K381
K382
K386
Phosphorylation
Acethylation
Methylation
Ubiquitination
O-glycosylation
ADP-ribosylation
Sumoylation
Ubiquitination

Figure 8. Overview of p53 PTMs and interacting proteins. Each domain is target of different and/or concomitant PTMs that regulate p53 function. p53 interacts directly with different PTM enzymes, transcriptional co-factors, and other nuclear or cytoplasmic proteins (some examples depicted in the white boxes associated with the p53 interacting domain) that modulate p53 function. 14-3-3 – dimeric kinase C inhibitor protein 1; ABL1 – tyrosine-protein kinase ABL1; ASPP1/2 – apoptosis-stimulating of p53 protein 1/2; BAK – pro-apoptotic Bcl-2 homologous antagonist/killer; Bcl-2 – apoptosis regulator Bcl-2; Bcl-xL – Bcl-2-like protein 1; BRCA2 – breast cancer type 2 susceptibility protein; CBP – CREB-binding protein; CDK2 – cyclin-dependent kinase 2; CHK1 – serine/threonine-protein kinase Chk1; CK2 – casein kinase II; DAXX – death domain-associated protein 6; HIF-1*α* - hypoxia-inducible factor 1*α*; HIPK2 – homeodomain-interacting protein kinase 2; HSP90 – heat shock proteins; HZF – zinc finger protein 385A; IASPP – RelA-associated inhibitor; JNK1 – mitogen-activated protein kinase 8; NCL – nucleolin; NPM – nucleophosmin; P300 – histone acetyltransferase p300; PC4 – activated RNA polymerase II transcriptional coactivator p15; PIN1 – peptidyl-prolyl cis-trans isomerase NIMA-interacting 1; PIRH2 – RING finger and CHY zinc finger domain-containing protein 1; PLK1 – serine/threonine-protein kinase PLK1; PML – promyelocytic leukemia protein; RAD51 – DNA repair protein RAD51 homolog 1; S100 – S100 calcium binding protein; SMAD2/3 – mothers against decapentaplegic homolog 2/3; SSB – SPRY domain-containing SOCS box protein; TFAM – transcription factor A, mitochondrial; TIP60 – histone acetyltransferases KAT5; UBC9 – SUMO-conjugating enzyme UBC9; WWP1 – NEDD4-like E3 ubiquitin-protein ligase WWP1. Image based on [20, 112, 120, 121].

upon binding to some regulatory proteins, such as S100 calcium binding protein, sirtuins, RING finger and CHY zinc finger domain-containing protein 1 (PIRH2), cyclin-dependent kinase 2 (CDK2)/cyclin A and CBP (**Figure 8**). For instance, p53 NRD acquires an *α*-helix shape when bound to S100B, or a *β*-sheet with sirtuins, or no conformational change occurs with CDK2/ciclin A [17].

The tetramerization of p53 is affected by PTMs and regulators/co-factors interaction. The OD is constituted by a short *β*-strand followed by an *α*-helix. The tetramerization is facilitated by protein-protein interactions via DBD and OD [17]. Although, inter-DBD interactions are more important for the dimer formation, the OD also contributes for dimer stabilization via an antiparallel intermolecular *β*-sheet and helix-packing interactions. Thereafter the OD is involved in the dimerization of two dimers via a tight packaging of their hydrophobic helix interfaces, rendering a thermodynamic stable homotetramer [134, 135]. At the center of the tetrameric interface, the side chains of residue L344 from all four subunits are in direct contact burying the leucine-rich nuclear export signal (NES; residues 340–351) [136]. Upon MDM2 binding, p53 suffers a conformational change making the *C*-terminal lysine residues accessible for ubiquitination [137]. If p53 is monoubiquitinated rather than polyubiquinated, it leads to tetramer dissociation and NES exposure [138] targeting for nuclear export/sub-cellular trafficking with p53 stabilization and ability to exhibit transcription-independent functions [139], escaping from degradation (**Figure 3**) [140]. In opposition, it was described that MDM2 and p53 deubiquitination by ubiquitin carboxyl- terminal hydrolase (USP)7, and p53 deubiquitination upon DNA damage by USP10 and USP42, leads to p53 stabilization and nuclear accumulation [141-143]. Oligomerization state may be also controlled by other proteins. For instance, S100 proteins inhibit oligomerization by binding to OD of monomers [144, 145]. In opposition, dimeric kinase C inhibitor protein 1 (14-3-3) bind to phosphorylated p53 NRD, promoting the formation of tetramers [146]. Oligomerized state correlates with nuclear localization, while dimeric and monomeric forms can transit or be degraded [17, 147]. This balance of protein levels and spatial locations allows to create a path of spatiotemporal cell fate decision.

Methylated or ubiquitinated p53 correlates with unstressed cells. In contrast, phosphorylation, acetylation, neddylation or sumoylation are more frequent in cells upon DNA damage/stress stimuli [120]. One PTM may influence the occurrence of another, unlocking additional layers of regulation reflected in protein stability, function, protein-protein interaction, and recruitment of transcriptional co-factors and machinery, biasing DNA-binding toward target genes [48, 148].

5. Mutant p53

TP53 mutations occur in more than half of human cancers with colorectal, head and neck, esophagus, female genital organs, pancreas, and skin cancers exhibiting the highest prevalence (35–43%; International Agency for Research on Cancer (IARC) TP53 Database, R19 August 2018) [149]. *TP53* mutations occur in both germline (associated with Li Fraumeni syndrome) and sporadic contexts, and can be found throughout the whole gene [149]. Missense mutations are the most frequent alterations in *TP53* (about 75%) and mainly occur in the DBD (about 80%) [150]. Of note that there are six hotspot missense mutations in codons 175, 245, 248, 249, 273, and 282 localized in the p53 DBD with the highest clinical significance (**Figure 9**).

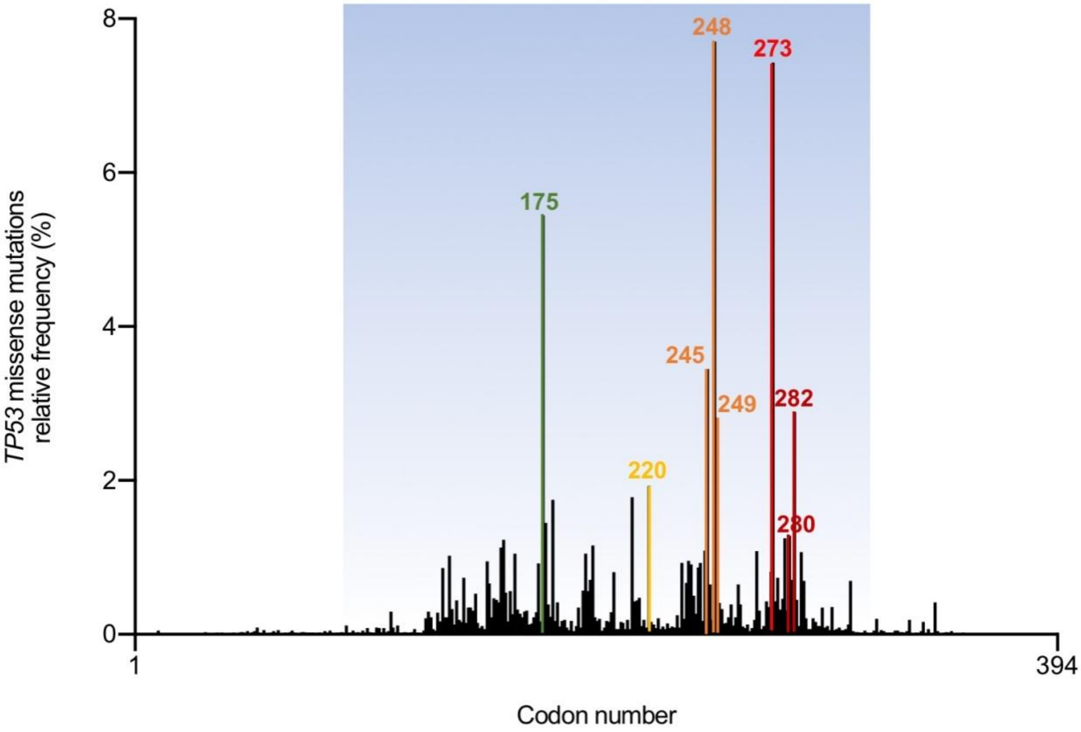

Figure 9. *TP53* missense mutations frequency in human cancers. The *TP53* missense mutations relative frequency *per* codon. The highest mutation frequencies occur in *TP53* DBD region (in fading blue box, residues 93–312), specifically in codons 175, 245, 248, 249, 273, and 282, the so called hotspot, and with lower frequency, for example, in codons 280 and 220. These codons codify for residues with important roles in the structure-function relationship. (Graph constructed with GraphPad 7 and data from IARC TP53 Database, R19 August 2018 [149]).

TP53 mutations in the TAD are associated with loss of transactivation of specific genes, such as *CDKN1A*, being incapable of inducing cell cycle, but not compromising apoptosis. *TP53* mutations in OD often halt tetramerization translating into loss of function (LOF). *TP53* mutations in the DBD exhibit diverse degrees of functionality and consequently different pathological relevance (reviewed in [19]). Besides being primarily associated with LOF of wtp53 (**Figure 1**) [19], *TP53* mutations in the DBD commonly occur in a single allele; therefore first stage tumors are heterozygotes, expressing both wt and mutp53. Although wtp53 is still expressed, it is observable a DNE of mutp53 over wtp53, forming heterotretamers (wtp53 dimer plus mutp53 dimer), but with no transcriptional activity (**Figure 1**) [19]. During tumor progression, the loss of heterozygoty is commonly observed and associated with gain of function (GOF) of sporadic or inherited *TP53* mutations (**Figure 1**) [30]. GOF can be manifested by transcriptional regulation through interaction with diverse transcriptional factors or co-factors. For instance, mutp53 heterooligomerizes with p63 or p73 blocking their tumor suppressor activity, by inhibiting their transcriptional activity, or stimulating the transcription of non-canonical genes [151, 152]. On the other hand, mutp53 transcriptional GOF may occur when it associates with other transcriptional factors or co-factors, such as protein C-ets-1/2 (Ets1/2), yes-associated protein (YAP1), peptidyl-prolyl cis-trans isomerase NIMA-interacting 1 (Pin1) or promyelocytic leukemia protein (PML), with transcription enhancement of their set of target genes [151, 152]. Both scenarios result in altered gene expression patterns that contribute to survival, tumor progression, and more aggressive phenotypes [152]. GOF has been strongly associated with some specific mutp53 forms, such as R175H, R248W, R273H, and R280K (reviewed in [19, 152, 153]). Also, genomic studies in cancer cells harboring different mutp53 forms have highlighted the array of genes upregulated by mutp53 and some interacting partners (reviewed in [10, 152, 154, 155]).

It is also interesting to note that mutp53 is expressed in cancer cells in higher levels than wtp53 in normal cells, indicating that mutp53 is somehow more stable than wtp53, accumulating in tumors [156]. Initially, it was thought that the MDM2 regulatory axis would not work on mutp53, once canonical genes transcription is halted [152]. Nevertheless, MDM2 may be expressed by other pathways [157] and evidences have suggested that mutp53 levels can be controlled by MDM2 in normal tissues, but not in tumor tissues [158]. This raised the possibility of additional events in tumorigenesis responsible for mutp53 accumulation. Indeed, in cancer, the occurrence of mutp53 is also associated with increased levels of HSP70 or HSP90, that often bind to and stabilize mutp53, and/or participate into aggregosomes impairing the activity of MDM2 or other E3 ligase regulatory proteins like the carboxy terminus of HSP70-interacting protein (CHIP), culminating in mutp53 accumulation and potentiating its GOF [115]. Indeed, diverse mutp53 forms have been described as aggregation-prone localized in the cytoplasm and perinuclear region, rather than in the nucleus as functional wtp53 [159]. These aggregosomes may have a prion-like amyloid behavior [160] and have also been associated with the DNE and GOF events by sequestration of wtp53, TAp63 and TAp73. Co-aggregation is possible once these isoforms share highly conserved aggregating sequences in the same structural motif [159, 161].

5.1. Mutant p53 deleterious effects on DNA binding and protein stability

Through the crystallographic model of wtp53 DBD bound to DNA, Cho and colleagues unveiled the deleterious effects of common cancer mutations [104, 107]. Subsequent studies have been pursued to further understand the mutational effect on the p53 structure, stability and function [107]. In this context, based on the known p53 intrinsic instability, a superstable quadrupole mutp53 DBD was developed (T-p53-C; M133L, V120A, N239Y, N268D) and used in structural studies (**Table 1**), enabling its handling without compromising its function [93, 162]. These mutations maintain the basic structural scaffold and turn p53 DBD structural framework more rigid, increasing its thermodynamic stability in 2.6 kcal/mol (compared to wtp53 DBD) [93]. The most frequent *TP53* mutations occur in high conserved sequence regions and coincide with key amino acids residues for DNA recognition and structural stability (**Figure 6**) [163, 164]. Indeed, single amino acid mutations in the p53 DBD can result in the removal of DNA-contact residues, distortions or conformational changes in different parts of the DNA-binding surface, creation of internal cavities, or formation of surface crevices in regions remote from the DNA-binding site. Based on this, mutp53 forms have been classified into contact (*e.g.,* R248Q, R248W, R273H, R273C, R280K) and structural (*e.g.,* G245S, G245D, R249S, R175H, Y220C, R282W) [107].

Mutp53 studies by X-ray crystallography and NMR have enlightened local-structural changes and their impact on DNA recognition, which are summarized in **Table 1**. In particular, NMR and *in silico* simulations data have provided insights in structural changes of L3, with L2 rearrangements, in contact mutp53 R248Q caused by the change of arginine to glutamine [165, 166]. Although deprived of structural data, it is speculated that the substitution of the arginine for a tryptophan in contact mutp53 R248W may abolish the anchoring of p53 to DNA minor groove due to the hydrophobicity and steric clash of tryptophan, preventing the establishment of hydrogen-bonds to DNA [107]. The same may occur to other contact mutp53 forms, such as S241F and C277F [107]. In contact mutp53s R273H and R273C, the histidine and cysteine redisues, respectively, alter the hydrogen-bonding network in the DNA-binding surface, compromising the buttressing of those residues and direct contacts to DNA backbone phosphates due to being shorter than arginine [92, 167, 168]. Despite the unavailability of structural data, contact mutp53 R280K exhibits loss of DNA-binding ability with impairment of canonical target genes transcription. Although, the switch of arginine to lysine is not profoundly different, somehow the absence of arginine guanidinium group affects p53 DNA-binding ability [169]. Conformational changes observed in DNA-binding region of structural mutp53 G245S are small with the L3 overall conformation conserved. Nevertheless, the serine side chain displaces a structural water molecule leading to small structural shifts in the proximal residues. This is enough to disturb the protein-protein interface of the dimer, reducing DNA-binding affinity [168]. Conversely, structural mutp53 R249S leads to a large conformational change of L3, affecting p53 DBD anchoring to DNA minor groove via R248 contacts. The guanidinium group of the R249 is responsible for stabilizing the L3 hairpin conformation by establishing one salt bridge interaction with D171 and hydrogen-bonds with G245 and M246. When the arginine residue changes to serine (R249S), these interactions are abolished. Consequently, L3 acquires more flexibility along with M246 displacement elicited by M243 from its buried location within the hydrophobic zinc-cluster region, leading to the formation of a short *α*-helix. This significant conformational change ultimately displaces R248, halting mutp53 DNA interaction [167]. Additionally, NMR data evidenced an increased flexibility of the *β*-sandwich close to the DNA-binding surface [170]. The residue R282 (H2 *C*-terminal) is responsible for maintaining the structural integrity of LSH motif, by packing H2 to S2-S2' *β*-hairpin, anchoring it to the protein core. Through the crystallographic model of structural mutp53 R282W, it was observed that the inclusion of a hydrophobic and bulky tryptophan compromised those anchoring interactions. Consequently, the L1 flexibility increases with displacement of the DNA-contact residue K120, affecting DNA recognition [168, 171]. Structural mutp53 Y220C occurs far away from the DNA-binding surface, but with deleterious effects on overall protein stability. The mutation occurs in the periphery of the *β*-sandwich hydrophobic core, at the beginning of the loop that connects S7 and S8, leading to a mutation-induced crevice on p53 surface [168]. Other mutations in the *β*-sandwich may occur within its hydrophobic core, such as V143A and F270L. Valine and phenylalanine side chains form an integral part of the hydrophobic core network and these mutations create internal cavities. Of note that, these cavities occur without collapse of the surrounding structure guaranteed by other hydrophobic residues, but they cause a strong destabilization of the core domain [168]. Although no structural data of zinc region structural mutp53 R175H is available, it is possible to speculate the causes of p53 abrogated activity. Residue R175 (L2) is embedded between L2 and L3, next to the zinc-cluster, and its guanidinium group is responsible for stabilizing this region by establishing hydrogen-bonds with P191 and M237 and one salt bridge with D184. If the arginine is replaced by a histidine (R175H), besides being shorter than arginine, histidine's bulkiness could lead to structural distortions and interfere with zinc-binding [107]. Such effects may justify the observed complete loss of DNA-binding ability by R175H [88, 172]. In fact, if the mutation is R175A (not occurring in cancer), bearing a smaller side chain, residual binding [88] or wt-like activity (also in R175C or R175L with smaller side chains) [173] can be observed. In contrast, the introduction of large bulky side chains (*e.g.,* R175W and R175Y) abrogated the wt-like functions in cancer cells [173].

Table 1. Impact of mutations on p53 DBD structural features.

Variable (DBD)	**Amino acid location and biochemical mutation type**	**Mutp53 structural modifications**	**Thermo-dynamic stability**[&]	**Estimated folded protein at 37 ºC**[#]	**DNA-binding affinity at 20 ºC**[#]	**Structural elucidation of p53 DBD (PDB ID code ex.)**	**Ref**
Wtp53							
with DNA	*NA*	*NA*	*NA*	*NA*	+ + +	1TUP*, 1TSR*, 2AC0, 2ADY, 2AHI, 2ATA	[88, 99, 104]
w/o DNA	*NA*	*NA*	+	+ + +	*NA*	2OCJ, 1UOL*	[88, 174]
Mutp53							
DNA contact region							
S241F	L3; Uncharged polar to aromatic non-polar/Small to large residue	Increase of hydrophobicity and steric clash halts DNA contacts (theoretical interpretation)	*ND*	*ND*	*ND*	*ND*	[107]
R248Q	L3; Cationic to uncharged polar residue	Alteration of L3 conformation (NMR data)	+/−	+ + +	−	*ND*	[88, 165]
R248W	L3; Cationic to non-polar aromatic bulky residue	Increase of hydrophobicity and steric clash halts DNA contacts (theoretical interpretation)	*ND*	*ND*	*ND*	*ND*	[107]
R273C	S10; Cationic to uncharged polar/Large to small residue	Alteration of hydrogen bonds network in DNA-binding surface affecting buttressing residues and DNA contacts	*ND*	*ND*	*ND*	2J20*, 4IBQ	[92, 168]
R273H	S10; Aliphatic to aromatic/ Large to bulky-small residue	Alteration of hydrogen bonds network in DNA-binding surface affecting buttressing residues	+	+ + +	−	2BIM*, 4IBS, 4IJT	[88, 92, 110, 167]

Variable (DBD)	Amino acid location and biochemical mutation type	Mutp53 structural modifications	Thermo-dynamic stability[&]	Estimated folded protein at 37 ºC[#]	DNA-binding affinity at 20 ºC[#]	Structural elucidation of p53 DBD (PDB ID code ex.)	Ref
		and DNA contacts					
C277F	S10-H2 turn; Uncharged polar to aromatic non-polar/Small to large residue	Increase of hydrophobicity and steric clash halts DNA contacts (theoretical interpretation)	*ND*	*ND*	*ND*	*ND*	[107]
R280K	H2; Large to small residue	Compromised DNA contacts (theoretical interpretation)	*ND*	*ND*	–	*ND*	[107, 169]
Structural – DNA region							
F134L	S2’; Aromatic to aliphatic residue	*ND*	–	–	–	*ND*	[88]
H168R	L2;Aromatic to aliphatic residue	Alteration of L2 conformation	*ND*	*ND*	*ND*	2BIN*	[167]
G245S	L3; Non-polar to uncharged polar/Small to large residue	Small distortion of L3/dimerization interface	+/–	+ + +	+	2J1Y*	[88, 110, 168]
G245D	L3; Non-polar to anionic/ Small to large residue	Small distortion of L3 and LSH (*in silico* data)	*ND*	*ND*	*ND*	*ND*	[175]
R249S	L3; Cationic to uncharged polar/Large to small residue	Alteration of L3 conformation affecting R248-mediated DNA anchoring and of dimer interface; increased flexibility of the *β*-sandwich	+/–	+ + +	–	2BIO*, 3D05, 3DO6, 3DO7	[88, 110, 167, 170]
R282Q	H2; Cationic to uncharged polar residue	Flexibility is decreased in L1 and increased in L3	*ND*	*ND*	*ND*	2PCX	[176]
R282W	H2; Aliphatic to aromatic/ Cationic to non-polar bulky residue	Impaired LSH anchoring to *β*-sandwich, increase of L1 flexibility	–	–	+ +	2J21*	[88, 110, 168]
Structural – Zinc region							
R175A	L2; Cationic to non-polar/ Large to small residue	Interference with zinc binding (smaller effect than R175H) (theoretical interpretation)	+/–	+ + +	+	*ND*	[88, 107]
R175H	L2; Aliphatic to aromatic/ Large to bulky-small residue	Alteration of L2 and L3 conformation, loss of zinc binding (theoretical interpretation)	–	–	–	*ND*	[88, 107, 110]
M237I	L3; Large to small residue/	*ND*	–	+/–	–	*ND*	[88]

Variable (DBD)	Amino acid location and biochemical mutation type	Mutp53 structural modifications	Thermo-dynamic stability[&]	Estimated folded protein at 37 ºC[#]	DNA-binding affinity at 20 ºC[#]	Structural elucidation of p53 DBD (PDB ID code ex.)	Ref
	Decrease in atom electro-negativity						
C242S	L3; Decrease in atom electro-negativity	Zinc ligand substitution with loss of zinc coordination (theoretical interpretation)	−	+/−	−	*ND*	[88, 107]
Structural – β-sandwich							
V143A	S3; Large to small residue	Internal hydrophobic cavity	−	−	+	2J1W*	[88, 110, 168]
L145Q	S3; Non-polar to uncharged polar/Small to large residue	*ND*	−	+/−	+/−	*ND*	[88]
P151S	S3/S4 turn; Non-polar to uncharged polar residue	*ND*	−	−	+/−	*ND*	[88]
V157F	S4;Aliphatic to aromatic/Small to large-bulky residue	Internal hydrophobic cavity	−	−	+ +	4KVP	[177]
I195T	S5; Non-polar to uncharged polar/Large to small residue	*ND*	−	−	−	*ND*	[88]
Y220C	S7-S8 turn; Large to small residue	Hydrophobic crevice in the *β*-sandwich surface at S7-S8 turn	−	−	+/−	2JIX*	[88, 168]
I232T	S8; Non-polar to uncharged polar/Large to small residue	*ND*	−	+/−	+	*ND*	[88]
I255F	S9; Aliphatic to aromatic residue	*ND*	−	−	+/−	*ND*	[88]
F270C	S10; Aromatic non-polar to uncharged polar/Large to small residue	Internal hydrophobic cavity (theoretical interpretation)	−	−	+/−	*ND*	[88]
F270L	S10; Aromatic to aliphatic/ Large to small residue	Internal hydrophobic cavity	*ND*	*ND*	*ND*	2J1Z*	[168]

*The protein has four stabilizing mutations (M133L, V203A, N239Y, N268D). [&]Difference in free energy of unfolding between wt- and mutp53 DBD at 10 ºC ($\Delta\Delta G_{\mathrm{D-N}}^{\mathrm{H_2O}}$), that is extrapolated to 37 ºC; free energy of wtp53 used as reference (0 kcal/mol); (+) stable protein ≤ 0.5 kcal/mol, (+/−) weakly destabilized protein 0.6-2.5 kcal/mol, (−) strongly destabilized protein ≥ 2.6 kcal/mol. [#]Relative folded protein and DNA-binding affinity: (+ + +) 100-85%, (+ +) 84-70%, (+) 69-55%, (+/−) 54-40%, (−) ≤ 39%. Ds – double strand; ex. – example; *NA* – not applicable; *ND* – not determined; w/o – without.

Regarding mutp53 stability, Bullock and colleagues have classified mutp53 DBD in accordance with its thermodynamic and kinetic stability, and DNA-binding affinity, relating it with the mutation-specific local structural changes (**Table 1**) [87, 88]. The mutp53 stability will dictate the relative amount of folded and potentially functional protein under physiological conditions. It was observed that mutp53 has higher propensity to aggregate than wtp53, being at least 50% of mutp53 denaturated at physiological temperature [88]. For example, the contact mutp53 R273H does not significantly destabilize the DBD, but it halts DNA-binding ability (**Table 1**) once it is a crucial residue for DNA recognition [88]. Surprisingly, although considered a contact mutation, mutp53 R248Q decreases its thermodynamic stability by inducing a structural distortion (**Table 1**) [88, 165, 166]. The structural distortion induced by mutp53s G245S and R249S slightly reduces protein thermal stability and halts DNA contacts, although G245S retains partial DNA binding at sub-physiological conditions (20 ºC) (**Table 1**). In addition, mutp53 R282W leads to increased protein destabilization, but at 20 ºC it retains partial DNA-binding ability (**Table 1**), once most contact residues are undamaged for interaction [88]. Similarly, in structural mutp53 Y220C, or in other *β*-sandwich mutants, despite the conservation of some DNA-binding affinity at 20 ºC, the mutation dramatically decreases p53 stability (**Table 1**) with expressive protein unfolding at physiological temperature. This makes *β*-sandwich structural mutp53 temperature-dependent in respect to their DNA-binding ability [88]. Nevertheless, the same is not verified for the zinc region structural mutp53s R175H, C242S, or M237I, which are extensively denaturated independently of the temperature, reinforcing the importance of the zinc ion tethering for the DBD correct folding [88].

It was demonstrated that mutp53 DBD plus OD lead to misfolding of the tetramer, but not of the monomer. Misfolding appears to involve the intramolecular association of DBD-DBD within the tetramer and to be promoted by destabilizing mutation in the DBD [89]. Also, in case of DNE, although there is a wtp53 dimer, the p53 DBD mutation, in mutp53 dimer, affects the overall tetramer stability leading to the loss of binding cooperativity to DNA impairing transcriptional activity [97, 98, 107, 178]. Moreover, mutations in the DBD not only affect DNA recognition, but may also interfere with binding to wtp53 target proteins. For instance, mutp53 forms bearing mutations that do not interfere with L2 and L3 conformation are still capable to interact with TP53-binding protein 2 (53BP2), however mutp53 G245S impairs this interaction [107]. Ang and colleagues demonstrated that p53 DBD mutations affect the melting temperature of the tetrameric full-length proteins in similar proportions as individual mutp53 DBD. Therefore, the thermodynamic stability of tetrameric full-length p53 is dictated by its DBD [110]. Importantly, mutp53 cellular half-time is not correlated with thermodynamic stability, as mutp53 tends to accumulate as described previously [115, 179].

Besides all the knowledge that has been generated around p53 structure and related topics, the elucidation of several mutants is still missing, including R175H, R248W, and R280K, and their impact on p53 conformation, stability and function.

6. Targeting mutant p53

The restoration of the activity to target proteins poses intrinsic difficulties as a therapeutic strategy, when compared to target inhibition [180]. Indeed, regarding mutp53, it could be arguable whether the reestablishment of its tumor suppressor function would be sufficient to counteract a context of multiple oncogenic alterations, including expression of *c*-Myc, GTPase HRas (RAS), or phosphoinositide 3-kinase (PI3K) cancer drivers. However, accumulated *in vitro* and *in vivo* studies have proven the concept that the reactivation of wt-like function to mutp53 is enough to elicit cell death and to halt tumor progression [30, 180]. Although, for long, mutp53 has been regarded as an undruggable target [31], some studies have shown that the insertion of artificial second-site mutations can alleviate the effect of inactivating *TP53* mutations. The purpose of these rescue mutations is to enable the establishment of new interactions within the protein, favoring stability and the correct conformation, or with the DNA, compensating the missing contacts caused by the original mutated residue [92, 94, 167, 177, 181-183]. In fact, this provided the conceptual basis for the feasibility of mutp53 reactivation, by enhancing specific-sequence DNA binding and transcription of wtp53 target genes. Another positive aspect on mutp53 as a therapeutic target has been its high expression levels in cancer cells [184, 185].

It is important to highlight that all mutants are not equal; indeed, there is an array of different mutants in respect to structure, stability, and function as previously explained. Contact mutants, for their structural similarity to wtp53, do not have well-defined hydrophobic pockets to be docked by small-molecules [31, 104]. Therefore, reactivation of contact mutp53 forms seems to be a daunting task since the therapeutic strategy must rely on the introduction of extra interaction points to compensate for the missing DNA contacts [31]. In contrast, structural mutants are found to be kinetic and thermodynamically destabilized, in a temperature-dependent (*e.g., β*-sandwich mutations) or -independent (*e.g.,* zinc region mutations) manner. As such, for both structural mutant forms, small-molecules that function as molecular chaperones, inducing an increase of the correctly folded protein at physiological temperature, may be a feasible therapeutic strategy, due to the conservation of the DNA-binding residues allowing DNA recognition [31, 88].

In the past two decades, strong efforts by academic and industry research groups has led to the identification of several small-molecules and peptides that stabilize p53 native conformation and restore sequence-specific DNA binding, rescuing wt-like transcriptional functions, ultimately resulting in cell death and tumor suppression (**Table 2**) (reviewed in [180, 186]). Among these mutp53-targeting agents, two small-molecules mutp53 reactivators have entered clinical trials, PRIMA-1^{MET} (APR-246; Phase I/II trials; NCT00900614, NCT02098343 [187, 188]) and COTI-2 (Phase I trial; NCT02433626 [189]).

The understanding of the precise mechanism of action underlying the p53 activation of a mutp53-targeting agent, as well as of its off-target effects, is an important issue for the design of new, more efficient and safe therapies. The p53 function can be activated by different mechanisms, such as genotoxic stress, increase of thermal stability or DNA-binding affinity, induction of correct refolding, and inhibition of p53 negative regulation. Although, some of mutp53-targeting agents have shown to bind and stabilize mutp53 (**Table 2**), the exact mechanism of mutp53 refolding or establishment of new DNA contacts are still far from being fully understood [180].

Table 2. Mutp53-targeting agents.

Chemical name (class)	Discovery strategy	Targeted mutp53	Mechanism of action	Observations	Ref
Reactivators - Cysteine-targeting alkylation					
CP-31398 (Styrylquinazoline)	Chemical library; Protein screen	V173A S241F R249S R273H	Michael addition[#] Binding: *ND*	Transcription of p53 target genes; p53-dependent and -independent *in vitro* antitumor activity	[190-193]
MIRA-1 (Maleimide)	Chemical library; Cellular screen	R175H P176Y/R248W R248Q R248W R273H R273H/P309S R280K R282W	Michael addition[#] Binding: *ND*	Rescue of wt conformation to mutp53s R248W, R175H; Restoration of DNA binding to mutp53s R175H, R248Q, P176Y/R248W, R280K, R282W; Transcription of p53 target genes by mutp53s R175H, R273H, R273H/P309S; p53-dependent and -independent *in vitro* and *in vivo* antitumor activity	[194]
STIMA-1 (Styrylquinazoline)	Chemical library; Cellular screen	R175H R273H	Michael addition[#] Binding: *ND*	Restoration of DNA binding to mutp53 R175H; Transcription of p53 target genes by mutp53s R175H, R273H; p53-dependent and -independent *in vitro* antitumor activity	[193]
KSS-9 (Piperlongumine derivative)	Rational design	R175H	Michael addition[#] Binding: *ND*	Rescue of wt conformation; Restoration of DNA binding to mutp53; Transcription of p53 target genes; p53-dependent and -independent *in vitro* antitumor activity	[195]
PRIMA-1 **PRIMA-1^{MET}**	Chemical library; Cellular	R175H R273H D259Y/K286E	Metabolized to methylene quinuclidinone,	Enhanced thermal stability of wtp53, mutp53s R175H, R273H; Rescue of wt conformation to	[196-205]

Chemical name (class)	**Discovery strategy**	**Targeted mutp53**	**Mechanism of action**	**Observations**	**Ref**
(Quinuclidinone)	screen	K286E S241F R273C P223L/V274F	Michael addition Binding: mutp53s 175H, R273H	mutp53s R175H; Transcription of wtp53 target genes by mutp53s R175H, R273H, D259Y/K286E, K286E, S241F, R273C, P223L/V274F; p53-dependent and -independent *in vitro* and *in vivo* antitumor activity	
PK11007 (Sulfonylpyrimidine)	Chemical library; Protein screen (thermal stability-based)	Y220C V143A	Binds p53 by nucleophilic aromatic substitution Binding: mutp53 Y220C	Enhanced thermal stability of mutp53; Transcription of p53 target genes; p53-dependent and -independent *in vitro* antitumor activity	[206]
HO-3867 (Diarylidenyl piperidone curcumin analogue)	Chemical library; Cellular screen	K132Q R156P Y163H R175H H193R L194F Y205F P223L/V274F C238Y N239D S241F G245S G245V M246I R248Q R248W R249S R273H C277F R280K E285K	Binds p53 by Michael addition Binding: mutp53 Y220C	Rescue of wt conformation to mutp53s P223L/V274F, R273H, R280K; Transcription of p53 target genes by mutp53s K132Q, R156P, Y163H, R175H, H193R, L194F, Y205F, C238Y, N239D, S241F, G245S, G245V, M246I, R248W, R248Q, R249S, R273H, C277F, R280K, E285K; p53-dependent *in vitro* and *in vivo* antitumor activity	[207, 208]
Thermal stabilizers					
3-Benzoylacrylic acid (Benzoylacrylate)	Chemical library; Protein screen (thermal stability-based)	Y220C R175H G245D R249S R282W	Michael addition Binding: mutp53 Y220C	Enhanced thermal stability of mutp53s Y220C, R175H, G245D, R249S, R282W; Absence of *in vitro* antitumor activity evaluation	[209]
Reactivators - Zinc chelators					
ZMC1/ NSC319726 (Thiosemicarbazone)	Database analysis; Cellular assay	R175H C176F C238S C242S C242F G245S	Zn^{2+} chelator Binding: mutp53 R175H	Increases cellular zinc concentration; Rescue of wt conformation to mutp53s R175H, C176F, C238S, C242S; Transcription of p53 target genes by mutp53s R175H, C176F, C238S, C242S, G245S; p53-dependent and -independent *in vitro* and *in vivo* antitumor activity	[210, 211]
COTI-2 (Thiosemicarbazone)	Rational drug design; Virtual drug screening	R175H	Zn^{2+} chelator Binding: *ND*	p53-dependent and -independent *in vitro* and *in vivo* antitumor activity	[212-214]
Reactivators - Non-covalent binding					
PK083 (Carbazole)	Rational drug design; Virtual drug screening	Y220C	Binding to a cleft in *C*-terminal of mutp53 Y220C DBD	Enhanced thermal stability; Rescue of wt conformation to mutp53; *In vitro* antitumor activity	[215, 216]
PK7088 (Pyrazole)	Rational drug design; Protein	Y220C	Binding to a cleft in *C*-terminal of	Enhanced thermal stability; Rescue of wt conformation to mutp53; Transcription of p53	[216, 217]

Chemical name (class)	**Discovery strategy**	**Targeted mutp53**	**Mechanism of action**	**Observations**	**Ref**
	screen (NMR-based)		mutp53 Y220C DBD	target genes; Weak *in vitro* antitumor activity	
PK5196 (Halogen-phenol derivative)	Rational drug design; Protein screen (NMR-based)	Y220C	Binding to a cleft in *C*-terminal of mutp53 Y220C DBD	Enhanced thermal stability; *In vitro* antitumor activity	[216, 218]
MB725 (Aminobenzothiazole)	Rational drug design; Protein screen (NMR-based)	Y220C	Binding to a cleft in *C*-terminal of mutp53 Y220C DBD	Enhanced thermal stability; Transcription of p53 target genes; p53-dependent *in vitro* antitumor activity	[216]
pCAPs (Peptides)	Phage peptide display-protein screen	V135A S241F R249S R280K	Binding to unknown local of mutp53s R175H and R249S	Rescue of wt conformation to mutp53s R175H, R249S; Restoration of DNA binding to mutp53s R175H, R249S; Transcription of p53 target genes by mutp53s V135A, S241F, R280K; p53-dependent *in vitro* and *in vivo* antitumor activity	[219]
CDB3 (Peptide)	Rational drug design; Protein screen (NMR-based)	R175H I195T R249S R273H	Binding to wt and mutp53s R249S, R273H, nearby DNA binding surface and G245S, R175H unknown local	Enhanced thermal stability of wt and mutp53s R175H, R249S, R273H; Rescue of wt conformation to mutp53s R175H, R249S, R273H; Enhanced DNA binding to mutp53 I195T; Transcription of p53 target genes by mutp53s R175H, R273H; p53-dependent *in vitro* antitumor activity	[170, 220, 221]
SCH529074 (Piperazinylquinazoline)	Chemical library; DNA-binding assay	R175H S241F R248W R249S R273H	Binding to wtp53 nearby DNA binding surface	Protects wtp53 conformation from thermal denaturation; Rescue of wt conformation to mutp53s S241F, R248W, R273H; Restoration of DNA binding to mutp53s R175H, R249S, R273H; Transcription of p53 target genes by mutp53s R175H, S241F R248W, R249S, R273H; Blocks MDM2-mediated ubiquitination of p53; p53-dependent *in vitro* and *in vivo* antitumor activity	[222]
Stictic acid	Chemical library; Virtual screening	R175H G245S	*In silico* binding to wtp53 and mutp53s R175H, R273H, G245S to a transiently open pocket (L1/S3)	Enhanced thermal stability of mutp53s R175H, G245S; Transcription of p53 target genes by mutp53s R175H, G245S; p53-dependent and *in vitro* antitumor activity	[223]
Curcumin, Flavokawain B, alpinetin	Crude extracts; Cellular screen	R273H	*In silico* binding to mutp53 R273H bridging DNA binding surface to DNA sequence	p53-dependent and -independent *in vitro* antitumor activity	[224]
Reactivators - Chaperone-mediated effect					
Chetomin (Epidithiodioxopiperazine)	Natural products database; Cellular luciferase reporter screen	R175H	Binds to HSP40	Rescue of wt conformation to mutp53; Transcription of p53 target genes; MDM2 negative regulation; p53-dependent and -independent *in vitro* and *in vivo* antitumor activity	[225]

Chemical name (class)	Discovery strategy	Targeted mutp53	Mechanism of action	Observations	Ref
Reactivators - Unknown binding					
SLMP53-1 (Tryptophan-derived isoindolinone)	Chemical library; Yeast-targeted screening assay	R280K	*ND*	Restoration of DNA binding to mutp53; Transcription of p53 target genes; p53-dependent *in vitro* and *in vivo* antitumor activity	[226]
Ellipticine (Alkaloid)	Chemical library; Cellular screen	R175H L194F S241F R249S R273C R273H	*ND*	Restoration of DNA binding to mutp53s R175H, S241F; Rescue of wt conformation to mutp53 S241F; Transcription of p53 target genes by mup53s R175H; L194F, S241F, R249S, R273C, R273H; p53-dependent *in vitro* antitumor activity	[227]
P53R3 (Piperazinylquinazoline)	Chemical library; DNA-binding assay	M237I R175H R273H R248W	*ND*	Restoration of DNA binding to mutp53s R175H, M237I, R273H; Transcription of p53 target genes by mup53 M237I; p53-dependent *in vitro* antitumor activity	[228]
PEITC (Phenethyl isothiocyanate)	Cellular screen	R175H	*ND*	Rescue of wtp53 conformation to mutp53; Transcription of p53 target genes; p53-dependent *in vitro* and *in vivo* antitumor activity	[229]
WR-1065 (Aminothiol)	Active metabolite of amifostine; Cellular screen	V272M	*ND*	Restoration of DNA binding; Rescue of wt conformation to mutp53; Transcription of p53 target genes; p53-dependent and -independent *in vitro* antitumor activity	[230]
Disruptors of protein-protein interaction					
RETRA (Thiazolthiophenyl ethanone)	Chemical library; Cellular screen	R273H	Disrupts mutp53-TAp73 complexes	Increase of TAp73 expression; Transcription of p53-shared target genes; TAp73-dependent *in vitro* and *in vivo* antitumor activity	[231]
Prodigiosin (Pyrrolyl pyrromethane)	Chemical library; Cellular screen	R273H S241F R248Q	Disrupts mutp53-p73 complexes	Transcription of p53-shared target genes; p73-dependent *in vitro* antitumor activity	[232]
LEM2 (Xanthone)	Yeast-targeted screening assay	R273H	Disrupts mutp53-TAp73 and MDM2-TAp73 complexes	Enhanced thermal stability of TAp73; Transcription of TAp73- and p53-shared target genes; TAp73-dependent *in vitro* antitumor activity	[233]
Reacp53 (Peptide)	Structure based rational design; Cellular screen	R175H R248Q	Binds to mutp53 aggregation prone region (S9)	Inhibits mutp53 aggregates; Shifts the folding equilibrium toward the wt conformation; Transcription of p53 target genes; p53-dependent *in vitro* and *in vivo* antitumor activity	[234]
ATRA (Retinoic acid; tretinoin)	Chemical library; Mechanism based-screen (protein active site)	R273H R280K	Disrupts mutp53-Pin1 interaction (via Pin1 inhibition and degradation)	*In vitro* and *in vivo* antitumor activity	[235]
Inductors of mutp53 degradation					
17-AAG; 17-DMAG (Demethoxygeldanamycin	HSP90 inhibitor; Cellular evaluation	L194F R273H R273H/P309S R280K	Inhibits HSP90 with increase of MDM2 and CHIP function	*In vivo* antitumor activity in synergism with SAHA	[236, 237]

Chemical name (class)	Discovery strategy	Targeted mutp53	Mechanism of action	Observations	Ref
derivatives)					
Geldanamycin (Benzoquinone ansanamycin)	HSP90 inhibitor; Cellular evaluation	R175H L194F R248Q R273H R280K R172H (mouse)	Inhibits HSP90 with increase of MDM2 and CHIP function	*In vitro* antitumor activity	[238, 239]
Ganetespib (Phenylindolyl triazolone)	HSP90 inhibitor; Cellular evaluation	C124R R172H L194F S241F R248Q R273H C275F	Inhibits HSP90 with mutp53 degradation	*In vivo* and *in vitro* antitumor activity	[237]
SAHA (Suberoyl-anilide hydroxamic acid)	HDAC inhibitor; Cellular evaluation	L194F P223L/V274F R249S R273H R273H/P309S R280K	Inhibits HDAC6/8 (HSP90 machinery) with mutp53 CHIP-ubiquitin/proteasome-mediated degradation; Decreased association with YY-1 transcription factor halting GOF	*In vivo* and *in vitro* antitumor activity	[237, 240-242]
Sodium butyrate	HDAC inhibitor; Cellular evaluation	R249S R280K	Inhibits HDAC8 (HSP90 machinery) with decreased association with YY-1 transcription factor halting GOF	*In vitro* antitumor activity	[242]
Arsenic compounds	Cellular evaluation	R175H H179Y/R282W R248W R270H R273H R273H/P309S	Induce mutp53 nuclear proteasome-mediated degradation	Besides inducing mutp53 degradation, arsenic compounds stabilize wtp53 levels in cancer cells; *In vitro* antitumor activity	[243]
Gambogic acid (Xanthone)	Cellular evaluation	R175H G266E R273H R280K	Depletes mutp53 via HSP90-CHIP ubiquitin/proteasome-mediated degradation	*In vitro* antitumor activity	[244]
Spautin-1 (Fluorobenzylquinazolin amine)	USP inhibitor; Cellular evaluation	P98S P151H S158inF A161T R175C/D/H L194F S227K/R S241F G245C R248L/Q/W E258K G266E R273H/L R280K R282W	Inhibits deubiquitinating enzymes leading to mutp53 lysosome-mediated degradation	*In vitro* antitumor activity	[245]
YK-3-237 (Chalcone)	Chemical library; Cellular evaluation	V157F M237I R249S R273H R280K	Activates deacetylase SIRT1 reducing p53 levels	Transcription of p53 target genes; p53-dependent *in vitro* antitumor activity	[246]
NSC59984 (Methylpiperazinyl nitrofuranyl propenone)	Chemical library; p53-reporter gene cellular	R175H/L S241F R273H/P309F	Induces MDM2-ubiquitin-proteasome-mediated	Transcription of p53 target genes; p73-dependent *in vitro* and *in vivo* antitumor activity	[247]

Chemical name (class)	**Discovery strategy**	**Targeted mutp53**	**Mechanism of action**	**Observations**	**Ref**
	screen		degradation		
Disulfiram (Tetraethylthiuram disulfide)	Cellular evaluation	R273H	Thiol-conjugation with mutp53 proteasome-mediated degradation	*In vivo* and *in vitro* antitumor activity	[248]

[#]The compound is a Michael acceptor suggesting that the mechanism of action occurs by Michael addition to p53 cysteine-thiol groups, nevertheless the reaction was not determined. *ND* – not determined. CHIP – E3 ubiquitin-protein ligase CHIP; HDAC – histone deacetylase; HSP – heat shock protein; Pin1 – peptidyl-prolyl cis-trans isomerase NIMA-interacting 1; SIRT-1 – NAD-dependent protein deacetylase sirtuin-1; USP – ubiquitin carboxyl-terminal hydrolase; YY-1 – transcriptional repressor protein YY1.

Most mutp53-targeting compounds have been identified by synthetic chemical libraries, rational drug design, or evaluation of known compounds, using *in vitro* target protein-based or cell-based screening models [180]. Both screening approaches have some pitfalls. Whereas protein-based assays may lead to the identification of compounds with poor bioavailability, cellular based-assays pose higher challenges to unravel the p53-dependent antitumor mechanism of action [180]. In this scope, the engineered yeast cell-based screening model has risen as an efficient strategy to circumvent the limitations of both protein- and cellular-based assays, once the target-based approach is preserved, while drug bioavailability and cytotoxicity are also evaluated [226, 249]. This was the strategy followed by our research group (**Figure 10**), which was responsible for the successful discovery of several small-molecules with proven *in vitro* and *in vivo* p53-dependent antitumor activity, namely the mutp53 R280K reactivator SLMP53-1 (**Table 2; Figure 11**) [226, 250], and the dual inhibitor of the mutp53/MDM2-TAp73 interactions LEM2 (**Table 2; Figure 11**) [233].

6.1. Cysteine targeting compounds

Some of the identified p53 reactivators can covalently bind to cysteines, by nucleophilic (Michael addition) or nucleophilic aromatic addition, forming adducts with mutp53, which contributes for the stability, refolding and rescue of the wt-like function to mutp53. These compounds are soft electrophiles, so called Michael acceptors (in Michael addition reaction) that preferentially react with soft nucleophiles, normally represented in cells by thiol groups in reduced glutathione and cysteines of proteins [180]. Specifically, p53 has ten cysteine residues in its DBD, being that some are solvent accessible and detain interesting nucleophilic character behaving as potential targets for Michael addition modification, such as C124, C182, C229, and C277 [104, 209]. Of note that, C176, C238,

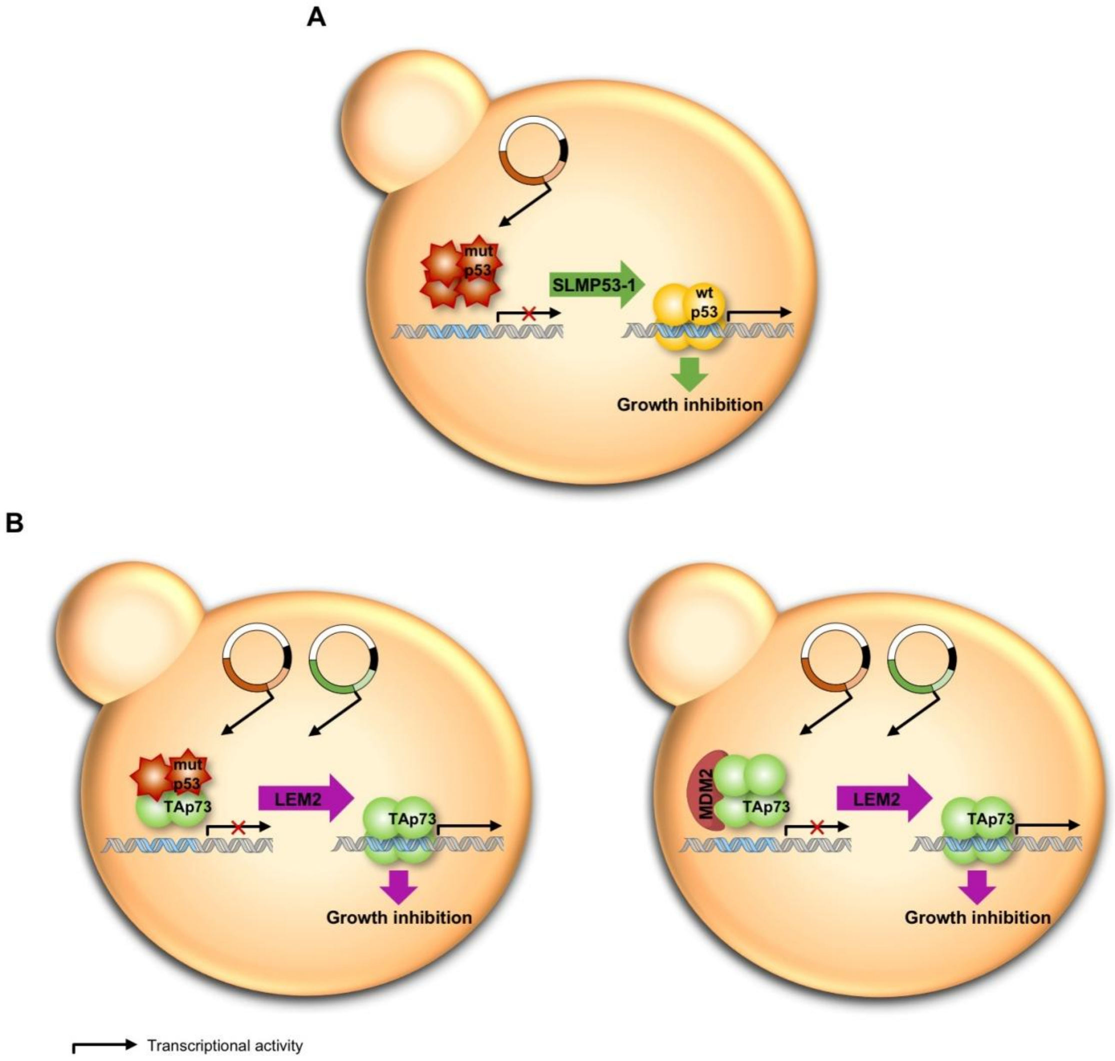
A
mut p53
SLMP53-1
wt p53
Growth inhibition
B
mut p53
TAp73
LEM2
TAp73
Growth inhibition
MDM2
TAp73
LEM2
TAp73
Growth inhibition
Transcriptional activity

Figure 10. Bioengineered yeast cell-based systems for the screening of compounds targeting (A) mutp53, (B) mutp53/MDM2-TAp73 interactions. (A) SLMP53-1 was identified using *Saccharomyces cerevisiae* cells expressing human mutp53 R280K [226]. **(B)** LEM2 was identified using two yeast cell-based systems: co-expressing human TAp73 and MDM2, mimicking the inhibitory effect of MDM2 on TAp73-induced growth inhibition; co-expressing mutp53 and TAp73, mimicking the GOF of mutp53 by inhibiting TAp73-induced growth inhibition [233].

and C242 are considered inert since they are buried and protected from alkylation by zinc coordination [209].

CP-31398, the first reported mutp53 reactivator [190], its derivative STIMA-1 [193], MIRA-1 and analogues [194], and KSS-9 [195] (**Table 2; Figure 11**) are compounds with a reactive double carbon-carbon bond (Michael acceptors), suggesting cysteine-targeting by thiol-binding [209]. They were described as capable to stabilize and reactivate wt-like function to both contact and structural mutp53 forms. Nevertheless, these compounds also exert their antitumor activities by targeting other p53-independent pathways, such as activation of caspase-9 or tubulin inhibition [180, 195, 251, 252].

PRIMA-1 [196, 197] and PRIMA-1^{MET} [198] (**Table 2; Figure 11**), the latter exhibiting higher potency probably due to its higher lipophilicity and cell permeability, were described to be converted into their active metabolite methylene quinuclidinone (MQ; **Table 2; Figure 11**), acting like a strong Michael acceptor targeting cysteines of both contact mutp53 R273H and structural mutp53 R175H [199]. This covalent binding was suggested to occur with the C124 residue by a molecular modeling study that unveiled a transiently open pocket near L1/S3 region [223]. Later, Zhang and colleagues, unveiled that MQ-mediated thermal stabilization of wtp53, and mutp53s R175H and R273H occurred by binding to C277 residue, while both binding to C124 and C277 were required for PRIMA-1^{MET}-mediated functional restoration of mutp53 R175H in cancer cells [205]. Refolding of the structural mutp53 R175H was also observed in cancer cells by immunostaining using specific-folded (PAB1620) and -unfolded (PAB240) anti-p53 antibodies [205]. Besides restored mutp53-mediated transcription-dependent and -independent apoptosis [196, 197, 253], MQ may also exert its antitumor function by inhibiting the antioxidant enzyme thioredoxin reductase 1 and by depleting cellular glutathione inducing oxidative stress in cancer cells [254, 255]. PRIMA-1^{MET} presented *in vivo* antitumor activity [256, 257], and its human safety has been assessed in phase I/IIa clinical trials in patients with leukemias, lymphomas, or prostate cancer [187]. Currently, PRIMA-1^{MET} is under phase IIb proof-of-concept clinical trial in patients with *TP53* mutations and recurrent high-grade serous ovarian cancer [188].

PK11000 (**Figure 11**) is a hit compound with cysteine-thiol-binding ability by nucleophilic aromatic substitution [206]. It was shown that it contributes to the stability of wtp53 and mutp53 Y220C by covalently binding to C182 and C277. It was also verified that PK11000, and its bulkier derivative PK11007 (**Table 2; Figure 11**), preserved the DNA-binding ability, as C277 is responsible for weak polar interactions with DNA major groove and its modification can compromise DNA binding [206]. Between these derivatives, PK11007 showed to induce the highest thermal stabilization to mutp53 Y220C and to have higher cytotoxicity against cancer cells harboring mutp53s Y220C and V143A, when compared to those expressing wtp53. Despite the restoration of the wt-like transcriptional activity to mutp53, the antitumor effects were also related with other p53-independent activities, namely to the activation of unfolded protein response pathways, glutathione (GSH) depletion via thiol-binding with ROS increase [206].

HO-3867 (**Table 2; Figure 11**) is a curcumin analogue with proven selective cysteine-thiol-binding ability to C182 and C277 in mutp53 Y220C [207]. It increased folded wt-like conformation to mutp53s R273H, R280K, and P223L/V274F, and rescued the transcriptional activity to mutp53s R273H, L194F, and P223L/V274F. It also displayed *in vitro* and *in vivo* antitumor activity dependent on mutp53 status. The *in vitro* studies elucidated the ability of HO-3867 to induce the transcription of wtp53 targets to a wide panel of mutp53 forms [207].

6.2. Thermal stabilizers

3-Benzoylacrylic acid (**Table 2; Figure 11**) was described to increase the thermal stability of mutp53 Y220C [209]. As a compound with Michael acceptor activity, it was observed that the effect on mutp53 was attributable to its cysteine-thiol-binding ability instead of binding to the induced Y220C-induced cleft. In accordance to cysteines reactivity, 3-benzoylacrylic acid primarily binds to C124 and C141, followed by C135, C182 and C277. It was also verified that its stabilizing activity was extended to other structural mutp53 forms, namely R175H, G245S, R249S, and R282W. Nevertheless, the covalent binding to cysteines compromised the DNA-binding ability [209]. Although, this study contributed to the knowledge of mutp53 thermal stabilization via cysteine-targeting, the ability of 3-benzoylacrylic acid to reactivate wt-like functions to mutp53 was not unveiled.

6.3. Zinc chelating compounds

As previously mentioned, zinc is essential for the correct folding of p53 DBD [104]. In fact, the addition of zinc to cells or its administration to mice with tumors rescued the DNA-binding ability of mutp53s R175H and R273H with tumor suppression [258, 259], which has reinforced the potential of zinc as a therapeutic strategy.

The metallochaperone ZMC1 (**Table 2; Figure 11**), capable to facilitate intracellular zinc transport working as an ionophore [260], was reported to buffer optimal intracellular zinc concentrations and to provide the zinc ion to the native binding site, contributing to the improvement of zinc:mutp53 R175H binding [211]. ZMC1 exhibited selective antitumor activity to cancer cells harboring mutp53 R175H, stimulating the rescue of wt-like conformation to mutp53 and inducing the transcription of p53 target genes. It elicited *in vivo* antitumor activity in p53$^{R172H/R172H}$ mice (equivalent to human mutp53 R175H) [210]. ZMC1 also restored wt-like structure and function to other zinc-deprived mutp53 forms, such as C242S [211]. Additionally, ZMC1 affected REDOX balance of the cell and induced transactivation of rescued mutp53 R175H via K120 acetylation [211].

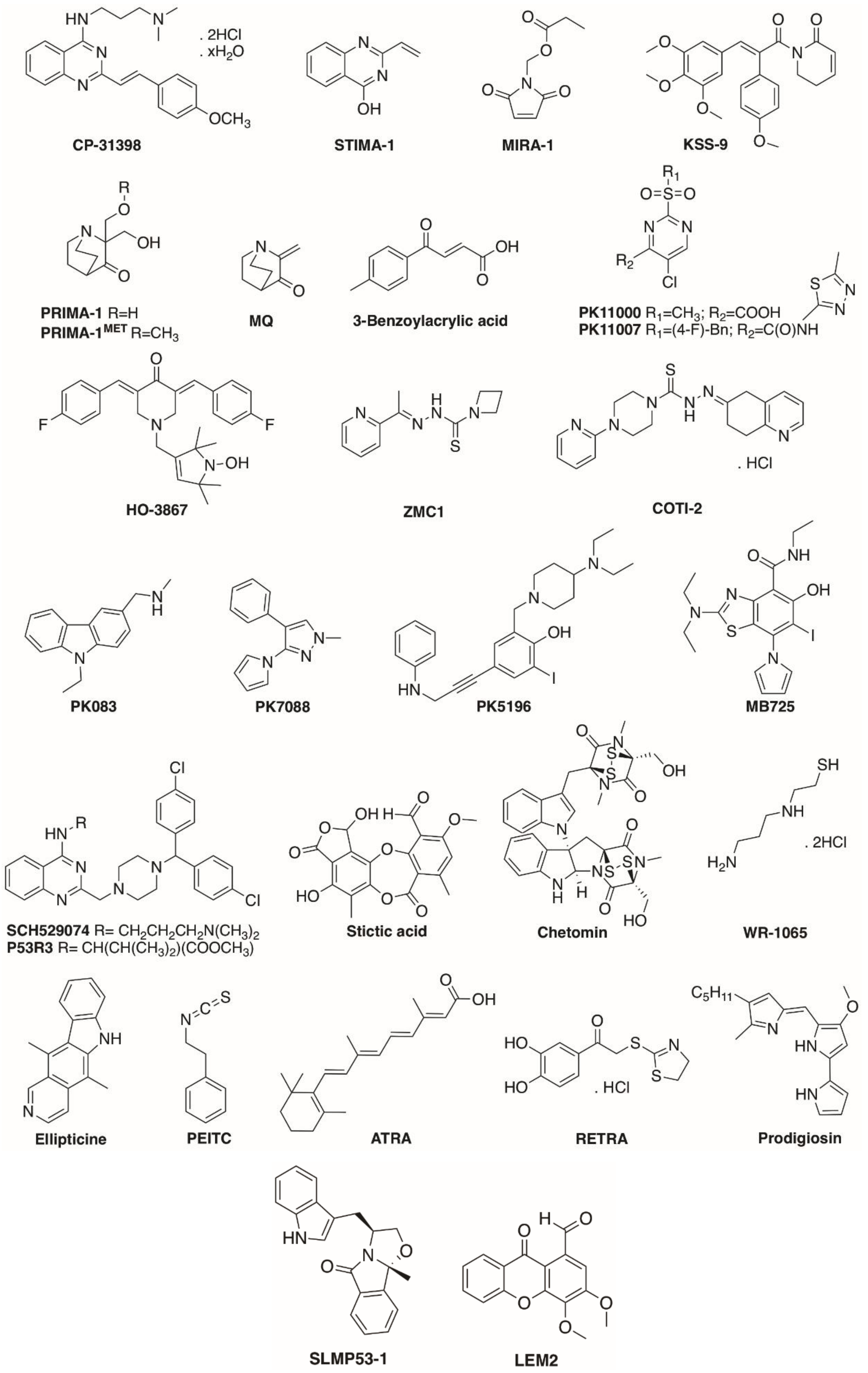
CP-31398
STIMA-1
MIRA-1
KSS-9
PRIMA-1 R=H
PRIMA-1MET R=CH3
MQ
3-Benzoylacrylic acid
PK11000 R1=CH3; R2=COOH
PK11007 R1=(4-F)-Bn; R2=C(O)NH
HO-3867
ZMC1
COTI-2
PK083
PK7088
PK5196
MB725
SCH529074 R= CH2CH2CH2N(CH3)2
P53R3 R= CH(CH(CH3)2)(COOCH3)
Stictic acid
Chetomin
WR-1065
Ellipticine
PEITC
ATRA
RETRA
Prodigiosin
SLMP53-1
LEM2

Figure 11. Chemical structures of mutp53-targeting small-molecules.

COTI-2 (**Table 2; Figure 11**) was described to restore wt-like function to mutp53 R175H and other mutp53 forms by a mechanism that involved zinc chelation [212]. It also affected the phosphoinositide 3-kinase/RAC-alpha serine-threonine-protein kinase/mechanistic target of rapamycin (PI3K/AKT/mTOR) pathway [213]. Currently, COTI-2 is under phase I clinical trial for safety assessment in gyneacological tumors and head and neck cancers [189].

6.4. Non-covalent binding compounds

Other compounds are capable to reactivate wt-like function to mutp53 by non-covalent binding to mutp53, contributing to protein stability and sequence-specific DNA binding.

The cleft on the surface of the *β*-sandwich of mutp53 Y220C (composed by a central site and two lateral subsites) has been used in rational drug design [168]. PK083, PK7088, PK5196, and MB725 (**Table 2; Figure 10**) were identified by virtual and NMR-based screenings, as binders of mutp53 Y220C cleft [215-218]. Interestingly, comparing to PK083 and PK7088, PK5196 (fragment-based designed) bears an iodine responsible for the establishment of a halogen-oxygen interaction with L145 in the central site, and an acetylene linker that allowed to reach to another subsite establishing CH-π stacking interactions with P153, optimizing the binding affinity [218]. Further, the development of aminobenzothiazole derivatives, like MB725, was based on structure-guided design by finding a third transiently open subsite in mutp53 Y220C hydrophobic pocket, rendering higher binding affinities [216]. Despite all compounds induced mup53 Y220C thermal stabilization and *in vitro* antitumor activity (weak effect observed by PK7088), only MB725 exhibited interesting selectivity towards mutp53 Y220C-expressing cancer cells [216-218].

p53 conformation activating peptides (PCAPs) (**Table 2**) were capable to bind and rescue wt-like conformation to structural mutp53s R175H and R249S [219]. An enhancement of DNA binding was also observed in mutp53 forms R175H and R249S. Further, reactivation of wtp53 transcriptional activity with antitumor activity was verified for mutp53s S241F, V135A, and R280K [219].

The CBD3 peptide (**Table 2**) was rationally designed based on the binding region of 53BP2, a co-factor that enhances p53-mediated transactivation, preferentially stimulating apoptosis [220]. It was demonstrated that the CBD3 peptide binds to L1, H2 and S8, which are located at one edge of the p53 DNA-binding surface, and differs from the initial binding site of 53BP2 (between L3 and H2). Nevertheless, this approach successfully enhanced the thermal stability, wt-like conformation, DNA-binding capacity and function of mutp53 [220].

SCH529074 (**Table 2; Figure 11**) was described to bind specifically to p53 DBD in a saturated manner, restoring wt-like DNA binding to mutp53s R273H and R249S by acting as a molecular chaperone similarly to peptide CDB3 [220, 222]. Indeed, binding of SCH529074 and CBD3 to p53 DBD was observed as mutually exclusive, suggesting that these molecules compete to a common binding region, acting via the same mechanism. SCH529074 binding to the p53 DBD was specifically displaced upon cognate RE presence, probably allowing a conformational rearrangement with effective binding of p53 DBD to the DNA sequence and recycling intracellular free drug [220, 222]. As CDB3 [111, 170, 220], SCH529074 increased the thermal stability to several mutp53 DBD forms, increasing wt-like folded form and DNA binding [222]. It was unveiled that SCH529074 and CDB3 binding to p53 was disturbed by the second-site mutation of residue N268R, but not by N268D in S10 [222]. Both mutations were described to contribute to protein stability and DNA binding [162]. Nevertheless, arginine is a larger amino acid than aspartic acid, and both residues present distinct pKa, making that N268R possibly induces higher rigidity, and alteration of the hydrogen bonding network and the chemical environment, thereby interfering with the binding of conformational stabilizers SCH529074 and CDB3 [222]. It was also observed that SCH529074, CDB3 and mutp53 N268R blocked MDM2-mediated ubiquitination [222], suggesting that some specific conformation is needed for MDM2 docking and ubiquitination. SCH529074 and CBD3 induced the transcription of wtp53 target genes in cancer cells expressing different mutp53 forms [221, 222], and SCH529074 exhibited *in vivo* antitumor activity [222].

Stictic acid (**Table 2; Figure 11**) was shown to bind *in silico* with high affinity to the L1/S3 site, a transiently-open pocket in p53 DBD [223]. It was also observed that stictic acid induced *in vitro* thermal stabilization of mutp53s R175H and G245S, and the transcription of p53 target genes in cancer cells expressing mutp53 [223].

The natural compounds curcumin, flavokawain B, and alpinetin (**Table 2**) were shown to have p53-dependent antitumor properties [224]. By an *in silico* study, Malami and colleagues hypothesized about the mechanism of action of these compounds in reactivating mup53. They described the ability of these compounds to bind and bridge the interface of DNA-binding surface of contact mutp53 R273H and the DNA sequence, compensating the missing contacts induced by the mutation [224]. Nevertheless, the experimental validation of this hypothesis is still required. Of note that curcumin has been described to target different pathways [261], and belongs to the category of pan-assay interference compounds (PAINs) [262], so it is likely that other p53-independent mechanisms underlying its antitumor activity might be involved in mutp53-expressing cancer cells.

6.5. Compounds indirectly-targeting mutp53

Chetomin (**Table 2; Figure 11**) was described as selectively targeting cancer cells expressing the structural mutp53 R175H rather than wtp53 or contact mutp53 R273H, with induction of canonical p53 target genes [225]. These observations were attributed to the ability of chetomin to directly interact with HSP40, increasing its binding to mutp53 R175H [225]. HSP40 is a binding partner of p53, acting as chaperone that assists in protein conformation and stability for DNA binding [115].

6.6. Compounds targeting mutp53 with unknown binding mechanism

There are compounds which mutp53 reactivation has been proven, nevertheless the putative mechanism of action was poorly understood or unexplored.

Regarding SLMP53-1 (**Table 2; Figure 11**), this compound activated wtp53, restored DNA binding ability with wt-like transcriptional activity to mutp53 R280K, and caused p53-dependent cell cycle arrest and apoptosis, leading to *in vitro* and *in vivo* antitumor activity [226].

Ellipticine, an alkaloid, was shown to induce wt-like p53 transcriptional activity to a diverse panel of mutp53 forms, with rescue of DNA binding to S241F and R175H, and wt-like conformation to S241F. Interestingly, although the *in vivo* ability of ellipticine to restore sequence-specific DNA binding of mutp53 was demonstrated, the *in vivo* antitumor activity was not disclosed [227].

WR-1065 (**Table 2; Figure 11**) is an active metabolite of the cycloprotective compound amifostine that, besides its multiple mechanisms of action, it was described as a reactivator of a structural temperature-dependent mutp53 [230]. At physiological temperature, WR-1065 restored wt-like conformation to mutp53 V272M with reestablishment of DNA binding and transcription of canonical p53 target genes, as well as p53-dependent cell cycle arrest [230].

P53R3 (**Table 2; Figure 11**) has shown to be more selective and potent in rescuing wt-like function to mutp53 than PRIMA-1 [228]. It presented *in vitro* p53-dependent antitumor activity, restoring DNA binding to mutp53, and inducing the transcription of p53 target genes [228].

6.7. Disruptors of protein-protein interaction

Besides mutp53 reactivation, there are other strategies to target mutp53 envisioning the abrogation of its GOF effects. In this context, compounds able to reestablish TAp63/p73-dependent antitumor activity through disruption of the mutp53 interaction with these tumor suppressors represent a reliable anticancer therapeutic strategy [180, 186]. Also, compounds that prevent the interaction of mutp53 with other transcription co-factors involved in the transcription of non-canonical target genes, eliciting neomorphic oncogenic responses, are interesting to consider. Particularly, the active metabolite of vitamin A, ATRA (**Table 2; Figure 11**), was shown to bind to Pin1 inducing its degradation [235]. Pin1 promotes the inhibition of TAp63 by mutp53 and oncogenic mutp53 transcriptional activity [263]. Therefore, the degradation of Pin1 may block mutp53 GOF, although more studies on ATRA mechanism of action are needed. ATRA was approved by FDA for treatment of acute promyelocytic leukemia [235].

The compound RETRA (**Table 2; Figure 11**) is active in TAp73- and mutp53 R273H-expressing tumor cells [231]. Similarly, prodigiosin (**Table 2; Figure 11**) showed to be more potent in TAp73-expressing tumor cells with mutp53s R273H, S241F, and R248Q than R175H [232]. Although their mechanism of action needs further understanding, the ability of RETRA and prodigiosin to induce TAp73-dependent antitumor activity involving the transcription of p53-shared target genes, and disruption of the mutp53 interaction with TAp73 were disclosed [231, 232].

Recently, it was reported that the xanthone derivative LEM2 (**Table 2; Figure 11**) induced a TAp73-dependent antitumor response in p53-null or mutp53-expressing cancer cells [233]. LEM2 was capable to halt the GOF of mutp53 over TAp73. The free TAp73 was thermally stabilized by LEM2, eliciting the transcription of p53-shared target genes with tumor suppression, namely in patient-derived neuroblastoma cells [233].

As previously mentioned, some mutp53 forms may aggregate in cellular context due to exposure of specific amino acid sequences prone to amyloid-like aggregation during protein unfolding [264, 265]. Reacp53 (**Table 2; Figure 11**), a cell penetrating peptide rationally designed to dock the aggregation-prone S9 amino-acid sequence (residues 252–258), was shown to halt mutp53 aggregation, dislocating the thermodynamic equilibrium to the wt-like correctly folded soluble form. Besides wt-like conformation rescue, Reacp53 also induced the transcription of p53 target genes and exhibited *in vitro* and *in vivo* antitumor activity [234].

Pradhan and colleagues have studied the nucleation and aggregation process of structural mutp53 DBD forms [266]. By molecular dynamics simulations, they found that the S6-S7 turn adopted different conformations among wtp53 (“closed” state) and diverse mutp53 forms (“opened” state). It was also observed that the “opened” state of S6-S7 turn exposed S9 (the aggregation prone region), whereas the “closed” state kept S9 buried and inaccessible. These observations suggested that the conformational state of the S6-S7 turn relates to the thermodynamic stability of the DBD, previously hinted by Ng and colleagues [166]. As such, the “opened” state of S6-S7 turn represents the destabilized state of mutp53 and might be an initial event in the onset of unfolding and aggregation [266], posing a putative binding pocket to prevent these protein events. Despite requiring experimental validation, *in silico* screen of FDA approved drugs suggested that this pocket is very likely druggable and functional [266].

6.8. Compounds depleting mutp53

Other compounds targeting mutp53 can lead to its degradation with benefit to tumor suppression (**Table 2**). High levels of mutp53 depend on chaperone HSP90 for relative stability, turning this molecule an interesting therapeutic target. Indeed, inhibitors of HSP90, like 17DMAG, geldanamycin and ganetespib, and/or histone deacetylase (HDAC) inhibitors, like SAHA targeting HDAC6 (inducer of HSP90) and sodium butyrate targeting HDAC8, destabilize mutp53 with suppression of its transcriptional GOF [237, 241, 242] by inducing its MDM2 or CHIP-mediated degradation.

Although none of the above discussed mutp53-targeting compounds have reached the clinic, the structural and mechanistic diversity among them is encouraging. It is reasonable to expect that some of them will prove effective clinical applications in a near future [180]. Moreover, although the potential of reactivating wt-like functions to mutp53 with canonical genes transcription has been proven, it does not always translate into cell death or halt tumor growth, as it also depends on cancer cell context [48, 180]. Despite all the strategies pointed above to target mutp53, drugging mutp53 still prompts researchers and clinicians to investigate new possibilities in the universe of mutp53 pharmacology, structure, and biology. Of note that, computational approach has proven to be a useful tool, with two putative transiently open pockets in the p53 DBD structure reported as potential binding sites for stabilizing small-molecules [223, 266]. The pharmacological reactivation of mutp53 also poses a great opportunity in combination therapy with anticancer drugs known to trigger cancer cell death by p53-dependent apoptosis or to inhibit mutp53 downstream pathways [180].

7. Nanotechnology as a strategy to improve pharmacokinetics of drug candidates for anticancer therapy

Despite many advances in drug discovery and development, based on rational drug design approaches, simulation software and high-throughput screenings of diverse chemical libraries of natural and synthetic compounds [267], many promising small-molecules have failed their clinical translation or have been associated with secondary morbidity costs. Specifically, in pharmacological cancer treatments, low specificity in tissue distribution, intolerable toxic side effects, limited targeting with inefficient tumor drug concentration, biodegradation, rapid drug clearance, and multiple drug resistance, are examples of pharmacokinetic- and toxicity-related problems [268-271].

In this context, nanotechnology has raised as an encouraging strategy to overcome these limitations [272], with many nanotechnology anticancer products entering the clinic or in clinical trials (reviewed in [267, 273]). In general, compounds with low solubility and high permeability (class II, Biopharmaceutic Classification System (BCS)), or with low solubility and low permeability (class IV, BCS) are eligible to nanodelivery system design [274-276]. In fact, nanotechnology can offer the opportunity to mask the physicochemical properties of small-molecules, to formulate tissue- or cell-targeted therapies, and to control drug release via grafted or loaded nanoparticles (NPs) with the therapeutic drugs [267]. For the oral administration route, NPs can protect drugs from gastrointestinal degradation, increasing drug bioavailability by solubility enhancement and/or uptake by endocytic mechanisms [267]. Considering the intravenous route scenario, NPs prolong bloodstream circulation reducing rapid drug clearance, allow drug release with fewer plasma concentration fluctuations, enable penetration in the tissue system, and facilitate cell uptake with targeted and efficient drug delivery sparing normal tissue. Thus, NPs improve the efficacy of drug therapy while constraining undesirable effects [267]. However, despite the advantages that nanotechnology poses in drug nanodelivery systems, there are several limitations to overcome for their clinical application. Some are related with enzymatic degradation and immune elimination due to opsonization [277]. Another concern is related with the efficacy of NPs targeting, since a meta-analysis has evidenced that tumor accumulation of NPs was typically less than 1% [278]. Nonetheless, targeting strategies often increase cellular-uptake [279]. Additionally, there is a scarce knowledge about NPs toxicity, which should deserve further research to their safe clinical application [267].

There is a myriad of nanomaterials from different sources to produce NPs for drug delivery, *i.e.,* lipid- (*e.g.*, micelles, liposomes, solid-lipid NPs), polymeric- (*e.g.*, dendrimers, polymer-drug conjugates, nanospheres), and inorganic-based (*e.g.*, gold, porous silicon, carbon nanotubes). The selection of the nanomaterial is based on the bio-physicochemical features of the small-molecule [267]. The efficacy of these nanodelivery systems depends on their size, shape, target selectivity, biological activity, efficiency of uptake and drug concentration, among other inherent bio-physicochemical characteristics, and also on biological barriers and physicochemical properties of the host environment [271]. In next subsection, mesoporous silicon (PSi) NPs will be described under the scope of the present thesis.

7.1. Mesoporous silicon nanoparticles

Mesoporous silica ($PSiO_2$) and PSi-based materials are attractive materials due to their unique physicochemical properties and potential versatile biomedical applications, specifically in cancer therapy and bioimaging [280-282]. $PSiO_2$ and PSi nanoparticles differ on their fabrication by “bottom-up” or “top-down” approaches, respectively [283]. Additionally, they have been proposed as drug delivery vectors of a wide variety of chemotherapeutic agents, such as cisplatin, docetaxel, and sorafenib, which are drugs with anticancer activity but commonly associated with poor selectivity or undesirable side effects [284-286]. The mesoporous nanosystems are designed to carry and release their cargos to a specific location, particularly for cancer treatment into the interstitial fluid, tumor surface or intracellular compartment, at a controllable release rate, without compromising the patient’s health [282].

Mesoporous stands for materials with pores diameter ranging from 2 to 50 nm, allowing high payloads of drugs and protecting them from premature release and degradation before reaching the target site [282, 287, 288]. PSi NPs are characterized by high surface-to-volume ration, large surface area (up to 700-1,000 m^2/g) and pore volume (>0.9 cm^3/g), and a robust framework with chemical, thermal, and mechanical stability [289]. The possibility to tune pore size and surface chemistries raises the advantage of PSi NPs to act as selective storage related with size and hydrophobicity of drugs [282, 283]. PSi nanomaterials are produced by electrochemical anodization, which renders irregular pore structure and unstable hydrogen-terminated PSi. Thus, PSi nanomaterials are commonly submitted to additional reactions of oxidation, carbonization or hydrosilylation, rendering materials not only with increased surface stability, but also with hydrophilic or hydrophobic properties (**Figure 12**) [290]. Thus, porous size and surface chemistry may affect loading and release profiles (**Figure 12**), as surface chemistry influences the physicochemical interactions (covalent attachment or physical adsorption) between the surface of the carrier and the small-molecules of the cargo [291]. Porous are interconnected and open, therefore accessible to solvents or fluids not only for easy loading, but also for drug release [290]. Physical desorption mechanisms give some grade of controlled release, whereas covalent bonds break or degradation of nanoparticles matrix lead to prolonged drug release [282]. Nevertheless, if additional control or fine tune of the drug release profile is needed, the “gate-keeping” approach offers the opportunity to cloak the pores with environment responsive materials or self-sealing approach (**Figure 12**) [282, 290]. PSi surface is also amenable to be functionalized with different biomolecules for targeted therapy and site-specific delivery of the cargo (**Figure 12**) [292].

Although cellular uptake can be optimized by tailoring PSi NPs shape, size, pore, charge or surface chemistry/functionalization, it is important to understand that these properties also dictate biocompatibility (**Figure 12**) [282]. To apprehend PSi NPs biocompatibility, it is necessary to consider the route of administration, the biodistribution, and the multiple biological elements and boundaries that are in close or immediate contact with NPs [282]. PSi cytotoxicity was described to be size-, shape-, surface charge- and concentration-dependent [290, 293-302]. Biodegradability is directly proportional to pore size and porosity of PSi NPs. Porosity below 70% renders bioactive and slowly biodegradable PSi NPs, and higher than 70% leads to PSi complete dissolution. Surface chemistry/functionalization also influences biodegradability, for example, carbonization slows down the process. PSi NPs are decomposed into orthosilicic acid species, which are known to be harmless to cells and easily excreted in urine (**Figure 12**) [290, 303-305]. Interestingly, an enhancement of PSi degradation can be observed under pathological conditions due to increased levels of ROS, printing oxidation on silicon framework and catalyzing its degradation [306].

Although some challenges remain to be fully-addressed for the clinical translation of PSi NPs, such as intracellular uptake and trafficking, biodistribution, degradation and clearance, and production scalability, they have received increasing attention based on all the advantages and applications described above.

The exploration of effective solutions to overcome drug low bioavailability can be also made by changing its physico-chemical properties, such as size reduction, salt formation, use of surfactants, and drug amorphization [307]. The conversion of the crystalline form of compounds to the amorphous one has been considered as a promising and potentially “universal” strategy that can be applied to therapeutic agents with effective increase of their solubility and dissolution rate. This strategy is based on the knowledge that the amorphous state is the highest internal energy form of a solid material with enhanced thermodynamic properties (enthalpy and entropy), no molecular order and high

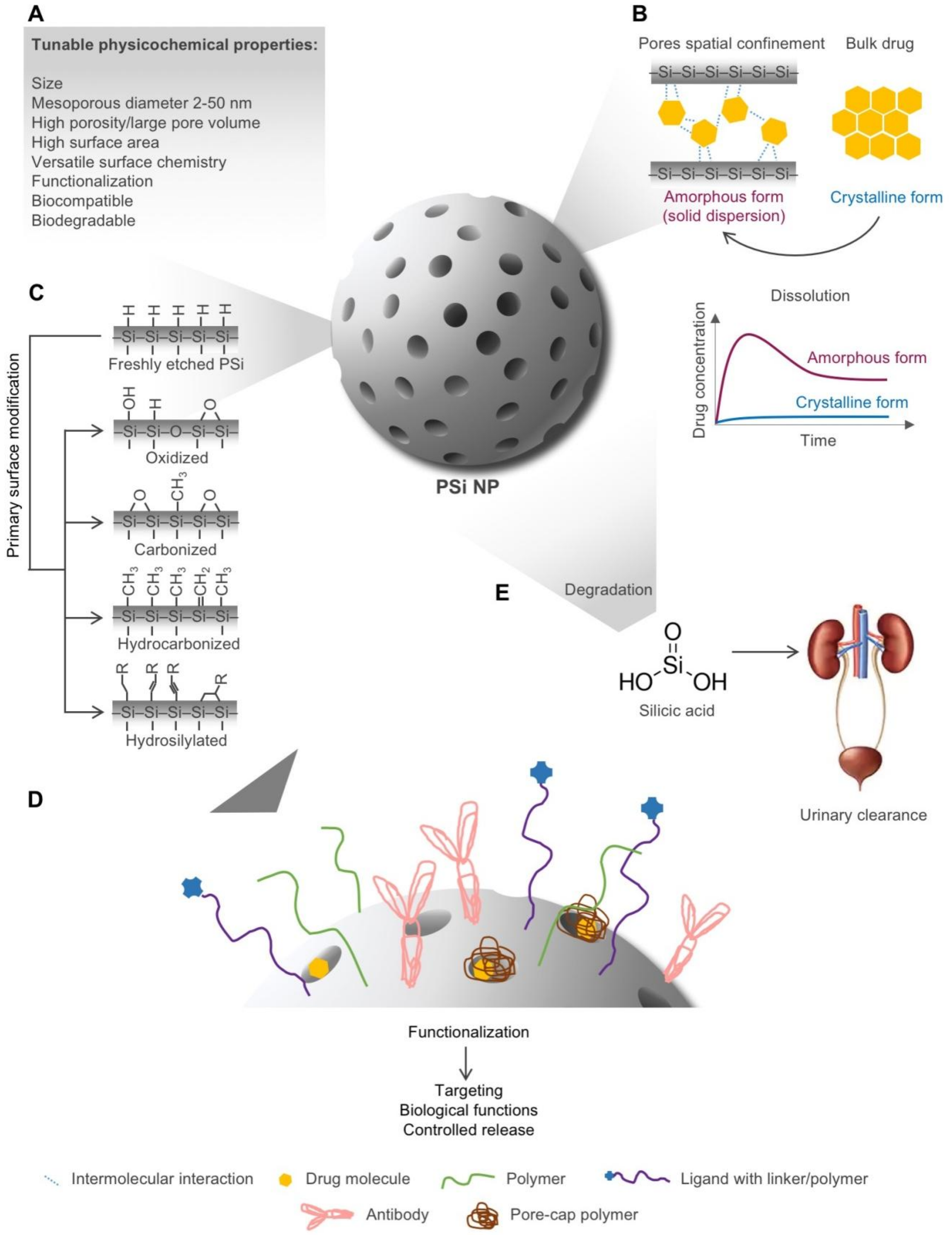
A
Tunable physicochemical properties:
Size
Mesoporous diameter 2-50 nm
High porosity/large pore volume
High surface area
Versatile surface chemistry
Functionalization
Biocompatible
Biodegradable
B
Pores spatial confinement
Bulk drug
Amorphous form (solid dispersion)
Crystalline form
Dissolution
Drug concentration
Amorphous form
Crystalline form
Time
C
Primary surface modification
Freshly etched PSi
Oxidized
Carbonized
Hydrocarbonized
Hydrosilylated
PSi NP
E
Degradation
Silicic acid
Urinary clearance
D
Functionalization
Targeting
Biological functions
Controlled release
Intermolecular interaction
Drug molecule
Polymer
Ligand with linker/polymer
Antibody
Pore-cap polymer

Figure 12. Physicochemical properties and structure of PSi NPs that disclose their potential as drug carriers. (A) PSi NPs have tunable physicochemical properties. **(B)** PSi narrow pores increase drug solubility and dissolution rate by promoting the conversion into its amorphous form, constituting an amorphous solid dispersion. **(C)** PSi surface chemistry allows different stabilization chemical treatments resulting in distinct functional groups terminations. **(D)** These functional groups constitute the base for further functionalization of PSi NPs by grafting different crosslinker

molecules, polymers, antibodies, and ligands, or to cap the drug-loaded pores leading to targeted- and/or controlled-release drug delivery. **(E)** PSi can also be degraded into orthosilicic acid forms in physiological fluids, leading to its excretion.

molecular mobility [308]. These physical differences, towards the crystalline state (organized molecular framework and low Gibbs free energy), make the amorphous state to exhibit higher relative solubility (thermodynamic process) and dissolution rate (kinetic process) [309, 310]. Nonetheless, the attractive properties of amorphous materials can also be a limitation, as the high internal energy and molecular mobility may be responsible for their increased chemical reactivity and propensity to recrystallize during manufacturing, storage or upon dissolution [308, 311].

Many efforts have been focused on critical factors involved in recrystallization and effective methods to stabilize amorphous compounds to benefit from their advantages [312]. Traditionally, solid polymer dispersions have been the preferred method to enhance amorphous drug stability [313]. However, polymer-based formulations have some drawbacks, such as hygroscopic properties that often lead to phase separation and recrystallization [312]. Thus, alternative methods in amorphous compounds stabilization have been proposed, namely mesoporous systems, such as PSi.

PSi systems have a high surface free Gibbs energy. Upon drug incorporation in the mesoporous, generally by a solvent deposition method (*e.g.,* immersion), the drug molecules are adsorbed on the mesoporous material surface and lose their crystalline form. Consequently, the global system transits to lower Gibbs free energy with gains on the physical stability [314]. In addition to thermodynamic factors, the mesoporous systems promote drug amorphization by spatial constraints (**Figure 12**), as the pore size limits the amount of incorporated drug molecules and their mobility. Molecular mobility is also affected by intermolecular interactions of the drug with the mesopores surface (**Figure 12**), which depends on surface chemistry. Altogether, these factors deter nucleation and crystal growth [291, 314-318]. Indeed, when compared to the crystalline drug, PSi systems have allowed the formulation of amorphous solid dispersions, physically stable over time, with enhanced drug dissolution rate, and for different therapeutic agents, such as itraconazole, ibuprofen, indomethacin, paclitaxel, doxorubicin, and furosemide (reviewed in [312, 313]).

8. Scope and aims

The present doctoral thesis was developed under the general scope of developing new anticancer drug candidates by targeting p53 and TAp73. In particular, it was intended to:

I. Elucidate the molecular mechanism of action of the mutp53 R280K reactivator SLMP53-1;
II. Improve the bioavailability of the TAp73 activator LEM2 for *in vivo* antitumor studies.

To achieve the proposed goals, the following research work was carried out:

i) Production of recombinant human mutp53 R280K DBD (**Chapter II**);
ii) Structural elucidation of mutp53 R280K DBD (**Chapter II**);
iii) Study of the SLMP53-1 binding ability to mutp53 R280K DBD (**Chapter III**);
iv) Study of the capacity of SLMP53-1 to reactivate multiple mutp53 forms (**Chapter III**);
v) Improvement of LEM2 bioavailability by developing PSi-based nanodelivery systems (**Chapter IV**).

Therefore, this thesis encompassed multidisciplinary approaches and integrated strategies from different scientific fields, including biotechnology, chemistry, molecular biology, computation, oncobiology, and pharmacology.

Collectively, the knowledge obtained in the present thesis will certainly contribute to the advance of p53 pharmacology and p53-targeting anticancer drug development strategy. Most importantly, it will certainly boost the potential clinical translation of SLMP53-1 and LEM2, or improved derivatives.

Chapter II

The crystal structure of the R280K mutant of human p53 explains the loss of DNA binding

This chapter contains parts of the following article:

Ana Sara Gomes*, Filipa Trovão*, Benedita Andrade Pinheiro, Filipe Freire, Sara Gomes, Carla Oliveira, Lucília Domingues, Maria João Romão, Lucília Saraiva, Ana Luísa Carvalho, (2018), “*The crystal structure of the R280K mutant of human p53 explains the loss of DNA binding”* International Journal of Molecular Sciences, 19(4). pii: E1184. doi: 10.3390/ijms19041184.

*The authors contributed equally to the work.

1. Summary

So far, different mutp53 forms with clinical impact have been studied regarding their thermodynamic stability and DNA binding, some of which were structurally elucidated as previously discussed in **Chapter I**. These studies have contributed to the understanding of the biology/biochemistry of this molecular hub, and to the rational design of p53-reactivating agents as anticancer drug candidates. The present work focuses on the mutation of residue R280, which is involved in direct DNA recognition and interacts with a structural water molecule contributing for overall stability and proximal residues correct positioning. It is known that, when this residue is mutated (R280K), the DNA transcription is halted. Therefore, we aimed to understand the phenomena underlying the former observation. Herein, the recombinant mutp53 R280K DBD (without the four stabilizing mutations) was produced for the first time, and its crystal structure was determined in the absence of DNA to a resolution of 2.0 Å. The structure was compared with previously reported wtp53 DBD structures, isolated and in complex with DNA. These comparisons allowed to understand that mup53 R280K has a similar structure to wtp53, and that the lysine is unable to establish hydrogen-bonds to the DNA leading to loss of DNA binding, which related to impaired transcriptional activity.

2. Materials and methods

2.1. Expression plasmid construction of mutp53 R280K DBD

The DBD of the mutp53 R280K (residues 94–312) was PCR-amplified from vector pLS76 [319] with Vent DNA polymerase (New England Biolabs, Ipswich, MA, USA), using the forward primer 5' TGC **TCTAGA** AAT AAT TTT GTT TAA CTT TAA GAA GGA GAT ATA CAT *ATG* TCA TCT TCT GTC CCT TCC 3' and the reverse primer 5' CCG **CTCGAG** TCA GGT GTT GTT GGG CAG 3'. The restriction sites *XbaI* and *XhoI* (in bold) were included in the forward and reverse primers, respectively, and a start codon (italics) and a stop codon (underlined) were also respectively included. PCR products were digested with *XbaI* and *XhoI* (New England Biolabs) and inserted into the same restriction sites of the pETM20 expression vector (EMBL, Heidelberg, Germany). For that, digested DNA fragments were gel purified using the Qiaquick Gel Extraction Kit (QIAgen, Hilden, Germany) and ligated with T4 DNA ligase (Promega, Madison, WI, USA), according to the manufacturer's protocols, originating the plasmid pETM20-mutp53 R280K (**Annex I, Figure S1**). This plasmid was propagated and maintained in *E. coli* NZ5*α* (NZYTech, Lisboa, Portugal). The sequence of the insert in the plasmid was confirmed by sequencing

(GATC Biotech, Constance, Germany) with T7 primers pair. The expression plasmid pETM20-mutp53 R280K was then transformed into the expression strain *E. coli* NZYBL21 (DE3) (NZYTech).

2.2. Recombinant production and purification of mutp53 R280K DBD

Protein production and purification were based on [87], with further optimization. *E. coli* BL21 (DE3) cells, harboring the recombinant plasmid pETM20-mutp53 R280K, were grown at 37 ºC (310 K) in LB (Luria-Bertani broth) medium supplemented with 100 µg/mL of ampicillin until $OD_{600\ nm}$ of 1.2. The bacterial culture was thereafter supplemented with 10 µM of $Zn(CH_3COO)_2$, and recombinant protein expression induced with 1 mM IPTG (isopropyl β-D-thiogalactoside) overnight at 25 ºC (298 K). Afterward, cells were recovered by centrifugation and lysed in 50 mM HEPES (4-(2-hydroxyethyl)-1-piperazineethanesulfonic acid) pH 7.5, 5 mM dithiothreitol (DTT), 10 µM $Zn(CH_3COO)_2$, and 100 mM phenylmethylsulfonyl fluoride (PMSF) using sonication. Cellular remains were removed by centrifugation. Preliminary purification analysis was performed by differential scanning fluorimetry (DSF) and dynamic light scattering (DLS) (**Annex I, Figure S2**). Supernatant was filtrated (0.2 µm) and loaded onto a HiTrapTM Heparin HP column (GE Healthcare, Little Chalfont, Buckinghamshire, UK). Proteins were eluted with a NaCl step gradient (0, 100, 200, and 250 mM, 1 mL/min, and 0.7 mL/min for the last concentration), in ÄKTA start system (GE Healthcare) (**Annex I, Figure S3 A, B**). The eluted fractions, containing the mutp53 R280K, were pooled and further purified by gel filtration chromatography using a Superdex-75 column (GE Healthcare) in a Shimadzu high performance liquid chromatography (HPLC; 0.5 mL/min) and the selected buffer with 50 mM HEPES pH 7.5, 150 mM NaCl, 5 mM DTT, 10 µM $Zn(CH_3COO)_2$, and 5% (*v*/*v*) glycerol as the running buffer. Peak fractions were analyzed by sodium dodecyl sulfate (SDS)-polyacrylamide gel electrophoresis (Blue Coomassie staining) (**Annex I, Figure S3 C, D**) and fractions containing pure protein (~25 kDa) were concentrated using an Amicon® Ultra-15 Centrifugal Filter Unit (Cut-off: 10 kDa; Cycles: 3500 g, 10 min, 4 ºC (277 K); MerckMillipore, Burlington, MA, USA) for crystallization assays.

2.3. Differential scanning fluorimetry (DSF) screening for buffer optimization

A protocol was adapted from [320]. Briefly, two screenings were made, one for buffers/pH and another for additives. Ninety-six-well plates were used (MicroAmp® fast

96-well reaction plate (0.1 mL) from Applied Biosystems, Foster City, CA, USA) and were placed on ice. A reaction mixture of 20 µL was prepared in each well: 11 µL of the buffer/additive solution to be screened, 2 µL at 15 µM of mutp53 R280K DBD in 50 mM Tris.HCl at pH 7.2, 5 mM DTT, 300 mM NaCl (final concentration of 1.5 µM), and 7 µL of SYPRO® Orange dye (5×; prepared in Protein Thermal Shift Dye KitTM, from Applied Biosystems) was added and mixed. The plate was sealed, centrifuged (1 min, 200 *g*, 4 ºC (277 K)) to remove air bubbles, and placed on ice for 5 min in a dark place to equilibrate. DSF was performed using a StepOnePlus Real-Time PCR system (Applied Biosystems) with ROX (rhodamine X; 575/602 nm, absorption/emission) filters. The temperature scan was performed using the range from 25 to 95 ºC (298 to 368 K), at 1 ºC/min. Data were exported and melting temperatures (Tm) were analyzed in Microsoft Office Excel. Best conditions represented in **Annex I, Figure S4**.

2.4. Crystallization of mutp53 R280K DBD

Crystallization screens were performed using an automated crystallization robot (Oryx8, Douglas Instruments, Hungerford, UK) on 96-wells plates, where 0.67 µL of protein solution (6.6 mg/mL in selected buffer) were mixed with 0.33 µL reservoir buffer (1 µL drops with a proportion of 2:1). The best crystals were grown at 20 ºC (293 K) using a sitting drop vapor diffusion technique against a reservoir containing 35% (*w*/*v*) polyethylene glycol (PEG) 3350. Colorless plate-shaped crystals appeared within a week and continued to grow for one more week (**Annex I, Figure S5 A, B**). Crystals were stabilized in the harvest buffer (38% (*w*/*v*) PEG 3350) and flash-frozen in cryoprotectant buffer (38% (*w*/*v*) PEG 3350, 10% glycerol) with liquid nitrogen.

2.5. Data collection, structure solution, and refinement

X-ray diffraction data from crystals of mutp53 R280K DBD were collected at the ID30A-3 beamline of the European Synchrotron Radiation Facility (ESRF, Grenoble, France), to a maximum resolution of 2.0 Å, using an energy of 12.81 keV (**Annex I, Figure S5 C**), a crystal-to-detector distance of 144.8 mm, and an oscillation angle of 0.15º. The diffraction data were indexed in $P2_1$, and integrated and scaled using the CCP4 software package [321]. The structure was solved by molecular replacement using *PhaserMR* [322], with a wtp53 DBD (PDB ID code 2OCJ) as the search model [174]. All subsequent refinement cycles were carried out in the *Phenix* platform [323], using the program phenix.refine [324] with the web server *PDB-REDO* [325]. All residues had backbone and angles in the allowed region of the Ramachandran plot, with 99.7% in the favored region. The resulting R_{work} and R_{free} were 0.20 and 0.24, respectively. All data collection and refinement statistics are summarized in **Table 1**. Figures were generated with UCSF Chimera [326] and PyMOL [105].

Table 1. X-ray diffraction, model building, and refinement statistics (values for the outer shell are given in parentheses).

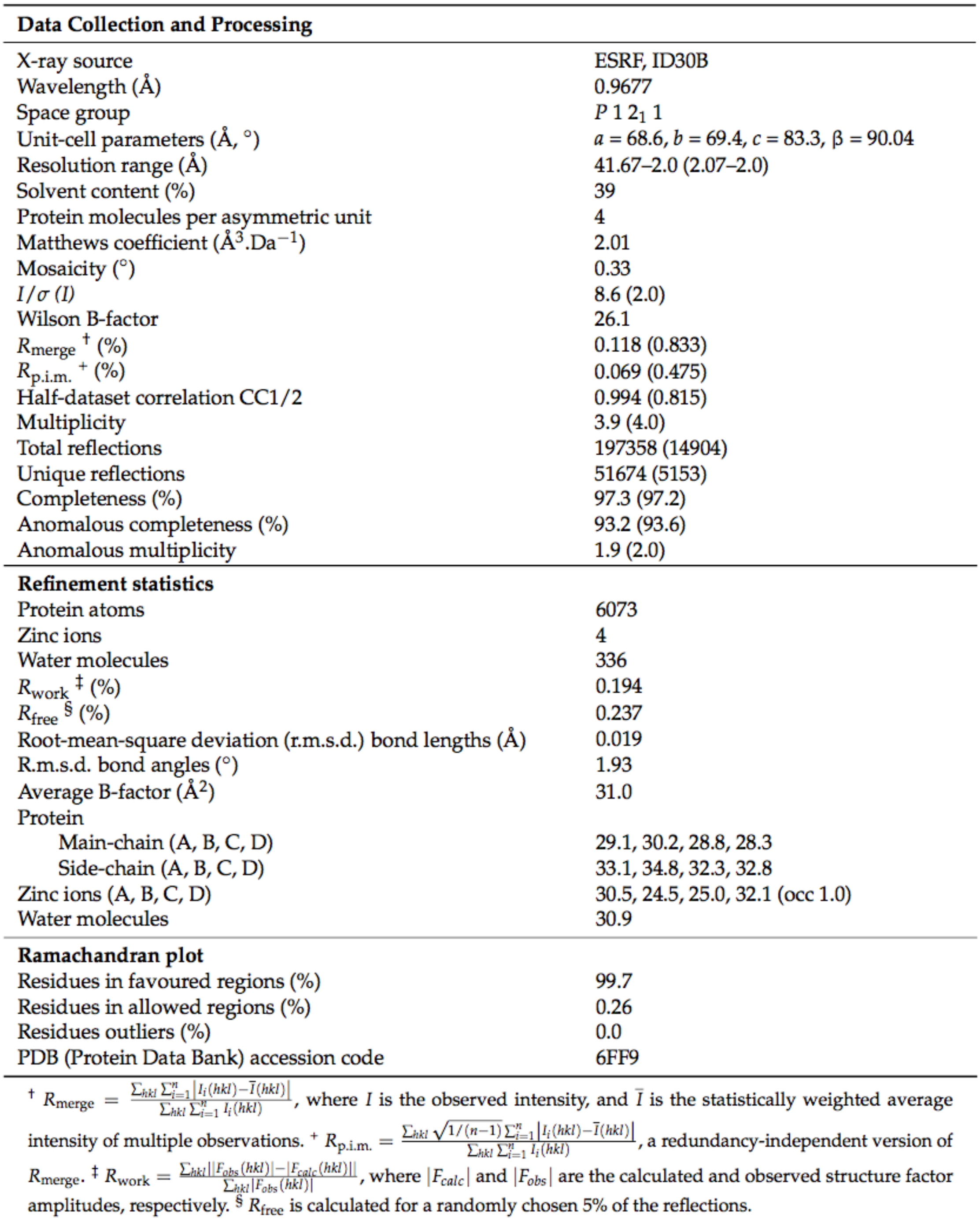

Data Collection and Processing	
X-ray source	ESRF, ID30B
Wavelength (Å)	0.9677
Space group	$P\,1\,2_1\,1$
Unit-cell parameters (Å, °)	$a = 68.6$, $b = 69.4$, $c = 83.3$, $\beta = 90.04$
Resolution range (Å)	41.67–2.0 (2.07–2.0)
Solvent content (%)	39
Protein molecules per asymmetric unit	4
Matthews coefficient (Å^3.Da^{-1})	2.01
Mosaicity (°)	0.33
$I/\sigma\,(I)$	8.6 (2.0)
Wilson B-factor	26.1
R_{merge} † (%)	0.118 (0.833)
$R_{p.i.m.}$ $^{+}$ (%)	0.069 (0.475)
Half-dataset correlation CC1/2	0.994 (0.815)
Multiplicity	3.9 (4.0)
Total reflections	197358 (14904)
Unique reflections	51674 (5153)
Completeness (%)	97.3 (97.2)
Anomalous completeness (%)	93.2 (93.6)
Anomalous multiplicity	1.9 (2.0)
Refinement statistics	
Protein atoms	6073
Zinc ions	4
Water molecules	336
R_{work} ‡ (%)	0.194
R_{free} § (%)	0.237
Root-mean-square deviation (r.m.s.d.) bond lengths (Å)	0.019
R.m.s.d. bond angles (°)	1.93
Average B-factor (Å^2)	31.0
Protein	
Main-chain (A, B, C, D)	29.1, 30.2, 28.8, 28.3
Side-chain (A, B, C, D)	33.1, 34.8, 32.3, 32.8
Zinc ions (A, B, C, D)	30.5, 24.5, 25.0, 32.1 (occ 1.0)
Water molecules	30.9
Ramachandran plot	
Residues in favoured regions (%)	99.7
Residues in allowed regions (%)	0.26
Residues outliers (%)	0.0
PDB (Protein Data Bank) accession code	6FF9

† $R_{merge} = \frac{\sum_{hkl}\sum_{i=1}^{n}\left|I_i(hkl)-\bar{I}(hkl)\right|}{\sum_{hkl}\sum_{i=1}^{n}I_i(hkl)}$, where I is the observed intensity, and $\bar{I}$ is the statistically weighted average intensity of multiple observations. $^{+}$ $R_{p.i.m.} = \frac{\sum_{hkl}\sqrt{1/(n-1)}\sum_{i=1}^{n}\left|I_i(hkl)-\bar{I}(hkl)\right|}{\sum_{hkl}\sum_{i=1}^{n}I_i(hkl)}$, a redundancy-independent version of R_{merge}. ‡ $R_{work} = \frac{\sum_{hkl}\left||F_{obs}(hkl)|-|F_{calc}(hkl)|\right|}{\sum_{hkl}|F_{obs}(hkl)|}$, where $|F_{calc}|$ and $|F_{obs}|$ are the calculated and observed structure factor amplitudes, respectively. § R_{free} is calculated for a randomly chosen 5% of the reflections.

3. Results

3.1. Expression and purification of mutp53 R280K DBD

After expression in BL21 (DE3) *E. coli* cells, the mutp53 R280K DBD (residues 94–312) was purified by cation exchange followed by heparin-affinity chromatography, as described by Bullock and colleagues [87]. However, the produced protein was shown to be not suitable for crystallographic assays since it was very unstable, presenting aggregation after 24 h. By DSF and DLS preliminary assays, performed with protein samples after each step of purification, it was possible to infer that after the cation exchange chromatography the protein was unfolded. In fact, in DSF, a high interaction of recombinant mutp53 R280K with SYPRO®Orange was detected through high relative fluorescence units (RFU) at low temperatures, indicating that the protein was already unfolded at the starting point (**Annex I, Figure S2 A**). Furthermore, protein size analysis through DLS revealed that the protein was in poorer conditions, with an increase of aggregated protein population, when purified by cationic exchange followed by heparin-affinity chromatography than directly purified in heparin column plus gel SEC. Probably, heparin-affinity chromatography rescued mutp53 R280K DBD folding after cationic exchange, showing also a protein population around 6 nm (in accordance with its molecular weight and globular-like shape; **Annex I, Figure S2 B, C**), due to the affinity of transcriptional factor DBD to heparin as it mimics DNA negative charges [327]. These results led us to consider that a smoother purification process should be adopted, and an optimization of buffer should be pursued. As such, the purification was optimized by performing only heparin-affinity chromatography, followed by SEC (**Annex I, Figure S3**). Additionally, to improve protein stability, DSF screening of different buffers and additives was performed to select the best buffer (**Annex I, Figure S4**). It was also verified that buffer supplementation with zinc(II) ion, which is a required factor for the correct folding of p53 DBD [328], contributes to protein stability. Considering the thermal stabilization of mutp53 R280K DBD, the selected buffer was 50 mM HEPES pH 7.5, 150 mM NaCl, 5 mM DTT, 10 µM $Zn(CH_3COO)_2$, and 5% (*v*/*v*) glycerol. Altogether, the purification protocol was optimized to produce mutp53 suitable for biophysical assays, particularly crystallography.

3.2. Crystallization and structural elucidation of mutp53 R280K DBD

After recombinant mutp53 R280K DBD production and concentration, the pure protein was crystallized using polyethylene glycol (PEG) 3350 as a precipitant. Crystals grew in space group $P2_1$, which contains four molecules in the asymmetric unit and each molecule comprises amino acid residues 97 to 290. Coordinates and observed structure factor amplitudes for the human mutp53 R280K DBD, to 2.0 Å resolution, have been deposited in the Protein Data Bank in Europe (PDB ID code 6FF9). The overall fold of the mutp53 R280K structure is similar to the wtp53 DBD structure in the absence of DNA [162] (**Figure 1**). Like other p53 structures already reported, the mutp53 R280K DBD presents an immunoglobulin-like *β*-sandwich fold with two twisted antiparallel *β*-sheets of four (S1, S3, S8, and S5) and five (S10, S9, S4, S7, and S6) strands, respectively, forming a hydrophobic inner core (**Figure 1 A**). The structure also contains a series of loops (L1, L2, and L3) at opposite ends of the *β*-sandwich and two short helices (H1 and H2) at one of the two ends. The two large loops (L2 and L3) and a loop-sheet-helix (LSH) motif compose the DNA binding surface. As observed in wtp53 and in some mutp53 forms [17, 92, 104, 110, 167], in mutp53 R280K the L2 and L3 are stabilized by a zinc(II) ion, which is tetrahedrally-coordinated to C176, H179, C238, and C242 (**Figure 1 C**). The LSH motif contains L1, the S2-S2' hairpin, and the *C*-terminal residues of the extended *β*-strand S10, as well as the H2 helix. In this structure, it was also possible to observe two extra short helices (H_{S1} and H1'), as observed in other mutp53 forms [92, 94].

The superposition of the four molecules of mutp53 R280K DBD present in the asymmetric unit shows root-mean-square deviation (r.m.s.d.) values of 0.40 Å, 0.32 Å, and 0.35 Å for 193 backbone atoms (molecule A superposed on molecules B, C, and D, respectively) (**Figure 1 B**). Contrary to the DNA-binding interface, the turn between S7 and S8 (residues 220–229), stands out as the region with the major structural variation. As reported in other p53 DBD structures, this region shows an inherent flexibility [162, 174, 329]. The maximal distance observed between C^{α} atoms of V225 is 6.19 Å. Additionally, at 2.0 Å resolution, it was also possible to confirm the mutation of mutp53 R280K DBD at position 280, as the density for K280 was clear in all four molecules present in the asymmetric unit (**Figure 1 C**). This K280 is located at the H2, which belongs to the LSH motif of the DNA binding surface.

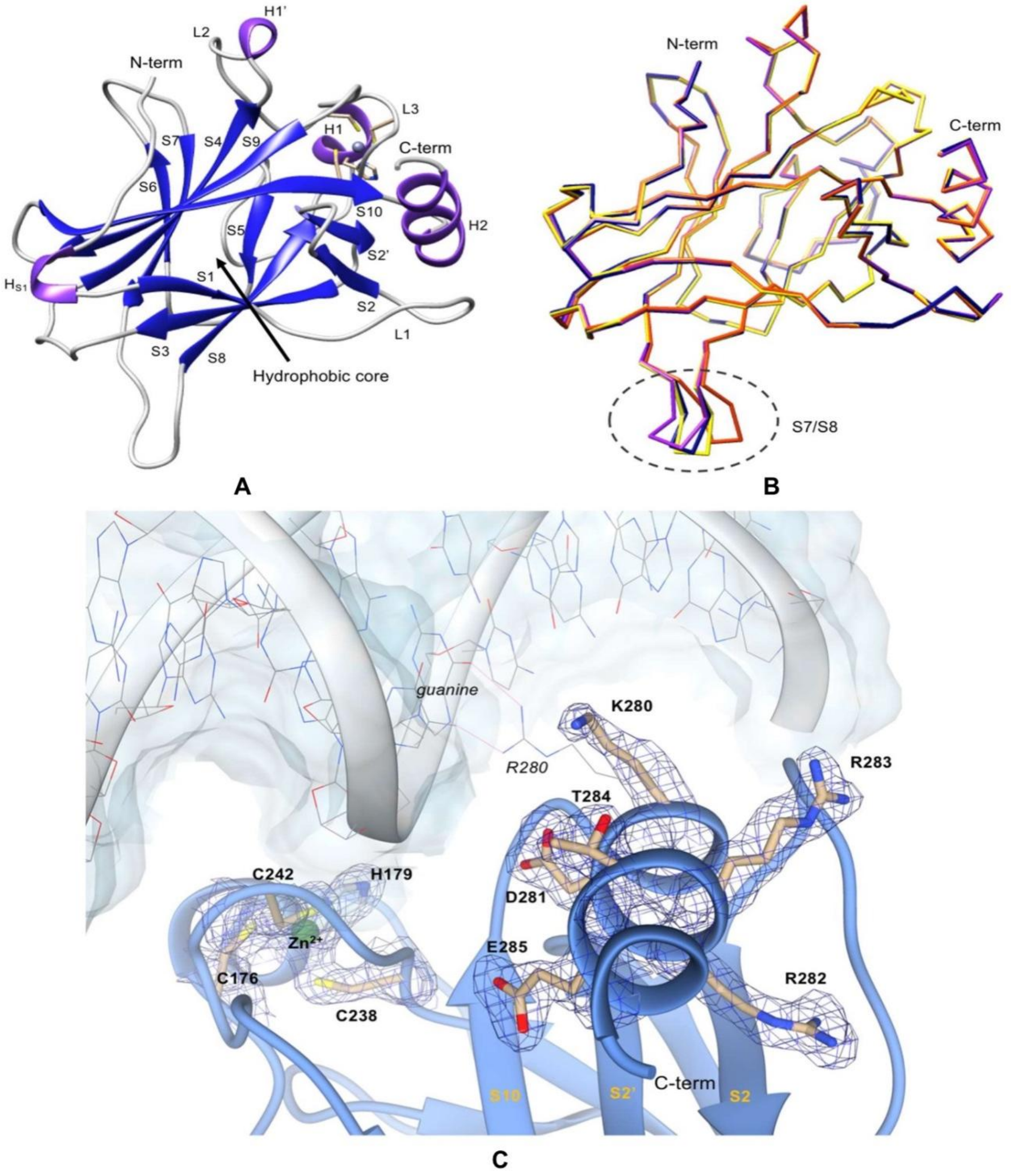
H1'
L2
N-term
L3
S7
S4
S9
H1
C-term
S6
S10
H2
S5
S2'
H$_{S1}$
S1
S2
L1
S3
S8
Hydrophobic core
A
N-term
C-term
S7/S8
B
guanine
K280
R280
R283
T284
C242
H179
D281
Zn^{2+}
E285
C176
R282
C238
S10
S2'
C-term
S2
C

Figure 1. Crystal structure of mutp53 R280K DBD. (A) Ribbon diagram of mutp53 R280K DBD; strands are shown in dark blue, helices in purple, linked by gray coils. The zinc(II) ion is represented by a gray sphere near L3 and H1 and its coordinating amino acid residues (C176, H179, C238, C242) are shown as yellow sticks. **(B)** Backbone superposition of the four molecules of mutp53 R280K DBD in the asymmetric unit of the crystals. Molecule A, purple; molecule B, yellow; molecule C, blue; molecule D, orange. Encircled by a gray dashed line is the region with the highest structural variation, the S7/S8 turn. **(C)** Electron density map calculated around the *C*-terminus residues and the zinc(II) ion, in green ($2mF_o$-DF_c map at 1σ level and 2 Å resolution). The mutp53 R280K DBD polypeptide chain is represented in blue ribbon. Clear electron density for the

lysine residue at position 280 is seen in all molecules of the asymmetric unit in the mutp53 R280K DBD domain structure. The DNA fragment and the arginine residue of the wtp53 (PDB ID code 2AC0) are superposed to illustrate the orientation of the protein in relation to the DNA and are depicted in color-coded wire-frame and labeled in italic. The two direct hydrogen contacts with guanine, that are disrupted in the mutp53 R280K structure, are depicted as pink thin lines. Residues from mutp53 R280K are labeled in bold, while residues in the wtp53-DNA complex are labeled in italics.

3.3. Comparison of mutp53 R280K with wtp53 structural model

The studied contact mutation R280K disables the binding of p53 to DNA, halting DNA transcription as previously reported [169]. To further understand the effect of R280K mutation on DNA binding, the mutp53 R280K DBD structure was compared with DNA-free and DNA-bound wtp53 DBD.

The superposition of the mutp53 R280K DBD monomer structure with the DNA-free wtp53 DBD structure (PDB ID code: 2OCJ, [174]) results in average r.m.s.d. values of 0.3 Å (for 193 aligned residues) among the independent monomers. These r.m.s.d. values are similar to those found in the independent superposition of each of the four molecules of the mutp53 R280K DBD. Also, no relevant structural changes were found between monomers, besides the S7/S8 turn (inherent flexibility) (**Figure 2 A**). Furthermore, the R280K mutation did not affect the overall p53 structural conformation, harboring one zinc(II) ion coordinated to four amino acid residues. As seen in other crystal structures of unbound p53, although four molecules were commonly found in the asymmetric unit, their packing was quite diverse and does not reflect the dimer of dimers arrangement observed in the B-DNA (decameric half sites)-bound complex [99]. Still, when superposed with the DNA-free wtp53 structure, the dimer of mutp53 matches the dimer of wtp53 (with an r.m.s.d. of 0.3 Å for 386 aligned residues). Also, the contacts in these dimers show similar interfaces in the two structures, forming hydrogen bonds and salt bridges, involving the H_{S1} (molecule A) with the L3 and H1 (molecule B), and the S9/S10 turn (molecule A) with the H1 (molecule B). The interaction between dimers is also stabilized by hydrogen bonds and salt bridges, which involve the L1 with the S6, and the H2 with the S9/S10 and S5/S6.

When comparing the mutp53 R280K DBD structure with the DNA-bound wtp53 (PDB ID code: 2AC0, [99]), slightly higher r.m.s.d. values (between 0.66 and 0.71 Å) are observed. The overall structure of the mutp53 R280K DBD monomer is also similar to that of the wtp53 monomer in complex with DNA; however, some significant structural differences can be found in certain regions, such as the S7/S8 turn, L1, and L2 (**Figure 2 B**). The variations observed in the S7/S8 turn are due to the inherent flexibility of this

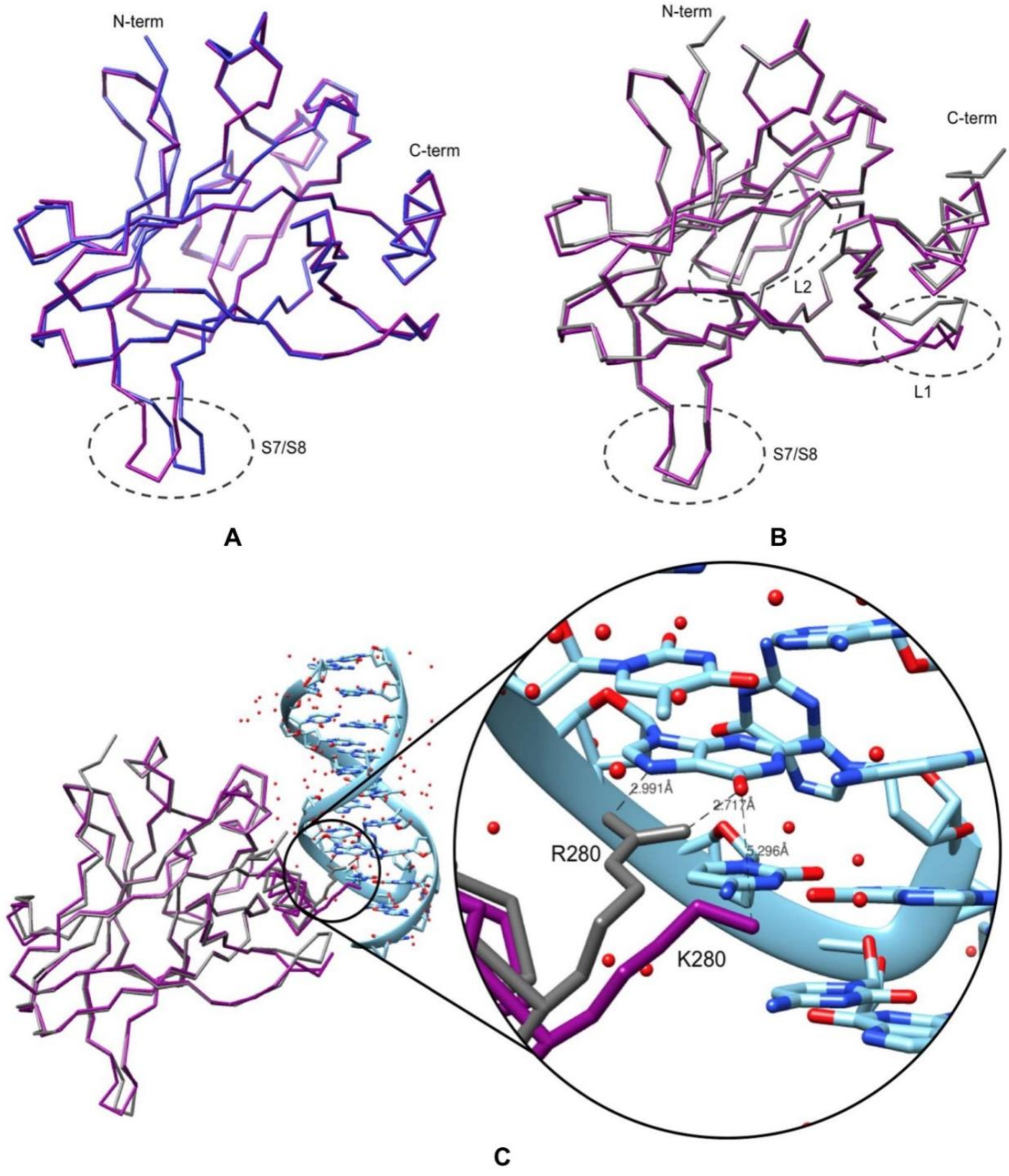

Figure 2. Comparison of mutp53 R280K DBD (backbone in purple) with (A) human DNA-free (PDB ID code: 2OCJ, blue) and (B) DNA-bound (PDB ID code: 2AC0, gray) wtp53 DBD structures. Regions with the highest structural variations are encircled by gray dashed lines. In **(A)**, the S7/S8 turn is the region with the highest structural variation, while in **(B)**, the S7/S8 turn, L1, and L2 are the regions with the most significant structural differences. The L2 is located at the back in this figure. **(C)** Backbone superposition of mutp53 R280K DBD (purple) with the p53 DBD in complex with DNA (PDB ID code: 2AC0, gray). The double-stranded DNA is represented in cyan blue. The side chains at position 280 are shown in both structures, lysine from mutp53 and arginine from wtp53. The hydrogen contacts between the R280 and guanine, and a hypothetical contact between K280 and guanine, are represented by gray dashed lines; carbon atoms are colored light blue, nitrogens are navy blue and oxygens are red. Atomic distances are indicated.

region. The L1 and L2 loops variations result from the absence of DNA. In the L1, K120 and S1 have the largest deviations, and the C^{α} atoms are displaced by 2.44 and 4.14 Å, respectively. It is already known that K120 contributes to DNA binding with two hydrogen bonds, so when bound to DNA, the L1 needs to rearrange and fit into the major groove of the DNA molecule [174]. Another structural difference is observed in the L2 near the DNA binding-surface (C182-G187), where the C^{α} atoms of S183 and G187 are displaced by 1.60 and 1.15 Å, respectively.

Most relevant to this study are the structural differences observed at the mutation site (R280). In the DNA-bound wtp53 structure, the guanidinium group of R280 forms two hydrogen bonds with a guanine nucleotide of consensus DNA [17], while K280 (in mutp53 R280K) would only be capable of forming one hydrogen bond with DNA. Superposition of both monomer structures clearly shows that the distance between K280 (from mutp53 R280K) and the DNA molecule is longer, a consequence of the shorter side chain of lysine compared to arginine, limiting an effective hydrogen bond [330] [331]. Associated with this is the known fact that arginine presents a more positively-charged side chain compared to lysine, which favors electrostatic interaction with the negatively-charged DNA molecule. Therefore, due to the increased distance and its characteristics, mutp53 R280K is unable to form stabilizing interactions with DNA, which consequently causes its loss of function, despite other well-established contacts that could be maintained.

The residue R280 besides being involved in DNA recognition, it also takes part in an extended hydrogen bonding network with proximal (D281, A276, C277) and distal (R273) residues comprising a structural water molecule, essential for the DNA major groove docking via the water molecule and the correct positioning of R273 and R280 by D281 buttressing [17]. This network occurs in both DNA-bound and free wtp53 models, although in the DNA-free wtp53 the water molecule does not establish the interactions to the DNA (**Figure 3 A, B**). In mutp53 R280K model, structural water molecules are found next to S10/H2 region in the four molecules, occupying the same position (**Figure 3 C**). Nevertheless, the side chain of R273 may adopt a different conformation when in presence of another water molecule (verified to molecules B and D, **Figure 3 C**). The superposition of wtp53 models and mutp53 R280K evidenced that the structural water molecule rearranges similarly in the models, although the K280 does not establishes hydrogen bond with the water molecule (**Figure 3 D**). Further, once again, the lysine besides being shorter than arginine, also occupies a more distant position. Consequently, K280 does not establish hydrogen bonds neither to the water molecule, or to the residue D281 possibly damaging the buttressing effect of the hydrogen bonding network. Also, the side chain of C277 adopted a different conformation, possibly establishing interactions with K280.

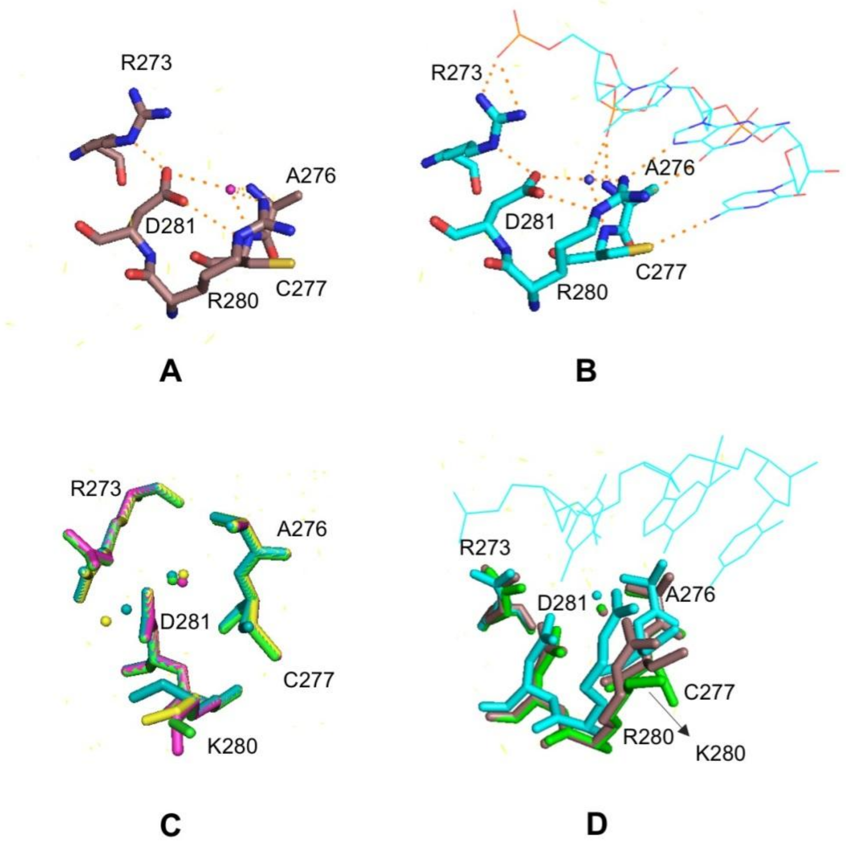
R273
A276
D281
C277
R280
A
R273
A276
D281
C277
R280
B
R273
A276
D281
C277
K280
C
R273
D281
A276
C277
R280
K280
D

Figure 3. Comparison of sequence-specific DNA recognition region of mutp53 R280K DBD (green residues) with human DNA-free (PDB ID code: 2OCJ, brown) and DNA-bound (PDB ID code: 2AC0, cyan) wtp53 DBD models. View of some DNA-contact residues that recognize the DNA major groove in stick models, and structural water molecule represented as a sphere. Representation of the hydrogen bonding network involving those residues and the structural water molecule in DNA-free (**A**, PDB ID code: 2OCJ, molecule C, brown) and DNA-bound (**B**, PDB ID code: 2AC0, molecule D, cyan) wtp53 DBD models. In the DNA-bound wtp53 model **(B)** the hydrogen bonding network is extended to the DNA. **(C)** Comparison the spatial arrangement of the residues and water molecules of the four molecules of mutp53 R280K DBD model (molecule A, green; molecule B, cyan; molecule C, magenta; molecule D, yellow). **(D)** Comparison among wtp53 and chain A of mutp53 R280K DBD models.

4. Discussion

There is a wide range of highly frequent mutp53 forms occurring in the DBD region. The structural studies carried out with different mutp53 forms have unveiled the impact of missense mutations on p53 structure, stability and DNA binding, highlighting the delicate balance and complexity of this molecular hub. This raised the perception that not all mutp53 forms are equal, adding to the functional diversity observed in mutp53 forms [19, 107]. These data are therefore of high relevance to clinically address cancers bearing mutp53.

The described crystal structure of mutp53 R280K provides a deeper understanding about this mutp53 structure as well as its impact on DNA binding. In fact, the mutp53 R280K DBD crystal structure revealed that, as in wtp53 [104], there is a correct folding of mutp53 R280K DBD with zinc(II) ion coordination, without any crevice and or distortions of structural elements important for stability. Therefore, it is most likely that mutp53 R280K thermodynamic stability would be closer to wtp53 [88], as the contact mutp53 R273H [88] and not as mutp53 R248Q that is more destabilized due to L3 distortion [88, 165].

Residue R280 has been reported as a pillar in DNA recognition, once it makes two invariant hydrogen bonds to guanine base, that occupies a constant position in p53 target genes RE, being part of the p53 DNA consensus region [99]. Most importantly, the mutp53 R280K DBD model indicated that the loss of function is likely related to the inability of the residue K280 to establish those two hydrogen bonds with DNA, a consequence of the shorter side chain of lysine compared to arginine, as also observed in other contact mutp53 forms R273H and R273C [92, 167]. Also, as observed in mutp53 R273C, the hydrogen bond network in the DNA-binding surface is altered, compromising an effective binding to the DNA. Furthermore, it was reported that the replacement of an arginine residue by lysine can affect protein stability [332] and, in the case of p53, its DNA binding efficiency. Overall, these results provide relevant insights about the crucial role of R280 for DNA recognition, correct spatial orientation of neighboring residues side chains, and protein-DNA complex stability.

This knowledge may help in unravelling the biology and function of mutp53. Additionally, it may contribute to the rational design of new targeted anticancer therapies. In fact, candidate drugs for the reactivation of mutp53 R280K function could, for example, fill in the cavity created by the absence of the arginine side chain, restoring the missing hydrogen contacts and/or strengthening the electrostatic interaction with establishment of a stable DNA-bound p53 complex.

Chapter III

SLMP53-1 reactivates mutant p53 by targeting DNA-binding domain

Ana Sara Gomes*, Helena Ramos*, Sara Gomes, Joana B Loureiro, Joana Soares, Valentina Barcherini, Paola Monti, Gilberto Fronza, Carla Oliveira, Lucília Domingues, Margarida Bastos, Daniel FAR Dourado, Ana Luísa Carvalho, Maria João Romão, Benedita Andrade Pinheiro, Alexandra Carvalho, Filipa Marcelo, Maria MM Santos, Lucília Saraiva, (2018), *"SLMP53-1 reactivates mutant p53 by targeting DNA-binding domain",* under revision.

*The authors contributed equally to the work.

1. Summary

Mutp53 is one of the most relevant target candidates in anticancer therapy. Recently, we have reported the *(S)*-tryptophanol-derived oxazoloisoindolinone, SLMP53-1, as a new reactivator of mutp53 R280K, which is also able to activate wtp53. SLMP53-1 restored DNA-binding ability, and subsequent transcriptional activity, to mutp53 R280K. Additionally, it displayed *in vitro* and *in vivo* p53-dependent antitumor activity against tumors bearing wtp53 or mutp53 R280K, with no apparent undesirable toxicity. However, there was still a lack of understanding about the molecular mechanism by which SLMP53-1 reactivates mutp53 R280K, as well as its potential to reactivate other mutp53 forms besides R280K.

In the present work, by saturation transfer difference (STD)-NMR, it is shown that the mutp53 reactivator SLMP53-1 directly binds to mutp53 R280K DBD, an interaction further supported by cellular thermal shift assay (CETSA). Accordingly, *in silico* studies unveil that SLMP53-1 establishes non-covalent interactions with positively charged regions of mutp53 R280K DBD. The ability of SLMP53-1 to restore wt-like function to diverse hotspot mutp53 forms is also demonstrated. Collectively, this work brings new insights into mutp53 druggability, revealing a new reactivator of mutp53 with a distinct binding mode from the already reported reactivators.

2. Materials and methods

2.1. Compounds

(S)-tryptophanol-derived oxazoloisoindolinone SLMP53-1 was synthesized using the protocol previously described by us [226]. For all experiments, SLMP53-1 was dissolved in dimethyl sulfoxide (DMSO) or DMSO-d_6 from Sigma-Aldrich (Sintra, Portugal).

2.2. Yeast and mammalian expression vectors

The yeast expression vectors pLLS89 (*GAL1-10, LEU2*) encoding full-length human mutp53 (R175H, G245D, G245S, R248Q, R248W, R273H, R273C or R282W) were constructed through *SgraI/StuI* (New England Biolabs, Ipswich, Massachusetts, USA) digestion of available pLS76 (*ADH1, LEU2*) vectors [333] and subsequent ligation (T4 DNA ligase, New England Biolabs) of the gel purified mutp53 fragment in a *SgraI/StuI* digested and gel purified pLLS89-based vector (generous gift of Prof. Alberto Inga). The creation of the mutp53 expression vectors was confirmed after XL1-Blue *E. coli* extraction (GenEluteTM Plasmid Miniprep Kit, Sigma-Aldrich, St. Louis, Missouri, USA) by digestion and DNA sequencing (BMR Genomics, Padua, Italy).

The full-length coding sequence of mutp53 was PCR-amplified from the yeast vector with Vent DNA polymerase (New England Biolabs, Werfen, Porto, Portugal), using the primers pair 5′ GG**G GTA CC**A TGG AGG AGC CGC AGT CAG 3′ and 5′ CCG **CTC GAG** TCA GTC TGA GTC AGG CCC TTC 3′, where the restriction sites for *KpnI/XhoI* (in bold) were included, respectively. The PCR products and the mammalian expression vector pcDNA3 (Invitrogen, Alfagene, Lisboa, Portugal) were digested with *KpnI/XhoI* (New England Biolabs, Werfen), purified from agarose gel, and ligated with T4 DNA ligase (Promega, VWR, Carnaxide, Portugal), originating the expression vectors pcDNA3-mutp53. These constructs were propagated in NZY5*α E. coli* cells (NZYTech, Lisboa, Portugal) as described in **Chapter II**. The sequence of each mutp53 in the constructed vectors was confirmed by sequencing (Eurofins GATC Biotech, Konstanz, Germany) with specific pcDNA3 primers. pcDNA3-mutp53 vectors were extracted using the PureYieldTM Plasmid Miniprep System kit (Promega, VWR).

2.3. Saturation transfer difference (STD)-NMR

NMR experiments were recorded on Bruker Avance 600 MHz spectrometer equipped with 5 mm inverse detection triple-resonance z-gradient cryogenic probe head at 298 K. All the following reagents used in NMR experiments were from Sigma-Aldrich. ^{1}H-NMR characterization of SLMP53-1, in the same buffer conditions used during STD-NMR analysis, was carried out through standard 2D-TOCSY, 2D-NOESY and HSQC experiments. For STD-NMR experiments, the recombinant human mutp53 R280K DBD produced in *E. coli*, as described in **Chapter II**, was previously dialyzed (pore with 8 kDa cut off; Tube-O-Dialyzer^{TM}, Micro from G-Biosciences, VWR) during 24 h, at 4 ºC, against 25 mM sodium phosphate (NaPi) pH 7.5, 1 mM DTT-d_{10}, 100 mM NaCl, 1% (*v/v*) glycerol-d_8, 10 µM $Zn(CH_3COO)_2$, 7% (*v/v*) DMSO-d_6, 0.025% (*m/v*) NaN_3 in D_2O buffer solution. STD-NMR experiments were performed using a mutp53 R280K:SLMP53-1 molar ratio of 1:10 with a final protein concentration of 25 µM and 250 µM of SLMP53-1. To increase the solubility of SLMP53-1 in the deuterated buffer solution, 7% (*v/v*) DMSO-d_6 was included in the sample for STD-NMR. The effect of DMSO on protein stability was checked by DLS and DSF assays (**Annex II, Figure S3**). Deuterated sodium trimethylsilyl propionate was also used as internal reference in the STD-NMR experiments. The STD-NMR spectra were acquired with 1,920 transients in a matrix with 65k data points in T2, using a spectral window of 12,335.5 Hz centered at 2,820.9 Hz. An excitation sculpting module with gradients was employed to suppress the water proton signals. Selective saturation of the protein resonances (on resonance spectrum) was performed by irradiating at -0.5 ppm using a series of Eburp2.1000-shaped 90° pulses (50 ms, 1 ms delay between pulses) and distinct saturation times (0.5, 1 and 2 s). For the reference spectrum (off resonance), the sample was irradiated at 100 ppm. To calculate the STD-derived epitope mapping of SLMP53-1, the STD intensities of the SLMP53-1 protons were normalized with respect to the proton with the highest STD response. The STD obtained with 1 s of saturation time was considered to derive the epitope mapping. TopSpin 3.5.7 software was used for analysis (Bruker, Billerica, Massachusetts, USA).

2.4. Computational modeling and molecular docking

The starting structure for the modeling was the mutp53 R280K DBD monomer (PDB ID code: 6FF9), described in **Chapter II**, and the correspondent wtp53 structure (PDB code: 2OCJ; **Annex II, PDB files**) [174]. We also considered the structure of mutp53 Y220C DBD for molecular docking validation (PDB ID code: 3ZME; **Annex II, Figure S4, PDB file**). Missing hydrogen atoms were added to this structure according to the assigned protonation states. The ligand SLMP53-1 was geometry optimized in Gaussian09 using B3LYP [334] and a Polarizable Continuum Model (PCM) solvent description [335]. Atomic partial charges were calculated resorting to the Restrained Electrostatic Potential (RESP) [336] method from HF/6-31G(d) single point energy calculations.

For the docking of SLMP53-1 to mutp53 R280K DBD monomer we started by identifying all the pockets in the crystal structure using the CASTp server [337]. Molecular docking was performed using the AutoDock 4.2 suite of programs with the Lamarckian genetic algorithm (LGA) [338]. Two grid boxes were centered on residues 249 and 280 of chain A. A total of 100 LGA runs were carried out for the free protein model. The population was 300, the maximum number of generations was 27,000 and the maximum number of energy evaluations was 2,500,000.

2.4.1. Molecular dynamics (MD) simulations

MD simulations were performed for mutp53 R280K DBD with SLMP53-1 using the Amber 18 molecular dynamics program with the parm99SB [339] and GAFF force fields [340]. The structures were placed within an octahedral box of TIP3P waters [341, 342] and counter ions were added to make the entire system neutral. The zinc atoms in p53 were described with the semi-bonded model [343, 344]. The systems were subjected to two initial energy minimizations and to 500 ps of equilibration in a NVT ensemble using Langevin dynamics with small restraints on the protein (10 kcal/mol) to heat the system from 0 to 300 K. Production simulations were carried out at 300 K in the NPT ensemble using Langevin dynamics with a collision frequency of 1.0 ps^{-1}. Constant pressure periodic boundary conditions were imposed with an average pressure of 1 atm. Isotropic position scaling was used to maintain pressure with a relaxation time of 2 ps. The time step was set to 2 fs. SHAKE constraints were applied to all bonds involving hydrogen atoms [345-347]. The particle mesh Ewald (PME) method [348] was used to calculate electrostatic interactions with a cut off distance of 10 Å. Three replicas with different initial velocities were performed for each system. The total combined time of the simulations was 50 ns. The reference structures of the simulations were calculated as described [349].

2.5. Yeast assay

S. cerevisiae CG379 (Yeast Genetic Stock Center, University of California, Berkeley, CA, USA) was transformed with pLLS89 expressing human mutp53 (or empty vector as control), using the LiAc/SS Carrier DNA/PEG method [350]. Yeast cells expressing human wtp53 were obtained in previous work [226]. For expression of human wtp53 or mutp53, cells (routinely grown in minimal selective medium) were incubated in galactose selective medium with all the amino acids required for yeast growth (50 µg/mL) except leucine as described [226], in the presence of 10 µM of SLMP53-1 or 0.1% DMSO, for approximately 42 h (time required by control yeast incubated with DMSO to achieve 0.4 OD_{600}). Yeast growth was analyzed by colony-forming unit counts as described [226]. Percentage of growth inhibition was calculated considering the wtp53-induced yeast growth inhibition as 100%.

2.6. Human cancer cell lines and growth conditions

Human breast adenocarcinoma MDA-MB-231 cells, expressing mutp53 R280K, and human non-small cell lung cancer NCI-H1299 cells, lacking p53 expression due to a homozygous partial deletion of the *TP53* gene, were purchased from ATCC (Rockville, MD, USA). Cells were cultured in Roswell Park Memorial Institute (RPMI)-1640 with UltraGlutamine (Lonza, VWR), supplemented with 10% fetal bovine serum (FBS, Merck Millipore, VWR), and incubated at 37 °C with 5% CO_2. Cells were routinely tested for mycoplasma infection using the MycoAlert™ PLUS mycoplasma detection kit (Lonza, VWR). Cells were recently characterized and authenticated, by short tandem repeat DNA profiling [351].

2.7. Cellular thermal shift assay (CETSA)

To evaluate drug target interactions in cells, the CETSA analysis was performed basically as described [352-354]. Briefly, MDA-MB-231 cell lysates were incubated with 10 µM SLMP53-1 or solvent for 1 h at room temperature, and then heated at different temperatures for 3 min, cooled to room temperature for 3 min, and placed on ice. Soluble protein was detected by western blot. At 40 °C, the increase in non-denatured p53 of lysates treated with 10–50 µM SLMP53-1 was calculated relative to solvent at 25 ºC, set as 1.

2.8. Transient transfection assay of mutp53 in human NCI-H1299 cancer cells

NCI-H1299 cells were transfected at 7.5×10^3 cells/well density in 96-well plates with 75 ng of pcDNA3-mutp53 (or empty vector), using ScreenFect®A (ScreenFectA GmbH, GRiSP, Porto, Portugal) according to the manufacturer's instructions.

2.9. Sulforhodamine B (SRB) assay

NCI-H1299 transfected cells were seeded in 96-well plates at 7.5×10^3 cells/well density, followed by analysis of SLMP53-1 effect on cell proliferation after 48 h treatment with serial dilutions (3.13–50 µM) of compound, as described [355]. The solvent (DMSO; maximum concentration used 0.25%) was included as control. IC_{50} (concentration that causes 50% of growth inhibition) values were determined as described [355].

2.10. Western blot analysis

To evaluate the expression levels of human wtp53 and mutp53 in yeast, cells were grown in galactose selective medium for 42 h. To evaluate the expression levels of ectopic human mutp53 in NCI-H1299 cells, transfected cells were seeded in 6-well plates at 2.25×10^5 cells/well density for 48 h. Yeast and human tumor cells were lysed and protein fractions were analyzed as described [355]. Antibodies are listed in **Table S1** (**Annex II**).

2.11. Statistical analysis

Data were statistically analyzed using the GraphPad Prism 7 (GraphPad software, California, USA). Differences between means were tested for significance using the Student's t-test (**p<0.01; ***p<0.001).

3. Results

3.1. SLMP53-1 directly binds to mutp53 R280K DBD

To investigate whether SLMP53-1 could bind to mutp53 R280K, ligand-based NMR experiments were performed. To this end, the recombinant human mutp53 R280K DBD was produced in *E. coli* and purified, as described in **Chapter II**, and used to carry out the STD-NMR experiments. The STD-NMR technique is suitable for ligand-protein interaction studies, providing a reliable mapping of ligand epitopes by elucidating which ligand protons are in closer contact with the protein [356]. The STD-NMR results showed that all measured SLMP53-1 protons exhibited STD enhancements on the STD-NMR spectrum, which unequivocally shows the binding of the compound to mutp53 R280K DBD (**Figure 1 A**). To deduce the epitope mapping of SLMP53-1 in the presence of mutp53 R280K DBD (**Figure 1 B**), the STD-NMR spectrum recorded with one second of saturation time was used, and the STD intensities of all the measured protons were normalized to the proton with the highest STD enhancement. Accordingly, the indole moiety presented the highest percentage of STD (superior to 85%), closely followed by the aromatic ring in the isoindolinone moiety (around 84–69%) (**Figure 1 B**). In contrast, the methyl group in the isoindolinone moiety only received STD enhancement around 40–55% (**Figure 1 B**). This pointed out that the indole moiety is more intimately in contact with protein, than the rest of the small-molecule.

The binding of SLMP53-1 to mutp53 R280K was also supported by CETSA, using the MDA-MB-231 cancer cells expressing mutp53 R280K. In this assay, the impact of SLMP53-1 on mutp53 R280K thermal stabilization was evaluated by measuring the amount of soluble mutp53 R280K upon heating of MDA-MB-231 cell lysates. In fact, whereas unbound (non-stabilized) proteins denature and precipitate after heating, ligand-bound (stabilized) proteins remain in solution [357]. The results showed that 10 μM

SLMP53-1 induced a slight mutp53 R280K thermal stabilization at 39 ºC and 40 ºC (**Figure 1 C**). Consistently, at 40 °C, SLMP53-1 caused concentration-dependent mutp53 R280K thermal stabilization, with a two-fold increase of non-denatured mutp53 R280K thermal stabilization achieved at 50 µM SLMP53-1, when compared to solvent (**Figure 1 D**). In fact, considering the amount of mutp53 R280K obtained with DMSO at 25 ºC, a complete protein stabilization was achieved with 50 µM SLMP53-1 at 40 °C.

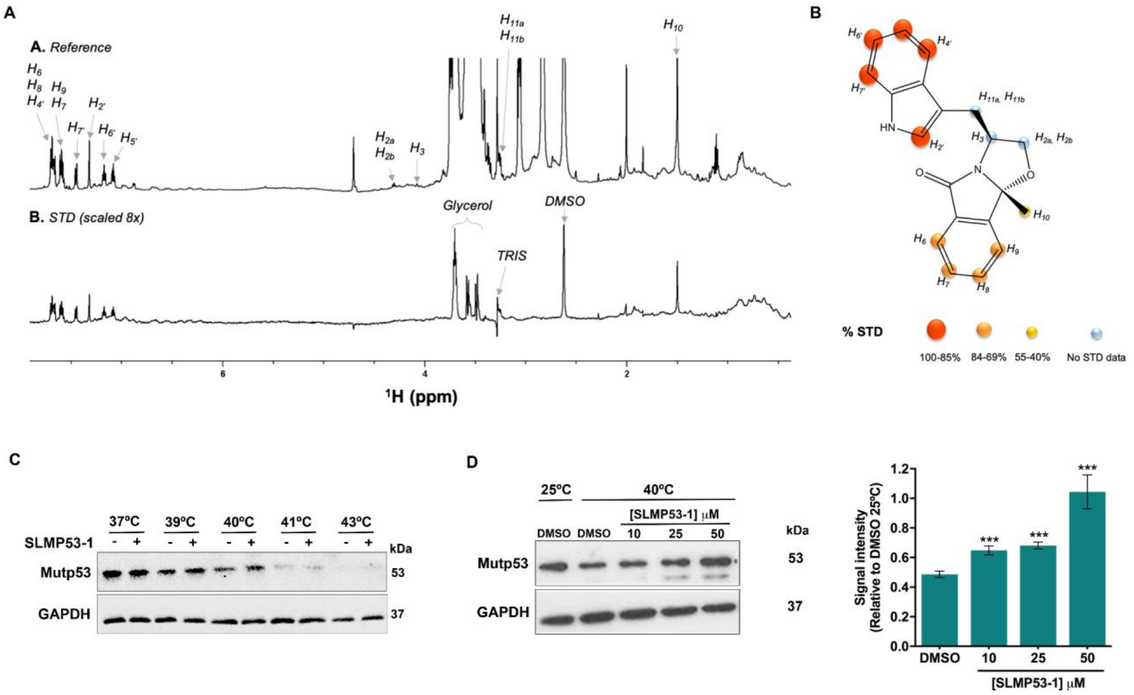

Figure 1. SLMP53-1 binds to mutp53 R280K DBD. (A) STD spectrum of SLMP53-1 (250 µM) in the presence of mutp53 R280K (25 µM), and the reference spectrum (off resonance) of SLMP53-1 (250 µM) in the presence of mutp53 R280K (25 µM). STD-NMR experiment recorded at 298 K and 600 MHz, with tsat = 1 s and on-resonance = -0.5 ppm. **(B)** Proposed SLMP53-1 epitope mapping with STD percentages based on the normalization of STD-NMR difference spectrum peaks intensities; differences were normalized towards the peak with highest STD and a ranking of STD percentage was defined between 100 to 40%. In **(C)** and **(D)**, CETSA experiments were performed in mutp53 R280K-expressing MDA-MB-231 cancer cells lysates. **(C)** Cellular lysate samples treated with DMSO (-) or 10 µM SLMP53-1 (+) were heated at different temperatures; immunoblot represents one of three independent experiments. **(D)** Cellular lysate samples treated with increasing concentrations of SLMP53-1 were heated at 40 °C; immunoblot represents one of five independent experiments; plotted data represent the amount of non-denatured mutp53 after heating at 40 °C, in SLMP53-1-treated cellular lysates relatively to DMSO at 25 °C (set as 1); data are mean ± SEM of five independent experiments; values significantly different from DMSO at

40 °C: ***$p<0.001$ (unpaired Student's t-test). In **(C)** and **(D)**, GAPDH was used as a loading control.

The molecular dynamics (MD) simulations of SLMP53-1 with mutp53 R280K DBD monomer, the most predominant form of p53 DBD in solution [97], proposes the binding of SLMP53-1 to positively charged solvent-exposed surface regions of mutp53 R280K DBD that are rich in lysines and arginines. **Figure 2** shows the two binding modes proposed by the docking calculations (in **Anne II, Figure S1**) and MD simulations. In both binding poses, SLMP53-1 establishes cation-π interactions, specifically with residues R283, H168, R248 and R249, a hydrogen bond with residue N247 and methyl-π interactions with residues K120 and K280 (**Figure 2; Annex II, PDB files**). However, the STD epitope mapping is better interpreted considering the ligand binding mode displayed in blue (**Figure 2**). Indeed, in this binding mode, the indole moiety is pointing towards the protein surface, while the methyl group is more solvent exposed. Without excluding the existence of the binding mode displayed in green, and the possibility of having a dual binding mode in solution, our STD data indicate that the binding mode of SLMP53-1 displayed in blue should be the most populated (**Figure 2**). Moreover, the indole group exhibits more negative partial charges than the isoindolinone group [358, 359], which can explain the preferential interactions of this moiety to the positively charged surfaces of the protein (**Annex II, MOL file**).

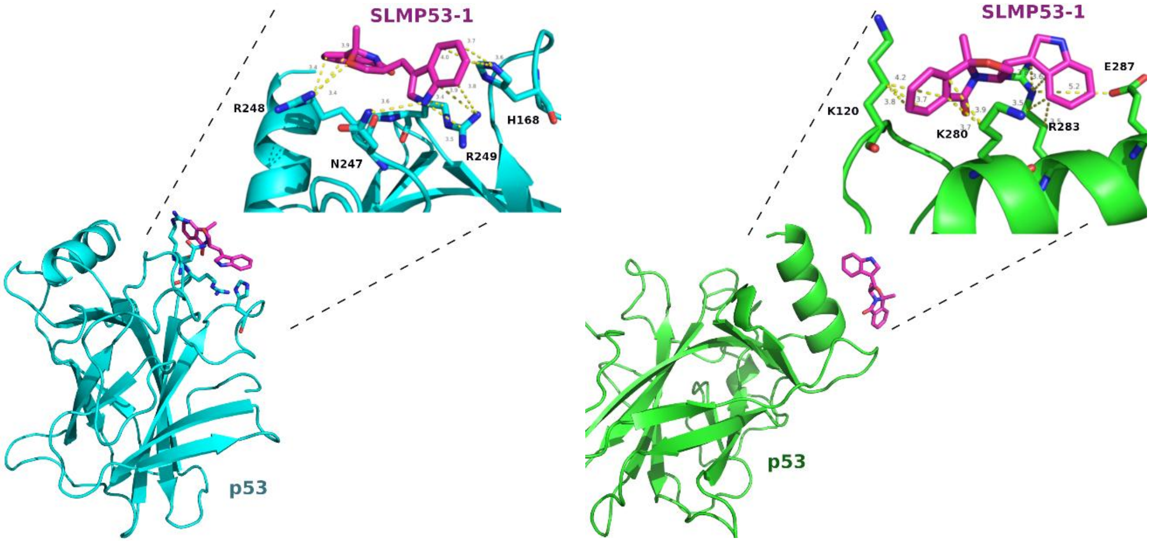

Figure 2. Binding modes of SLMP53-1 to mutp53 R280K DBD monomer. Image shows the binding sites of mutp53 R280K (PDB ID code: 6FF9, in blue and green) with SLMP53-1 (in pink) derived from the MD simulations (replicas 1). The interacting residues are highlighted. Structures are provided in **Annex II, PDB files**.

Consistently with an activation of wtp53 by SLMP53-1 [226], the docking on the wtp53 structure (R280-PDB ID code: 2OCJ) showed the ability of SLMP53-1 to bind to the same protein regions as in mutp53 R280K structure (**Annex II, PDB files**). These results are supported by the induction of wtp53 thermal stabilization by SLMP53-1 revealed by CETSA (**Annex II, Figure S2 A**).

3.2. SLMP53-1 restores wt-like function to distinct hotspot mutp53 forms

It was previously demonstrated that SLMP53-1 was able to restore wt-like function to contact mutp53 R280K, but not to structural mutp53 Y220C [226]. Based on that, we interrogated whether the activity of SLMP53-1 was restricted to mutp53 R280K, or instead it would be also observed in other mutp53 forms, including structural ones. To answer this question, the yeast assay, previously developed to screen reactivators of mutp53 R280K and Y220C [226], was applied to other contact (R248Q, R248W, R273H, R273C) and structural (R175H, G245D, G245S, R282W) mutp53 forms, known for their high prevalence and clinical relevance in human cancers [152, 153, 155, 360]. To this end, the heterologous expression of each human mutp53 was carried out in yeast, and their effect on the growth of transformed yeast was analyzed (**Figure 3 A, B**). By western blot analysis, we confirmed no substantial differences among mutp53 protein expression levels (**Figure 3 A**). Contrary to the growth inhibitory effect induced by wtp53 (set as 100%), none of the expressed mutp53 considerably interfered with yeast cell growth (**Figure 3 B, DMSO**). Since potential reactivators of mutp53 would restore the wt-like growth inhibitory effect to mutp53 expressed in yeast, as observed for R280K [226], we next evaluated the effect of SLMP53-1, at 10 μM (concentration that caused the maximal effect on mutp53 R280K, reestablishing over 79% of wtp53-induced growth inhibitory effect) [226], on the growth of mutp53-expressing yeast cells. Despite the negligible effect on G245S and R273C, SLMP53-1 restored the p53-induced growth inhibition to the remaining tested mutp53 forms by more than 50% (**Figure 3 B**).

To validate the results obtained in yeast, the effect of SLMP53-1 was evaluated on the same set of hotspot mutp53 forms ectopically expressed in p53-null NCI-H1299 cancer cells, through analysis of cell proliferation by SRB assay, after 48 h treatment (**Figure 3 C, D**). In human cancer cells, no considerable differences among mutp53 protein expression levels were detected by western blot analysis (**Figure 3 C**). Notably, like in yeast, SLMP53-1 caused a significant reduction of the IC_{50} values in NCI-H1299 cells expressing mutp53 R175H, G245D, R248Q, R248W, R273H, and R282W (**Figure 3**

D) when compared with empty vector. These results unveiled the ability of SLMP53-1 to reactivate distinct contact and structural hotspot mutp53 forms.

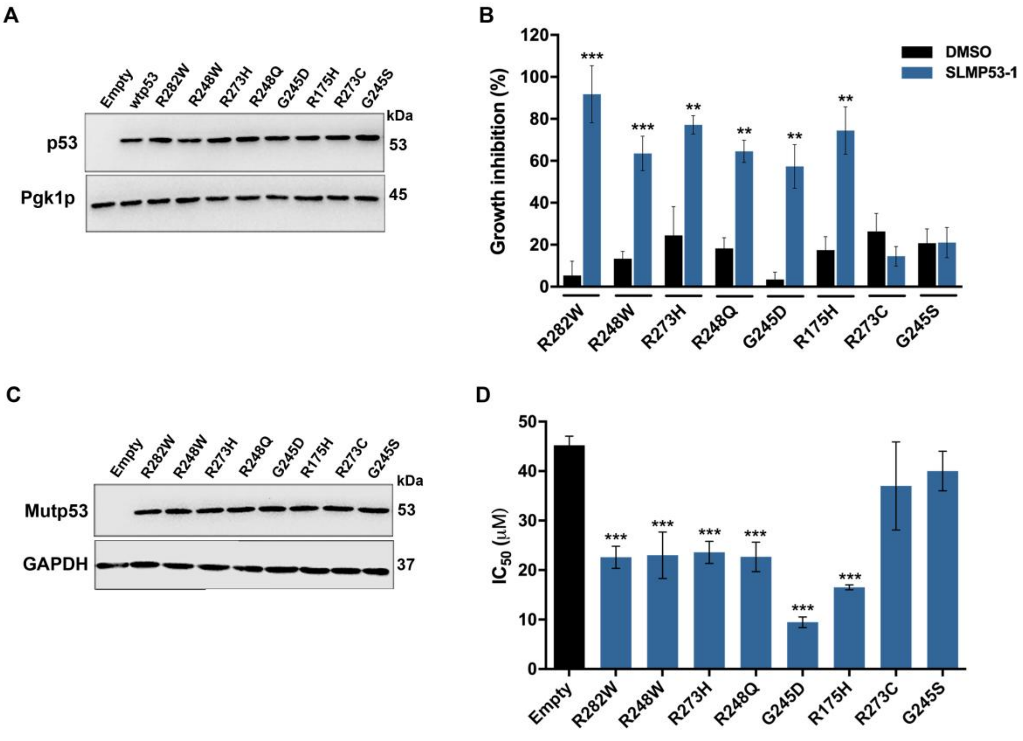

Figure 3. SLMP53-1 reactivates distinct hotspot mutp53 forms. (**A)** Immunoblot of human wtp53 and mutp53 forms expressed in yeast, after 42 h incubation of yeast cells treated with solvent; results represent one out of three independent experiments; Pgk1p was used as loading control. **(B)** Percentage of growth inhibition obtained in mutp53-expressing yeast treated with 10 µM SLMP53-1 or DMSO, for 42 h. Plotted data correspond to the percentage of growth inhibition achieved with wtp53-expressing yeast cells treated with DMSO (set as 100%); data are shown as mean ± SEM of 4–8 independent experiments; values significantly different from DMSO: $^{**}p<0.01$; $^{***}p<0.001$ (unpaired Student’s t-test). **(C)** Immunoblot of mutp53 forms ectopically expressed in NCI-H1299 cancer cells after 72 h incubation; results represent one out of three independent experiments; GAPDH was used as loading control. **(D)** Growth inhibitory effect of SLMP53-1 on NCI-H1299 cancer cells transfected with pcDNA3 encoding human mutp53 (or empty vector). Plotted data of IC_{50} values were determined by SRB assay after 48 h treatment with SLMP53-1; data are shown as mean ± SEM of 3–8 independent experiments; values significantly different from empty vector: $^{***}p<0.001$ (unpaired Student’s t-test).

4. Discussion

Because of its high prevalence in human cancers and critical role in tumor formation and progression, mutp53 is one of the most promising targets in anticancer drug development [361]. Therefore, the search for more efficient and selective therapeutic options, capable of reactivating a broader panel of mutp53 forms, remains a priority, particularly in the context of improved personalized cancer treatment.

The promising pre-clinical results achieved with SLMP53-1 in our previous work [226] led us to further delve into the molecular mechanism of action of this potential anticancer drug candidate. The STD-NMR showed that SLMP53-1 binds to mutp53 R280K DBD, a result further supported by CETSA using human cancer cells expressing full-length mutp53 R280K. The STD-NMR results also unveiled that the aromatic groups, especially the indole moiety of SLMP53-1, are crucial for its binding to the protein.

Our attempts to understand where SLMP53-1 would bind in mutp53 R280K were not conclusive, once experimental limitations due to SLMP53-1 low solubility did not allow to saturate the protein in ^{1}H, ^{15}N-heteronuclear single-quantum coherence (HSQC) experiments to obtain an accurate and consistent chemical shift perturbation of any amino acid residue (**Annex II, Figure S5**). Therefore, we pursued *in silico* analysis by performing docking and MD of mutp53 R280K DBD monomer with SLMP53-1. The results pointed out that SLMP53-1 establishes cation- and methyl-π interactions and hydrogen bonds with positively charged regions of mutp53 R280K DBD, implicating residues from L2 and L3 or L1 and H2. Indeed, under physiological conditions, protein surfaces rich in arginines and lysines are frequently positively charged, and have been recognized to establish non-covalent interactions with aromatic ligands [362, 363]. In addition, cation-π interactions have been reported for their major role in ligand-binding and protein stability, as it is a strong driving force, among non-covalent bonds, in biological complexation processes [364]. These results therefore corroborate the possibility of non-covalent binding of SLMP53-1 to mutp53 R280K DBD positively charged regions. This surface interaction of SLMP53-1 to mutp53 R280K DBD may lead to protein stabilization, retrieving its DNA-binding ability and transcriptional activity. In fact, this hypothesis of mutp53 reactivation by SLMP53-1 is supported by other works, which have reported surface transient interactions of peptides and a small-molecule with wt and mutp53, possibly involving protein L1, H2 and S8, although the exact binding local of the small-molecule has not been yet defined [220, 222]. Collectively, our work suggests a pivotal role of the aromatic regions of the ligand, in particular of the indole group, in the pharmacophore of mutp53 reactivators, and a molecular mechanism of mutp53 reactivation non-dependent on covalent bonds or hydrophobic pockets as described for other mutp53 reactivators. Particularly, PRIMA-1^{MET}

is transformed into a metabolite that is a Michael acceptor, which binds covalently to p53 free cysteines (C124 and C277), with adducts formation, inducing protein stabilization in both contact and structural mutp53 forms [199, 205]. On the other hand, the carbazole derivative PK083, the pyrazole derivative PK7088 and aminobenzothiazole derivative MB725 bind to a hydrophobic pocket in the cleft induced by the Y220C amino acid substitution in mutp53 structure [215-217].

This work also showed that, besides wtp53 and mutp53 R280K [226], SLMP53-1 further reactivates an array of hotspot mutp53 forms with high clinical relevance. To carry out this analysis, the yeast-based screening assay previously developed for mutp53 forms Y220C and R280K [226] was extended to a broader panel of mutp53 forms. Herein, the suitability of this simplified cell system to screen for potential reactivators of mutp53 was validated using p53-null human cancer cell lines with ectopic expression of mutp53. The ability of SLMP53-1 to reactivate wtp53, as well as contact and structural mutp53 forms supports that its molecular mechanism of action is irrespective of the formation of pockets derived from specific mutation sites. Supplementary data from this work showed that, despite the ability of SLMP53-1 to also induce wtp53 thermal stabilization, this was not observed for all mutp53s, namely R248W and R175H (**Annex II, Figure S2 B**). This indicated that the thermal stabilization was not the mechanism of action by which SLMP53-1 is capable of reactivating different mutp53 forms. Of note that, the lack of thermal stabilization for these mutp53s, does not mean an absence of protein-ligand interaction. In fact, a known limitation of CETSA is that not all binding events change the thermal stability of the target protein [345, 365].

Interestingly, all mutp53 tested appear to have a similar functional activity when tested in yeast growth assay. Nevertheless, this homogeneity contrasts with the heterogeneous ability of SLMP53-1 to reactivate mutp53 occurring at the same codon but with different amino acid substitutions. Thus, it would be worth doing further studies to better understand the inability of SLMP53-1 to reactivate mutp53 forms Y220C, R273C, and G245S. By addressing this question, deeper insights on p53 pharmacology will be achieved, paving new ways in anticancer drug discovery by targeting mutp53.

Chapter IV

Hyaluronic acid and folic acid functionalized mesoporous silicon nanoparticles for enhancement of LEM2 anticancer activity

Ana Sara Gomes, Alexandra Correia, Antti Rahikkala, Flavia Fontana, João Pedro Martins, Zehua Liu, Dongfei Liu, Madalena M Pinto, Emília Sousa, Lucília Saraiva, Hélder Santos, (2019), “*Hyaluronic acid and folic acid functionalized mesoporous silicon nanoparticles for enhancement of LEM2 anticancer activity”*, manuscript in preparation.

1. Summary

Cancer pharmacology still presents many therapeutic challenges. Particularly, new alternative therapies with higher potency and selectivity to cancer cells are needed to be developed. LEM2 is a xanthone derivative small-molecule with valuable TAp73-dependent antitumor activity against a wide panel of cancer cell lines, including patient-derived neuroblastoma cells. Despite this, its low solubility, particularly in aqueous solutions, has limited the study of its *in vivo* antitumor activity.

Drug nanodelivery systems have been used as a strategy to overcome shortcomings related to drugs bioavailability, selectivity, toxicity, as well as to control drug release. As such, this work was focused on the development of nanodelivery systems based on PSi material functionalized with hyaluronic acid (HA) or folic acid (FA) for the targeted delivery of LEM2 in cancer cells. HA or FA was successfully achieved by amine coupling reactions to NPs surface. Developed LEM2-loaded NPs improved LEM2 solubility in aqueous solutions, and its antitumor activity in cancer cells.

2. Materials and methods

2.1. General

The xanthone derivative LEM2 was synthesized and purified as described elsewhere [233]. All chemicals and solvents used were purchased from Sigma-Aldrich (Espoo, Finland). Purified water was obtained by Milli-Q® Integral 15 Water Purification System (Merck Millipore, Burlington, Massachusetts, USA). Polymers COOH-PEG-NH_2 (5 kDa) was from Sigma-Aldrich and hyaluronic acid (HA; 50 kDa) was from Creative PEG Works (Durham, North Carolina, USA). NPs were dispersed with ultrasound either with bath sonication or tip sonication (30% amplitude, 10 s). Centrifugations were performed in L-70 Ultracentrifuge (Beckman, Brea, California, USA) or 5415D Centrifuge (Eppendorf AG, Germany, Hamburg). RPMI 1640, L-glutamine, non-essential amino acids (NEAA), penicillin (100 IU/mL), streptomycin (100 mg/mL) and trypsin (2.5%) were purchased from HyClone™ (GE Healthcare Life Sciences, Little Chalfont, Buckinghamshire, UK). Heat inactivated FBS, Hank's balanced salt solution (10× HBSS) and Versene were from Gibco® (ThermoFisher Scientific, Waltham, Massachusetts, USA). Triton X-100 was purchased from Merck Millipore.

2.2. Production of UnTHCPSi and APTES-TCPSi NPs

The cores undecylenic acid modified thermally hydrocarbonized mesoporous silicon (UnTHCPSi) and 3-aminopropyltriethoxysilane modified thermally carbonized mesoporous silicon (APTES-TCPSi) NPs were kindly provided by Prof. Salonen's group (University of Turku, Finland) and were produced as described in [293, 366-371]. Briefly, the PSi structure was attained by electrochemical anodization of monocrystalline boron doped boron-doped p^+-type Si(100) (resistivity of 0.01–0.02 Ω•cm) with a 1:1 (*v/v*) hydrofluoric acid (38%)-ethanol electrolyte. The application of repeated pulses of constant etching current (50 mA/cm^2)/high density (electropolishing) etching current on the Si wafers leads to a multilayer structure with high porosity fracture planes. The multilayer PSi free-standing films were stabilized by thermal hydrocarbonization (THCPSi) with a N_2-acetylene (1:1) flow at 500 °C, or by thermal carbonization (TCPSi) with two-stepped acetylene flow at 500 and 820 °C. To obtain the carboxylic functionalized UnTHCPSi, the THCPSi film was functionalized through a thermal treatment in undecylenic acid (Un) for 16 h at 120 ºC. UnTHCPSi films were then milled in a solution of 5% (*v/v*) undecylenic acid:dodecane. A homogeneous particle size was obtained by ultracentrifugation [293, 366, 367, 369]. To obtain APTES-TCPSi, the multilayer TCPSi films were pre-treated with 1:1 (*v/v*) aqueous hydrofluoric acid (HF) (38%)-ethanol solution to partially reactivate the stabilized surface by producing hydroxyl groups for silanization. Thereafter, the HF-treated TCPSi films were allowed to react with 3-aminopropyltriethoxysilane (APTES) in anhydrous toluene solution for 1 h at 25 °C, followed by washing steps with increasing gradient of toluene to methanol and finally milled. After obtaining the desired particle size, UnTHCPSi and APTES-TCPSi were storage in ethanol. The surface carboxylic acids or amines groups belonging to the Un or APTES, respectively, were used as linkers for further modifications [368, 370, 371].

2.3. Nanoparticles functionalization

UnTHCPSi and APTES-TCPSi functionalization was based on a 1-ethyl-3-(3-dimethylaminopropyl) carbodiimide (EDC)/*N*-hydroxysuccinimide (NHS) amine coupling chemistry in an aqueous buffer solution. All conjugations were performed in sequential coupling reactions with activation of precursor carboxylic groups, amine coupling, and washing steps as described elsewhere [366, 369, 372]. To avoid unspecific cross-coupling among COOH-PEG-NH_2 molecules with EDC/NHS activation/coupling, the PEG-primary amine was protected via reaction with di-*tert*-butyldicarbonate $(BOC)_2O$ [373]. For this, COOH-PEG-NH_2 was dissolved in dichloromethane (DCM; 2 mL), followed by addition of trimethylamine (TEA) in a 1:6 molar ratio (PEG:TEA), stirring in ice for 10 min. Then, $(BOC)_2O$ was added in a 1:3 molar ratio [PEG: $(BOC)_2O$], stirring in ice for 30 min, and let to react overnight at room temperature. Reaction mixture was dried by compressed air and the crude was dissolved in Milli-Q water, dialyzed for 24 h and COOH-PEG-NH-BOC obtained by lyophilization.

Specifically, for flow cytometry analysis UnTHCPSi and APTES-TCPSi were labelled with AlexaFluor^{TM} 488 and fluorescein isothiocyanate (FITC), respectively, prior to further functionalization. Briefly, UnTHCPSi labelling procedure was based on EDC/NHS amine coupling [369, 374], in which 3 mg of NPs were dispersed in 10 mM 2-(*N*-morpholino) ethanesulfonic acid (MES) saline buffer with 12 mg (0.1 mmol) of NHS and 16 µL (0.2 mmol) of EDC (≥97.0%) at a final pH 5.2. The activation of carboxylic acid groups was let to occur at 300 rpm for 90 min, protected from light. Afterwards, the AlexaFluor 488 hydrazide was added to the reaction mixture at 1:100 ratio (w/w) (dye:NPs), and the nucleophilic reaction proceeded for 2 h under the same conditions. UnTHCPSi-AlexaFluor 488 NPs were rinsed three times with Milli-Q water, and centrifuged at 13,400 rpm, for 10 min, to eliminate excess of reagents. For APTES-TCPSi labelling, FITC was dissolved in dimethyl sulfoxide (DMSO; 3 mL) with 3 mg of NPs in a final ratio of 1:100 (w/w) (dye:NPs), and let to react at 300 rpm for 2 h, protected from light [375]. APTES-TCPSi-FITC NPs were rinsed and centrifuged to eliminate excess of reagents.

2.3.1. UnTHCPSi-SP-PEG-FA and APTES-TCPSi-PEG-FA

UnTHCPSi (6 mg) were dispersed in 10 mM MES buffer with 24 mg (0.1 mmol) of NHS and 31.98 µL (0.2 mmol) of EDC at final pH 5.2. The activation of carboxylic acid groups was let to occur at 300 rpm, for 90 min, protected from light. Afterwards, the free-amine spermine (SP) crosslinker was added to the reaction mixture at a 2:1 ratio (w/w) (linker:NPs), and the nucleophilic reaction proceeded overnight under the same conditions. UnTHCPSi-SP were rinsed and centrifuged. UnTHCPSi-SP or APTES-TCPSi NPs were dispersed in a previously prepared solution (12 mL) of activated COOH-PEG-NH_2-BOC in MES buffer with 24 mg (0.1 mmol) of NHS and 31.98 µL (0.2 mmol) of EDC at a final pH 5.2, with a final ratio of 1.5:1 (w/w) (polymer:NPs). UnTHCPSi-SP-PEG-NH-BOC or APTES-TCPSi-PEG-NH-BOC NPs were rinsed with Milli-Q water and then ethanol with intercalated centrifugations. The BOC group was removed by adding the NPs in DCM (3 mL) and trifluoracetic acid (1 mL) [376], stirred for 30 min in ice, dried, washed with ethanol and Milli-Q water. As final step, UnTHCPSi-SP-PEG-NH_2 or APTES-TCPSi-PEG-NH_2 were added to a previously prepared solution (12 mL) of activated COOH-FA in

MES buffer with 24 mg (0.1 mmol) of NHS and 31.98 µL (0.2 mmol) of EDC at a final pH 5.2, with a final ratio of 1.5:1 (w/w) (ligand:NPs). NPs were rinsed, centrifuged and stored in Milli-Q water at 1.5 mg/mL, at 4 ºC, for further experiments.

2.3.2. UnTHCPSi-SP-HA and APTES-TCPSi-HA

A solution of 12 mg of COOH-HA was prepared in 12 mL of MES buffer with 24 mg (0.1 mmol) of NHS and 31.98 µL (0.2 mmol) of EDC, at a final pH 5.2. The activation of carboxylic acid groups was let to occur at 300 rpm for 90 min, protected from light. Afterwards, 6 mg of UnTHCPSi-SP (as produced in **1.3.1.**) or APTES-TCPSi NPs were dispersed in the reaction mixture at a final ratio of 2:1 (w/w) (polymer:NPs), and amine coupling reaction proceeded overnight under the same conditions. NPs were rinsed, centrifuged and stored in Milli-Q water at 1.5 mg/mL, at 4 ºC for further experiments.

2.4. Physicochemical characterization of NPs

2.4.1. Pore volume and diameter, and specific surface area of UnTHCPSi and APTES-TCPSi

The physicochemical properties of UnTHCPSi and APTES-TCPSi were characterized by Prof. Salonen's group (University of Turku, Finland) (**Annex III, Table S1**), as described in [293, 368]. Briefly, the pore properties were determined with nitrogen sorption at 77 K (Tristar 3000, Micromeritics Inc.). The pore volume was obtained by calculating the isotherm using the total adsorption value. The Barrett-Joyner-Halenda theory was applied, using the desorption branch of the isotherm, to calculate pore diameter. The Brunauer-Emmett-Teller theory was used to calculate the specific surface area [368].

2.4.2. Functionalization, size, dispersity, and surface charge of modified NPs

The NPs success of functionalization was confirmed through evaluation of physicochemical properties of modified NPs, comparing with unmodified ones (UnTHCPSi and APTES-TCPSi). NPs were analyzed by the following methods in Milli-Q water, at 10 µg/mL, final pH 6.8. Hydrodynamic diameter (Z-average, d. nm), polydispersity index (PdI) and zeta(ζ)-potential of modified and unmodified NPs were determined by Dynamic and Electrophoretic Light Scattering (DLS and ELS) with a disposable polystyrene cuvette

(SARSTEDT AG & Co., Nümbrecht, Germany), and a disposable folded capillary cell (DTS1070, Malvern Panalytical Ltd., Malvern, UK), using a Zetasizer Nano ZS instrument (Malvern Instruments Ltd, Malvern, UK). Size and morphology were also checked by transmission electron microscopy (TEM) [293, 372]. For that, small droplets of NPs suspension were placed on top of carbon-coated copper TEM grid, and dried at room temperature. Pictures were taken with Jeol JEM-1400 microscope (Jeol Ltd., Tokyo, Japan) at 80 kV. NPs functionalization was also analyzed by Fourier Transform Infrared (FTIR) Spectroscopy. For that, 1 mg of NPs samples were lyophilized, and placed in vacuum. KBr pellets were prepared with NPs samples and analyzed using a spectrometer Nicolet iS10 from ThermoFisher Scientific with Smart OMNI-Transmisson accessory. FTIR spectra were recorded in the wavenumber region of 4000−650 cm^{-1} with a resolution of 4 cm^{-1} with 16 scans at room temperature using OMNIC^{TM} 8.3 software (ThermoFisher Scientific).

2.5. LEM2 loading in unmodfied and modified NPs

Drug loading was performed by the immersion method [283, 377]. For that, LEM2 was dissolved in dichloroethane (DCE), at a final concentration of 5 mg/mL. NPs (200 μg) were dispersed in 250 μL of LEM2 solution, at room temperature, stirring at 300 rpm for 2 h, protected from light. Loaded NPs were centrifuged at 13,200 rpm, for 10 min, and washed with 50 μL of ethanol to remove the excess of unloaded drug. Loaded NPs were then dispersed in 1 mL of DCE and stirred for 1 h, protected from light. After that, NPs were centrifuged and the amount of LEM2 in the supernatant was analyzed by HPLC (Agilent 1 260, Agilent Technologies, USA). The HPLC method was established using a C18 column (4.6 × 150 mm, 5 µm, Supelco Discovery, USA) with a mobile phase of methanol/water (70:30) in an isocratic system, at room temperature. The injected volume was 20 µL, the analysis flow rate was 0.7 mL/min, and the detection was performed at 240 nm. A calibration curve of LEM2 (0.047–48.5µg/mL) in DCE was established in triplicate, and the quantification of LEM2 was based on the total area under the curve (**Annex III, Figure S1**). The loading degree, LD (%), was calculated based on the following equations [283]:

$$A\ (\mu\mathrm{g}) = [LEM2\ \mu\mathrm{g/mL}] \times Vtotal\ (mL)$$

$$LD\ (\%) = \left(\frac{A}{m\ NPs\ (\mu g) + A}\right) \times 100$$

A *= total mass of LEM2* m *= mass of nanoparticles* $LD\ (\%)$ *= loading degree*

2.6. Payload release studies of LEM2-loaded unmodified and modified NPs

Release studies were carried out as described elsewhere [377]. Briefly, LEM2-loaded NPs (200 µg) were gently dispersed in 5 mL of 10 mM HBSS-HEPES (4-(2-hydroxyethyl)-1-piperazineethanesulfonic acid) at pH 7.4 or 10 mM HBSS-MES (pH 6.5), at 37 ºC, 300 rpm, for 3 h. Aliquots of 100 µL were taken at 1’, 3’, 5’, 10’, 15’, 20’, 30’, 60’, 120’ and 180’ time-points and replaced by pre-warmed buffer solutions to maintain the release volumes. Samples were then centrifuged at 13,400 rpm and supernatants were analyzed by HPLC, as described in section 1.5., to quantify released LEM2. LEM2-loaded unmodified NPs and bulk LEM2 (considering the highest LD%) were used as controls.

2.7. Stability study of unmodified and modified NPs in tumor cell culture medium

The stability of NPs in tumor cell culture medium was studied in RPMI 1640 with 10% FBS (pH 8), as described in [378]. For that, 100 µg bare NPs were dispersed in 750 µL of RPMI 1640 with 10% FBS, and stirred for 2 h, at 37 ºC. Aliquots of 100 µL were taken at 5’, 20’, 15’, 30’ 60’, 90’ and 120’ time-points and diluted in 900 µL Milli-Q water. Thereafter, size, PdI, and ζ-potential were analyzed by DLS and ELS in Zetasizer Nano ZS.

2.8. Human cancer cell lines (general)

Human breast adenocarcinoma MDA-MB-231 and colon adenocarcinoma HCT116 cell lines from ATCC (Rockville, Maryland, USA) were harvested in RPMI 1640 with 10% FBS, 1% NEAA, 1% L-glutamine and 1% penicillin-streptomycin in 25 cm^2 flasks. Cells were incubated in BB 16 gas incubator (Heraeus Instruments GmbH, Hanau, Germany) at 37 ºC, 5% CO_2 and 95% relative humidity.

2.8.1. *In vitro* cytotoxicity studies of bare NPs and LEM2 loaded NPs in MDA-MB-231 and HCT116 cancer cells

The *in vitro* cytotoxicity of bare and LEM2-loaded UnTHCPSi, APTES-THCPSi, UnTHCPSi-SP-PEG-FA, APTES-TCPSi-PEG-FA, UnTHCPSi-SP-HA, and APTES-TCPSi-HA was assessed by CellTiter-Glo® Luminescent Cell Viability assay, as described in [379]. MDA-MB-231 and HCT116 cancer cells were seeded in a 96-well microplate with flat bottom (Corning Inc. Life Sciences, New York, USA), at 5 × 10^3 cells per well Cells were let to attach for 24 h, at 37 ºC [226]. Bare and LEM2-loaded NPs were dispersed in cell harvesting medium and serial dilutions were made. Cells were treated by adding 100 µL of NPs suspension in each well. Final concentrations of bare NPs ranged from 37.5 to 600 µg/mL. LEM2-loaded NPs final concentration treatments corresponded to 0.3 and 0.625 µM of LEM2, accordingly with obtained LD (%). Also, serial dilutions of bulk LEM2 (stock solution at 5 mM in DMSO) were made in cell harvesting medium and cells were treated with final concentrations ranging from 0.3 to 5 µM. Cell harvesting medium and 1% Triton X-100 were used as negative and positive controls, respectively. Treated cancer cells were incubated for 48 h, at 37 °C. Afterwards, cancer cells were washed with 10 mM HBSS-HEPES (pH 7.4), and 100 µL of the CellTiter-Glo® Luminescent Cell Viability assay reagent was added to each well and let to lyse the cells and react for 15 min with stirring, protected from light. The percentage of viable cells was determined by measuring the luminescence, using a Varioskan Flash fluorometer (Thermo Fisher Scientific).

2.8.2. *In vitro* NPs uptake and association studies in MDA-MB-231 and HCT116 cancer cells

Qualitative cellular uptake and association evaluation was performed by TEM. To this end, 13 mm round shape coverslips were placed at the bottom of 24-well plate (Corning Inc. Life Sciences), and the MDA-MB-231 and HCT116 cancer cells were seeded at 1 × 10^5 cells per well (500 µL) in RPMI 1640 with 10% FBS. Cells were let to attach for 24 h, at 37 ºC. Culture medium was removed, and 500 µL of modified and unmodified NPs (non-labbeled), dispersed in 10 mM HBSS-HEPES (pH 7.4) at 50 µg/mL or only HBSS-HEPES (pH 7.4) (negative control), were added to each well. Treatments were performed for 3 h, at 37 ºC, followed by aspiration of NPs suspension and cells wash with 10 mM HBSS-HEPES (pH 7.4). Cells fixation procedure was followed as described in [366]. Briefly, to each well, a solution of 2.5% glutaraldehyde in 0.1 M phosphate buffered saline (PBS; pH 7.4) was added, for 15 min, at room temperature. Cells were washed twice with HBSS-HEPES (pH 7.4) and sodium cacodylate buffer (NaCac) for 3 min, followed by addition of 1% osmium tetroxide in 0.1 m NaCac buffer (pH 7.4). Cells were dehydrated with an ethanol gradient from 30 to 100% (10 min each) and then embedded in epoxy resin. Ultrathin sections (60 nm) were cut parallel to the coverslip and stained with uranyl acetate and lead citrate. Sections were analyzed and images were acquired by TEM using Jeol JEM-1400 microscope with acceleration voltage of 80 kV.

For quantitative cellular uptake and association evaluation, live cells were analyzed by flow cytometry. For that, cells were seeded at 4 × 10^5 cells per well (500 µL) in RPMI 1640 with 10% FBS in 24-well plate and allowed to attach at 37 °C for 24 h. Culture medium was removed, and 500 µL of modified and unmodified fluorescently-labelled NPs dispersed in 10 mM HBSS-HEPES (pH 7.4) at 50 µg/mL or only HBSS-HEPES (pH 7.4) (negative control), were added to each well. Treatments were performed for 3 h, at 37 ºC, followed by aspiration of the NPs suspension and cells wash with 10 mM HBSS-HEPES (pH 7.4). Cells were detached with Versene, centrifuged, washed and suspended in 700 µL PBS (pH 7.4). Cells were analyzed, collecting 10,000 events in each sample, using a LSR II flow cytometer (BD Biosciences, San Jose, California, USA) with excitation/detection filters for 482/520 nm. The analysis was repeated after incubation of the cells with 0.005% (*v/v*) trypan blue, for 4 min, followed by washing, allowing to quench the fluorescence of NPs associated on the surface of the cell membrane. Data analysis was made using FlowJo^{TM} 10.4 software (FlowJo LLC, Ashland, Oregon, USA).

2.9. Statistical analysis

The experiments were performed in triplicate (n=3) and data is presented as mean ± standard deviation (SD; in NPs physicochemical characterization, stability, loading and release assays) or standard error of the mean (SEM; in cellular assays). Data were analyzed statistically by applying One-way analysis of variance (ANOVA) multiple comparisons test (flow cytometry analysis) or Two-way ANOVA (cells viability assay) using the GraphPad Prism 7 software (GraphPad Software, California, USA). Considered levels of significant differences: *$p<0.05$, **$p<0.01$, ***$p<0.001$.

3. Results

3.1. Preparation and physicochemical characterization of the nanoparticles

Cellular membrane folate receptor (FR) and CD44 have been reported as appealing targets for anticancer targeted drug delivery by decorating the nanosystems with their natural ligands FA or HA, respectively [380-383]. Herein, the PSi core was prepared by top-down methodology, based on electrochemical anodization, followed by surface stabilization by thermal hydrocarbonization (THCPSi) or thermal carbonization (TCPSi), and modification by undecylenic acid (UnTHCPSi) or 3-aminopropyltriethoxysilane (APTES-TCPSi). Surface functionalization of UnTHCPSi and APTES-TCPSi cores with FA or HA was conceived. To this end, since FA is a small ligand, to increase of blood circulation half-time of NPs by preventing opsonization, a polymer of 5 kDa was added (COOH-PEG-NH_2) [384, 385]. Specifically, for UnTHCPSi NPs the biocompatible amine-homobifunctionalized crosslinker SP [386] was necessary to transform the –COOH-terminal of its surface into –NH_2 available to react with –COOH-terminal of PEG. This ensured the subsequent conjugation of the carboxylic acid of FA with the NH_2-terminal of PEG, maintaining the free amine of FA, which is necessary for receptor recognition [387]. **Scheme 1** resumes the design strategy of the NPs modification. All reactions of NPs with crosslinker, polymer, or ligand were performed by the EDC/NHS amine coupling chemistry [374, 388]. Such reaction is based on –COOH activation with EDC/NHS coupling reaction followed by amine coupling by adding the amine substrate.

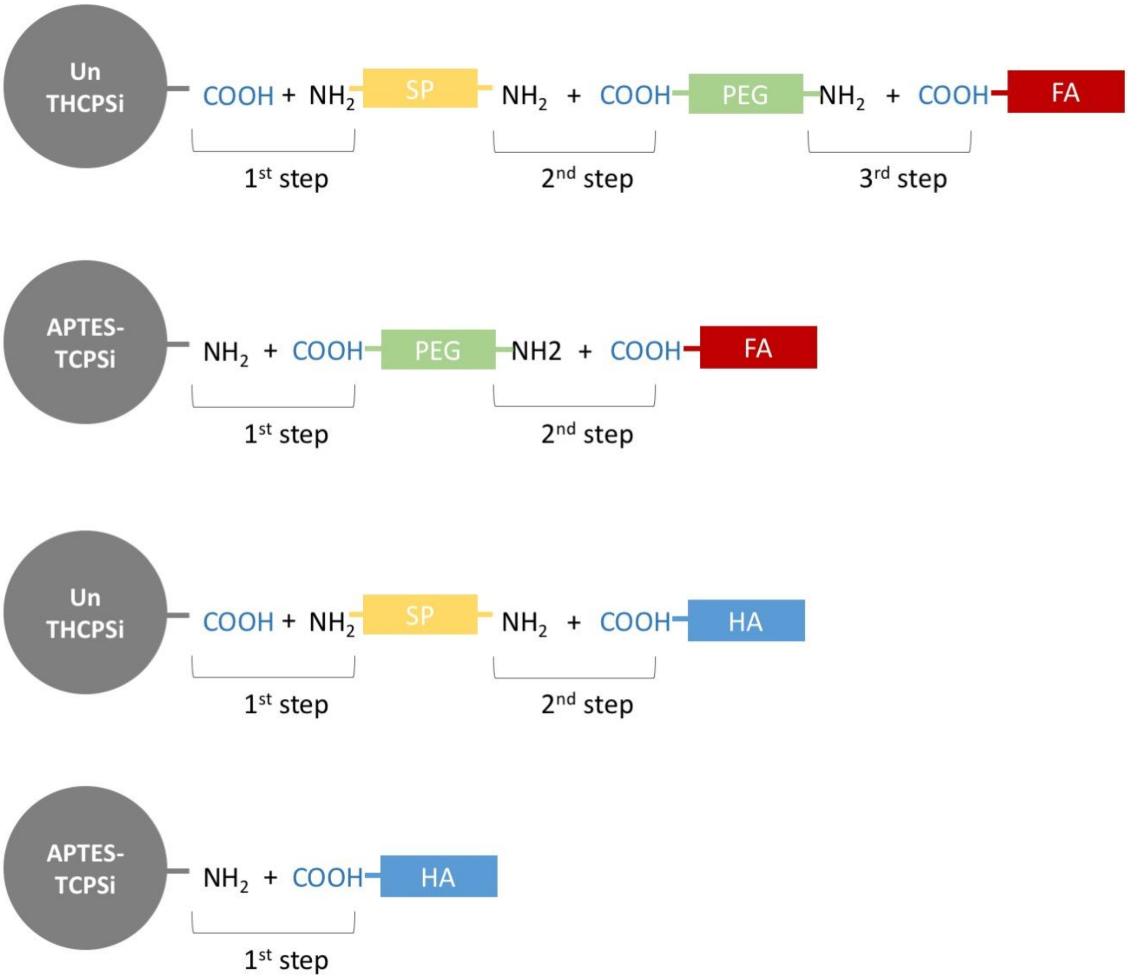
Un THCPSi
COOH + NH2
SP
NH2 + COOH
PEG
NH2 + COOH
FA
1st step
2nd step
3rd step
APTES-TCPSi
NH2 + COOH
PEG
NH2 + COOH
FA
1st step
2nd step
Un THCPSi
COOH + NH2
SP
NH2 + COOH
HA
1st step
2nd step
APTES-TCPSi
NH2 + COOH
HA
1st step

Scheme 1. NPs functionalization strategy to target FR and CD44. Conjugation steps are highlighted.

To confirm the success of the functionalization with FA or HA, a physicochemical characterization of NPs was pursued. Particularly, NPs functionalization was monitored by ζ-potential, size, and PdI measurements in DLS and ELS (**Table 1**). Indeed, it was possible to identify differences on surface charge between unmodified (UnTHCPSi and APTES-TCPSi) and modified NPs (HA- or FA-functionalized NPs). UnTHCPSi presented the most negative value (**Table 1**), followed by HA conjugation, a glycosaminoglycan rich in –COOH/COO$^-$ groups. FA conjugation rendered NPs with surface charge closer to neutrality (**Table 1**), due to PEG neutral charge [389] and since the FA amine may be in its free state at the used pH (folic acid pKa of 3.5 and 4.3) [390]. In addition, unmodified APTES-TCPSi presented a positive charge due to –NH_2/NH_3^+ groups from APTES moiety, which changed radically to negative values with HA conjugation, and closer to neutrality with FA conjugation (**Table 1**). When modified with HA or FA, both NPs cores presented similar values, indicating the occurrence of functionalization. NPs were well dispersed in solution with low values of PdI (**Table 1**). Moreover, values of the hydrodynamic diameter of size average measurement indicated small fluctuations on the size among unmodified and modified NPs (**Table 1**).

Table 1. ζ-potential, size, and PdI of unmodified and modified NPs.

	UnTHCPSi	UnTHCPSi-SP-HA	UnTHCPSi-SP-PEG-FA	APTES-TCPSi	APTES-TCPSi-HA	APTES-TCPSi-PEG-FA
ζ-potential (mV)	-34.43±1.19	-26.84±4.68	-7.18±6.72	15.97±0.65	-29.29±0.83	-5.72±16.46
Size average (d. nm)	207.00±1.01	369.32±73.04	286.16±82.74	331.5±7.81	247.62±29.07	333.18±93.48
PdI	0.15±0.02	0.28±0.15	0.18±0.03	0.19±0.03	0.18±0.05	0.26±0.07

Measurements were made in Milli-Q water at pH 6.8. Presented data are mean ± SD (n=3).

The analysis of the chemical groups was performed by FTIR. This methodology allows to identify changes in molecules due to new covalent bonds or by the change of the chemical environment promoted by non-covalent interactions [391, 392]. The analysis of FTIR spectra revealed that NPs were successfully functionalized by FA or HA, when comparing the differences observed between the spectra of modified and unmodified NPs, having HA and FA spectra as references (**Figure 1 A**). The differences detected were in the region of 2000 to 1000 cm^{-1} wavelengths. Particularly, using a FTIR vibrational pattern table [393, 394], in NPs modified with HA it was possible to observe new bands when compared to unmodified NPs, which appear at 1632 cm^{-1} (**a**; C=O amide stretch), 1559 cm^{-1} (**b**; N–H amide bend), 1405–1375 cm^{-1} (**c**; C–H CH_2 bend and O–H bend in plane), and 1260 cm^{-1} (**d**; C–O stretch) wavelengths, corresponding to the same wavelengths of some bands of the HA. On the other hand, NPs modified with FA spectra showed new bands at 1693 cm^{-1} (**e**; C=O amide stretch), 1605 cm^{-1} (**f**; N–H amide bend), 1572–1484 cm^{-1} (**g**; C=C aromatic stretch, multiple bands), 1403 cm^{-1} (**h**; C–H CH_2 bend), and 1300 cm^{-1} (**i**; C–N stretch) wavelengths, which correspond to FA reference bands (**Figure 1 A**). Furthermore, to check NPs morphology of newly modified NPs comparing to unmodified ones, TEM analysis was performed (**Figure 1 B**). In general, the appearance of unmodified and modified NPs was similar, and size values did not vary much from those obtained by DLS.

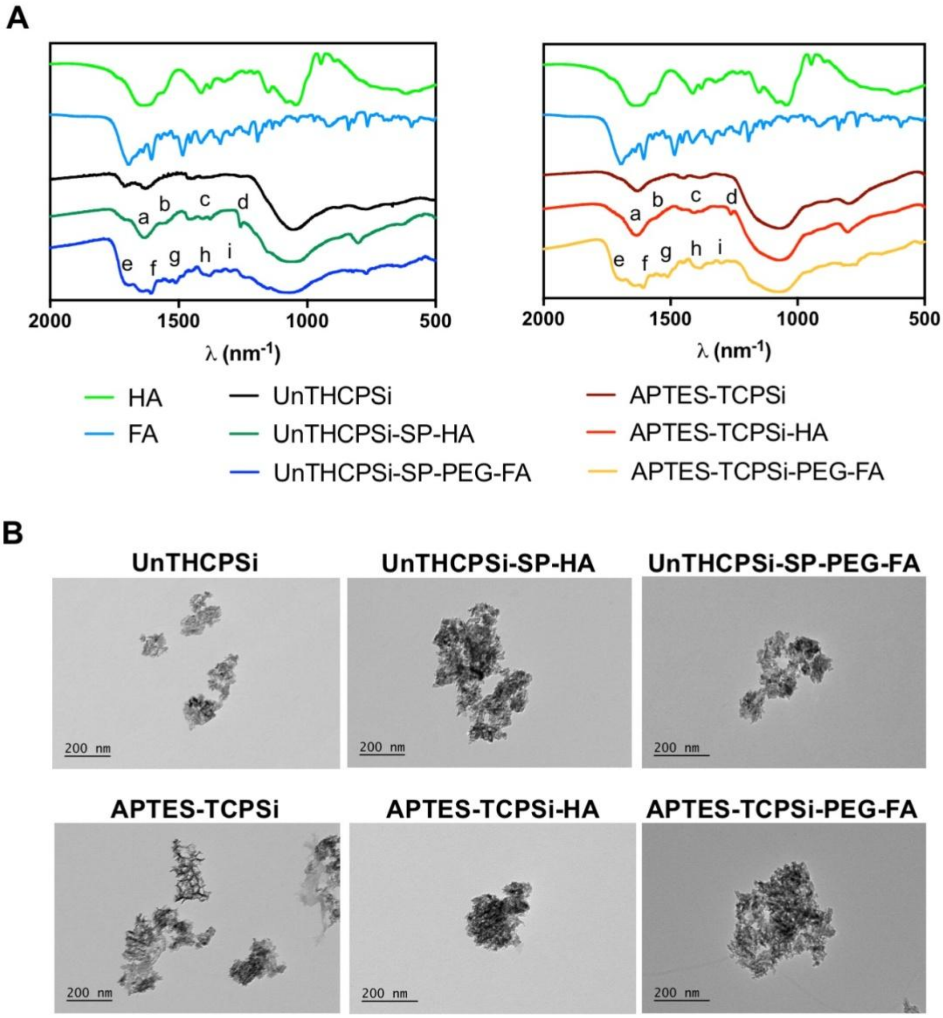

Figure 1. Physicochemical characterization of modified NPs. (A) FTIR spectra of modified and unmodified NPs, FA and HA in KBr pellets. Bands that appear, change in intensity, or are dislocated due to conjugation are highlighted and labeled **a-i**. **(B)** TEM images of unmodified and modified NPs.

3.2. LEM2 loading, *in vitro* release profile, and stability of the nanoparticles

After NPs functionalization, it was important to investigate the amount of LEM2 that the NPs could carry and deliver to the target cells. For that, the LD (%) was obtained and release studies were performed. The LD (%) was determined by the immersion method [283], in which the unmodified and modified NPs were dispersed in a LEM2 solution in DCE, allowing the incorporation of the compound within the pores. The compound is loaded due to its higher affinity to NPs pores surface than to the solvent through physical adsorption processes and physical confinement contributing to drug amorphization [291, 318, 395]. Among other solvents tested (*i.e.*, ethanol, methanol, acetonitrile, DMSO, diethyl ether, *n*-hexane and ethyl acetate), DCE showed to be the best solvent, reaching the highest concentration of a saturated solution of LEM2 (5 mg/mL). The obtained LD (%) values are presented in **Table 2,** varying around 0.4 to 3% for tested NPs. Unmodified and modified UnTHCPsi NPs presented lower LD (%) values than unmodified and modified APTES-TCPSi.

Table 2. LEM2 loading degrees (LD) % of unmodified and modified NPs.

	UnTHCPSi	**UnTHCPSi-SP-HA**	**UnTHCPSi-SP-PEG-FA**	**APTES-TCPSi**	**APTES-TCPSi-HA**	**APTES-TCPSi-PEG-FA**
LD (%) (w/w)	0.97±0.16	0.43±0.11	0.47±0.12	2.33±0.94	2.67±1.06	1.99±0.97

Presented data are mean±SD (n=3).

The LEM2 payload release study indicated that a pH-independent burst release of LEM2 occurred immediately after NPs dispersion in buffer solution with a concentration maintenance of LEM2 for 3 h (**Figure 2**), with no detection of drug degradability. In opposition, bulk LEM2 remained undetectable throughout the experiment. At pH 7.4, unmodified and modified UnTHCPSi released LEM2 in rates higher than 80%, at 3 h. However, the same was not verified at pH 6.5, with higher rates for UnTHCPSi-SP-HA (>80%) and UnTHCPSi-SP-PEG-FA (60 to 80%) compared to unmodified ones (around 40%) (**Figure 2**). Regarding unmodified and modified APTES-TCPSi, the same LEM2 release profiles were obtained for both pH, with higher release rates obtained for APTES-TCPSi-PEG-FA (>90%) and lower release rates for APTES-TCPSi and APTES-TCPSi-HA (20 to 30%) (**Figure 2**).

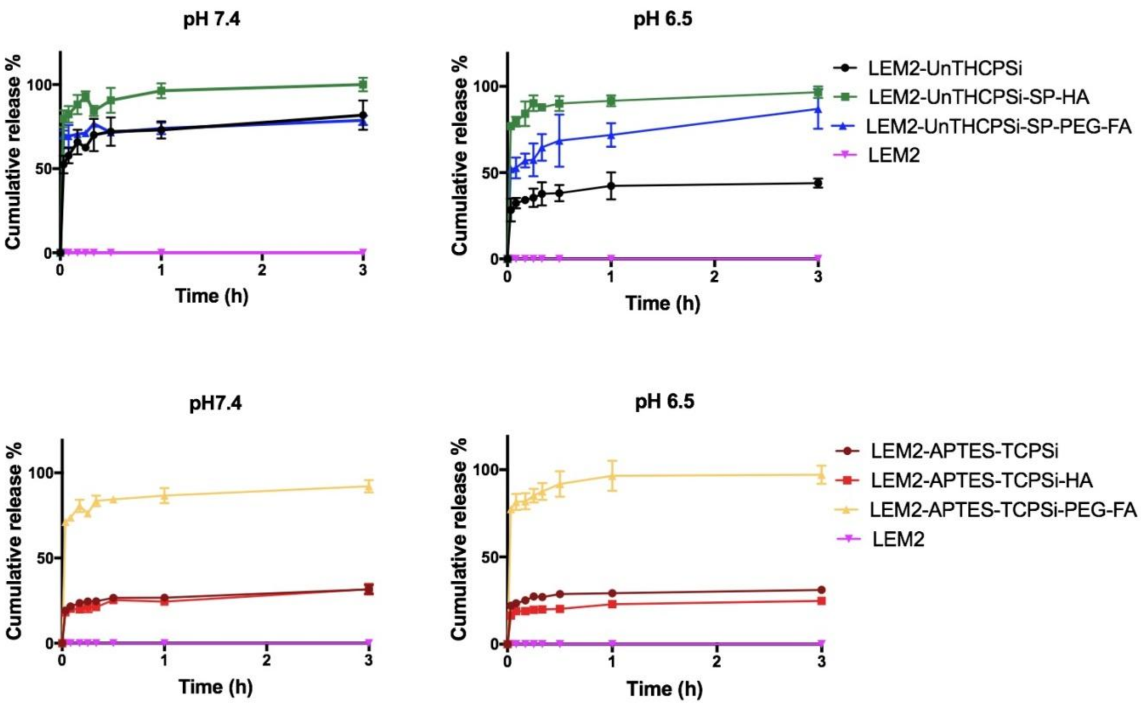

Figure 2. Release studies of LEM2-loaded NPs. Release profiles of LEM2-loaded modified and unmodified NPs (200 µg) in 5 mL of HBSS-HEPES (pH 7.4, blood-like) and HBSS-MES (pH 6.5, tumor microenvironment-like) during 3 h, at 37 ºC. Unmodified NPs and bulk LEM2 (in the same amount of LEM2 incorporated in NPs calculated based on the highest LD%) were used as controls. The amount of LEM2 released is presented in cumulative % and data are mean ± SEM (n=3).

It was also important to assess the NPs stability in cell culture medium for cancer cell viability studies. For that, ζ-potential, size, and PdI of NPs were measured for 2 h in RPMI 1640 with 10% FBS, at 37 ºC (**Figure 3**). NPs were shown to be stable throughout the experiment, with no surface charge alteration (constant ζ-potential) or aggregation, with unchanged size and PdI (**Figure 3**). These evidences supported the NPs stability in cell culture medium suitable for further *in vitro* studies with cancer cells.

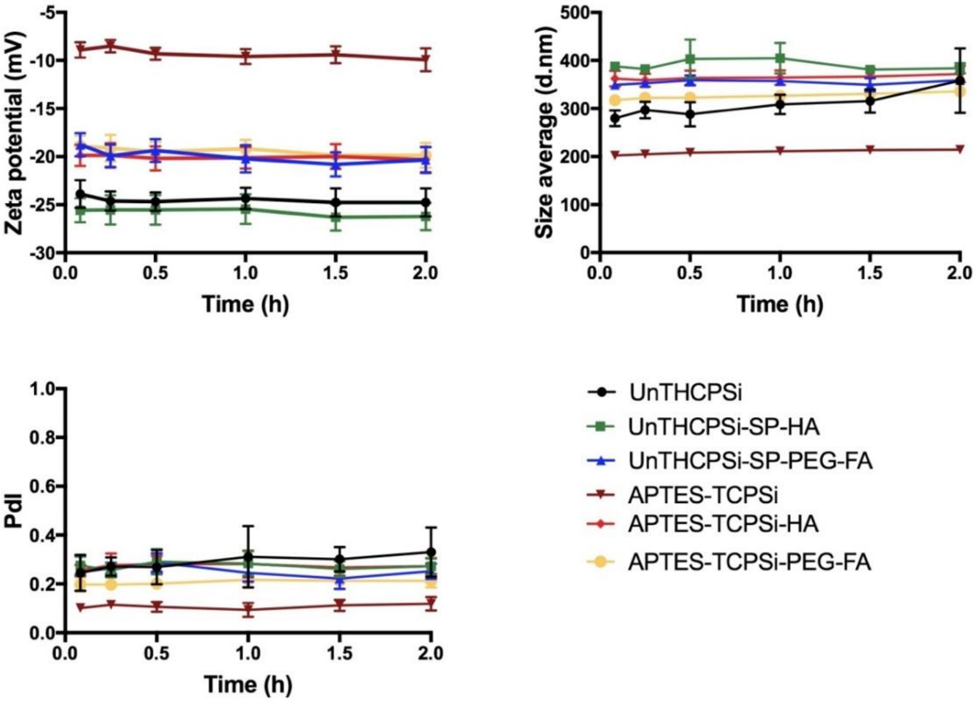

Figure 3. Stability studies of bare NPs. Bare NPs (100 µg) stability in 750 µL of RPMI 1640 with 10% FBS culture medium during 2 h, at 37 ºC, was assessed by ζ-potential, size average and PdI. Presented data are mean ± SD (n=3).

3.3. Modified and unmodified nanoparticles are taken-up and cytocompatible, increasing LEM2 cytotoxicity in human cancer cells

Bare NPs were analyzed to check whether they could be *per se* cytotoxic in HCT116 and MDA-MB-231 cancer cells. Cell viability was evaluated based on quantification of the total amount of ATP of metabolically active cells [396, 397]. HCT116 and MDA-MB-231 cancer cells were chosen due to the known cytotoxicity of LEM2 against these cells [233], and due to their expression of both CD44 and FR [398-402]. To determine the highest non-toxic concentration of bare NPs, cells were treated with a concentration range of NPs, from 37.5 to 600 µg/mL. The highest amount of NPs (600 µg/mL) correspond to the maximum of bare NPs required to attain 5 µM LEM2, according to the lowest LD (%). The results showed that all NPs exhibited a concentration-dependent toxic effect on both cell lines. In general, NPs (unmodified or modified NPs, with UnTHCPSi or APTES-TCPSi cores) revealed to be toxic to the highest concentrations (300 and 600 µg/mL), with a reduction around 50% of cell viability, in both cancer cell lines (**Figure 4**). The exception occurred with 300 µg/mL of modified UnTHCPSi-SP-HA, which did not cause a marked reduction in cell viability (**Figure 4**). In general, the two lowest NPs concentrations of 37.5 and 75 µg/mL showed to be cytocompatible, with cell viability values around 80 to 100% in both tested cancer cell lines (**Figure 4**). It was also observed that NPs modified with HA were more cytocompatible than unmodified or modified with FA, the latter with a tendency for lower cell viability values at all concentrations in both cancer cell lines (**Figure 4**). Regarding the core used, unmodified UnTHCPSi (negatively charged) NPs were found to compromise cell viability

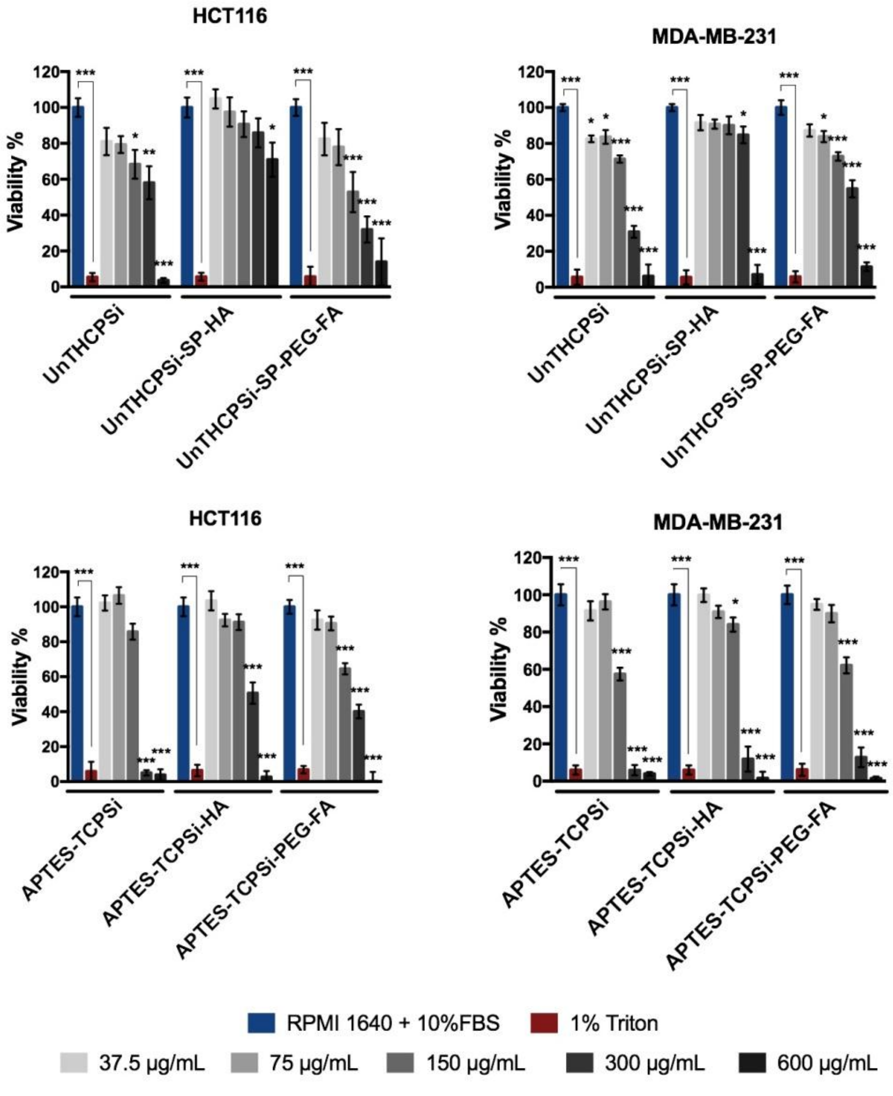

Figure 4. Bare modified and unmodified NPs concentration-dependent cytocompatibility in human cancer cells. Cell viability in HCT116 and MDA-MB-231 cancer cells was evaluated after bare NPs (37.5–600 µg/mL) treatment, for 48 h. Cells treated with harvesting medium or 1% Triton X-100 were used as negative and positive controls, respectively. Presented data are mean ± SEM (n=3). Significant differences between means (negative control *vs* NPs treatments) were statistically analyzed by Two-way ANOVA with Dunnet's multiple comparisons (*$p<0.05$, **$p<0.01$, and ***$p<0.001$).

in a greater extent for lower concentrations than APTES-TCPSi (positively charged), while for higher concentrations APTES-TCPSi were more cytotoxic than UnTHCPSi NPs. In general, HCT116 cancer cells were less sensitive to bare-NPs treatment than MDA-MB-231 ones.

Cancer cells were thereafter treated with bulk LEM2 and LEM2-loaded NPs, with two concentrations of LEM2 (0.3 and 0.625 µM), for which bulk LEM2 had no cytotoxic activity (**Figure 5**). The amount of NPs was adjusted to both LEM2 concentrations for treatment, according to previously obtained LD (%) (not considering the release rate), corresponding to NPs concentrations lower than 75 µg/mL, with no impact on cell viability as referred above. LEM2-loaded UnTHCPSi-SP-PEG-FA, APTES-TCPSi-HA and APTES-TCPSi-SP-FA NPs increased LEM2 cytotoxicity at both tested LEM2 concentrations in both cancer cell lines by reducing their viability (**Figure 6**). Only effects corresponding to more than 50% inhibition of cell viability will be described. In HCT116 cancer cells, LEM2-loaded UnTHCPSi-SP-PEG-FA, APTES-TCPSi-HA and APTES-TCPSi-SP-FA NPs, at both concentrations, revealed to induce a significant reduction of cell viability compared to bulk LEM2 (**Figure 6**). Specifically, LEM2-UnTHCPSi-SP-PEG-FA NPs reduced the viability of HCT116 cancer cells to 21.42 ± 7.68% at 0.625 µM. LEM2-APTES-TCPSi-HA NPs reduced cell viability to 39.58 ± 7.22% (at 0.3 µM) and 12.96 ± 2.50% (at 0.625 µM). The treatment of HCT116 cancer cells with LEM2-APTES-TCPSi-SP-FA NPs, at 0.3 and 0.625 µM, exhibited cell viabilities of 20.98 ± 12.74% and 11.94 ± 4.30%, respectively (**Figure 6**). MDA-MB-231 cancer cells showed to be more resistant to LEM2 cytotoxicity (**Figure 5, 6**). Nevertheless, a similar profile was observed in MDA-MB-231 cancer cells with a significant reduction of cell viability for both concentrations of LEM2-loaded UnTHCPSi-SP-PEG-FA, APTES-TCPSi-HA and APTES-TCPSi-SP-FA NPs (**Figure 6**). Cell viability obtained with LEM2-APTES-TCPSi-HA NPs was 36.50 ± 1.30% (at 0.625 µM). For LEM2-APTES-TCPSi-SP-FA NPs treatment, the cell viability decreased to 46.82 ± 2.25% (at 0.3 µM) and 30.82. ± 2.40% (at 0.625 µM) (**Figure 6**).

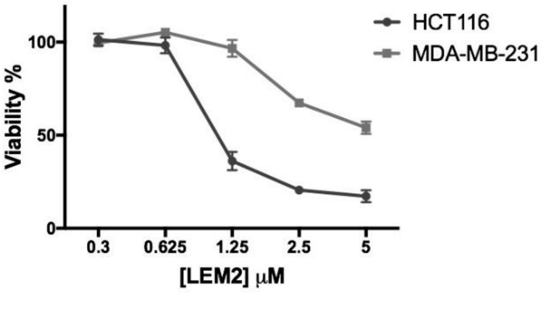

Figure 5. Bulk LEM2 cytotoxic effect in human cancer cell lines. Cell viability in HCT116 and MDA-MB-231 cancer cells was evaluated after LEM2 (0.3 to 5 µM) treatment, for 48 h. Cells

treated with harvesting medium or 1% Triton X-100 were used as negative and positive controls, respectively. Presented data are mean ± SEM (n=3).

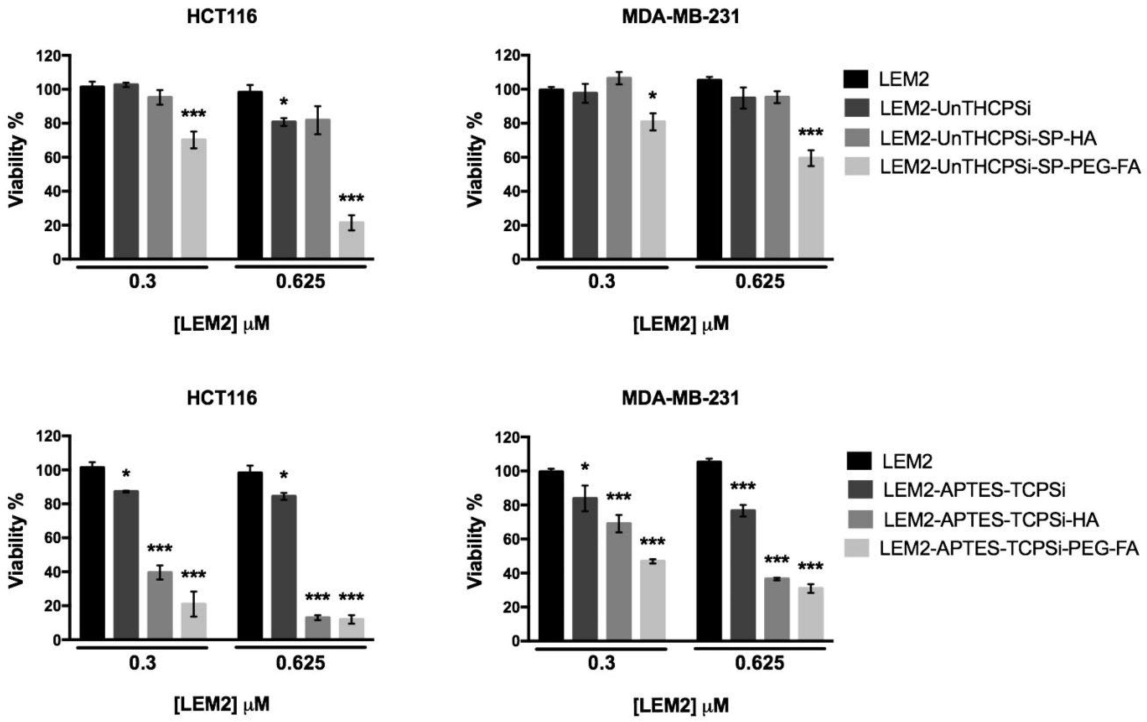

Figure 6. LEM2-loaded modified NPs increase LEM2 cytotoxicity in human cancer cells. Cell viability in HCT116 and MDA-MB-231 cancer cells was evaluated after LEM2-loaded NPs treatment, for 48 h. Cells treated with RPMI 1640 with 10% FBS or 1% Triton X-100 were used as negative and positive controls, respectively. The amount of LEM2-loaded NPs was calculated through LD (%), to treat cells with the same amount of LEM2 at concentrations of 0.3 and 0.625 μM. Treatment with bulk LEM2 was used as negative control at the same concentrations. Presented data are mean ± SEM (n=3). Significant differences between means (negative control *vs* NPs treatments) were statistically analyzed by Two-way ANOVA with Dunnet's multiple comparisons test (**p*<0.05, ***p*<0.01, and ****p*<0.001).

It was also relevant to confirm whether modified NPs were taken-up by cancer cells. For this, cells were treated with bare unmodified and modified NPs and analyzed by TEM and flow cytometry, as represented in **Figures 7–9**. TEM images allowed to detect that NPs were associated with cell membranes and taken-up by cancer cells being confined in large vesicles (with a rough size varying from 200 to 1000 nm), within cell cytoplasm (**Figure 7, 8**). In addition, it became evident that some cells presented plasma membrane protrusions next to NPs (**Figure 7, 8**). These results were in accordance with

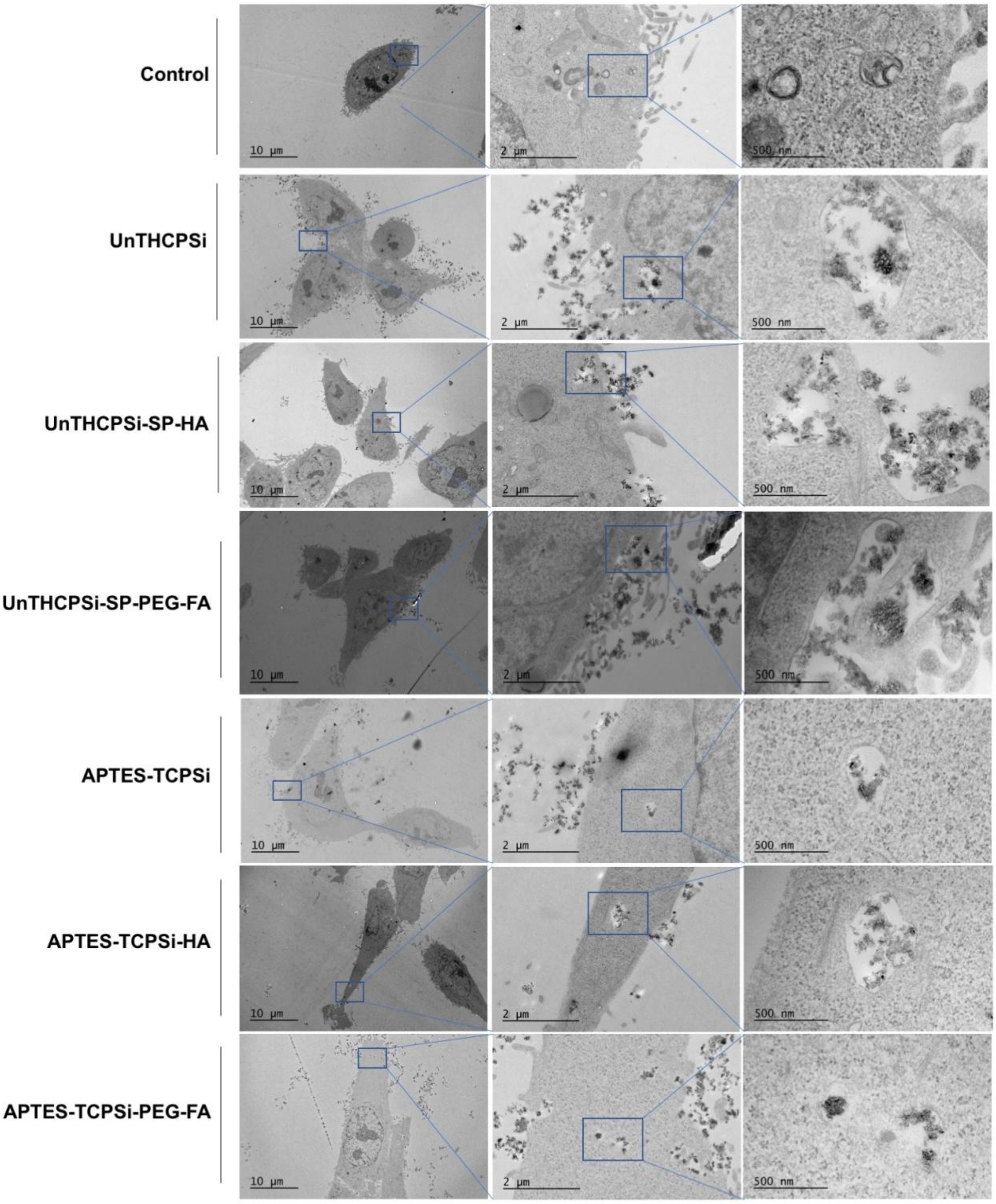
Control
UnTHCPSi
UnTHCPSi-SP-HA
UnTHCPSi-SP-PEG-FA
APTES-TCPSi
APTES-TCPSi-HA
APTES-TCPSi-PEG-FA
10 µm
2 µm
500 nm

Figure 7. Modified and unmodified NPs are taken-up by HCT116 cancer cells (qualitative analysis). TEM images with NPs internalization by HCT116 cancer cells after 3 h treatment with modified and unmodified bare NPs at 50 µg/mL, or vehicle (negative control). From left to right: first image 500×, second image 4000×, third image 15000×. TEM imagens were recorded at an acceleration voltage of 80 kV, representing one of three independent experiments.

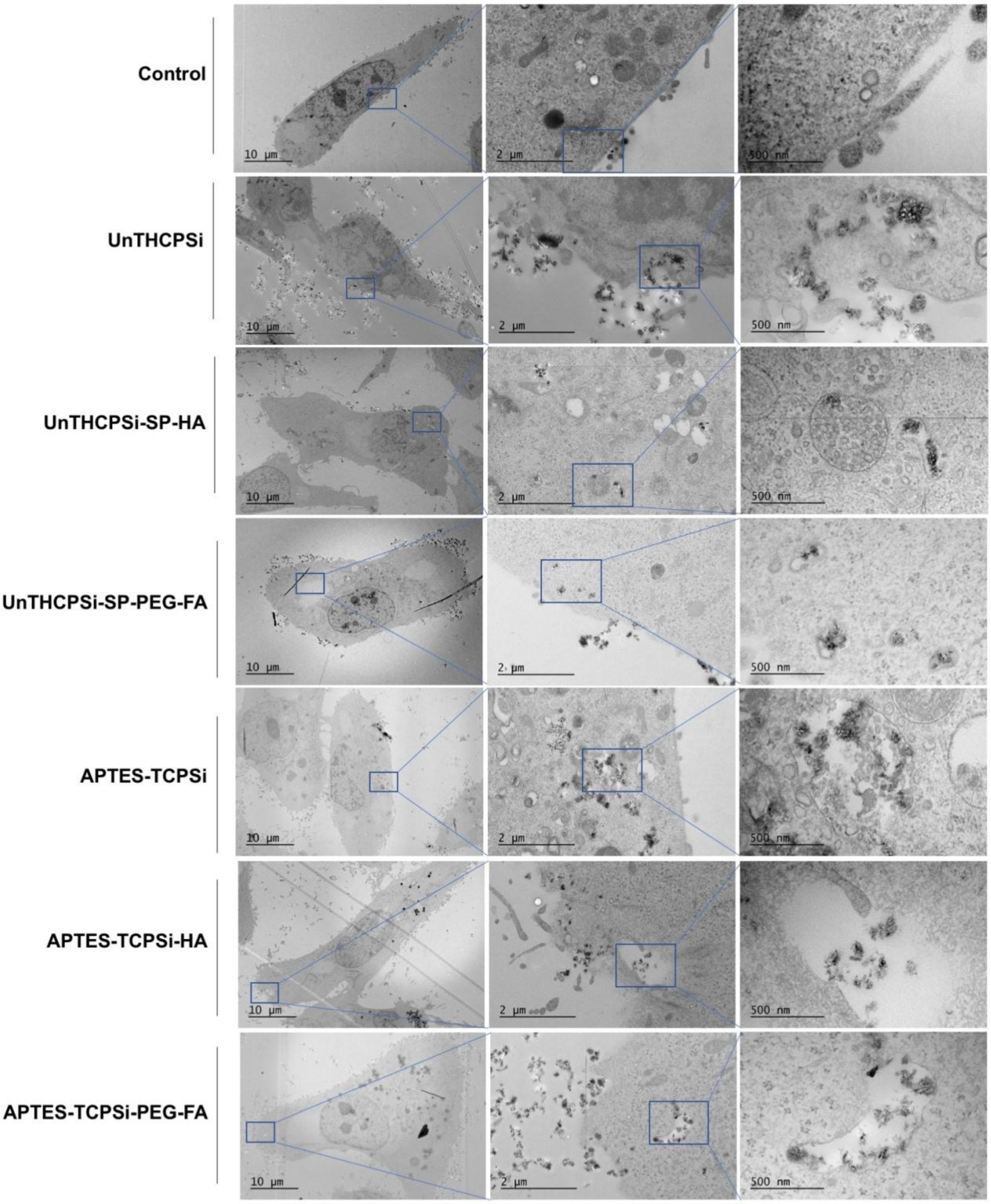
Control
UnTHCPSi
UnTHCPSi-SP-HA
UnTHCPSi-SP-PEG-FA
APTES-TCPSi
APTES-TCPSi-HA
APTES-TCPSi-PEG-FA
10 μm
2 μm
500 nm

Figure 8. Modified and unmodified NPs are taken-up by MDA-MB-231 cancer cells (qualitative analysis). TEM images with NPs internalization by MDA-MB-231 cancer cells after 3 h treatment with modified and unmodified bare NPs at 50 μg/mL, or vehicle (negative control). From left to right: first image 500×, second image 4000×, third image 15000×. TEM imagens were recorded at an acceleration voltage of 80 kV, representing one of three independent experiments.

the flow cytometry analysis, where cells were treated with fluorescently-labelled NPs. Interestingly, in the flow cytometry analysis, NPs treatment increased side scattered light (SSC) values, meaning that an intensification of cells granularity/complexity was induced (**Annex III, Figure S2**). Indeed, this observation of SSC increase, correlating with NP-cell interactions or internalization, has been reported as a parameter in uptake studies [403]. Setting the fluorescence filters, it was also possible to detect fluorescent NPs interacting with cells, as cells population treated with NPs suffered a clear shift towards higher fluorescence intensities when compared to negative control (**Annex III, Figure S2, S3**), indicating that NPs were taken-up or associated with the cell membranes surface. Nevertheless, no significant increase in uptake/association of modified NPs was detected when compared to unmodified NPs (**Figure 9**). To distinguish the uptake from association, after acquiring data, cells were incubated with trypan blue, which can quench fluorescence of cell membrane-associated NPs, followed by new acquisition (represented in plots with a Q; **Figure 9**). These results indicated that most cells had taken-up the NPs and a small subset was just superficially interacting with NPs.

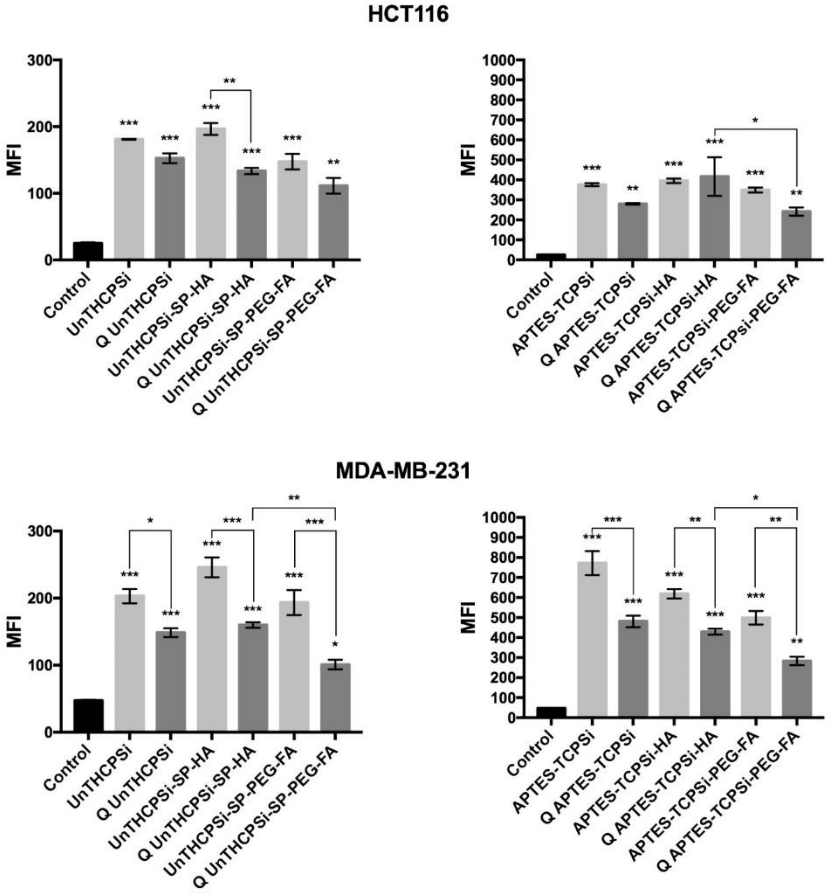

Figure 9. Modified and unmodified NPs are taken-up by human cancer cells (quantitative analysis). Mean fluorescence intensity (MFI) analysis was plotted for each sample of flow

cytometry analysis of HCT116 and MDA-MD-231 cancer cells treated with fluorescent NPs (Alexa488 for UnTHCPSi core; FITC for APTES-TCPSi core) for 3 h, at 50 µg/mL or vehicle as negative control. Non-quenched samples represent association and uptake, and quenched samples (Q; after trypan blue incubation) represent effective uptake. Approximately 10,000 events were acquired per sample. MFI data is presented in mean ± SEM (n=3) and significant differences between means (negative control *vs* NPs treatments) were statistically analyzed by one-way ANOVA and Tukey's multiple comparisons test (**p*<0.05, ***p*<0.01, and ****p*<0.001).

4. Discussion

Herein, PSi-based LEM2 nanodelivery systems were developed to overcome its low solubility to enable further *in vivo* studies. In general, PSi NPs improve the solubility of poorly-water soluble drugs, reduce the pH-dependency of the dissolution process, and the release is generally by simple diffusion and faster than the bulk drug [303].

Freshly produced PSi is reactive due to its surface hydride groups that slowly oxidize when exposed to atmospheric conditions. This phenomenon can lead to physicochemical changes and to undesirable reactions with the payloads [404]. The NPs used in the present work were further stabilized by thermal hydrocarbonization or by thermal carbonization, based on acetylene decomposition at 400–600 ºC or over 600 ºC, respectively. While thermal hydrocarbonization renders –C-H terminated nanoparticles (THCPSi) with hydrophobic properties, thermal carbonized nanoparticles (TCPSi) are slightly more hydrophilic due to the presence of –Si-OH groups [289, 290, 303, 405]. Both THCPSi and TCPSi NPs are suitable for hydrophobic drugs loading [291]. To further facilitate surface functionalization reactions, THCPSi film was treated with Un rendering UnTHCPSi NPs with –COOH terminations, and TCPSi was treated with APTES (APTES-TCPSi) that confers a $-NH_2$-terminated surface [293, 367, 368]. Therefore, UnTHCPSi and APTES-TCPSi NPs were selected as the core to develop the drug delivery systems for LEM2.

Using the EDC/NHS coupling chemistry approach [388], the functionalization of NPs was well-succeeded, with the preparation of UnTHCPsi-SP-PEG-FA, UnTHCPSi-SP-HA, APTES-TCPSi-PEG-FA, and APTES-TCPSi-HA NPs. Once PSi pores are open and easily accessed, LEM2 was loaded into the NPs by immersion, a simple and convenient method, despite the high amount of drug that can be wasted [286, 290]. By this method, drug loading occurs mainly by physical adsorption of the drug molecules by PSi NPs pores surface/functionalization shell. Moreover, PSi NPs can increase water-solubility and dissolution rate of a hydrophobic drug. This is possible due to drug physical adsorption to the pores surface with a restrained volume, avoiding crystalline structure formation and favoring the amorphous state of the drug by physical confinement [291]. Although high LD (%) of payload can be achieved with PSi due to high porosity/pore volume [406], herein the obtained LD (%) were low. This can be attributed to a higher affinity of the compound to the solvent than to the PSi, or to a low concentration of LEM2 in solution. Despite this, it was not possible to obtain higher LD (%) with other solvents, such as DMSO or acetonitrile, in which LEM2 solubility is lower. Another reason to the obtained low LD (%) could be related with the washing step using ethanol to remove the reminiscent excess of LEM2 and DCE, avoiding possible solvent-related cytotoxicity. Also, due to DCE immiscibility in water, if excess of DCE was not removed, it would compromise NPs dispersion in aqueous solution for cancer cells treatment. By the reasons pointed above, we proceeded with the obtained LD (%) for the release and cytotoxicity studies.

The release profile indicated that LEM2 was burst released, in line with PSi NPs without sealed pores [290, 291]. This indicated that modified and unmodified NPs increased the solubility and dissolution rate of LEM2 in aqueous buffers when compared to undetectable amounts of bulk LEM2. When drug release is low, it may be attributable to the retention of a portion of the cargo in PSi NPs by the establishment of stronger interactions between the cargo molecules and the PSi surface, or due to small crystalline nucleus of drug creating pores blockage [407]. APTES-TCPSi and APTES-TCPSi-HA NPs presented low drug release rates. However, this can be associated with problems in drug loading, as the immersion method can have reproducibility problems [286], rather than to the establishment of covalent bonds among LEM2 and APTES-PSi surface. In fact, although LEM2 bears an aldehyde group capable to react with primary amines generating imines, the low release rate was not observed for all NPs. As such, these experiments should be repeated. Of note that the pH showed to be not a critical factor in LEM2 release. Additionally, NPs were found to be stable in cell culture medium, maintaining their dispersity, an important factor for cancer cell treatment.

Consistently to previously described work [408], the NPs herein developed also revealed to be cytocompatible in cancer cells at concentrations lower than 75 µg/mL. Also in line with previous works reporting the cytocompatibility of HA modified NPs [372], herein these NPs revealed to be more cytocompatible than FA modified NPs. This can be probably related to the fact that HA modified NPs detain a more negative ζ-potential. Surprisingly, unmodified UnTHCPSi NPs exhibit lower cell viability than APTES-THCPsi ones. This was an unexpected observation once positive-surface charge is usually related with higher cytotoxicity. Indeed, positive charges are attracted to the negative charge of cell membranes, leading to higher up-take rates, and potentially related with ROS production [409]. In addition, the NPs hydrophobicity also correlates with increased up-take and maybe cytotoxicity [410], possibly justifying the observed slight reduction of cell viability induced by low concentrations of UnTHCPSi compared with APTES-TCPSi. Nevertheless, further studies should be performed to confirm these results. On the contrary, the influence of NPs charge in cell viability at higher concentrations of both NPs cores correlates with a previous study [408].

LEM2-loaded NPs increased LEM2 potency by improving its solubility and delivering it intracellularly, therefore increasing its bioavailability. Indeed, LEM2-loaded NPs decreased cancer cell viability compared to bulk LEM2 at the same tested concentrations, with no NPs-associated cytotoxicity. Although no evident selectivity was observed, the NPs cellular uptake was also confirmed. Cellular membrane FR and CD44 are associated with the selective NPs internalization via ligand-receptor mediated endocytosis [382, 411]. Based on the inexistence of significant differences between HA- or FA-modified and unmodified NPs uptake obtained in this work, it was hypothesized that modified NPs could be internalized by selective and non-selective mechanisms, whereas unmodified NPs would be just internalized by non-selective mechanisms. To answer this question, competitive assays with cancer cells pre-treated with an excess of natural ligands of FR and CD44 should be performed. Nevertheless, the large intracellular vesicles containing NPs and plasma membrane protrusions observed by TEM, as well as the NPs size ranging around 250–350 nm, raised the possibility that the principal NPs cellular internalization process occurring could be macropinocytosis [412]. Further uptake studies should be therefore performed to better elucidate the mechanism of cellular internalization of these NPs in these cancer cells. Also, the chemical content of NPs surface should be analyzed to further understand the rate of NPs functionalization. In fact, the degree of HA- or FA-functionalization could be not appropriate for efficacious targeting [413]. PEG and other cytocompatible polymers have been described as a strategy to overcome macrophages opsonization, therefore increasing the circulation time in blood. Also, PEG could also be responsible for cellular uptake inhibition [414]. Nevertheless, our data indicated that NPs functionalized with PEG were not prevented from being internalized.

Altogether, although all tested PSi NPs improved LEM2 solubility, the HA-functionalization is more appealing because of the higher NPs stability (more negative measured ζ-potential) and cytocompatibility in cancer cells compared to FA-NPs. Among the two used PSi cores, the APTES-TCPSi-HA NPs showed to be more effective in the enhancement of LEM2 antitumor activity.

Nishimori and colleagues studied the *in vivo* safety of silica NPs in mice, reporting that NPs (300 nm) did not elicit a toxic effect at 100 mg/kg [415]. In addition, Tanaka and colleagues showed that also negatively- and positively-charged PSi NPs did not induce *in vivo* toxicity for particles ranging from some hundreds of nanometers to few micrometers

[416]. Nevertheless, due to the low LEM2 LD (%) obtained with the developed nanodelivery systems, it would be needed a large quantity of LEM2-loaded NPs *per* administration in mice, more than it would be feasible considering their safety. Therefore, this reason limits the studies of the antitumor activity of LEM2 in xenograft mice models. As such, although the PSi technology presents many advantages with promising translation into therapy [290], before pursuing *in vivo* studies an optimization to increase the loading degree should be done. For instance, LEM2-PSi NPs could be encapsulated in a polymeric system via microfluidics technology, which has been reported as increasing loading efficiency [370, 417].

Chapter V

General discussion and future perspectives

Despite the continuous progress in cancer research and treatment, millions of people still die annually from this disease. The tumor suppressor protein p53 is frequently mutated and its reactivation represents an encouraging hope in personalized anticancer therapy. Despite this, the clinical use of p53-targeting agents is still not a reality. Interestingly, p53 has been regarded as a non-druggable target due to the lack of evident pockets in its native-like conformation [104] making it not possible to be reactivated. However, such considerations were defied by compounds that form adducts by covalently binding to p53 cysteines causing its reactivation [199, 206, 207]. Also, specific mutp53 forms, namely Y220C, possess a hydrophobic crevice suitable for binding [167, 215-217]. In fact, efforts have been made in the search for druggable p53 regions, leading to the *in silico* identification of two putative binding pockets transiently open, namely in L1/S3 and S6/S7 turn regions in the p53 DBD with the wt-like conformation [223, 266]. These works have defended that those pockets may accommodate small-molecules capable of contributing to the thermodynamic stability of mutp53 and therefore its reactivation [223, 266]. In addition, the possibility to modulate mutp53 activity by interacting with its DBD surface also raised new hopes in designing mutp53 reactivators [220, 222]. A more detailed understanding of the molecular mechanism of reported mutp53 reactivators would be important in order to drive an efficient translation of these compounds into the clinic.

Up to the present thesis, it was demonstrated the ability of SLMP53-1 to restore wt-like function to mutp53 R280K by restoring its DNA-binding ability and subsequent transcriptional activity with promising *in vivo* p53-dependent antitumor activity [226]. These results led us to further investigate the molecular mechanism of action of this potential anticancer drug candidate. The results showed that SLMP53-1 binds to mutp53 R280K, unveiling that the aromatic groups, especially the indole moiety of SLMP53-1, are crucial for its binding to the protein. Further SLMP53-1 may interact to mutp53 R280K DBD positively charged surface regions (**Figure 1 A**), causing the observed protein stabilization, with reestablishment of its DNA-binding ability and transcriptional activity. In fact, this putative binding mode, rooting mutp53 reactivation by SLMP53-1, is supported by other works, which have reported surface transient interactions of peptides and a small-molecule with wt and mutp53, showing also protein thermal stabilization [220, 222]. Collectively, our work suggests a molecular mechanism of mutp53 reactivation non-dependent on covalent bonds or hydrophobic pockets as described for other mutp53 reactivators, such as PRIMA-1^{MET} and the aminobenzothiazole derivative MB725 [215, 216]. Since wt and many mutp53 forms (particularly contact mutants, such as R280K) do not have well-defined pockets to accommodate ligands, this thesis highlights alternatives to the design and development of new mutp53 reactivators.

Furthermore, with this thesis, it was also possible to expand the yeast cell-based assay, previously established for mutp53s R280K and Y220C [226] to other mutp53 forms, namely R175H, G245D, G245S, R248Q, R248W, R273H, and R273C. This gave us the opportunity to demonstrate that SLMP53-1 was capable to reactivate some of the most prevalent mutp53s (R175H, G245D, R248Q, R248W, R273H AND R282W). The corroboration of these results in cancer cell lines ectopically expressing the same mutp53 allowed the validation of the yeast assay as an efficient screening approach to search for new mutp53 reactivator agents (**Figure 1 A**).

Altogether, the advance on the elucidation of SLMP53-1 molecular mechanism of action, as well as the confirmation of its ability to reactivate a broad panel of mutp53 forms greatly reinforce the potential clinical translation of SLMP53-1 as an anticancer drug candidate.

It is known that mutation in R280 residue (R280K) halts the p53 DNA-binding ability and transcriptional activity (LOF) [169]. The contact mutp53 R280K has been also described to acquire GOF with clinical relevance associated with invasive phenotypes [153], and related to interactions with other transcription factors/co-factors, such as sterol regulatory element-binding protein 2 (SREBP-2) and Pin1 [152]. Particularly, mutp53 R280K has been involved in the transcription of SREBP-2 target genes, and of other non-canonical p53 target genes like dual specificity mitogen-activated protein kinase kinase 3 (*MAP2K3*, involved in cell proliferation), histone H3-like centromeric protein A (*CENP-A*, related to chromosomal instability), and more recently reported ectonucleoside triphosphate diphosphohydrolase 5 (*ENTPD5*, promoting cell proliferation and colonization) [152, 153, 418, 419]. Regarding its clinical relevance, mutp53 R280K has been associated with different cancer types, such as bladder, breast, and esophagus cancers (data from IARC TP53 Database, R19 August 2018 [149, 420]). However, despite these data, the structural characterization of mutp53 R280K was still missing. In the present thesis, the recombinant human mutp53 R280K DBD was produced in *E. coli* and its structural model was obtained by X-ray crystallography for the first time. The recombinant production of mutp53 R280K DBD was optimized, rendering a protein suitable for further assays, without demanding a superstable version of the DBD with four stabilizing mutations [93, 162]. Even though the stabilizing mutations were described as not interfering with the overall protein conformation and activity [93, 162], we rather preferred to guarantee that the original tertiary structure and residues interactions stayed closer to what naturally occurs in cellular context. The structural model of mutp53 R280K DBD, and its comparison to free and DNA-bound wtp53 models, allowed to understand that although the lysine side chain is also positively charged under physiological conditions, it does not have a guanidinium group and it is shorter than arginine, making the residue K280 more distant from DNA. Therefore, contrary to R280, the K280 residue is not capable of establishing the two invariant hydrogen bonds to guanine or to enter the extended hydrogen bonding network with other residues and one structural water molecule, which are essential for the correct positioning of residues for DNA interaction. Similarly, such effects were also observed for mutp53s R273H and R273C [92, 167]. These findings allowed us to confirm that the loss of DNA binding by mutp53 R280K is related to its inability to form stabilizing interactions with the DNA bases, rather than to other major structural rearrangements, once mutp53 R280K DBD has a similar conformation to wtp53 (**Figure 1 A**).

Many drugs with anticancer potential fail in their translation to the clinics due to problems related to pharmacokinetics [421, 422]. LEM2 is a new dual inhibitor of MDM2/mup53-TAp73 interactions with interesting *in vitro* antitumor activity, which opens new hopes as an unconventional anticancer therapeutic strategy against cancers lacking p53 or with impaired p53 pathwayS [233]. As others xanthone derivatives [423], LEM2 has limited aqueous solubility, posing problems to pursue *in vivo* assays, and therefore limiting its potential clinical translation. In this thesis, four PSi-based nanodelivery systems were developed, varying the surface core chemical treatment and functionalization for active targeting, which successfully increased LEM2 solubility when compared to bulk drug. Such effect was reflected on the increased LEM2 antitumor activity in cancer cells, particularly with the APTES-TCPSi-HA formulation (**Figure 1 B**). Despite the reduced LEM2 loading degree, which still limits its application in *in vivo* assays, the results herein obtained recognize PSi-based nanodelivery systems as a promising strategy to improve LEM2 antitumor activity and bioavailability.

In conclusion, the results achieved in the present thesis bring new insights on mutp53 structure, biology, and druggability, and boosts the clinical translation of SLMP53-1 for cancer treatment. It is also a valuable starting point for the development of nanodelivery systems for LEM2, which will be relevant for the potential use of this potent TAp73 activator in anticancer therapy.

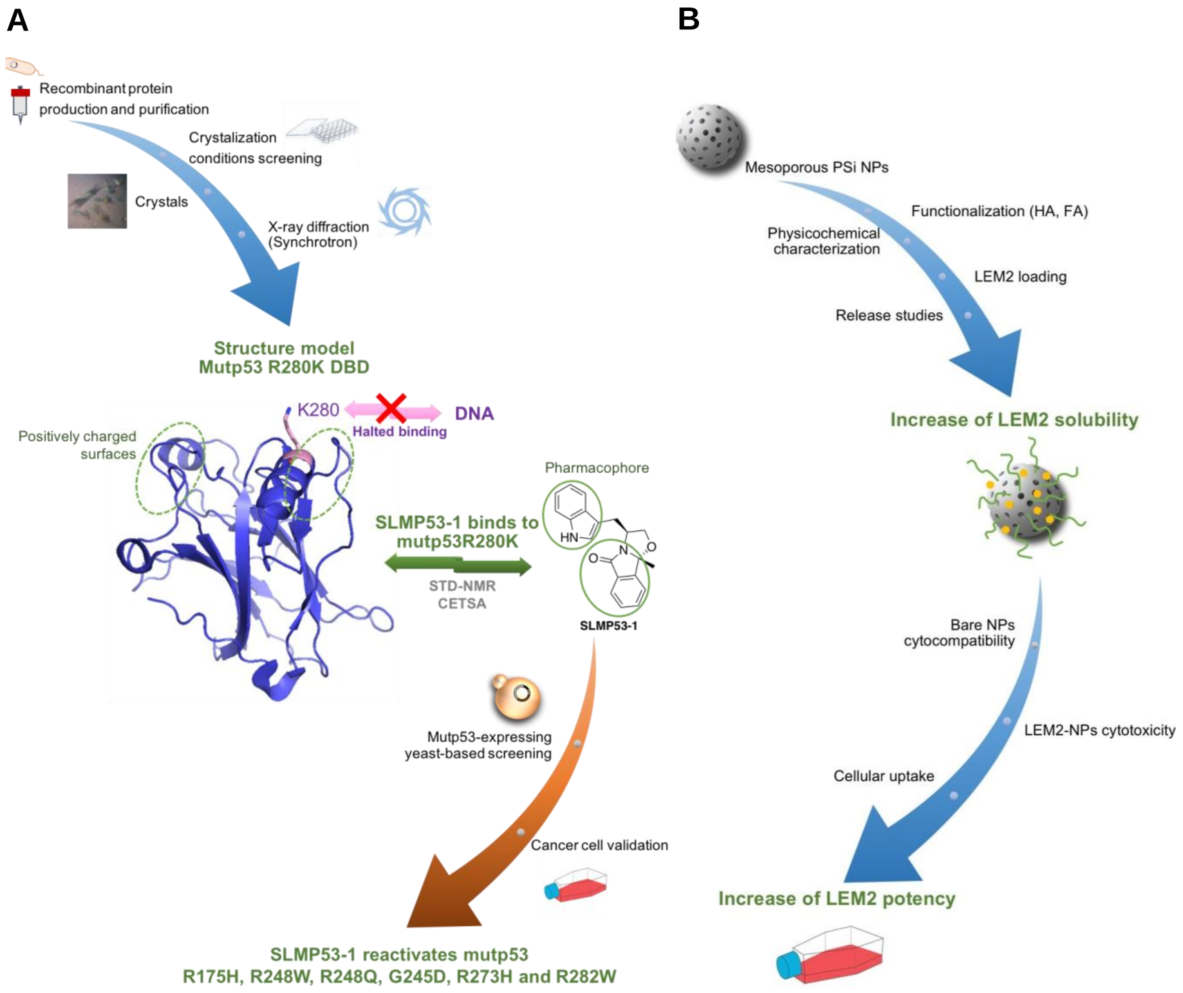
A
Recombinant protein production and purification
Crystalization conditions screening
Crystals
X-ray diffraction (Synchrotron)
Structure model Mutp53 R280K DBD
Positively charged surfaces
K280
DNA
Halted binding
Pharmacophore
SLMP53-1 binds to mutp53R280K
STD-NMR
CETSA
HN
O
N
O
SLMP53-1
Mutp53-expressing yeast-based screening
Cancer cell validation
SLMP53-1 reactivates mutp53 R175H, R248W, R248Q, G245D, R273H and R282W
B
Mesoporous PSi NPs
Functionalization (HA, FA)
Physicochemical characterization
LEM2 loading
Release studies
Increase of LEM2 solubility
Bare NPs cytocompatibility
LEM2-NPs cytotoxicity
Cellular uptake
Increase of LEM2 potency

Figure 1. Schematic representation of the major outcomes achieved in this doctoral thesis. **(A)** Research work aiming the elucidation of: mutp53 R280K DBD structure; molecular mechanism of action underlying mutp53 R280K reactivation by SLMP53-1; and SLMP53-1 capability to reactivate other mutp53 forms (Chapters II and III). **(B)** Research work aiming the development of PSi-based nanodelivery systems to improve LEM2 solubility and potency (Chapter IV). Major outcomes are highlighted in green.

As future perspectives, it would be important to go deeper into the molecular mechanism of action of SLMP53-1, particularly to study the complex compound-DNA-mutp53, to gain knowledge about the exact binding sites of SLMP53-1 to mutp53, binding affinity, and to validate the transient binding hypothesis raised in this thesis. Interestingly, besides mutp53 Y220C [226], SLMP53-1 showed to be also unable to reactivate mutp53s G245S and R273C. Further studies should be performed in order to elucidate the structural and biochemical differences of the mutp53s pairs G245D/S and R273C/H in order to understand the observed selectivity of SLMP53-1 to distinct mutp53 forms. Also, it would be valuable to investigate which mechanisms are involved in mutp53 reactivation by SLMP53-1, since the thermal stabilization is not the common mechanism among the different tested mutp53 forms. Beyond these interesting issues, the knowledge emerged from this thesis will allow the future development of new mutp53 reactivators with improved properties to be considered as anticancer drug candidates.

Concerning the structural elucidation of mutp53, it would be valuable to further understand the structural and functional differences of other mutp53 forms. In particular, the classical categorization of mutp53 in contact and structural forms, and the possibility to reactivate each class by establishing extra contacts to DNA or by increasing thermal stability, respectively [31, 206], seemS to be inadequate with the data obtained from mutp53 reactivators reports. In fact, many mutp53 reactivators are capable to reactivate both contact and structural mutp53 with restoration of DNA binding and transcriptional activity. Some of them have even induced thermal stability of both mutp53 classes and to increase the fraction of wt-like conformation to contact mutp53 forms [111, 194, 197, 207, 220, 222]. Other interesting issues to be further explored would be the mechanism underlying the mutp53 aggregation-prone ability [171, 234, 424, 425], the mutp53 interactome, map potential PTMs on mutp53, and study the impact of small-molecules, like SLMP53-1, in these events. All these studies would greatly contribute for a better understanding about mutp53 pathobiology and pharmacology, galvanizing the discovery and development of new mutp53 targeting agents, and to the subsequent advance of personalized cancer therapy.

Regarding LEM2, the results obtained are encouraging in order to pursue the optimization of the nanodelivery systems to increase the LEM2 cargo or to come up with other alternatives for LEM2 encapsulation, namely the use of microfluidics techniques or the development of nanocrystals [370, 417, 426-428]. Microfluidics may also boost the nanodelivery system translation into the clinics, as it is an advanced method to prepare NPs/nanocomposites with desired physicochemical characteristics in a high-throughput and reproducible manner, when comparing to other manufacturing process [426]. Nanocrystals, have been described as an interesting strategy to increase drug bioavailability, by improving the surface:size ratio and by drug amorphization [427-430]. Additionally, optimization of functionalization methods would contribute to increase the active-targeting and selectivity of cellular internalization. Therefore, the formulation of a suitable nanodelivery system for LEM2, ensuring its aqueous solubility, potency and safety, will certainly prompt its clinical translation.

References

1. IQVIA, Global oncology trends 2018, 2019, [Accessed on April 9th, 2019], Available from: https://www.iqvia.com/institute/reports/global-oncology-trends-2018.
2. Prager, G.W., et al., 2018, Global cancer control: Responding to the growing burden, rising costs and inequalities in access, ESMO Open, 3(2): p. e000285.
3. Bray, F., et al., 2018, Global cancer statistics 2018: Globocan estimates of incidence and mortality worldwide for 36 cancers in 185 countries, CA Cancer J Clin, 68(6): p. 394-424.
4. IARC-GLOBOCAN, Cancer today, 2018, [Accessed on April 9th, 2019], Available from: http://gco.iarc.fr/today/home.
5. IHME, Global burden disease (gbd) 2017 2019, [Accessed on April 9th, 2019], Available from: http://www.healthdata.org/gbd/gbd-2017-resources.
6. James, S.L.A., et al., 2018, Global, regional, and national incidence, prevalence, and years lived with disability for 354 diseases and injuries for 195 countries and territories, 1990–2017: A systematic analysis for the global burden of disease study 2017, The Lancet, 392: p. 1789–1858.
7. IARC-GLOBOCAN, Cancer tomorrow, 2018, [Accessed on April 9th, 2019], Available from: https://gco.iarc.fr/tomorrow/home.
8. CenterWatch, Fda approved drugs for oncology, 2019, [Accessed on April 9th, 2019], Available from: https://www.centerwatch.com/drug-information/fda-approved-drugs/therapeutic-area/12/oncology.
9. Hanahan, D. and Weinberg, R.A., 2011, Hallmarks of cancer: The next generation, Cell, 144(5): p. 646-674.
10. Aschauer, L. and Muller, P.A., 2016, Novel targets and interaction partners of mutant p53 gain-of-function, Biochem Soc Trans, 44(2): p. 460-466.
11. Solomon, H., Madar, S., and Rotter, V., 2011, Mutant p53 gain of function is interwoven into the hallmarks of cancer, J Pathol, 225(4): p. 475-478.
12. COSMIC, Hallmarks of cancer, TP53 [Accessed on April 9th, 2019], Available from: https://cancer.sanger.ac.uk/cosmic/census-page/TP53.
13. Lane, D.P. and Crawford, L.V., 1979, T antigen is bound to a host protein in sv40-transformed cells, Nature, 278(5701): p. 261-263.
14. Linzer, D.I. and Levine, A.J., 1979, Characterization of a 54k dalton cellular sv40 tumor antigen present in sv40-transformed cells and uninfected embryonal carcinoma cells, Cell, 17(1): p. 43-52.
15. Baker, S.J., et al., 1990, P53 gene mutations occur in combination with 17p allelic deletions as late events in colorectal tumorigenesis, Cancer Res, 50(23): p. 7717-7722.
16. Finlay, C.A., Hinds, P.W., and Levine, A.J., 1989, The p53 proto-oncogene can act as a suppressor of transformation, Cell, 57(7): p. 1083-1093.
17. Joerger, A.C. and Fersht, A.R., 2010, The tumor suppressor p53: From structures to drug discovery, Cold Spring Harb Perspect Biol, 2(6): p. a000919.
18. Levine, A.J. and Oren, M., 2009, The first 30 years of p53: Growing ever more complex, Nat Rev Cancer, 9(10): p. 749-758.
19. Sabapathy, K. and Lane, D.P., 2018, Therapeutic targeting of p53: All mutants are equal, but some mutants are more equal than others, Nat Rev Clin Oncol, 15(1): p. 13-30.
20. Collavin, L., Lunardi, A., and Del Sal, G., 2010, P53-family proteins and their regulators: Hubs and spokes in tumor suppression, Cell Death Differ, 17(6): p. 901-911.

21. Joerger, A.C., et al., 2009, Structural evolution of p53, p63, and p73: Implication for heterotetramer formation, Proc Natl Acad Sci U S A, 106(42): p. 17705-17710.

22. Krauskopf, K., et al., 2018, Regulation of the activity in the p53 family depends on the organization of the transactivation domain, Structure, 26(8): p. 1091-1100 e1094.

23. Candi, E., et al., 2014, How the tp53 family proteins tp63 and tp73 contribute to tumorigenesis: Regulators and effectors, Hum Mutat, 35(6): p. 702-714.

24. Muller, M., et al., 2006, One, two, three--p53, p63, p73 and chemosensitivity, Drug Resist Updat, 9(6): p. 288-306.

25. Marcel, V., et al., 2011, Biological functions of p53 isoforms through evolution: Lessons from animal and cellular models, Cell Death Differ, 18(12): p. 1815-1824.

26. Pflaum, J., Schlosser, S., and Muller, M., 2014, P53 family and cellular stress responses in cancer, Front Oncol, 4: p. 285.

27. Vilgelm, A., El-Rifai, W., and Zaika, A., 2008, Therapeutic prospects for p73 and p63: Rising from the shadow of p53, Drug Resist Updat, 11(4-5): p. 152-163.

28. Lane, D.P., 1992, Cancer. P53, guardian of the genome, Nature, 358(6381): p. 15-16.

29. Ischenko, I., et al., 2013, Direct reprogramming by oncogenic ras and myc, Proc Natl Acad Sci U S A, 110(10): p. 3937-3942.

30. Bieging, K.T., Mello, S.S., and Attardi, L.D., 2014, Unravelling mechanisms of p53-mediated tumour suppression, Nat Rev Cancer, 14(5): p. 359-370.

31. Joerger, A.C. and Fersht, A.R., 2016, The p53 pathway: Origins, inactivation in cancer, and emerging therapeutic approaches, Annu Rev Biochem, 85: p. 375-404.

32. Hollander, M.C., et al., 1999, Genomic instability in gadd45a-deficient mice, Nat Genet, 23(2): p. 176-184.

33. Hildesheim, J., et al., 2002, Gadd45a protects against uv irradiation-induced skin tumors, and promotes apoptosis and stress signaling via mapk and p53, Cancer Res, 62(24): p. 7305-7315.

34. Jackson, S.P. and Bartek, J., 2009, The DNA-damage response in human biology and disease, Nature, 461(7267): p. 1071-1078.

35. Hollander, M.C., et al., 2005, Deletion of xpc leads to lung tumors in mice and is associated with early events in human lung carcinogenesis, Proc Natl Acad Sci U S A, 102(37): p. 13200-13205.

36. Melis, J.P., et al., 2008, Mouse models for xeroderma pigmentosum group a and group c show divergent cancer phenotypes, Cancer Res, 68(5): p. 1347-1353.

37. Friedberg, E.C., et al., 2000, Defective nucleotide excision repair in xpc mutant mice and its association with cancer predisposition, Mutat Res, 459(2): p. 99-108.

38. Yoon, T., et al., 2005, Tumor-prone phenotype of the ddb2-deficient mice, Oncogene, 24(3): p. 469-478.

39. Schmitt, C.A., et al., 1999, Ink4a/arf mutations accelerate lymphomagenesis and promote chemoresistance by disabling p53, Genes Dev, 13(20): p. 2670-2677.

40. Eischen, C.M., et al., 1999, Disruption of the arf-mdm2-p53 tumor suppressor pathway in myc-induced lymphomagenesis, Genes Dev, 13(20): p. 2658-2669.

41. Liu, G., et al., 2004, Chromosome stability, in the absence of apoptosis, is critical for suppression of tumorigenesis in trp53 mutant mice, Nat Genet, 36(1): p. 63-68.

42. Barboza, J.A., et al., 2006, P21 delays tumor onset by preservation of chromosomal stability, Proc Natl Acad Sci U S A, 103(52): p. 19842-19847.

43. Eischen, C.M., et al., 2001, Bax loss impairs myc-induced apoptosis and circumvents the selection of p53 mutations during myc-mediated lymphomagenesis*,* Mol Cell Biol, 21(22): p. 7653-7662.

44. Michalak, E.M., et al., 2009, Puma and to a lesser extent noxa are suppressors of myc-induced lymphomagenesis*,* Cell Death Differ, 16(5): p. 684-696.

45. Dansen, T.B., et al., 2006, Specific requirement for bax, not bak, in myc-induced apoptosis and tumor suppression in vivo*,* J Biol Chem, 281(16): p. 10890-10895.

46. Hemann, M.T., et al., 2004, Suppression of tumorigenesis by the p53 target puma*,* Proc Natl Acad Sci U S A, 101(25): p. 9333-9338.

47. Timofeev, O., et al., 2013, P53 DNA binding cooperativity is essential for apoptosis and tumor suppression in vivo*,* Cell Rep, 3(5): p. 1512-1525.

48. Kastenhuber, E.R. and Lowe, S.W., 2017, Putting p53 in context*,* Cell, 170(6): p. 1062-1078.

49. Fischer, M., 2017, Census and evaluation of p53 target genes*,* Oncogene, 36(28): p. 3943-3956.

50. Nguyen, T.T., et al., 2018, Revealing a human p53 universe*,* Nucleic Acids Res, 46(16): p. 8153-8167.

51. Sullivan, K.D., et al., 2018, Mechanisms of transcriptional regulation by p53*,* Cell Death Differ, 25(1): p. 133-143.

52. Follis, A.V., et al., 2014, The DNA-binding domain mediates both nuclear and cytosolic functions of p53*,* Nat Struct Mol Biol, 21(6): p. 535-543.

53. Wang, B., et al., 2010, The p53 response element and transcriptional repression*,* Cell Cycle, 9(5): p. 870-879.

54. Luo, Q., et al., 2017, Dynamics of p53: A master decider of cell fate*,* Genes (Basel), 8(2).

55. Cairns, R.A., Harris, I.S., and Mak, T.W., 2011, Regulation of cancer cell metabolism*,* Nat Rev Cancer, 11(2): p. 85-95.

56. Liu, J., et al., 2015, Tumor suppressor p53 and its mutants in cancer metabolism*,* Cancer Lett, 356(2 Pt A): p. 197-203.

57. Vander Heiden, M.G., Cantley, L.C., and Thompson, C.B., 2009, Understanding the warburg effect: The metabolic requirements of cell proliferation*,* Science, 324(5930): p. 1029-1033.

58. Vousden, K.H. and Ryan, K.M., 2009, P53 and metabolism*,* Nat Rev Cancer, 9(10): p. 691-700.

59. Lu, J., Tan, M., and Cai, Q., 2015, The warburg effect in tumor progression: Mitochondrial oxidative metabolism as an anti-metastasis mechanism*,* Cancer Lett, 356(2 Pt A): p. 156-164.

60. Kawauchi, K., et al., 2008, P53 regulates glucose metabolism through an ikk-nf-kappab pathway and inhibits cell transformation*,* Nat Cell Biol, 10(5): p. 611-618.

61. Schwartzenberg-Bar-Yoseph, F., Armoni, M., and Karnieli, E., 2004, The tumor suppressor p53 down-regulates glucose transporters glut1 and glut4 gene expression*,* Cancer Res, 64(7): p. 2627-2633.

62. Robey, R.B., et al., 2015, Metabolic reprogramming and dysregulated metabolism: Cause, consequence and/or enabler of environmental carcinogenesis?*,* Carcinogenesis, 36 Suppl 1: p. S203-231.

63. Racker, E., 1972, Bioenergetics and the problem of tumor growth*,* Am Sci, 60(1): p. 56-63.

64. Warburg, O., 1930, Notiz uber den stoffwechsel dertumoren*,* Biochem. Zeitschr, 228(1/ 3): p. 257–258.

65. DeBerardinis, R.J., et al., 2008, The biology of cancer: Metabolic reprogramming fuels cell growth and proliferation, Cell Metab, 7(1): p. 11-20.

66. Gatenby, R.A. and Gawlinski, E.T., 2003, The glycolytic phenotype in carcinogenesis and tumor invasion: Insights through mathematical models, Cancer Res, 63(14): p. 3847-3854.

67. Hsu, P.P. and Sabatini, D.M., 2008, Cancer cell metabolism: Warburg and beyond, Cell, 134(5): p. 703-707.

68. Warburg, O., 1956, On the origin of cancer cells, Science, 123(3191): p. 309-314.

69. Zawacka-Pankau, J., et al., 2011, Inhibition of glycolytic enzymes mediated by pharmacologically activated p53: Targeting warburg effect to fight cancer, J Biol Chem, 286(48): p. 41600-41615.

70. Matoba, S., et al., 2006, P53 regulates mitochondrial respiration, Science, 312(5780): p. 1650-1653.

71. Andersen, J.L. and Kornbluth, S., 2013, The tangled circuitry of metabolism and apoptosis, Mol Cell, 49(3): p. 399-410.

72. Kitamura, N., et al., 2011, Mieap, a p53-inducible protein, controls mitochondrial quality by repairing or eliminating unhealthy mitochondria, PLoS One, 6(1): p. e16060.

73. Lebedeva, M.A., Eaton, J.S., and Shadel, G.S., 2009, Loss of p53 causes mitochondrial DNA depletion and altered mitochondrial reactive oxygen species homeostasis, Biochim Biophys Acta, 1787(5): p. 328-334.

74. Zhan, T., et al., 2011, Silybin and dehydrosilybin decrease glucose uptake by inhibiting glut proteins, J Cell Biochem, 112(3): p. 849-859.

75. Sols, A. and Crane, R.K., 1954, Substrate specificity of brain hexokinase, J Biol Chem, 210(2): p. 581-595.

76. Salani, B., et al., 2013, Metformin impairs glucose consumption and survival in calu-1 cells by direct inhibition of hexokinase-ii, Sci Rep, 3: p. 2070.

77. Wheaton, W.W., et al., 2014, Metformin inhibits mitochondrial complex i of cancer cells to reduce tumorigenesis, Elife, 3: p. e02242.

78. Bonnet, S., et al., 2007, A mitochondria-k+ channel axis is suppressed in cancer and its normalization promotes apoptosis and inhibits cancer growth, Cancer Cell, 11(1): p. 37-51.

79. Zhang, X., et al., 2014, Induction of mitochondrial dysfunction as a strategy for targeting tumour cells in metabolically compromised microenvironments, Nat Commun, 5: p. 3295.

80. Ben Sahra, I., et al., 2010, Targeting cancer cell metabolism: The combination of metformin and 2-deoxyglucose induces p53-dependent apoptosis in prostate cancer cells, Cancer Res, 70(6): p. 2465-2475.

81. Sinthupibulyakit, C., et al., 2009, P53 is an important factor for the radiosensitization effect of 2-deoxy-d-glucose, Int J Oncol, 35(3): p. 609-615.

82. Ahmad, I.M., et al., 2008, 2-deoxyglucose combined with wild-type p53 overexpression enhances cytotoxicity in human prostate cancer cells via oxidative stress, Free Radic Biol Med, 44(5): p. 826-834.

83. Agnoletto, C., et al., 2015, The anti-leukemic activity of sodium dichloroacetate in p53mutated/null cells is mediated by a p53-independent ilf3/p21 pathway, Oncotarget, 6(4): p. 2385-2396.

84. Allende-Vega, N., et al., 2015, The presence of wild type p53 in hematological cancers improves the efficacy of combinational therapy targeting metabolism, Oncotarget, 6(22): p. 19228-19245.

85. Huang, F., et al., 2009, Multiple conformations of full-length p53 detected with single-molecule fluorescence resonance energy transfer, Proc Natl Acad Sci U S A, 106(49): p. 20758-20763.

86. Tidow, H., et al., 2007, Quaternary structures of tumor suppressor p53 and a specific p53 DNA complex, Proc Natl Acad Sci U S A, 104(30): p. 12324-12329.

87. Bullock, A.N., et al., 1997, Thermodynamic stability of wild-type and mutant p53 core domain, Proc Natl Acad Sci U S A, 94(26): p. 14338-14342.

88. Bullock, A.N., Henckel, J., and Fersht, A.R., 2000, Quantitative analysis of residual folding and DNA binding in mutant p53 core domain: Definition of mutant states for rescue in cancer therapy, Oncogene, 19(10): p. 1245-1256.

89. Lubin, D.J., Butler, J.S., and Loh, S.N., 2010, Folding of tetrameric p53: Oligomerization and tumorigenic mutations induce misfolding and loss of function, J Mol Biol, 395(4): p. 705-716.

90. Tidow, H., et al., 2006, Effects of oncogenic mutations and DNA response elements on the binding of p53 to p53-binding protein 2 (53bp2), J Biol Chem, 281(43): p. 32526-32533.

91. Ahn, J.H., et al., 2017, Mutant p53 stimulates cell invasion through an interaction with rad21 in human ovarian cancer cells, Sci Rep, 7(1): p. 9076.

92. Eldar, A., et al., 2013, Structural studies of p53 inactivation by DNA-contact mutations and its rescue by suppressor mutations via alternative protein-DNA interactions, Nucleic Acids Res, 41(18): p. 8748-8759.

93. Nikolova, P.V., et al., 1998, Semirational design of active tumor suppressor p53 DNA binding domain with enhanced stability, Proc Natl Acad Sci U S A, 95(25): p. 14675-14680.

94. Suad, O., et al., 2009, Structural basis of restoring sequence-specific DNA binding and transactivation to mutant p53 by suppressor mutations, J Mol Biol, 385(1): p. 249-265.

95. Melero, R., et al., 2011, Electron microscopy studies on the quaternary structure of p53 reveal different binding modes for p53 tetramers in complex with DNA, Proc Natl Acad Sci U S A, 108(2): p. 557-562.

96. Wells, M., et al., 2008, Structure of tumor suppressor p53 and its intrinsically disordered n-terminal transactivation domain, Proc Natl Acad Sci U S A, 105(15): p. 5762-5767.

97. Weinberg, R.L., Veprintsev, D.B., and Fersht, A.R., 2004, Cooperative binding of tetrameric p53 to DNA, J Mol Biol, 341(5): p. 1145-1159.

98. Nicholls, C.D., et al., 2002, Biogenesis of p53 involves cotranslational dimerization of monomers and posttranslational dimerization of dimers. Implications on the dominant negative effect, J Biol Chem, 277(15): p. 12937-12945.

99. Kitayner, M., et al., 2006, Structural basis of DNA recognition by p53 tetramers, Mol Cell, 22(6): p. 741-753.

100. Tebaldi, T., et al., 2015, Whole-genome cartography of p53 response elements ranked on transactivation potential, BMC Genomics, 16: p. 464.

101. el-Deiry, W.S., et al., 1992, Definition of a consensus binding site for p53, Nat Genet, 1(1): p. 45-49.

102. Funk, W.D., et al., 1992, A transcriptionally active DNA-binding site for human p53 protein complexes, Mol Cell Biol, 12(6): p. 2866-2871.

103. Jordan, J.J., et al., 2008, Noncanonical DNA motifs as transactivation targets by wild type and mutant p53, PLoS Genet, 4(6): p. e1000104.

104. Cho, Y., et al., 1994, Crystal structure of a p53 tumor suppressor-DNA complex: Understanding tumorigenic mutations, Science, 265(5170): p. 346-355.

105. DeLano, W., 2002, Pymol: An open-source molecular graphics tool, CCP4 Newsletter on Protein Crystallography, 40: p. 82–92.

106. Wright, J.D., Noskov, S.Y., and Lim, C., 2002, Factors governing loss and rescue of DNA binding upon single and double mutations in the p53 core domain, Nucleic Acids Res, 30(7): p. 1563-1574.

107. Joerger, A.C. and Fersht, A.R., 2007, Structure-function-rescue: The diverse nature of common p53 cancer mutants, Oncogene, 26(15): p. 2226-2242.

108. Ho, W.C., Fitzgerald, M.X., and Marmorstein, R., 2006, Structure of the p53 core domain dimer bound to DNA, J Biol Chem, 281(29): p. 20494-20502.

109. Kantarci, N., Doruker, P., and Haliloglu, T., 2006, Cooperative fluctuations point to the dimerization interface of p53 core domain, Biophys J, 91(2): p. 421-432.

110. Ang, H.C., et al., 2006, Effects of common cancer mutations on stability and DNA binding of full-length p53 compared with isolated core domains, J Biol Chem, 281(31): p. 21934-21941.

111. Friedler, A., et al., 2003, Kinetic instability of p53 core domain mutants: Implications for rescue by small molecules, J Biol Chem, 278(26): p. 24108-24112.

112. Fernandez-Fernandez, M.R. and Sot, B., 2011, The relevance of protein-protein interactions for p53 function: The cpe contribution, Protein Eng Des Sel, 24(1-2): p. 41-51.

113. Walerych, D., et al., 2010, Atp binding to hsp90 is sufficient for effective chaperoning of p53 protein, J Biol Chem, 285(42): p. 32020-32028.

114. Walerych, D., et al., 2009, Hsp70 molecular chaperones are required to support p53 tumor suppressor activity under stress conditions, Oncogene, 28(48): p. 4284-4294.

115. Wawrzynow, B., Zylicz, A., and Zylicz, M., 2018, Chaperoning the guardian of the genome. The two-faced role of molecular chaperones in p53 tumor suppressor action, Biochim Biophys Acta Rev Cancer, 1869(2): p. 161-174.

116. Harris, S.L. and Levine, A.J., 2005, The p53 pathway: Positive and negative feedback loops, Oncogene, 24(17): p. 2899-2908.

117. Lev Bar-Or, R., et al., 2000, Generation of oscillations by the p53-mdm2 feedback loop: A theoretical and experimental study, Proc Natl Acad Sci U S A, 97(21): p. 11250-11255.

118. Espinosa, J.M., Verdun, R.E., and Emerson, B.M., 2003, P53 functions through stress- and promoter-specific recruitment of transcription initiation components before and after DNA damage, Mol Cell, 12(4): p. 1015-1027.

119. Morachis, J.M., Murawsky, C.M., and Emerson, B.M., 2010, Regulation of the p53 transcriptional response by structurally diverse core promoters, Genes Dev, 24(2): p. 135-147.

120. Kruse, J.P. and Gu, W., 2009, Modes of p53 regulation, Cell, 137(4): p. 609-622.

121. Maclaine, N.J. and Hupp, T.R., 2009, The regulation of p53 by phosphorylation: A model for how distinct signals integrate into the p53 pathway, Aging (Albany NY), 1(5): p. 490-502.

122. Raj, N. and Attardi, L.D., 2017, The transactivation domains of the p53 protein, Cold Spring Harb Perspect Med, 7(1).

123. Lee, H., et al., 2000, Local structural elements in the mostly unstructured transcriptional activation domain of human p53, J Biol Chem, 275(38): p. 29426-29432.

124. Kussie, P.H., et al., 1996, Structure of the mdm2 oncoprotein bound to the p53 tumor suppressor transactivation domain, Science, 274(5289): p. 948-953.

125. Botuyan, M.V., Momand, J., and Chen, Y., 1997, Solution conformation of an essential region of the p53 transactivation domain, Fold Des, 2(6): p. 331-342.

126. Feng, H., et al., 2009, Structural basis for p300 taz2-p53 tad1 binding and modulation by phosphorylation, Structure, 17(2): p. 202-210.

127. Bochkareva, E., et al., 2005, Single-stranded DNA mimicry in the p53 transactivation domain interaction with replication protein a, Proc Natl Acad Sci U S A, 102(43): p. 15412-15417.

128. Gsponer, J. and Babu, M.M., 2009, The rules of disorder or why disorder rules, Prog Biophys Mol Biol, 99(2-3): p. 94-103.

129. Liu, J., et al., 2006, Intrinsic disorder in transcription factors, Biochemistry, 45(22): p. 6873-6888.

130. Mohan, A., et al., 2006, Analysis of molecular recognition features (morfs), J Mol Biol, 362(5): p. 1043-1059.

131. Kumari, R., Kohli, S., and Das, S., 2014, P53 regulation upon genotoxic stress: Intricacies and complexities, Mol Cell Oncol, 1(3): p. e969653.

132. Reed, S.M. and Quelle, D.E., 2014, P53 acetylation: Regulation and consequences, Cancers (Basel), 7(1): p. 30-69.

133. West, L.E. and Gozani, O., 2011, Regulation of p53 function by lysine methylation, Epigenomics, 3(3): p. 361-369.

134. Mateu, M.G. and Fersht, A.R., 1998, Nine hydrophobic side chains are key determinants of the thermodynamic stability and oligomerization status of tumour suppressor p53 tetramerization domain, EMBO J, 17(10): p. 2748-2758.

135. Mora, P., et al., 2008, Solvent-exposed residues located in the beta-sheet modulate the stability of the tetramerization domain of p53--a structural and combinatorial approach, Proteins, 71(4): p. 1670-1685.

136. Stommel, J.M., et al., 1999, A leucine-rich nuclear export signal in the p53 tetramerization domain: Regulation of subcellular localization and p53 activity by nes masking, EMBO J, 18(6): p. 1660-1672.

137. Nie, L., Sasaki, M., and Maki, C.G., 2007, Regulation of p53 nuclear export through sequential changes in conformation and ubiquitination, J Biol Chem, 282(19): p. 14616-14625.

138. Carter, S., et al., 2007, C-terminal modifications regulate mdm2 dissociation and nuclear export of p53, Nat Cell Biol, 9(4): p. 428-435.

139. Green, D.R. and Kroemer, G., 2009, Cytoplasmic functions of the tumour suppressor p53, Nature, 458(7242): p. 1127-1130.

140. Li, M., et al., 2003, Mono- versus polyubiquitination: Differential control of p53 fate by mdm2, Science, 302(5652): p. 1972-1975.

141. Tavana, O. and Gu, W., 2017, Modulation of the p53/mdm2 interplay by hausp inhibitors, J Mol Cell Biol, 9(1): p. 45-52.

142. Yuan, J., et al., 2010, Usp10 regulates p53 localization and stability by deubiquitinating p53, Cell, 140(3): p. 384-396.

143. Hock, A.K., Vigneron, A.M., and Vousden, K.H., 2014, Ubiquitin-specific peptidase 42 (usp42) functions to deubiquitylate histones and regulate transcriptional activity, J Biol Chem, 289(50): p. 34862-34870.

144. van Dieck, J., et al., 2009, Modulation of the oligomerization state of p53 by differential binding of proteins of the s100 family to p53 monomers and tetramers, J Biol Chem, 284(20): p. 13804-13811.

145. Fernandez-Fernandez, M.R., Rutherford, T.J., and Fersht, A.R., 2008, Members of the s100 family bind p53 in two distinct ways, Protein Sci, 17(10): p. 1663-1670.

146. Rajagopalan, S., et al., 2008, 14-3-3 activation of DNA binding of p53 by enhancing its association into tetramers, Nucleic Acids Res, 36(18): p. 5983-5991.

147. Katz, C., et al., 2018, Wild-type and cancer-related p53 proteins are preferentially degraded by mdm2 as dimers rather than tetramers, Genes Dev, 32(5-6): p. 430-447.

148. Gu, B. and Zhu, W.G., 2012, Surf the post-translational modification network of p53 regulation, Int J Biol Sci, 8(5): p. 672-684.

149. Bouaoun, L., et al., 2016, Tp53 variations in human cancers: New lessons from the iarc tp53 database and genomics data, Hum Mutat, 37(9): p. 865-876.

150. Petitjean, A., et al., 2007, Impact of mutant p53 functional properties on tp53 mutation patterns and tumor phenotype: Lessons from recent developments in the iarc tp53 database, Hum Mutat, 28(6): p. 622-629.

151. Kim, M.P. and Lozano, G., 2018, Mutant p53 partners in crime, Cell Death Differ, 25(1): p. 161-168.

152. Freed-Pastor, W.A. and Prives, C., 2012, Mutant p53: One name, many proteins, Genes Dev, 26(12): p. 1268-1286.

153. Muller, P.A. and Vousden, K.H., 2014, Mutant p53 in cancer: New functions and therapeutic opportunities, Cancer Cell, 25(3): p. 304-317.

154. Garritano, S., et al., 2013, More targets, more pathways and more clues for mutant p53, Oncogenesis, 2: p. e54.

155. Walerych, D., Lisek, K., and Del Sal, G., 2015, Mutant p53: One, no one, and one hundred thousand, Front Oncol, 5: p. 289.

156. Prives, C. and White, E., 2008, Does control of mutant p53 by mdm2 complicate cancer therapy?, Genes Dev, 22(10): p. 1259-1264.

157. Manfredi, J.J., 2010, The mdm2-p53 relationship evolves: Mdm2 swings both ways as an oncogene and a tumor suppressor, Genes Dev, 24(15): p. 1580-1589.

158. Lang, G.A., et al., 2004, Gain of function of a p53 hot spot mutation in a mouse model of li-fraumeni syndrome, Cell, 119(6): p. 861-872.

159. Xu, J., et al., 2011, Gain of function of mutant p53 by coaggregation with multiple tumor suppressors, Nat Chem Biol, 7(5): p. 285-295.

160. Ano Bom, A.P., et al., 2012, Mutant p53 aggregates into prion-like amyloid oligomers and fibrils: Implications for cancer, J Biol Chem, 287(33): p. 28152-28162.

161. Wang, G. and Fersht, A.R., 2017, Multisite aggregation of p53 and implications for drug rescue, Proc Natl Acad Sci U S A, 114(13): p. E2634-E2643.

162. Joerger, A.C., Allen, M.D., and Fersht, A.R., 2004, Crystal structure of a superstable mutant of human p53 core domain. Insights into the mechanism of rescuing oncogenic mutations, J Biol Chem, 279(2): p. 1291-1296.

163. Soussi, T. and May, P., 1996, Structural aspects of the p53 protein in relation to gene evolution: A second look, J Mol Biol, 260(5): p. 623-637.

164. Walker, D.R., et al., 1999, Evolutionary conservation and somatic mutation hotspot maps of p53: Correlation with p53 protein structural and functional features, Oncogene, 18(1): p. 211-218.

165. Wong, K.B., et al., 1999, Hot-spot mutants of p53 core domain evince characteristic local structural changes, Proc Natl Acad Sci U S A, 96(15): p. 8438-8442.

166. Ng, J.W., et al., 2015, R248q mutation--beyond p53-DNA binding, Proteins, 83(12): p. 2240-2250.

167. Joerger, A.C., et al., 2005, Structures of p53 cancer mutants and mechanism of rescue by second-site suppressor mutations, J Biol Chem, 280(16): p. 16030-16037.

168. Joerger, A.C., Ang, H.C., and Fersht, A.R., 2006, Structural basis for understanding oncogenic p53 mutations and designing rescue drugs, Proc Natl Acad Sci U S A, 103(41): p. 15056-15061.

169. Malcikova, J., et al., 2010, Analysis of the DNA-binding activity of p53 mutants using functional protein microarrays and its relationship to transcriptional activation, Biol Chem, 391(2-3): p. 197-205.

170. Friedler, A., et al., 2004, Structural distortion of p53 by the mutation r249s and its rescue by a designed peptide: Implications for "mutant conformation", J Mol Biol, 336(1): p. 187-196.

171. Zhang, Y., et al., 2016, Gain of function of mutant p53: R282w on the peak?, Oncogenesis, 5: p. e196.

172. Dearth, L.R., et al., 2007, Inactive full-length p53 mutants lacking dominant wild-type p53 inhibition highlight loss of heterozygosity as an important aspect of p53 status in human cancers, Carcinogenesis, 28(2): p. 289-298.

173. Ryan, K.M. and Vousden, K.H., 1998, Characterization of structural p53 mutants which show selective defects in apoptosis but not cell cycle arrest, Mol Cell Biol, 18(7): p. 3692-3698.

174. Wang, Y., Rosengarth, A., and Luecke, H., 2007, Structure of the human p53 core domain in the absence of DNA, Acta Crystallogr D Biol Crystallogr, 63(Pt 3): p. 276-281.

175. Pintus, S.S., et al., 2013, The substitutions g245c and g245d in the zn(2+)-binding pocket of the p53 protein result in differences of conformational flexibility of the DNA-binding domain, J Biomol Struct Dyn, 31(1): p. 78-86.

176. Tu, C., et al., 2008, Impact of low-frequency hotspot mutation r282q on the structure of p53 DNA-binding domain as revealed by crystallography at 1.54 angstroms resolution, Acta Crystallogr D Biol Crystallogr, 64(Pt 5): p. 471-477.

177. Wallentine, B.D., et al., 2013, Structures of oncogenic, suppressor and rescued p53 core-domain variants: Mechanisms of mutant p53 rescue, Acta Crystallogr D Biol Crystallogr, 69(Pt 10): p. 2146-2156.

178. Aramayo, R., et al., 2011, Quaternary structure of the specific p53-DNA complex reveals the mechanism of p53 mutant dominance, Nucleic Acids Res, 39(20): p. 8960-8971.

179. Yamamoto, S. and Iwakuma, T., 2018, Regulators of oncogenic mutant tp53 gain of function, Cancers (Basel), 11(1).

180. Bykov, V.J.N., et al., 2018, Targeting mutant p53 for efficient cancer therapy, Nat Rev Cancer, 18(2): p. 89-102.

181. Baroni, T.E., et al., 2004, A global suppressor motif for p53 cancer mutants, Proc Natl Acad Sci U S A, 101(14): p. 4930-4935.

182. Brachmann, R.K., et al., 1998, Genetic selection of intragenic suppressor mutations that reverse the effect of common p53 cancer mutations, EMBO J, 17(7): p. 1847-1859.

183. Nikolova, P.V., et al., 2000, Mechanism of rescue of common p53 cancer mutations by second-site suppressor mutations, EMBO J, 19(3): p. 370-378.

184. Brosh, R. and Rotter, V., 2009, When mutants gain new powers: News from the mutant p53 field, Nat Rev Cancer, 9(10): p. 701-713.

185. Terzian, T., et al., 2008, The inherent instability of mutant p53 is alleviated by mdm2 or p16ink4a loss, Genes Dev, 22(10): p. 1337-1344.

186. Parrales, A. and Iwakuma, T., 2015, Targeting oncogenic mutant p53 for cancer therapy, Front Oncol, 5: p. 288.

187. NIH-ClinicalTrials, Safety study of apr-246 in patients with refractory hematologic cancer or prostate cancer, 2019, [Accessed on April 11th, 2019], Available from: https://www.clinicaltrials.gov/ct2/show/NCT00900614.

188. NIH-ClinicalTrials, P53 suppressor activation in recurrent high grade serous ovarian cancer, a phase ib/ii study of systemic carboplatin combination chemotherapy with or without apr-246, 2019, [Accessed on April 11th , 2019], Available from: https://www.clinicaltrials.gov/ct2/show/NCT02098343.

189. NIH-ClinicalTrials, Study of coti-2 as monotherapy or combination therapy for the treatment of malignancies (coti2-101), 2019, [Accessed on April 11th, 2019], Available from: https://www.clinicaltrials.gov/ct2/show/NCT02433626.

190. Foster, B.A., et al., 1999, Pharmacological rescue of mutant p53 conformation and function, Science, 286(5449): p. 2507-2510.

191. Madka, V., et al., 2013, P53-stabilizing agent cp-31398 prevents growth and invasion of urothelial cancer of the bladder in transgenic upii-sv40t mice, Neoplasia, 15(8): p. 966-974.

192. Rippin, T.M., et al., 2002, Characterization of the p53-rescue drug cp-31398 in vitro and in living cells, Oncogene, 21(14): p. 2119-2129.

193. Zache, N., et al., 2008, Mutant p53 targeting by the low molecular weight compound stima-1, Mol Oncol, 2(1): p. 70-80.

194. Bykov, V.J., et al., 2005, Reactivation of mutant p53 and induction of apoptosis in human tumor cells by maleimide analogs, J Biol Chem, 280(34): p. 30384-30391.

195. Punganuru, S.R., et al., 2016, Design and synthesis of a c7-aryl piperlongumine derivative with potent antimicrotubule and mutant p53-reactivating properties, Eur J Med Chem, 107: p. 233-244.

196. Bykov, V.J., et al., 2002, Mutant p53-dependent growth suppression distinguishes prima-1 from known anticancer drugs: A statistical analysis of information in the national cancer institute database, Carcinogenesis, 23(12): p. 2011-2018.

197. Bykov, V.J., et al., 2002, Restoration of the tumor suppressor function to mutant p53 by a low-molecular-weight compound, Nat Med, 8(3): p. 282-288.

198. Bykov, V.J., et al., 2005, Prima-1(met) synergizes with cisplatin to induce tumor cell apoptosis, Oncogene, 24(21): p. 3484-3491.

199. Lambert, J.M., et al., 2009, Prima-1 reactivates mutant p53 by covalent binding to the core domain, Cancer Cell, 15(5): p. 376-388.

200. Lambert, J.M., et al., 2010, Mutant p53 reactivation by prima-1met induces multiple signaling pathways converging on apoptosis, Oncogene, 29(9): p. 1329-1338.

201. Messina, R.L., et al., 2012, Reactivation of p53 mutants by prima-1 [corrected] in thyroid cancer cells, Int J Cancer, 130(10): p. 2259-2270.

202. Aryee, D.N., et al., 2013, Variability in functional p53 reactivation by prima-1(met)/apr-246 in ewing sarcoma, Br J Cancer, 109(10): p. 2696-2704.

203. Li, X.L., et al., 2015, Prima-1met (apr-246) inhibits growth of colorectal cancer cells with different p53 status through distinct mechanisms, Oncotarget, 6(34): p. 36689-36699.

204. Zhang, W., et al., 2016, Silencing of cd24 enhances the prima-1-induced restoration of mutant p53 in prostate cancer cells, Clin Cancer Res, 22(10): p. 2545-2554.

205. Zhang, Q., et al., 2018, Apr-246 reactivates mutant p53 by targeting cysteines 124 and 277, Cell Death Dis, 9(5): p. 439.

206. Bauer, M.R., Joerger, A.C., and Fersht, A.R., 2016, 2-sulfonylpyrimidines: Mild alkylating agents with anticancer activity toward p53-compromised cells, Proc Natl Acad Sci U S A, 113(36): p. E5271-5280.

207. Madan, E., et al., 2018, The curcumin analog ho-3867 selectively kills cancer cells by converting mutant p53 protein to transcriptionally active wildtype p53, J Biol Chem, 293(12): p. 4262-4276.

208. Selvendiran, K., et al., 2010, Safe and targeted anticancer efficacy of a novel class of antioxidant-conjugated difluorodiarylidenyl piperidones: Differential cytotoxicity in healthy and cancer cells, Free Radic Biol Med, 48(9): p. 1228-1235.

209. Kaar, J.L., et al., 2010, Stabilization of mutant p53 via alkylation of cysteines and effects on DNA binding, Protein Sci, 19(12): p. 2267-2278.

210. Yu, X., et al., 2012, Allele-specific p53 mutant reactivation, Cancer Cell, 21(5): p. 614-625.

211. Yu, X., et al., 2014, Small molecule restoration of wildtype structure and function of mutant p53 using a novel zinc-metallochaperone based mechanism, Oncotarget, 5(19): p. 8879-8892.

212. Silver, N.L.O., A. A.; Patel, A. A.; Tanaka, N.; Tang, L.; Zhou, G.; Myers, J. N., 2016, A novel third generation thiosemicarbazone, coti-2, is highly effective in killing head and neck squamous cell carcinomas (hnscc) bearing a variety of tp53 mutations, International Journal of Radiation Oncology: p. 942.

213. Salim, K.Y.V., S. M.; Danter, W. R.; Koropatnick, J. , 2016, Coti-2, a new anticancer drug currently under clinical investigation, targets mutant p53 and negatively modulates the pi3k/akt/mtor pathway, Eur. J. Cancer, 69(S9).

214. Salim, K.Y., et al., 2016, Coti-2, a novel small molecule that is active against multiple human cancer cell lines in vitro and in vivo, Oncotarget, 7(27): p. 41363-41379.

215. Boeckler, F.M., et al., 2008, Targeted rescue of a destabilized mutant of p53 by an in silico screened drug, Proc Natl Acad Sci U S A, 105(30): p. 10360-10365.

216. Baud, M.G.J., et al., 2018, Aminobenzothiazole derivatives stabilize the thermolabile p53 cancer mutant y220c and show anticancer activity in p53-y220c cell lines, Eur J Med Chem, 152: p. 101-114.

217. Liu, X., et al., 2013, Small molecule induced reactivation of mutant p53 in cancer cells, Nucleic Acids Res, 41(12): p. 6034-6044.

218. Wilcken, R., et al., 2012, Halogen-enriched fragment libraries as leads for drug rescue of mutant p53, J Am Chem Soc, 134(15): p. 6810-6818.

219. Tal, P., et al., 2016, Cancer therapeutic approach based on conformational stabilization of mutant p53 protein by small peptides, Oncotarget, 7(11): p. 11817-11837.

220. Friedler, A., et al., 2002, A peptide that binds and stabilizes p53 core domain: Chaperone strategy for rescue of oncogenic mutants, Proc Natl Acad Sci U S A, 99(2): p. 937-942.

221. Issaeva, N., et al., 2003, Rescue of mutants of the tumor suppressor p53 in cancer cells by a designed peptide, Proc Natl Acad Sci U S A, 100(23): p. 13303-13307.

222. Demma, M., et al., 2010, Sch529074, a small molecule activator of mutant p53, which binds p53 DNA binding domain (dbd), restores growth-suppressive function to mutant p53 and interrupts hdm2-mediated ubiquitination of wild type p53, J Biol Chem, 285(14): p. 10198-10212.

223. Wassman, C.D., et al., 2013, Computational identification of a transiently open l1/s3 pocket for reactivation of mutant p53, Nat Commun, 4: p. 1407.

224. Malami, I., et al., 2017, An in silico approach in predicting the possible mechanism involving restoration of wild-type p53 functions by small molecular weight compounds in tumor cells expressing r273h mutant p53, EXCLI J, 16: p. 1276-1287.

225. Hiraki, M., et al., 2015, Small-molecule reactivation of mutant p53 to wild-type-like p53 through the p53-hsp40 regulatory axis, Chem Biol, 22(9): p. 1206-1216.

226. Soares, J., et al., 2016, Reactivation of wild-type and mutant p53 by tryptophanolderived oxazoloisoindolinone slmp53-1, a novel anticancer small-molecule, Oncotarget, 7(4): p. 4326-4343.

227. Peng, Y., et al., 2003, Rescue of mutant p53 transcription function by ellipticine, Oncogene, 22(29): p. 4478-4487.

228. Weinmann, L., et al., 2008, A novel p53 rescue compound induces p53-dependent growth arrest and sensitises glioma cells to apo2l/trail-induced apoptosis, Cell Death Differ, 15(4): p. 718-729.

229. Aggarwal, M., et al., 2016, Reactivation of mutant p53 by a dietary-related compound phenethyl isothiocyanate inhibits tumor growth, Cell Death Differ, 23(10): p. 1615-1627.

230. North, S., et al., 2002, Restoration of wild-type conformation and activity of a temperature-sensitive mutant of p53 (p53(v272m)) by the cytoprotective aminothiol wr1065 in the esophageal cancer cell line te-1, Mol Carcinog, 33(3): p. 181-188.

231. Kravchenko, J.E., et al., 2008, Small-molecule retra suppresses mutant p53-bearing cancer cells through a p73-dependent salvage pathway, Proc Natl Acad Sci U S A, 105(17): p. 6302-6307.

232. Hong, B., et al., 2014, Prodigiosin rescues deficient p53 signaling and antitumor effects via upregulating p73 and disrupting its interaction with mutant p53, Cancer Res, 74(4): p. 1153-1165.

233. Gomes, S., et al., 2019, New inhibitor of the tap73 interaction with mdm2 and mutant p53 with promising antitumor activity against neuroblastoma, Cancer Lett, 446: p. 90-102.

234. Soragni, A., et al., 2016, A designed inhibitor of p53 aggregation rescues p53 tumor suppression in ovarian carcinomas, Cancer Cell, 29(1): p. 90-103.

235. Wei, S., et al., 2015, Active pin1 is a key target of all-trans retinoic acid in acute promyelocytic leukemia and breast cancer, Nat Med, 21(5): p. 457-466.

236. Li, D., et al., 2011, Functional inactivation of endogenous mdm2 and chip by hsp90 causes aberrant stabilization of mutant p53 in human cancer cells, Mol Cancer Res, 9(5): p. 577-588.

237. Alexandrova, E.M., et al., 2015, Improving survival by exploiting tumour dependence on stabilized mutant p53 for treatment, Nature, 523(7560): p. 352-356.

238. Blagosklonny, M.V., Toretsky, J., and Neckers, L., 1995, Geldanamycin selectively destabilizes and conformationally alters mutated p53, Oncogene, 11(5): p. 933-939.

239. Wang, C. and Chen, J., 2003, Phosphorylation and hsp90 binding mediate heat shock stabilization of p53, J Biol Chem, 278(3): p. 2066-2071.

240. Marks, P.A., 2007, Discovery and development of saha as an anticancer agent, Oncogene, 26(9): p. 1351-1356.

241. Li, D., Marchenko, N.D., and Moll, U.M., 2011, Saha shows preferential cytotoxicity in mutant p53 cancer cells by destabilizing mutant p53 through inhibition of the hdac6-hsp90 chaperone axis, Cell Death Differ, 18(12): p. 1904-1913.

242. Wang, Z.T., et al., 2016, Histone deacetylase inhibitors suppress mutant p53 transcription via hdac8/yy1 signals in triple negative breast cancer cells, Cell Signal, 28(5): p. 506-515.

243. Yan, W., et al., 2011, Mutant p53 protein is targeted by arsenic for degradation and plays a role in arsenic-mediated growth suppression, J Biol Chem, 286(20): p. 17478-17486.

244. Wang, J., et al., 2011, Gambogic acid-induced degradation of mutant p53 is mediated by proteasome and related to chip, J Cell Biochem, 112(2): p. 509-519.

245. Vakifahmetoglu-Norberg, H., et al., 2013, Chaperone-mediated autophagy degrades mutant p53, Genes Dev, 27(15): p. 1718-1730.

246. Yi, Y.W., et al., 2013, Targeting mutant p53 by a sirt1 activator yk-3-237 inhibits the proliferation of triple-negative breast cancer cells, Oncotarget, 4(7): p. 984-994.

247. Zhang, S., et al., 2015, Small-molecule nsc59984 restores p53 pathway signaling and antitumor effects against colorectal cancer via p73 activation and degradation of mutant p53, Cancer Res, 75(18): p. 3842-3852.

248. Paranjpe, A. and Srivenugopal, K.S., 2013, Degradation of nf-kappab, p53 and other regulatory redox-sensitive proteins by thiol-conjugating and -nitrosylating drugs in human tumor cells, Carcinogenesis, 34(5): p. 990-1000.

249. Leao, M., et al., 2013, Novel simplified yeast-based assays of regulators of p53-mdmx interaction and p53 transcriptional activity, FEBS J, 280(24): p. 6498-6507.

250. Saraiva, L.S., M. M. M.; Pereira, N. A. L.; Pereira, C.; Soares, J.; Gomes, S.; Leão, M.; Monteiro, A., *Tryptophanol-derived oxazoloisoindolinones: Small-molecule p53 activators. European patent application nº ep14739561.0 (pending) and us patent nº 20160347765 (granted)*. 2016.

251. Bou-Hanna, C., et al., 2015, Acute cytotoxicity of mira-1/nsc19630, a mutant p53-reactivating small molecule, against human normal and cancer cells via a caspase-9-dependent apoptosis, Cancer Lett, 359(2): p. 211-217.

252. Wang, W., et al., 2003, Stabilization of p53 by cp-31398 inhibits ubiquitination without altering phosphorylation at serine 15 or 20 or mdm2 binding, Mol Cell Biol, 23(6): p. 2171-2181.

253. Chipuk, J.E., et al., 2003, Pharmacologic activation of p53 elicits bax-dependent apoptosis in the absence of transcription, Cancer Cell, 4(5): p. 371-381.

254. Peng, X., et al., 2013, Apr-246/prima-1met inhibits thioredoxin reductase 1 and converts the enzyme to a dedicated nadph oxidase, Cell Death Dis, 4: p. e881.

255. Mohell, N., et al., 2015, Apr-246 overcomes resistance to cisplatin and doxorubicin in ovarian cancer cells, Cell Death Dis, 6: p. e1794.

256. Zache, N., et al., 2008, Prima-1met inhibits growth of mouse tumors carrying mutant p53, Cell Oncol, 30(5): p. 411-418.

257. Liu, D.S., et al., 2015, Apr-246 potently inhibits tumour growth and overcomes chemoresistance in preclinical models of oesophageal adenocarcinoma, Gut, 64(10): p. 1506-1516.

258. Puca, R., et al., 2011, Restoring p53 active conformation by zinc increases the response of mutant p53 tumor cells to anticancer drugs, Cell Cycle, 10(10): p. 1679-1689.

259. Margalit, O., et al., 2012, Zinc supplementation augments in vivo antitumor effect of chemotherapy by restoring p53 function, Int J Cancer, 131(4): p. E562-568.

260. Blanden, A.R., et al., 2015, Synthetic metallochaperone zmc1 rescues mutant p53 conformation by transporting zinc into cells as an ionophore, Mol Pharmacol, 87(5): p. 825-831.

261. Kasi, P.D., et al., 2016, Molecular targets of curcumin for cancer therapy: An updated review, Tumour Biol, 37(10): p. 13017-13028.

262. Baell, J. and Walters, M.A., 2014, Chemistry: Chemical con artists foil drug discovery, Nature, 513(7519): p. 481-483.

263. Girardini, J.E., et al., 2011, A pin1/mutant p53 axis promotes aggressiveness in breast cancer, Cancer Cell, 20(1): p. 79-91.

264. Ghosh, S., et al., 2014, Investigating the intrinsic aggregation potential of evolutionarily conserved segments in p53, Biochemistry, 53(38): p. 5995-6010.

265. Goldschmidt, L., et al., 2010, Identifying the amylome, proteins capable of forming amyloid-like fibrils, Proc Natl Acad Sci U S A, 107(8): p. 3487-3492.

266. Pradhan, M.R., et al., 2019, Simulations of mutant p53 DNA binding domains reveal a novel druggable pocket, Nucleic Acids Res, 47(4): p. 1637-1652.

267. Patra, J.K., et al., 2018, Nano based drug delivery systems: Recent developments and future prospects, J Nanobiotechnology, 16(1): p. 71.

268. Sinha, R., et al., 2006, Nanotechnology in cancer therapeutics: Bioconjugated nanoparticles for drug delivery, Mol Cancer Ther, 5(8): p. 1909-1917.

269. Patil, Y.B., et al., 2010, The use of nanoparticle-mediated targeted gene silencing and drug delivery to overcome tumor drug resistance, Biomaterials, 31(2): p. 358-365.

270. Misra, R., Acharya, S., and Sahoo, S.K., 2010, Cancer nanotechnology: Application of nanotechnology in cancer therapy, Drug Discov Today, 15(19-20): p. 842-850.

271. Wang, X., et al., 2008, Application of nanotechnology in cancer therapy and imaging, CA Cancer J Clin, 58(2): p. 97-110.

272. Mirza, A.Z.S., F. A., 2014, Nanomedicine and drug delivery: A mini review, Int Nano Lett, 4(94): p. 1-7.

273. Tran, S., et al., 2017, Cancer nanomedicine: A review of recent success in drug delivery, Clin Transl Med, 6(1): p. 44.

274. Williams, H.D., et al., 2013, Strategies to address low drug solubility in discovery and development, Pharmacol Rev, 65(1): p. 315-499.

275. Amidon, G.L., et al., 1995, A theoretical basis for a biopharmaceutic drug classification: The correlation of in vitro drug product dissolution and in vivo bioavailability, Pharm Res, 12(3): p. 413-420.

276. Lipinski, C., 2002, Poor aqueous solubility - an industry wide problem in drug discovery, American Pharmaceutical Reviews, 5(3): p. 82-85.

277. Locatelli, E.F., M. C. , 2012 Biodegradable plga-b-peg polymeric nanoparticles: Synthesis, properties, and nanomedical applications as drug delivery system. , Journal of Nanoparticle Research, 14(12): p. 1.

278. Wilhelm, S.T., A. J.; Dai, Q.; Ohta, S.; Audet, J.; Dvorak, H. F.; Chan, W. C. W. , 2016, Analysis of nanoparticle delivery to tumours, Nature Reviews Materials, 1(5): p. 1-12.

279. Bjornmalm, M., et al., 2017, Bridging bio-nano science and cancer nanomedicine, ACS Nano, 11(10): p. 9594-9613.

280. Vallet-Regi, M., et al., 2017, Mesoporous silica nanoparticles for drug delivery: Current insights, Molecules, 23(1).

281. Manzano, M. and Vallet-Regi, M., 2018, Mesoporous silica nanoparticles in nanomedicine applications, J Mater Sci Mater Med, 29(5): p. 65.

282. Shahbazi, M.A., Herranz, B., and Santos, H.A., 2012, Nanostructured porous si-based nanoparticles for targeted drug delivery, Biomatter, 2(4): p. 296-312.

283. Salonen, J., et al., 2008, Mesoporous silicon in drug delivery applications, J Pharm Sci, 97(2): p. 632-653.

284. Li, Z., et al., 2012, Mesoporous silica nanoparticles in biomedical applications, Chem Soc Rev, 41(7): p. 2590-2605.

285. Almeida, P.V., et al., 2017, A multifunctional nanocomplex for enhanced cell uptake, endosomal escape and improved cancer therapeutic effect, Nanomedicine (Lond), 12(12): p. 1401-1420.

286. Anglin, E.J., et al., 2008, Porous silicon in drug delivery devices and materials, Adv Drug Deliv Rev, 60(11): p. 1266-1277.

287. Prestidge, C.A., et al., 2007, Mesoporous silicon: A platform for the delivery of therapeutics, Expert Opin Drug Deliv, 4(2): p. 101-110.

288. Sing, K.S.W.E., D. H.; Haul, R. A. W.; Moscou, L.; Pierotti, R. A.; Rouquerol, J.; Siemieniewska, T., 1985, Reporting physisorption data for gas/solid systems with special reference to the determination of surface area and porosity, Pure and Applied Chemistry, 54: p. 603-619.

289. Salonen, J.L., V. P., 2008, Fabrication and chemical surface modification of mesoporous silicon for biomedical applications, Chemical Engineering Journal, 137(1): p. 162-172.

290. Li, W., et al., 2018, Tailoring porous silicon for biomedical applications: From drug delivery to cancer immunotherapy, Adv Mater, 30(24): p. e1703740.

291. Makila, E., et al., 2014, Confinement effects on drugs in thermally hydrocarbonized porous silicon, Langmuir, 30(8): p. 2196-2205.

292. Rosenholm, J.M., et al., 2012, Nanoparticles in targeted cancer therapy: Mesoporous silica nanoparticles entering preclinical development stage, Nanomedicine (Lond), 7(1): p. 111-120.

293. Bimbo, L.M., et al., 2010, Biocompatibility of thermally hydrocarbonized porous silicon nanoparticles and their biodistribution in rats, ACS Nano, 4(6): p. 3023-3032.

294. Bimbo, L.M., et al., 2012, Cellular interactions of surface modified nanoporous silicon particles, Nanoscale, 4(10): p. 3184-3192.

295. Bimbo, L.M., et al., 2012, Toxicological profile of therapeutic nanodelivery systems, Curr Drug Metab, 13(8): p. 1068-1086.

296. Bimbo, L.M., et al., 2011, Drug permeation across intestinal epithelial cells using porous silicon nanoparticles, Biomaterials, 32(10): p. 2625-2633.

297. Lin, Y.S. and Haynes, C.L., 2010, Impacts of mesoporous silica nanoparticle size, pore ordering, and pore integrity on hemolytic activity, J Am Chem Soc, 132(13): p. 4834-4842.

298. Rosenholm, J.M., et al., 2010, Cancer-cell-specific induction of apoptosis using mesoporous silica nanoparticles as drug-delivery vectors, Small, 6(11): p. 1234-1241.

299. Huang, X., et al., 2010, The effect of the shape of mesoporous silica nanoparticles on cellular uptake and cell function, Biomaterials, 31(3): p. 438-448.

300. Park, J.H., et al., 2009, Biodegradable luminescent porous silicon nanoparticles for in vivo applications, Nat Mater, 8(4): p. 331-336.

301. Sarparanta, M., et al., 2012, Intravenous delivery of hydrophobin-functionalized porous silicon nanoparticles: Stability, plasma protein adsorption and biodistribution, Mol Pharm, 9(3): p. 654-663.

302. Xia, B., et al., 2013, Engineered stealth porous silicon nanoparticles via surface encapsulation of bovine serum albumin for prolonging blood circulation in vivo, ACS Appl Mater Interfaces, 5(22): p. 11718-11724.

303. Santos, H.A., et al., 2014, Porous silicon nanoparticles for nanomedicine: Preparation and biomedical applications, Nanomedicine (Lond), 9(4): p. 535-554.

304. Hon, N.K., et al., 2012, Tailoring the biodegradability of porous silicon nanoparticles, J Biomed Mater Res A, 100(12): p. 3416-3421.

305. De Angelis, F., et al., 2010, Water soluble nanoporous nanoparticle for in vivo targeted drug delivery and controlled release in b cells tumor context, Nanoscale, 2(10): p. 2230-2236.

306. Tzur-Balter, A.S., G.; Segal, E. , 2015, Porous silicon for cancer therapy: From fundamental research to the clinic, Reviews in Chemical Engineering, 31(3): p. 193–207.

307. Kalepu, S. and Nekkanti, V., 2015, Insoluble drug delivery strategies: Review of recent advances and business prospects, Acta Pharm Sin B, 5(5): p. 442-453.

308. Hancock, B.C. and Zografi, G., 1997, Characteristics and significance of the amorphous state in pharmaceutical systems, J Pharm Sci, 86(1): p. 1-12.

309. Kaushal, A.M., Gupta, P., and Bansal, A.K., 2004, Amorphous drug delivery systems: Molecular aspects, design, and performance, Crit Rev Ther Drug Carrier Syst, 21(3): p. 133-193.

310. Hancock, B.C. and Parks, M., 2000, What is the true solubility advantage for amorphous pharmaceuticals?, Pharm Res, 17(4): p. 397-404.

311. Aaltonen, J.R., T., 2009, Towards physico-relevant dissolution testing: The importance of solid-state analysis in dissolution, Dissolution Technologies, 16: p. 47–54.

312. Laitinen, R., et al., 2013, Emerging trends in the stabilization of amorphous drugs, Int J Pharm, 453(1): p. 65-79.

313. Kanaujia, P.P., P.; Ng, W. K.; Tan, R. B. H., 2015, Amorphous formulations for dissolution and bioavailability enhancement of poorly soluble apis, Powder Technology, 285: p. 2-15.

314. Qian, K.K. and Bogner, R.H., 2012, Application of mesoporous silicon dioxide and silicate in oral amorphous drug delivery systems, J Pharm Sci, 101(2): p. 444-463.

315. Jackson, C.L.M., G. B., 1996, Vitrification and crystallization of organic liquids confined to nanoscale pores, Chemistry of Materials, 8(8): p. 2128–2137.

316. Prestidge, C.A.B., T. J.; Lau, C.-H.; Barnett, C.; Loni, A.; Canham, L., 2007, Mesoporous silicon: A platform for the delivery of therapeutics, Expert Opinion on Drug Delivery, 4(2): p. 101–110.

317. Qian, K.K.B., R. H., 2011, Spontaneous crystalline-to-amorphous phase transformation of organic or medicinal compounds in the presence of porous media, part 1: Thermodynamics of spontaneous amorphization. , Journal of Pharmaceutical Sciences, 100 (7): p. 2801–2815.

318. Makila, E., et al., 2016, Influence of surface chemistry on ibuprofen adsorption and confinement in mesoporous silicon microparticles, Langmuir, 32(49): p. 13020-13029.

319. Ishioka, C., et al., 1993, Screening patients for heterozygous p53 mutations using a functional assay in yeast, Nat Genet, 5(2): p. 124-129.

320. Niesen, F.H., Berglund, H., and Vedadi, M., 2007, The use of differential scanning fluorimetry to detect ligand interactions that promote protein stability, Nat Protoc, 2(9): p. 2212-2221.

321. Winn, M.D., et al., 2011, Overview of the ccp4 suite and current developments, Acta Crystallogr D Biol Crystallogr, 67(Pt 4): p. 235-242.

322. McCoy, A.J., et al., 2007, Phaser crystallographic software, J Appl Crystallogr, 40(Pt 4): p. 658-674.

323. Adams, P.D., et al., 2010, Phenix: A comprehensive python-based system for macromolecular structure solution, Acta Crystallogr D Biol Crystallogr, 66(Pt 2): p. 213-221.

324. Afonine, P.V., et al., 2012, Towards automated crystallographic structure refinement with phenix.Refine, Acta Crystallogr D Biol Crystallogr, 68(Pt 4): p. 352-367.

325. Joosten, R.P., et al., 2014, The pdb_redo server for macromolecular structure model optimization, IUCrJ, 1(Pt 4): p. 213-220.

326. Pettersen, E.F., et al., 2004, Ucsf chimera--a visualization system for exploratory research and analysis, J Comput Chem, 25(13): p. 1605-1612.

327. Xiong, S., Zhang, L., and He, Q.Y., 2008, Fractionation of proteins by heparin chromatography, Methods Mol Biol, 424: p. 213-221.

328. Blanden, A.R., et al., 2015, Reactivating mutant p53 using small molecules as zinc metallochaperones: Awakening a sleeping giant in cancer, Drug Discov Today, 20(11): p. 1391-1397.

329. Zhao, K., et al., 2001, Crystal structure of the mouse p53 core DNA-binding domain at 2.7 a resolution, J Biol Chem, 276(15): p. 12120-12127.

330. Kabsch, W. and Sander, C., 1983, Dictionary of protein secondary structure: Pattern recognition of hydrogen-bonded and geometrical features, Biopolymers, 22(12): p. 2577-2637.

331. Jeffrey, G.A., 1997, An introduction to hydrogen bonding.

332. Sokalingam, S., et al., 2012, A study on the effect of surface lysine to arginine mutagenesis on protein stability and structure using green fluorescent protein*,* PLoS One, 7(7): p. e40410.

333. Monti, P., et al., 2011, Dominant-negative features of mutant tp53 in germline carriers have limited impact on cancer outcomes*,* Mol Cancer Res, 9(3): p. 271-279.

334. Stephens, P.J.D., F. J.; Chabalowski, C. F.; Frisch, M. J. , 1994, Ab initio calculation of vibrational absorption and circular dichroism spectra using density functional force fields*,* The Journal of Physical Chemistry, 98: p. 11623-11627.

335. Tomasi, J., Mennucci, B., and Cammi, R., 2005, Quantum mechanical continuum solvation models*,* Chem Rev, 105(8): p. 2999-3093.

336. Bayly, C.I.C., P.; Cornell, W.; Kollman, P. A. , 1993, A well-behaved electrostatic potential based method using charge restraints for deriving atomic charges: The resp model.*,* The Journal of Physical Chemistry, 97: p. 10269-10280.

337. Tian, W., et al., 2018, Castp 3.0: Computed atlas of surface topography of proteins*,* Nucleic Acids Res, 46(W1): p. W363-W367.

338. Morris, G.M.G., D. S.; Halliday, R. S.; Huey, R.; Hart, W. E.; Belew, R. K.; Olson, A. J., 1998, Automated docking using a lamarckian genetic algorithm and an empirical binding free energy function. *,* Journal of Computational Chemistry, 19: p. 1639-1662.

339. Hornak, V., et al., 2006, Comparison of multiple amber force fields and development of improved protein backbone parameters*,* Proteins, 65(3): p. 712-725.

340. Wang, J., et al., 2004, Development and testing of a general amber force field*,* J Comput Chem, 25(9): p. 1157-1174.

341. Cádenas, R.R., L.; Lagúnez-Otero, J.; Cetina, R. , 2000, Semiempirical studies on the transition structure of the baeyer and villiger rearrangement. The reaction of acetone with alkyl and aryl peracids. *,* Journal of Molecular Structure: THEOCHEM 497: p. 211-225.

342. Iglesias-Arteaga, M.A.V.-H., G. A.; Méndez-Stivalet, J. M.; Galano, A.; Alvarez-Idaboy, J. R. , 2005, The baeyer-villiger reaction of 23-oxosapogenins.*,* ARKIVOC, vi: p. 109–126.

343. Pang, Y.P., 2001, Successful molecular dynamics simulation of two zinc complexes bridged by a hydroxide in phosphotriesterase using the cationic dummy atom method. *,* Proteins: Structure, Function, & Genetics, 45(3): p. 183-189.

344. Pang, Y.P.X., K.; Yazal, J. E.; Prendergas, F. G. , 2000, Successful molecular dynamics simulation of the zinc-bound farnesyltransferase using the cationic dummy atom approach*,* Protein Science, 9(10): p. 1857-1865.

345. Li, J.X., H.; Westb, G. M.; Jonesa, L. H., 2016, Label-free technologies for target identification and validation*,* Med. Chem. Commun., 7: p. 769-777

346. Miyamoto, S.K., P. A. , 1992, Settle: An analytical version of the shake and rattle algorithm for rigid water models.*,* Journal of Computational Chemistry, 13(8): p. 952-962.

347. Ryckaert, J.P.C., G.; Berendsen, H. J. C. , 1977, Numerical integration of the cartesian equations of motion of a system with constraints: Molecular dynamics of n-alkanes.*,* Journal of Computational Physics, 23: p. 327-341.

348. Darden, T.Y., D.; Pedersen, L. , 1993, Particle mesh ewald: An n·log(n) method for ewald sums in large systems. *,* The Journal of Chemical Physics, 98: p. 10089-10092.

349. Dourado, D., Swart, M., and Carvalho, A.T.P., 2018, Why the flavin adenine dinucleotide (fad) cofactor needs to be covalently linked to complex ii of the electron-transport chain for the conversion of fadh2 into fad*,* Chemistry, 24(20): p. 5246-5252.

350. Gietz, R.D. and Schiestl, R.H., 2007, Quick and easy yeast transformation using the liac/ss carrier DNA/peg method*,* Nat Protoc, 2(1): p. 35-37.

351. Reid, Y., et al., 2004, Authentication of human cell lines by str DNA profiling analysis, in Assay guidance manual, Sittampalam, G.S., et al., Editors: Bethesda (MD).

352. Raimundo, L., et al., 2018, Improving anticancer activity towards colon cancer cells with a new p53-activating agent, Br J Pharmacol, 175(20): p. 3947-3962.

353. Soares, J., et al., 2017, Dimp53-1: A novel small-molecule dual inhibitor of p53-mdm2/x interactions with multifunctional p53-dependent anticancer properties, Mol Oncol, 11(6): p. 612-627.

354. Tan, B.X., et al., 2015, Assessing the efficacy of mdm2/mdm4-inhibiting stapled peptides using cellular thermal shift assays, Sci Rep, 5: p. 12116.

355. Soares, J., et al., 2015, A tryptophanol-derived oxazolopiperidone lactam is cytotoxic against tumors via inhibition of p53 interaction with murine double minute proteins, Pharmacol Res, 95-96: p. 42-52.

356. Meyer, B. and Peters, T., 2003, Nmr spectroscopy techniques for screening and identifying ligand binding to protein receptors, Angew Chem Int Ed Engl, 42(8): p. 864-890.

357. Jafari, R., et al., 2014, The cellular thermal shift assay for evaluating drug target interactions in cells, Nat Protoc, 9(9): p. 2100-2122.

358. Dougherty, D.A., 1996, Cation-pi interactions in chemistry and biology: A new view of benzene, phe, tyr, and trp, Science, 271(5246): p. 163-168.

359. Mecozzi, S., West, A.P., Jr., and Dougherty, D.A., 1996, Cation-pi interactions in aromatics of biological and medicinal interest: Electrostatic potential surfaces as a useful qualitative guide, Proc Natl Acad Sci U S A, 93(20): p. 10566-10571.

360. Tanaka, N., et al., 2018, Gain-of-function mutant p53 promotes the oncogenic potential of head and neck squamous cell carcinoma cells by targeting the transcription factors foxo3a and foxm1, Oncogene, 37(10): p. 1279-1292.

361. Duffy, M.J., Synnott, N.C., and Crown, J., 2017, Mutant p53 as a target for cancer treatment, Eur J Cancer, 83: p. 258-265.

362. Gallivan, J.P. and Dougherty, D.A., 1999, Cation-pi interactions in structural biology, Proc Natl Acad Sci U S A, 96(17): p. 9459-9464.

363. Kumar, K., et al., 2018, Cation-pi interactions in protein-ligand binding: Theory and data-mining reveal different roles for lysine and arginine, Chem Sci, 9(10): p. 2655-2665.

364. Dougherty, D.A., 2013, The cation-pi interaction, Acc Chem Res, 46(4): p. 885-893.

365. Lim, Y.T., et al., 2018, An efficient proteome-wide strategy for discovery and characterization of cellular nucleotide-protein interactions, PLoS One, 13(12): p. e0208273.

366. Ferreira, M.P., et al., 2016, In vitro and in vivo assessment of heart-homing porous silicon nanoparticles, Biomaterials, 94: p. 93-104.

367. Kovalainen, M., et al., 2012, Mesoporous silicon (psi) for sustained peptide delivery: Effect of psi microparticle surface chemistry on peptide yy3-36 release, Pharm Res, 29(3): p. 837-846.

368. Makila, E., et al., 2012, Amine modification of thermally carbonized porous silicon with silane coupling chemistry, Langmuir, 28(39): p. 14045-14054.

369. Martins, J.P., et al., 2018, Engineered multifunctional albumin-decorated porous silicon nanoparticles for fcrn translocation of insulin, Small, 14(27): p. e1800462.

370. Liu, D., et al., 2015, Microfluidic assisted one-step fabrication of porous silicon@acetalated dextran nanocomposites for precisely controlled combination chemotherapy, Biomaterials, 39: p. 249-259.

371. Ollikainen, E., et al., 2017, The impact of porous silicon nanoparticles on human cytochrome p450 metabolism in human liver microsomes in vitro, Eur J Pharm Sci, 104: p. 124-132.

372. Almeida, P.V., et al., 2014, Amine-modified hyaluronic acid-functionalized porous silicon nanoparticles for targeting breast cancer tumors, Nanoscale, 6(17): p. 10377-10387.

373. Yan, F., et al., 2017, Palladium-catalyzed cyclization-heck reaction of allenamides: An approach to 3-methylene-5-phenyl-1,2,3,4-tetrahydropyridine derivatives, Org Lett, 19(1): p. 86-89.

374. ThermoScientific, *Easy molecular bonding crosslinking technology: Reactivity chemistries, applications and structure references*, in Crosslinking Technical Handbook. 2012. p. 1-53.

375. Xu, W.R., J.; Nissinen, T.; Suvanto, M.; Rilla, K.; Li, B.; Wang, Q.; Deng, F.; Lehto, V.-P., 2012, Amine surface modifications and fluorescent labeling of thermally stabilized mesoporous silicon nanoparticles, The Journal of Physical Chemistry C,, 116(42): p. 22307–22314.

376. Lundt, B.F., et al., 1978, Removal of t-butyl and t-butoxycarbonyl protecting groups with trifluoroacetic acid. Mechanisms, biproduct formation and evaluation of scavengers, Int J Pept Protein Res, 12(5): p. 258-268.

377. Shahbazi M. A., S.N., Mäkilä E., Araújo F., Correia A., Ramos T., Sarmento B., Salonen J., Hirvonen J., and Santos H. A., 2015, A prospective cancer chemo-immunotherapy approach mediated by synergistic cd326 targeted porous silicon nanovectors, Nano Research, 8(5): p. 1505–1521.

378. Bauleth-Ramos T., S.M.A., Liu D., Fontana F., Correia A., Figueiredo P., Zhang H., Martins J. P., Hirvonen J. T., Granja P., Sarmento B., and Santos H. A., 2017, Nutlin-3a and cytokine co-loaded spermine-modi ed acetalated dextran nanoparticles for cancer chemo-immunotherapy, Advanced Functional Materials, 27(1703303): p. 1-14.

379. Santos, H.A., et al., 2010, In vitro cytotoxicity of porous silicon microparticles: Effect of the particle concentration, surface chemistry and size, Acta Biomater, 6(7): p. 2721-2731.

380. Cheung, A., et al., 2016, Targeting folate receptor alpha for cancer treatment, Oncotarget, 7(32): p. 52553-52574.

381. Mattheolabakis, G., et al., 2015, Hyaluronic acid targeting of cd44 for cancer therapy: From receptor biology to nanomedicine, J Drug Target, 23(7-8): p. 605-618.

382. Seok, H.Y., et al., 2018, Cd44 targeting biocompatible and biodegradable hyaluronic acid cross-linked zein nanogels for curcumin delivery to cancer cells: In vitro and in vivo evaluation, J Control Release, 280: p. 20-30.

383. Zwicke, G.L., Mansoori, G.A., and Jeffery, C.J., 2012, Utilizing the folate receptor for active targeting of cancer nanotherapeutics, Nano Rev, 3.

384. Johnstone, S.A., et al., 2001, Surface-associated serum proteins inhibit the uptake of phosphatidylserine and poly(ethylene glycol) liposomes by mouse macrophages, Biochim Biophys Acta, 1513(1): p. 25-37.

385. Knop, K., et al., 2010, Poly(ethylene glycol) in drug delivery: Pros and cons as well as potential alternatives, Angew Chem Int Ed Engl, 49(36): p. 6288-6308.

386. Yuan W., L.H., 2017, Chapter 14 - polymer-based nanocarriers for therapeutic nucleic acids delivery, in Nanostructures for drug delivery: Micro and nano technologies, Andronescu E., G.A.M., Editor. Elsevier. p. 445-460.

387. Chen, C., et al., 2013, Structural basis for molecular recognition of folic acid by folate receptors, Nature, 500(7463): p. 486-489.

388. Hermanson, G.T., 2013, Chapter 3 - the reactions of bioconjugation, in Bioconjugate techniques. Elsevier Inc.

389. Fang, C., et al., 2006, In vivo tumor targeting of tumor necrosis factor-alpha-loaded stealth nanoparticles: Effect of mepeg molecular weight and particle size, Eur J Pharm Sci, 27(1): p. 27-36.

390. NIH-PubChem, Folic acid (compound), 2019, [Accessed on 12th, 2019], Available from: https://pubchem.ncbi.nlm.nih.gov/compound/folic_acid.

391. Vojta, D. and Vazdar, M., 2014, The study of hydrogen bonding and picdots, three dots, centeredpi interactions in phenolcdots, three dots, centeredethynylbenzene complex by ir spectroscopy, Spectrochim Acta A Mol Biomol Spectrosc, 132: p. 6-14.

392. McDonald, R.S., 1986, Review: Infrared spectrometry, Analytical Chemistry, 58 (9): p. 1906–1925.

393. Coates, J., 2006, Interpretation of infrared spectra, a practical approach, in Encyclopedia of analytical chemistry, Meyers, R.A., Editor. John Wiley & Sons, Ltd.

394. SigmaAldrich, Ir spectrum table & chart, 2019, [Accessed on April 12th, 2019], Available from: https://www.sigmaaldrich.com/technical-documents/articles/biology/ir-spectrum-table.html.

395. Hillerström A., A.M., Samuelsson J., Stam J., 2014, Solvent strategies for loading and release in mesoporous silica, Colloids and Interface Science Communications, 3: p. 5–8.

396. Crouch S. P. M., K.R., Slater K. J., and Fletcher J., 1993, The use of atp bioluminescence as a measure of cell proliferation and cytotoxicity, Journal of Immunological Methods, 160: p. 81-88.

397. Hannah R., B.M., Moravec R., and Riss T., 2001, Celltiter-glotm luminescent cell viability assay: A sensitive and rapid method for determining cell viability Cell Notes, (2): p. 11-13.

398. Fillmore, C.M. and Kuperwasser, C., 2008, Human breast cancer cell lines contain stem-like cells that self-renew, give rise to phenotypically diverse progeny and survive chemotherapy, Breast Cancer Res, 10(2): p. R25.

399. Kuo, C.T. and Lee, W.S., 2016, Progesterone receptor activation is required for folic acid-induced anti-proliferation in colorectal cancer cell lines, Cancer Lett, 378(2): p. 104-110.

400. Olsson, E., et al., 2011, Cd44 isoforms are heterogeneously expressed in breast cancer and correlate with tumor subtypes and cancer stem cell markers, BMC Cancer, 11: p. 418.

401. Sahlberg, S.H., et al., 2014, Evaluation of cancer stem cell markers cd133, cd44, cd24: Association with akt isoforms and radiation resistance in colon cancer cells, PLoS One, 9(4): p. e94621.

402. Zhou, J.Y., et al., 2016, Role of cd44(high)/cd133(high) hct-116 cells in the tumorigenesis of colon cancer, Oncotarget, 7(7): p. 7657-7666.

403. Jochums, A., et al., 2017, Revelation of different nanoparticle-uptake behavior in two standard cell lines nih/3t3 and a549 by flow cytometry and time-lapse imaging, Toxics, 5(3).

404. Haidary S. M., C.E.P., Ali N. K., 2012, Nanoporous silicon as drug delivery systems for cancer therapies, Journal of Nanomaterials, 2012: p. 1-15.

405. Salonen, J. and Makila, E., 2018, Thermally carbonized porous silicon and its recent applications, Adv Mater, 30(24): p. e1703819.

406. Santos, H.A. and Hirvonen, J., 2012, Nanostructured porous silicon materials: Potential candidates for improving drug delivery, Nanomedicine (Lond), 7(9): p. 1281-1284.

407. McCarthy, C.A., et al., 2018, Role of drug adsorption onto the silica surface in drug release from mesoporous silica systems, Mol Pharm, 15(1): p. 141-149.

408. Shahbazi, M.A., et al., 2013, The mechanisms of surface chemistry effects of mesoporous silicon nanoparticles on immunotoxicity and biocompatibility, Biomaterials, 34(31): p. 7776-7789.

409. Frohlich, E., 2012, The role of surface charge in cellular uptake and cytotoxicity of medical nanoparticles, Int J Nanomedicine, 7: p. 5577-5591.

410. Yin, H., Too, H.P., and Chow, G.M., 2005, The effects of particle size and surface coating on the cytotoxicity of nickel ferrite, Biomaterials, 26(29): p. 5818-5826.

411. Langston Suen, W.L. and Chau, Y., 2014, Size-dependent internalisation of folate-decorated nanoparticles via the pathways of clathrin and caveolae-mediated endocytosis in arpe-19 cells, J Pharm Pharmacol, 66(4): p. 564-573.

412. Behzadi, S., et al., 2017, Cellular uptake of nanoparticles: Journey inside the cell, Chem Soc Rev, 46(14): p. 4218-4244.

413. Wang, S. and Dormidontova, E.E., 2010, Nanoparticle design optimization for enhanced targeting: Monte carlo simulations, Biomacromolecules, 11(7): p. 1785-1795.

414. Verhoef, J.J. and Anchordoquy, T.J., 2013, Questioning the use of pegylation for drug delivery, Drug Deliv Transl Res, 3(6): p. 499-503.

415. Nishimori, H., et al., 2009, Silica nanoparticles as hepatotoxicants, Eur J Pharm Biopharm, 72(3): p. 496-501.

416. Tanaka, T., et al., 2010, In vivo evaluation of safety of nanoporous silicon carriers following single and multiple dose intravenous administrations in mice, Int J Pharm, 402(1-2): p. 190-197.

417. Herranz-Blanco, B.L., D.; Mäkilä, E.; Shahbazi, M. A.; Ginestar, E.; Zhang, H.; Aseyev, V.; Balasubramanian, V.; Salonen, J.; Hirvonen, J.; Santos, H. A., 2015, On-chip self-assembly of a smart hybrid nanocomposite for antitumoral applications, Advanced Functional Materials, 25(10): p. 1488-1497.

418. Bae, Y.H.S., J. M.; Park, H. J.; Jang, H. O.; Bae, M. K.; Bae, S. K., 2014, Gain-of-function mutant p53-r280k mediates survival of breast cancer cells, Genes & Genomics, 36(2): p. 171–178.

419. Vogiatzi, F., et al., 2016, Mutant p53 promotes tumor progression and metastasis by the endoplasmic reticulum udpase entpd5, Proc Natl Acad Sci U S A, 113(52): p. E8433-E8442.

420. IARC-*TP53*-Database, R19, august 2018, 2018, [Accessed on October 26th, 2018], Available from: http://p53.iarc.fr/TP53SomaticMutations.aspx.

421. Waring, M.J., et al., 2015, An analysis of the attrition of drug candidates from four major pharmaceutical companies, Nat Rev Drug Discov, 14(7): p. 475-486.

422. Hodgson, J., 2001, Admet--turning chemicals into drugs, Nat Biotechnol, 19(8): p. 722-726.

423. Gomes, A.S., et al., 2016, Drug-like properties and adme of xanthone derivatives: The antechamber of clinical trials, Curr Med Chem, 23(32): p. 3654-3686.

424. Silva, J.L., et al., 2018, Targeting the prion-like aggregation of mutant p53 to combat cancer, Acc Chem Res, 51(1): p. 181-190.

425. Silva, J.L., et al., 2014, Prion-like aggregation of mutant p53 in cancer, Trends Biochem Sci, 39(6): p. 260-267.

426. Liu, D., et al., 2018, Current developments and applications of microfluidic technology toward clinical translation of nanomedicines, Adv Drug Deliv Rev, 128: p. 54-83.

427. Liu, D.B., C. R.; Fan, J.; Li, W.; Correia, A.; Hirvonen, J.; Santos, H. A., 2017, A nano-in-nano vector: Merging the best of polymeric nanoparticles and drug nanocrystals, Advanced Functional Materials, 27: p. 1604508 (1604501-1604513).

428. Gigliobianco, M.R., et al., 2018, Nanocrystals of poorly soluble drugs: Drug bioavailability and physicochemical stability, Pharmaceutics, 10(3).

429. Junghanns, J.U. and Muller, R.H., 2008, Nanocrystal technology, drug delivery and clinical applications, Int J Nanomedicine, 3(3): p. 295-309.

430. Liu, D., et al., 2017, Core/shell nanocomposites produced by superfast sequential microfluidic nanoprecipitation, Nano Lett, 17(2): p. 606-614.

Annex I

Supporting information of Chapter II

Ana Sara Gomes*, Filipa Trovão*, Benedita Andrade Pinheiro, Filipe Freire, Sara Gomes, Carla Oliveira, Lucília Domingues, Maria João Romão, Lucília Saraiva, Ana Luísa Carvalho, (2018), “*The crystal structure of the R280K mutant of human p53 explains the loss of DNA binding”* International Journal of Molecular Sciences, 19(4). pii: E1184. doi: 10.3390/ijms19041184.

*The authors contributed equally to the work.

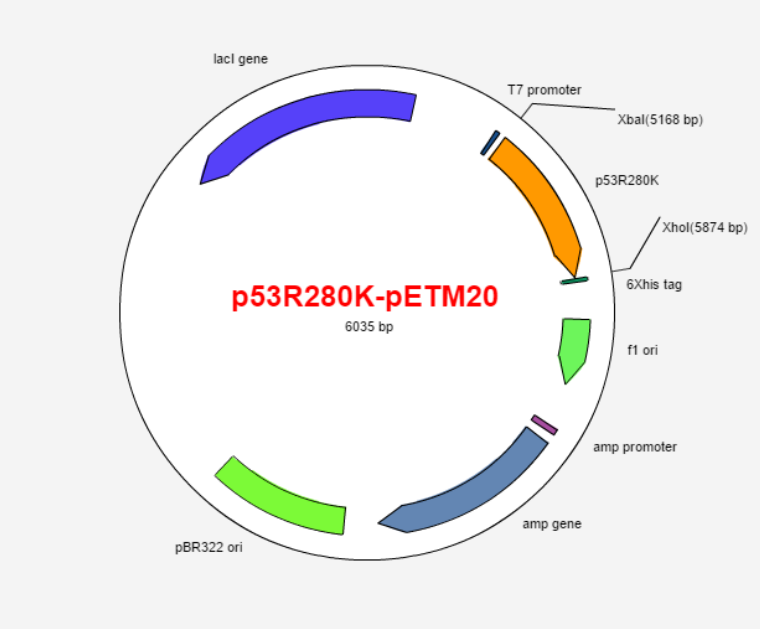
lacI gene
T7 promoter
XbaI(5168 bp)
p53R280K
XhoI(5874 bp)
6Xhis tag
f1 ori
amp promoter
amp gene
pBR322 ori
p53R280K-pETM20
6035 bp

Figure S1. Representation of the mutp53 R280K DBD-pETM20 plasmid construct.

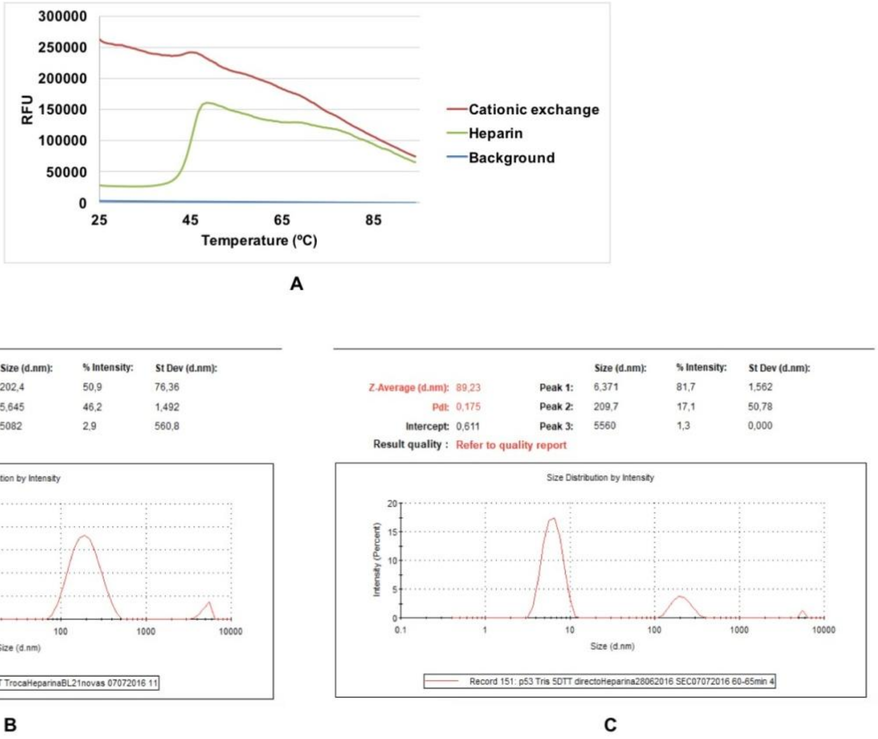

A

			Size (d.nm):	% Intensity:	St Dev (d.nm):
Z-Average (d.nm):	38,54	Peak 1:	202,4	50,9	76,36
PdI:	0,416	Peak 2:	5,645	46,2	1,492
Intercept:	0,681	Peak 3:	5082	2,9	560,8
Result quality :	Refer to quality report				

B

			Size (d.nm):	% Intensity:	St Dev (d.nm):
Z-Average (d.nm):	89,23	Peak 1:	6,371	81,7	1,562
PdI:	0,175	Peak 2:	209,7	17,1	50,78
Intercept:	0,611	Peak 3:	5560	1,3	0,000
Result quality :	Refer to quality report				

C

Figure S2. Chromatography-based purification affects mutp53 R280K DBD folding and aggregation states. (A) DSF preliminary experiments with mutp53 R280K DBD reveal that the protein is mainly unfolded after cationic exchange chromatography exhibiting high fluorescence at

low temperatures. In opposition, heparin-affinity chromatography rendered folded mutp53 R280K DBD (low fluorescence) that unfolds as temperature increases above 40 ºC, with increase of fluorescence. Thermal denaturation of mutp53 R280K DBD by DSF analysis in 50 mM Tris.HCl (pH 7.2), 300 mM NaCl, 5 mM DTT buffer. A reaction mixture (20 µL) was prepared in each well (of MicroAmp® Fast 96-well Reaction Plate, 0.1 mL, Applied Biosystems): 2 µL of mutp53 R280K DBD with final concentration 3 µM, 2 µL of SYPRO®Orange (10×; Protein Thermal Shift Dye KitTM, Applied Biosystems), 5 µL of dye buffer, and protein buffer to complete the 20 µL. Samples were analyzed in a StepOnePlus Real-Time PCR system (Applied Biosystems) scanning temperature range from 25 to 95 ºC, at 1 ºC/min, with ROX (rhodamine X; 575/602 nm) filters; RFU (relative fluorescence units). **(B)** DLS preliminary experiments with mutp53 R280K DBD purified by cationic exchange and heparin-affinity chromatography indicate that the protein population is heterogeneous and aggregation-prone with two main species, one with around 6 d.nm corresponding to mutp53 R280K monomer (~51%) and another with about 200 d.nm corresponding to aggregated protein (~46%). **(C)** DLS preliminary experiments with mutp53 R280K DBD purified by heparin-affinity and size exclusion chromatography (SEC) indicate that the protein population is mainly constituted by mutp53 R280K monomer (~82%) and another with less expression (about 200 d.nm) corresponding to aggregated protein (~17%). DLS graphs are presented in intensity percentage. Hydrodynamic diameter (d.nm) of mutp53 R280K DBD by DLS analysis in 50 mM Tris.HCl, 300 mM NaCl, 5 mM DTT (pH 7.2) buffer. Samples of mutp53 R280K DBD at 8 µM were prepared in 1 mL of protein buffer and were analyzed in Malvern Zetasizer, MODEL NANO ZS (Malvern Instruments Limited, UK), at 20 ºC.

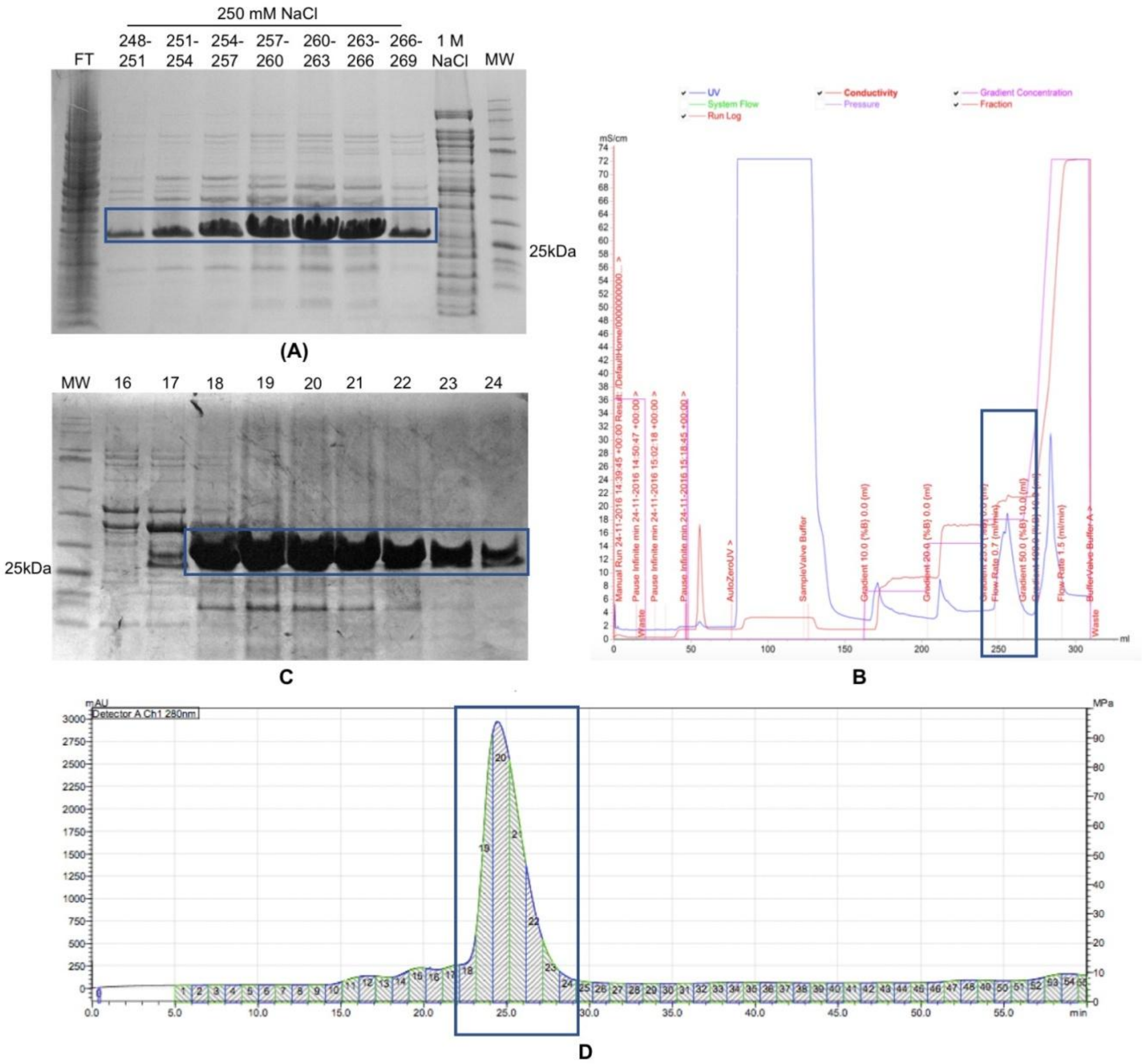

Figure S3. Purification of mutp53 R280K DBD. Blue squares delimitate the expressed and purified mutp53 R280K DBD protein. **(A)** SDS-page monitoring of mutp53 R280K DBD containing fractions eluted with 250 mM of NaCl (248–269 mL, 3 mL each fraction) after heparin-affinity chromatography. **(B)** Heparin-affinity chromatography profile (blue line - absorbance at 280 nm). **(C)** SDS-page monitoring of mutp53 R280K DBD after SEC. **(D)** SEC profile (absorbance at 280 nm). FT – flow through; MW – molecular weight.

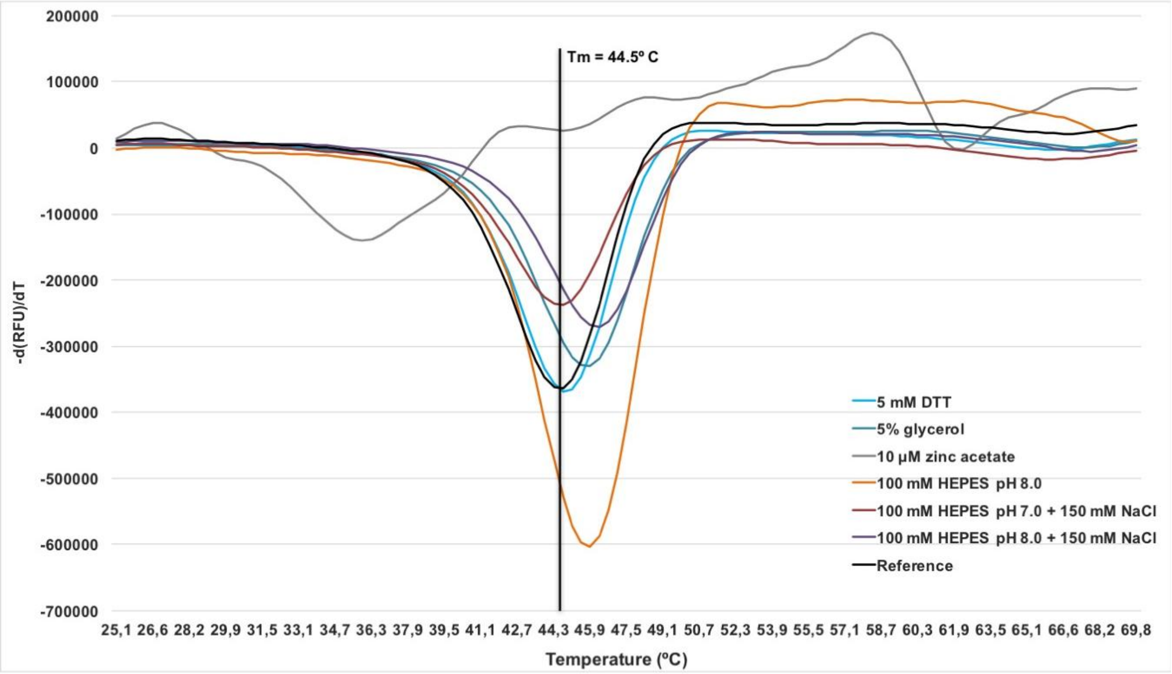

Figure S4. Thermal denaturation curves of mutp53 R280K DBD obtained using DSF screenings of buffers and additives. The black vertical line indicates the T_m of mutp53 R280K DBD (reference, black curve). The colored curves represent the thermal denaturation of the studied protein in different conditions of buffers and additives that exhibit an increase of T_m, therefore a thermal stability increase. Only the best conditions that enabled to disclose the final buffer composition were represented.

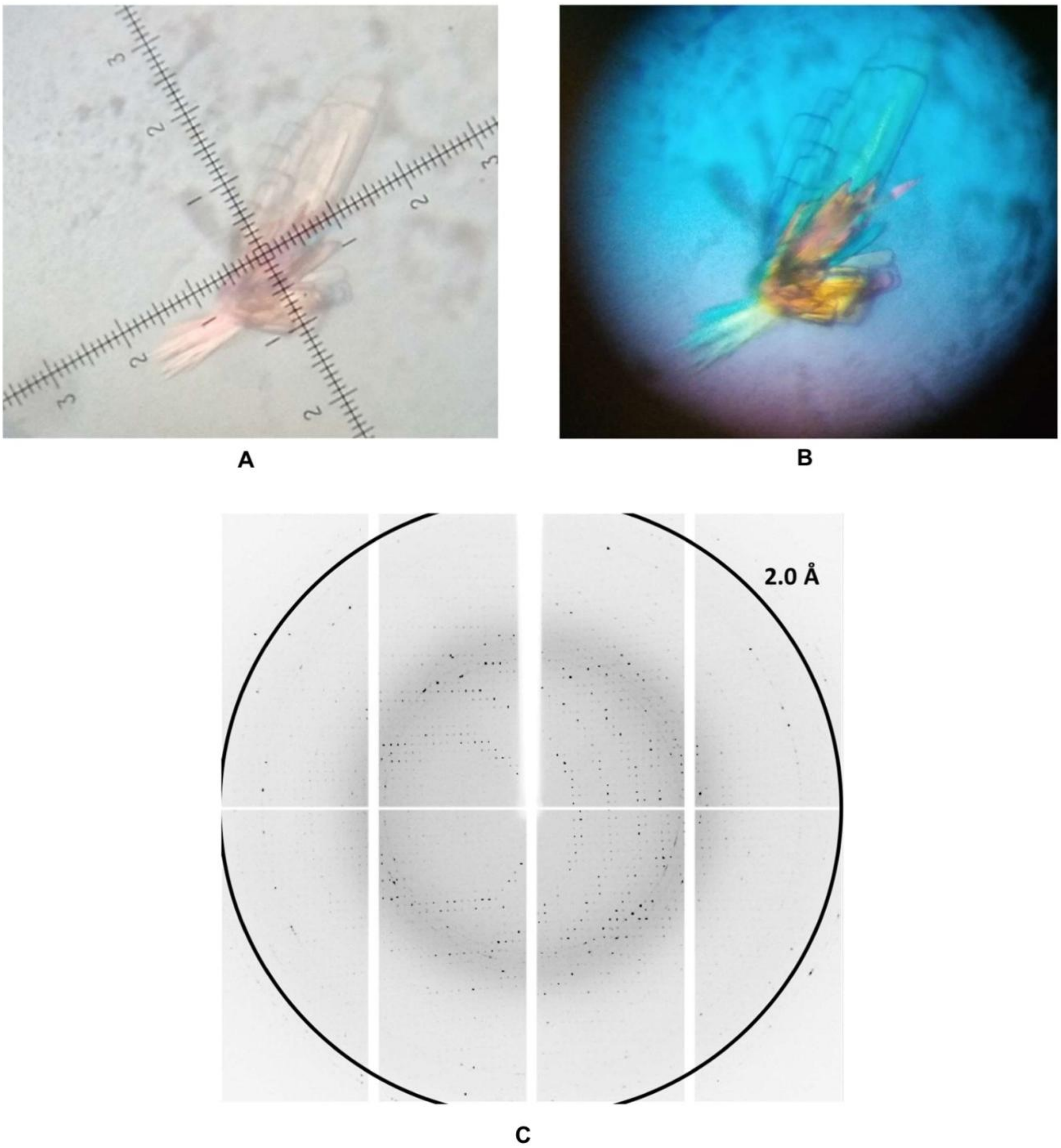

Figure S5. Mutp53 R280K DBD crystals and X-ray diffraction pattern. (A) Agglomerate of plate-shaped crystals of p53R280K grown by the sitting- drop vapour-diffusion method in selected buffer. **(B)** Same crystals viewed under polarized light. The average crystal size is 0.3 x 0.1 mm^2. **(C)** X-ray diffraction image of p53R280K. The circle delimitates the high-resolution limit at 2.0 Å. The diffraction image was obtained at 12.81 keV (ID30A-3, ESRF) using a crystal-to-detector distance of 144.8 mm and an oscillation angle of 0.15°.

Annex II

Supporting information of Chapter III

Ana Sara Gomes*, Helena Ramos*, Sara Gomes, Joana B Loureiro, Joana Soares, Valentina Barcherini, Paola Monti, Gilberto Fronza, Carla Oliveira, Lucília Domingues, Margarida Bastos, Daniel FAR Dourado, Ana Luísa Carvalho, Maria João Romão, Benedita Andrade Pinheiro, Alexandra Carvalho, Filipa Marcelo, Maria MM Santos, Lucília Saraiva, (2018), “*SLMP53-1 reactivates mutant p53 by targeting DNA-binding domain”,* under revision.

*The authors contributed equally to the work.

PDB files (please find the following files in the PDBs folder in the Flash Driver):

MD of mutp53 R280K (6FF9) with SLMP53-1 mode 1

MD of mutp53 R280K (6FF9) with SLMP53-1 mode 2

MD of wtp53 (2OCJ) with SLMP53-1 mode 1

MD of wtp53 (2OCJ) with SLMP53-1 mode 2

Docking of mutp53 Y220C with PK7242 (3ZME)

MOL file (please find the following files in the PDBs folder in the Flash Driver):

Atomic partial charges of SLMP53-1

Table S1. List of antibodies used in western blot experiments.

Antigen	Final Dilution	Supplier
Primary antibodies		
GAPDH (6C5) Mouse monoclonal	1:10000	Santa Cruz Biotechnology **Cat#sc-32233; RRID:AB_627679**
p53 (DO-1) Mouse monoclonal	1:5000	Santa Cruz Biotechnology **Cat #sc-126; RRID:AB_628082**
Pgk1p (22C5D8) Mouse monoclonal	1:10000	Invitrogen **Cat#459250**
Secondary antibodies		
Anti-mouse HRP-conjugated	1:5000	Santa Cruz Biotechnology **Cat #sc-2005; RRID:AB_631736**

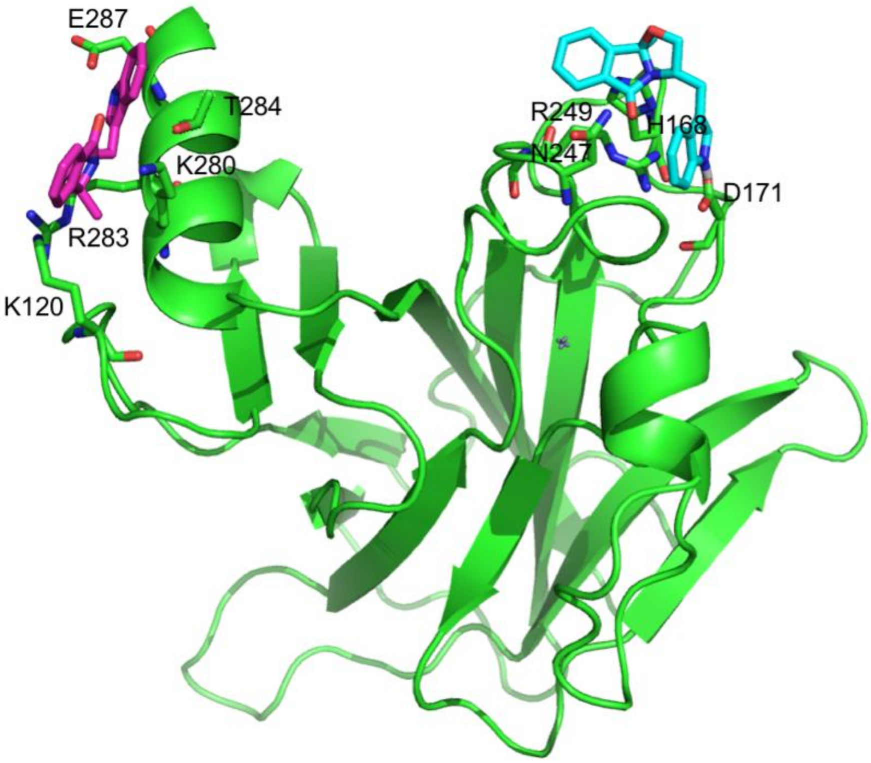
E287
T284
K280
R283
K120
R249
N247
H168
D171

Figure S1. Binding modes of SLMP53-1 to mutp53 R280K DBD monomer. Molecular docking image shows the binding sites of mutp53 R280K (PDB ID code: 6FF9, in green) with SLMP53-1 (in pink and blue) derived by AutoDock.

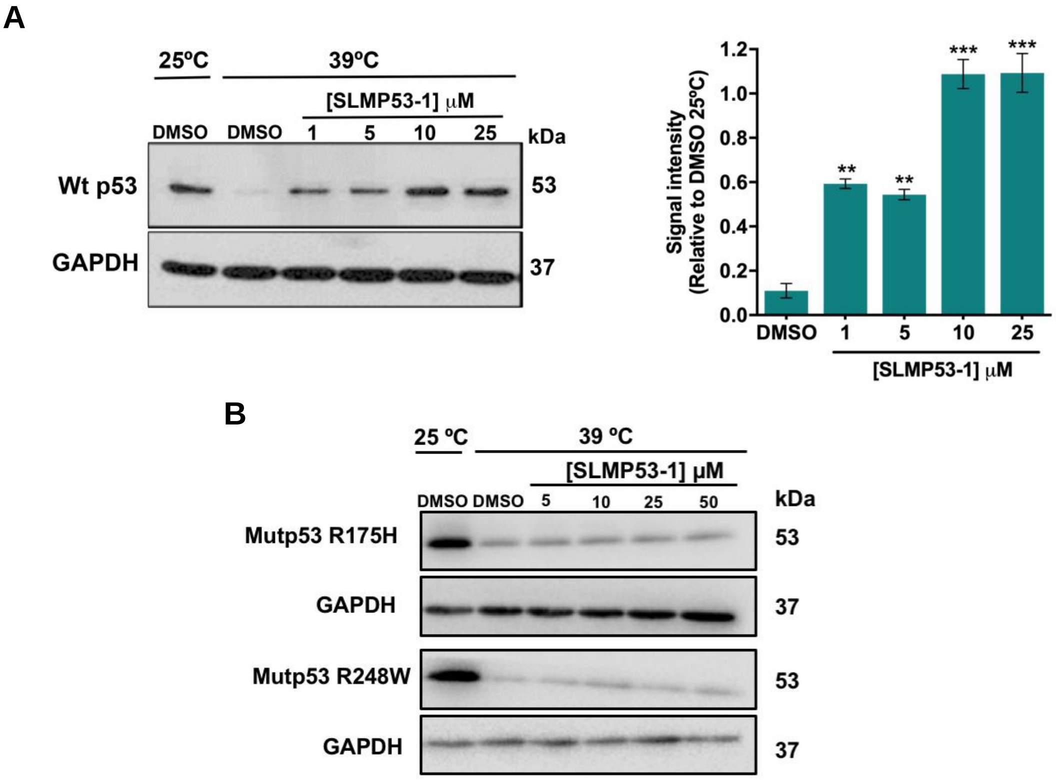

Figure S2. SLMP53-1 (A) induces wtp53 thermal stabilization, but (B) does not stabilize R175H and R248W. CETSA was performed in **(A)** wtp53-expressing HCT116 and **(B)** mutp53-expressing SK-BR3 (R175H) and SW837 (R248W) cancer cells lysates. Lysate samples were treated with increasing concentrations of SLMP53-1 and heated at 39 °C. Immunoblot represents one of three independent experiments; GAPDH was used as a loading control. Plotted data represent the amount of non-denatured wtp53 after heating at 39 °C, in SLMP53-1-treated HCT116 lysates relatively to DMSO at 25 °C (set as 1); data are mean ± SEM of three independent experiments; values significantly different from DMSO at 39 °C: ***p*<0.001, ****p*<0.001 (unpaired Student’s t-test).

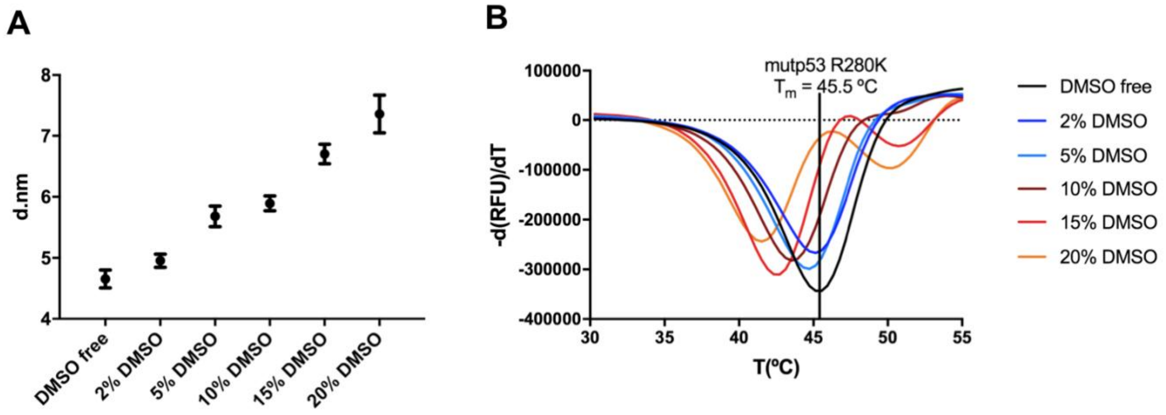

Figure S3. DMSO influence in structural and thermal stability of recombinant mutp53 R280K DBD. (A) Hydrodynamic diameter (d. nm) of mutp53 R280K DBD by Dynamic Light Scattering (DLS) analysis with increasing concentrations of DMSO (2–20%). Mutp53 R280K DBD in 50 mM Tris.HCl, 300 mM NaCl, 5 mM DTT (pH 7.2) buffer without DMSO was used as reference. With increasing DMSO concentration, the hydrodynamic diameter of mutp53 R280K also increases, suggesting protein oligomerization. Samples of mutp53 R280K DBD at 8 μM were prepared in 1 mL of protein buffer with proportional amount of DMSO (0–20%, (*v/v*)) and were analyzed in Malvern Zetasizer, MODEL NANO ZS (Malvern Instruments Limited, UK), at 20 ºC, in triplicates. **(B)** Thermal denaturation of mutp53 R280K DBD by Differential Scanning Fluorimetry (DSF) with increasing concentrations of DMSO (2–20%). Mutp53 R280K in 50 mM HEPES, 150 mM NaCl, 5 mM DTT, 10 μM $Zn(CH_3COO)_2$, 5% (*v/v*) glycerol (pH 7.5) buffer without DMSO was used as negative control, with T_m = 45.5 ºC (black thermal denaturation curve and T_m indicated with vertical line). DMSO concentration increment decreases mutp53 R280K DBD T_m (colored thermal denaturation curves) with observed differences up to 4 ºC when compared to wt-p53 T_m, indicating thermal destabilization. A reaction mixture (20 μL) was prepared in each well (of MicroAmp® Fast 96-well Reaction Plate, 0.1 mL, Applied Biosystems): 2 μL of mutp53 R280K DBD with final concentration 1.5 μM, 2 μL of SYPRO®Orange (5×; Protein Thermal Shift Dye KitTM, Applied Biosystems), 5 μL of dye buffer, proportional amount of DMSO (0–20%, (*v/v*)) and protein buffer to complete the 20 μL. Samples were analyzed in a StepOnePlus Real-Time PCR system (Applied Biosystems) scanning temperature range from 25 to 95 ºC, at 1 ºC/min, with ROX (rhodamine X; 575/602 nm) filters. **(A)** and **(B)** Data were analyzed in GraphPad Prism 7 software.

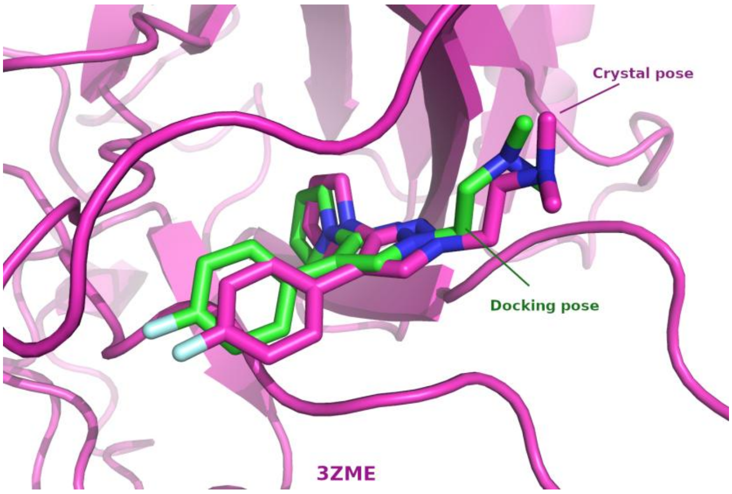
Crystal pose
Docking pose
3ZME

Figure S4. Superposition of the crystal structure of mutp53 Y220C DBD with ligand PhiKan7242. Docking pose predicted by autodock using crystallographic structure model PDB ID code: 3ZME (the r.m.s.d. of the ligands is 1.01 Å, after the protein alignment).

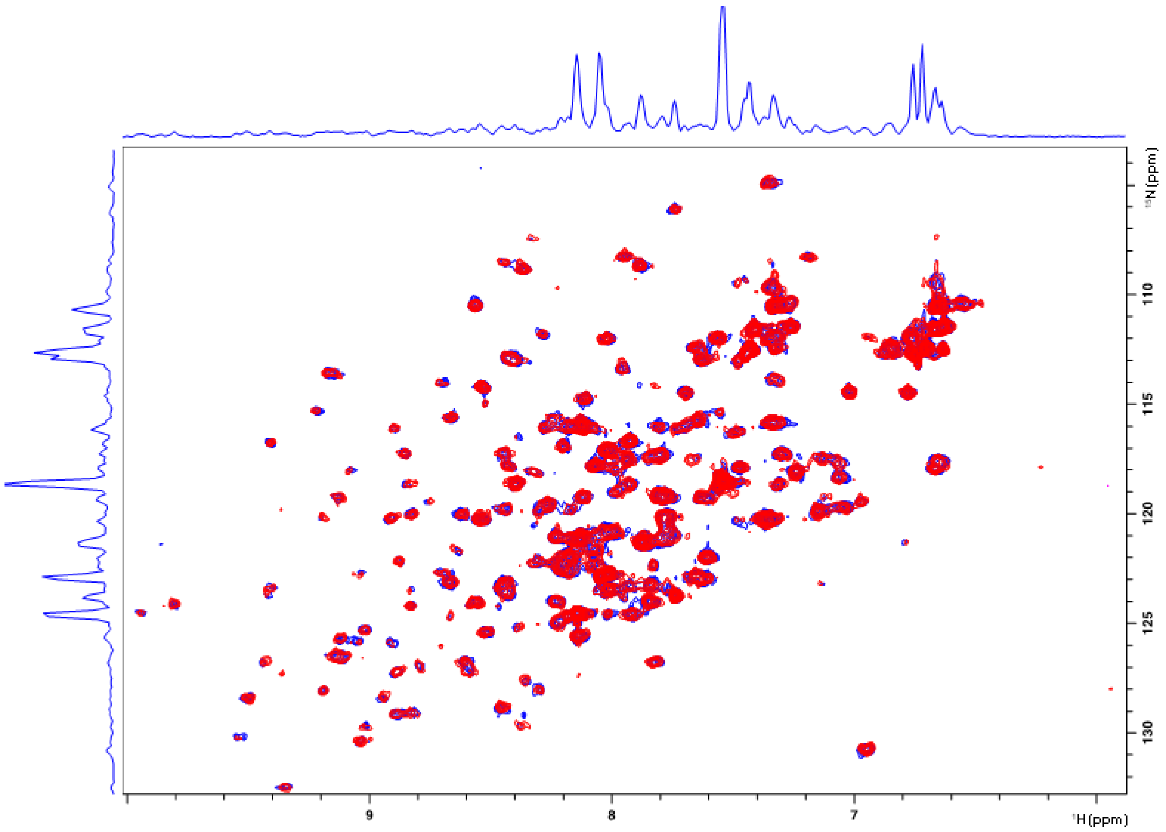

Figure S5. ^{1}H, ^{15}N-HSQC of mutp53 R280K DBD with SLMP53-1. To uncover the binding site in mutp53 R280K DBD–SLMP53-1 complex a chemical-shift perturbation (CSP) in ^{1}H, ^{15}N-HSQC analysis of the was performed. Experiments were performed using a protein:ligand molar ratio of 1:2.5 (mutp53 R280K DBD at 80 µM and SLMP53-1 at 200 µM final concentrations) in D_2O/DMSO-d_6 (93:7) 50 mM HEPES (pH 7.5), 150 mM NaCl, 5 mM DTT, 10 µM $Zn(CH_3COO)_2$, 5% (*v/v*) glycerol buffer. ^{1}H, ^{15}N-HSQC spectra of ^{15}N-labelled mutp53 R280K DBD alone (blue) and with SLMP53-1 (red) were acquired at 298 K on a Bruker Avance 600 MHz spectrometer using a 5-mm inversed cryogenic probe with the following parameters: 40 scans, 2,048 points in T2, delay time of 0.5 ms, 128 points in T1, and spectral widths of 16 and 36 ppm in T2 and T1, respectively. The recombinant protein mutp53 R280K DBD was expressed in M9 minimum medium with ^{15}N-labeled ammonium chloride and other production and purification steps were performed as described in Materials and Methods section of **Chapter II**.

Annex III

Supporting information of Chapter IV

Ana Sara Gomes, Alexandra Correia, Antti Rahikkala, Flavia Fontana, João Pedro Martins, Zehua Liu, Dongfei Liu, Madalena M Pinto, Emília Sousa, Lucília Saraiva, Hélder Santos, (2019), "*Hyaluronic acid and folic acid functionalized mesoporous silicon nanoparticles for enhancement of LEM2 anticancer activity*", manuscript in preparation.

Table S1. Specific surface area (A_S), pore volume (V_P) and pore diameter (D_P) of UnTHCPSi and APTES-TCPSi nanoparticles.

NPs	A_S (m^2/g)	V_P (cm^3/g)	D_P (nm)
UnTHCPSi	242 ± 1	0.73 ±0.01	12.0 ± 0.1
APTES-TCPSi	352 ± 3	0.76 ± 0.03	8.6 ± 0.4

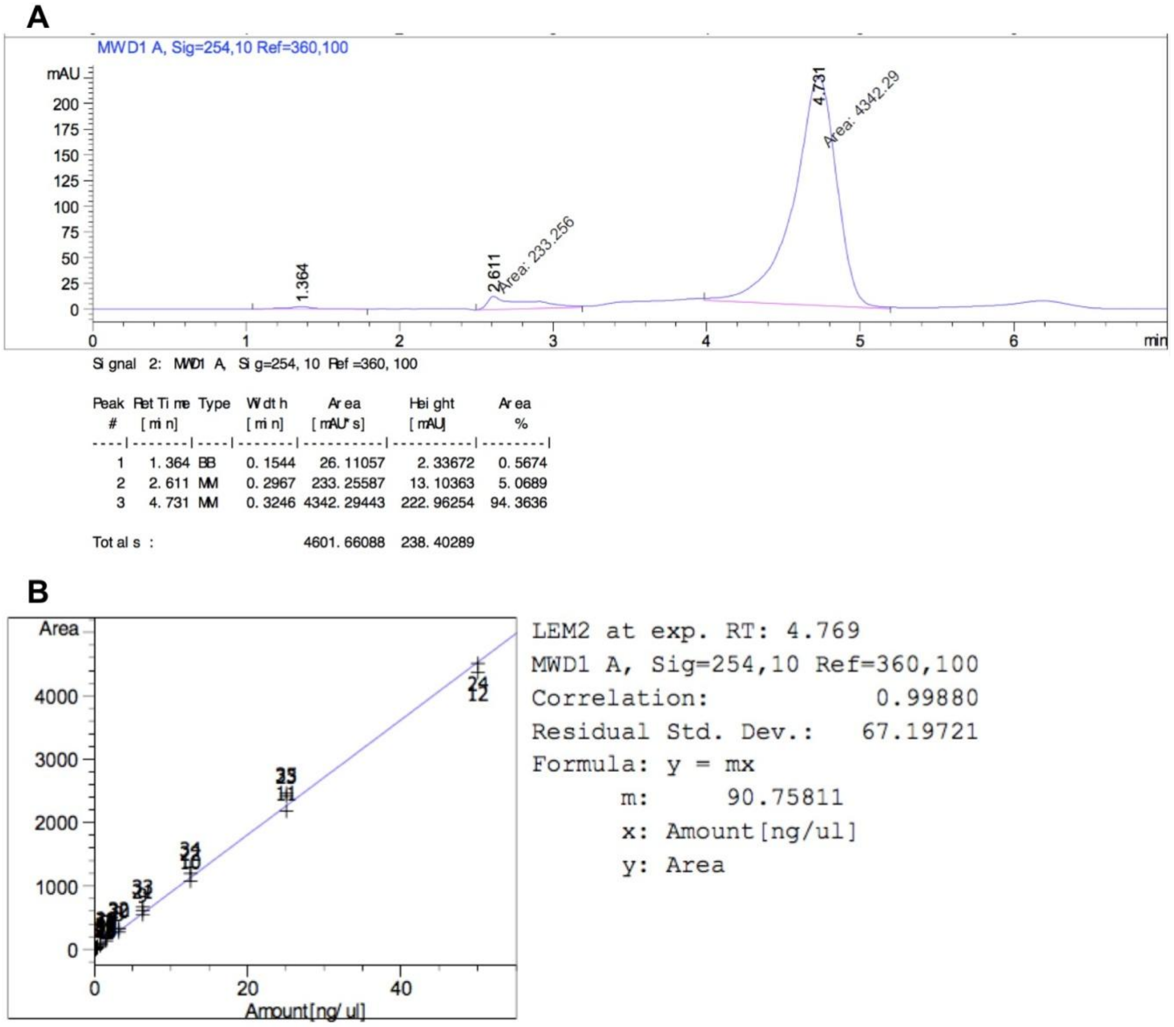

```
Signal 2: MWD1 A, Sig=254,10 Ref=360,100

Peak RetTime Type  Width     Area      Height     Area
  #   [min]        [min]   [mAU*s]     [mAU]       %
----|-------|----|-------|----------|----------|--------|
  1   1.364 BB    0.1544   26.11057    2.33672   0.5674
  2   2.611 MM    0.2967  233.25587   13.10363   5.0689
  3   4.731 MM    0.3246 4342.29443  222.96254  94.3636

Totals :                 4601.66088  238.40289
```

```
LEM2 at exp. RT: 4.769
MWD1 A, Sig=254,10 Ref=360,100
Correlation:             0.99880
Residual Std. Dev.:     67.19721
Formula: y = mx
       m:      90.75811
       x: Amount[ng/ul]
       y: Area
```

A
MWD1 A, Sig=254,10 Ref=360,100
mAU
200
175
150
125
100
75
50
25
0
1.364
2.611
Area: 233.256
4.731
Area: 4342.29
0
1
2
3
4
5
6
min
B
Area
4000
3000
2000
1000
0
0
20
40
Amount[ng/ul]
24
12
35
11
34
10
33
30

Figure S1. LEM2 (A) chromatogram and (B) calibration curve in DCE. (A) LEM2 retention time was about 4.7 min in a HPLC Agilent 1 260 with a C18 column (4.6 × 150 mm, 5 µm, Supelco Discovery), mobile phase of methanol/water (70:30) in an isocratic mode, at room temperature. The injected volume was 20 µL, the analysis flow rate was 0.7 mL/min, and the detection was performed at 240 nm. **(B)** LEM2 calibration curve (0.047–48.5µg/mL) in DCE in triplicate with correlation value (R) of 0.99880.

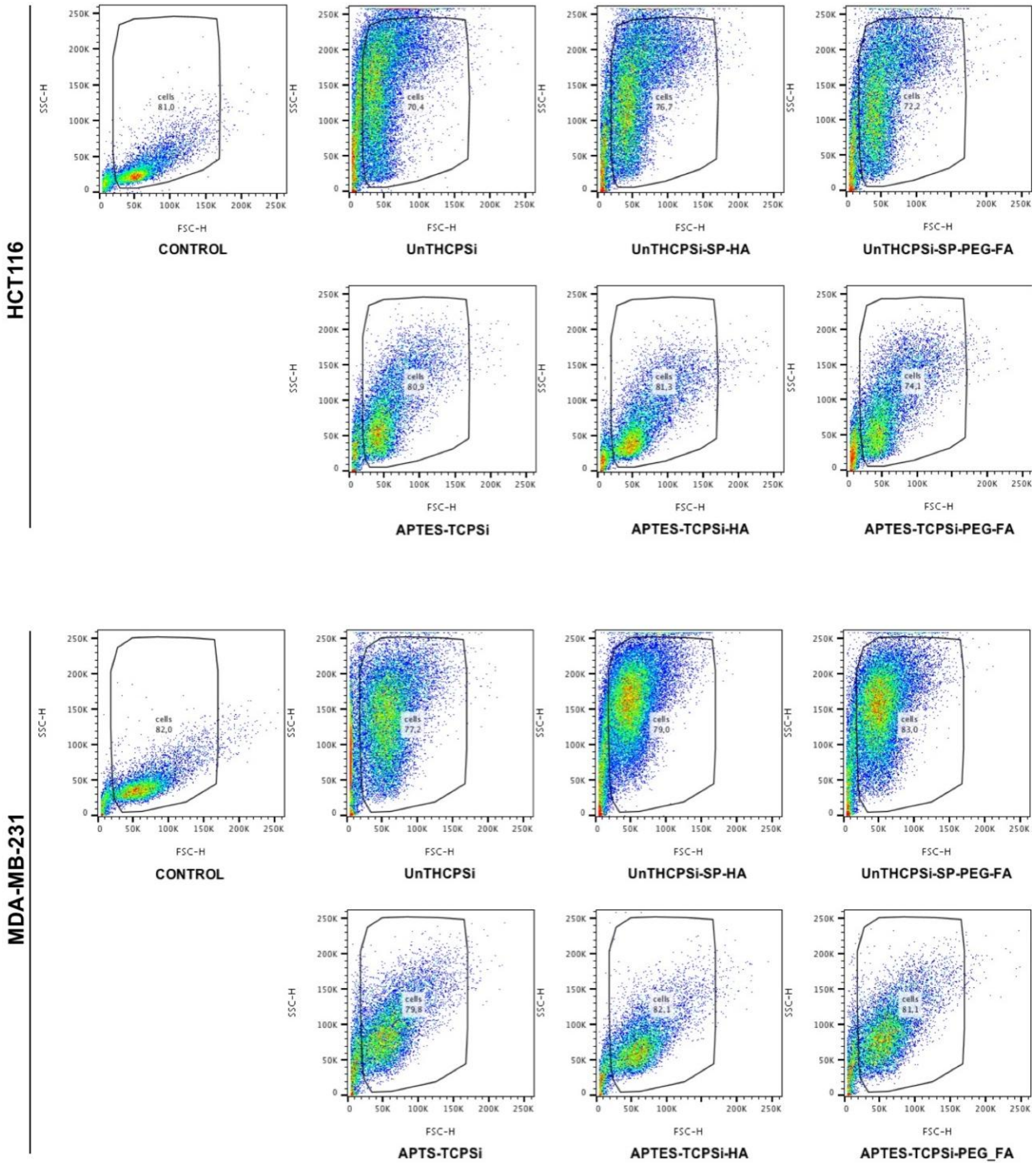

Figure S2. Human cancer cells granularity/complexity is affected upon NPs treatment. Density plots of side and forward scattered light (SSC and FSC) signals of HCT116 and MDA-MB-231 cancer cells treated with fluorescent NPs (Alexa488 for UnTHCPSi core; FITC for APTES-TCPSi core) for 3 h, at 50 μg/mL or vehicle as negative control (to define cells population). Black line indicates cells population gating for further analysis.

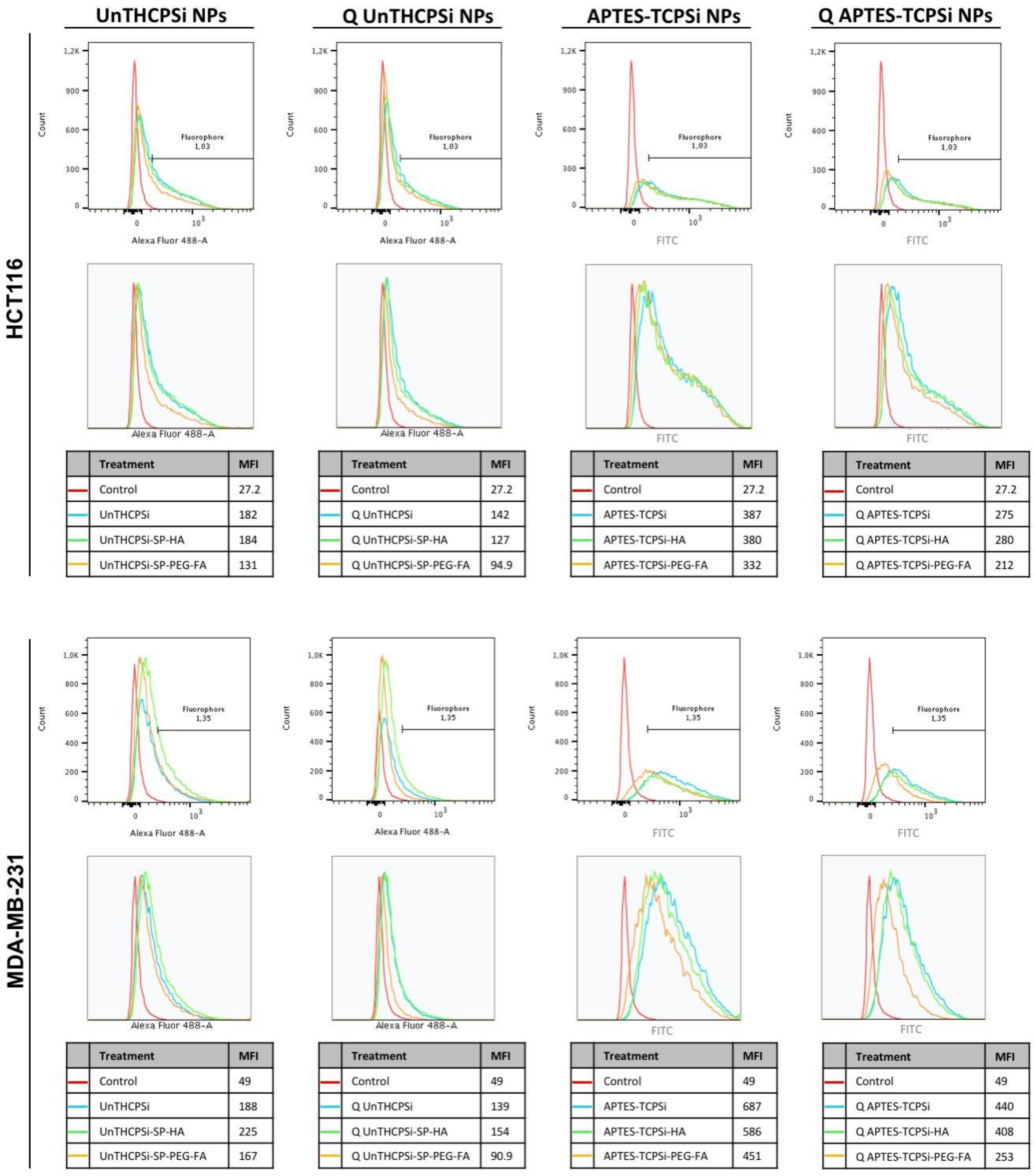

HCT116 – UnTHCPSi NPs

	Treatment	MFI
🟥	Control	27.2
🟦	UnTHCPSi	182
🟩	UnTHCPSi-SP-HA	184
🟧	UnTHCPSi-SP-PEG-FA	131

HCT116 – Q UnTHCPSi NPs

	Treatment	MFI
🟥	Control	27.2
🟦	Q UnTHCPSi	142
🟩	Q UnTHCPSi-SP-HA	127
🟧	Q UnTHCPSi-SP-PEG-FA	94.9

HCT116 – APTES-TCPSi NPs

	Treatment	MFI
🟥	Control	27.2
🟦	APTES-TCPSi	387
🟩	APTES-TCPSi-HA	380
🟧	APTES-TCPSi-PEG-FA	332

HCT116 – Q APTES-TCPSi NPs

	Treatment	MFI
🟥	Control	27.2
🟦	Q APTES-TCPSi	275
🟩	Q APTES-TCPSi-HA	280
🟧	Q APTES-TCPSi-PEG-FA	212

MDA-MB-231 – UnTHCPSi NPs

	Treatment	MFI
🟥	Control	49
🟦	UnTHCPSi	188
🟩	UnTHCPSi-SP-HA	225
🟧	UnTHCPSi-SP-PEG-FA	167

MDA-MB-231 – Q UnTHCPSi NPs

	Treatment	MFI
🟥	Control	49
🟦	Q UnTHCPSi	139
🟩	Q UnTHCPSi-SP-HA	154
🟧	Q UnTHCPSi-SP-PEG-FA	90.9

MDA-MB-231 – APTES-TCPSi NPs

	Treatment	MFI
🟥	Control	49
🟦	APTES-TCPSi	687
🟩	APTES-TCPSi-HA	586
🟧	APTES-TCPSi-PEG-FA	451

MDA-MB-231 – Q APTES-TCPSi NPs

	Treatment	MFI
🟥	Control	49
🟦	Q APTES-TCPSi	440
🟩	Q APTES-TCPSi-HA	408
🟧	Q APTES-TCPSi-PEG-FA	253

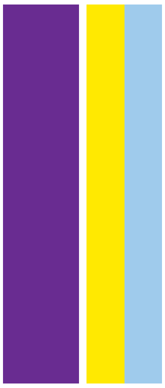Figure S3. Fluorescence signal of cancer cells treated with NPs. Histograms with tables summarizing mean fluorescence intensity (MFI) analysis of HCT116 and MDA-MB-231 cancer cells treated with fluorescent NPs (Alexa488 for UnTHCPSi core; FITC for APTES-TCPSi core) for 3 h, at 50 µg/mL or vehicle as negative control. Approximately 10,000 events were acquired for each sample. Histograms and tables represent one of three independent experiments.